Cryogenic phonon-scintillation detectors with NTD germanium readout

Philip Coulter

St Catherine's College

A thesis submitted in partial fulfilment of the requirements for the degree of Doctor of Philosophy at the University of Oxford, Trinity Term 2013

Abstract

Cryogenic detectors are an advanced technology for both dark matter and neutrinoless double beta decay searches, having the key advantage of a range of possible absorber materials that can be used for the detectors. Neutron transmutation doped germanium sensors are highly sensitive thermometers ideal for use at milli kelvin temperatures, with a simple repeatable resistance temperature relation. To discriminate between candidate events and background events simultaneous measurements can be made of the energy deposited in the detector as phonons and the energy emitted by the absorber crystal as scintillation light.

Phonon detectors with a calcium tungstate or calcium molybdate crystal as the target and an NTD sensor as a thermometer were made in Oxford, along with a light detector with a light-absorbing silicon layer on a sapphire crystal, also with an NTD thermometer. A system of electronics was designed and tested in Oxford to bias and readout the NTD thermometers, while the setup inside the cryostat was developed to provide a thermally and mechanically stable shielded environment for the detectors. As part of this, prototype semi-rigid kapton cabling for use in the EDELWEISS experiment was installed and tested in the cryostat.

Three different NTD germanium sensor types were characterized and calibrated in the cryostat and two of these selected for use on the phonon and light detectors. The detectors were operated at temperatures as low as 9 mK and tested with radioactive sources to produce energy spectra. Baseline resolutions of 1.7 keV and 2.5 keV, respectively, were achieved for the calcium molybdate and calcium tungstate phonon detectors. A working scintillation light detector was demonstrated as part of a phonon-scintillation detector module with a suggested application in double-beta decay searches.

Table of Contents

Acknowledgements

I would especially like to thank Professor Hans Kraus for the opportunity to do this work, and for the invaluable guidance and support throughout my time as a DPhil student.

Thanks to my colleagues in the lab for all the advice, assistance and encouragement.

I would also like to thank my family and friends for support and for welcome distractions from work throughout the last number of years.

Finally, I would like to thank STFC for funding this work.

Introduction

There is astrophysical evidence that the majority of the matter in the universe is non-baryonic and non luminous, and is instead some new form of matter known as dark matter [1-3]. There are several different candidates for this, with one of the more popular being weakly interacting massive particles (WIMPs). There are currently a number of different experiments attempting to directly detect these WIMPs, with one possible method of detection involving the use of cryogenic particle detectors [4]. Cryogenic detectors also provide a method of searching for neutrinoless double beta decays ($0\nu\beta\beta$) [5], a decay mode which requires the violation of lepton number conservation and the existence of Majorana neutrinos [6]. In addition to this, the measurement of the decay rate for this process provides a measurement of the neutrino mass.

Such cryogenic detectors have been made and operated in Oxford, using neutron transmutation doped germanium (NTD Ge) temperature sensors in a detector unit with two detectors, one to measure the heat produced in an interaction, the other measuring the scintillation light emitted from the main detector. The ratio of scintillation light emitted to heat may be used for background discrimination [7]. Detectors with calcium tungstate (used in dark matter searches) and calcium molybdate (a potential $0\nu\beta\beta$ candidate) were tested. This setup can then be used to investigate the properties of other potential target materials in the future.

The thesis begins with an overview of dark matter and neutrinoless double beta decay, and the use of cryogenic detectors in these searches. Then the setup of the detector, its surroundings and the readout system are described. The detectors were operated in an above ground laboratory in Oxford, meaning that the radioactive background is a major issue for the detectors affecting both the temperature stability of the detector

and the amount of pulses which may be used to give a reliable energy measurement. The shielding of the detector is used to provide a reduction of the number of energy depositions in the detector due to the radioactive background..

The setup of the detector itself affects the sensitivity and signal shape of the detector through its heat capacity and thermal connection to the heat bath. The amount of scintillation light expected from the phonon (heat) detector crystal, and the reflecting cavity used to maximise the light collected by the light detector are also described. Following this is an explanation of the readout electronics and the bias for the detector, and then the NTD Ge temperature sensors used in this thesis and a summary of responsivity measurements and associated parameter determination for three different sensors. Temperature models are then presented for both the response of the detector to a particle interaction and for the stabilisation of its operating temperature. The required stabilisation is achieved in two ways, with a heater and thermometer pairing providing temperature control of a stage in the cryostat and by thermally decoupling the detector housing from any fluctuations, reducing the size and frequency of temperature fluctuations at the detector.

Finally, the analysis method used for the data is described, with pulses identified and fit to extract a pulse height that can be converted to an energy value. Results are presented for the operation of the detectors in the presence of radioactive sources, allowing an estimation of the detectors' energy resolution and discrimination capability through measuring the phonon-scintillation energy ratio.

1. Dark Matter and Neutrinoless Double Beta Decay

This opening chapter will begin by describing the general idea of dark matter, along with some of the current astrophysical evidence for it and a few potential dark matter candidates. Following this, some experiments are presented which aim to detect indirect evidence of dark matter particles, by searching for their annihilation products. In section 1.5 several methods of directly detecting dark matter particles are described, including some involving cryogenic detectors similar to the ones developed throughout the thesis.

In the second part of the chapter, beginning in section 1.6, the concept of neutrinoless double beta decay is introduced, and its implications for lepton number and neutrino mass described. Finally some of the experimental searches for such neutrinoless double beta decays are described, including some which use cryogenic detectors with a target material containing potential neutrinoless double beta decay isotopes.

1.1 Dark Matter

In 1933 Fritz Zwicky measured the velocity distribution of galaxies in the Coma Cluster and used these to make an estimate of the mass of the cluster [8]. He found a mass to light ratio much higher than expected. Further evidence from astrophysical and cosmological observations backed this up and indicated that a large part of the universe is made up of matter, known as dark matter, that is non-baryonic and non-luminous [1-3]. This evidence is described in more detail in section 1.2.

To explain the implications of dark matter for cosmology a short description of the standard cosmological model is useful. Using general relativity, the Friedmann-Robertson-Walker metric may be derived with the assumption that four-dimensional

space time is isotropic and homogenous on large scales. This gives eq. 1.1 which describes the expansion or contraction of the universe over time,

$$ds^2 = -c^2dt^2 + a(t)^2\left(\frac{dr^2}{1-kr^2} + r^2d\Omega^2\right),$$

Eq. 1.1

where k is the curvature of spacetime, with values of $k = -1, 0, +1$, and $a(t)$ is a scale factor describing the expansion of the universe [1]. Using this metric, the Friedmann equation is found [9].

$$\left(\frac{\dot{a}}{a}\right)^2 + \frac{k}{a^2} = \frac{8\pi G_N}{3}\rho_{tot} + \frac{\Lambda}{3}.$$

Eq. 1.2

The term ρ_{tot} is the average energy density of the universe, and Λ is the cosmological constant. The cosmological constant, the curvature term and the density term all have different dependences on a, hence the relative size of these terms will affect how the universe evolves. The density term can be split up into several components corresponding to different types of particles which contribute to the energy density. These different components of the energy density are often be expressed in terms of a fraction of the critical density, ρ_{crit}, the density for a flat (Euclidean) universe (k=0) with no cosmological constant.

$$\rho_{crit} = \frac{3}{8\pi G_N}\left(\frac{\dot{a}}{a}\right)^2 = \frac{3H^2}{8\pi G_N},$$

Eq. 1.3

where H is the Hubble constant. These fractions are known as density parameters, Ω_i.

$$\Omega_i \equiv \frac{\rho_i}{\rho_{crit}}.$$

Eq. 1.4

The effect of the geometry, k, and the cosmological constant, Λ, may also be given in this form as Ω_k and Ω_Λ respectively. For a flat universe, these energy densities add up

to give a total density so that $\Omega = 1$. For $k = 1$ it will give a spherical geometry with $\Omega > 1$, and for $k = -1$ it will give a hyperbolic geometry with $\Omega < 1$. In the next section, results from the Planck collaboration [10] and others will be presented, showing that the total energy density Ω is close to 1 and that the energy density due to baryonic matter is significantly smaller than the total matter energy density.

Dark matter candidates may be divided into several different categories according to their effect on structure formation in the universe. Hot Dark Matter (HDM) consists of particles that travel at relativistic speeds, typically light particles such as neutrinos. On the other hand Cold Dark Matter (CDM) consists of non-relativistic particles, such as Axions or WIMPs. The CDM model fits better with observations of structure in the universe, and would generally be favoured over the HDM model [2, 11].

The model chosen for dark matter, and the properties of the candidate particle, will affect the dark matter density expected in the universe today. In the early universe dark matter particles were in thermal equilibrium with other particles, but as the universe cooled the interaction rate of the dark matter particles fell below the rate of expansion for the universe and they decoupled from the rest leaving a 'relic density' of particles which remains today [2]. The cross-section can therefore be related to the current density of dark matter [1].

$$\Omega_{DM} h^2 \approx \frac{3\times10^{-27} cm^3 s^{-1}}{\langle \sigma v \rangle}, \qquad \textbf{Eq. 1.5}$$

where v is the velocity of the particles, σ is the interaction cross-section of the particles and h is a dimensionless parameter related to the Hubble constant by

$$H = 100h\_kms^{-1}Mpc^{-1}. \qquad \textbf{Eq. 1.6}$$

The size of these parameters will be described in more detail later, but would be expected to have typical values of v = 220 km/s, $h = 0.67$ and $\Omega_{DM} \sim 0.25$. For the

CDM model and the expected dark matter density, this gives a value for the cross-section similar to that of the weak interaction.

1.2 Astrophysical evidence for Dark Matter

Astrophysical measurements have presented evidence for the theory of dark matter from a number of sources, suggesting the presence of a 'halo' of non-luminous matter around stars, galaxies and galaxy clusters. This evidence appears on a variety of scales, from the rotation curves of galaxies, to the velocity distributions of galaxy clusters and finally on a cosmological scale in the level of anisotropy of the cosmic microwave background or models of nucleosynthesis in the Big Bang. This section will summarize each of these in turn.

1.2.1 Rotation curves of spiral galaxies

In spiral galaxies the material within the galaxy is bound by gravity. Most of the observable material forms a thin disk, in which the stars and gas rotate about the centre of the galaxy in roughly circular orbits. Therefore observations of the velocities of stars within a spiral galaxy can be related to the mass density of the galaxy using Kepler's law: [3]

$$v = \sqrt{\frac{GM(r)}{r}}\,.$$

Eq. 1.7

The velocity is given by eq. 1.7 where v is the circular velocity at a radius r, and M(r) is the mass of the galaxy contained within radius r. This suggests that for the luminous matter alone, which is concentrated at the centre of the galaxy, the velocity should fall off with radius as $r^{-½}$.

This is not observed in actual measurements of rotation curves; in fact, the velocity levels off and the mass should increase proportional to r – this difference to the

expected mass distribution can be explained by a halo of non-luminous 'dark matter' around the centre of the galaxy.

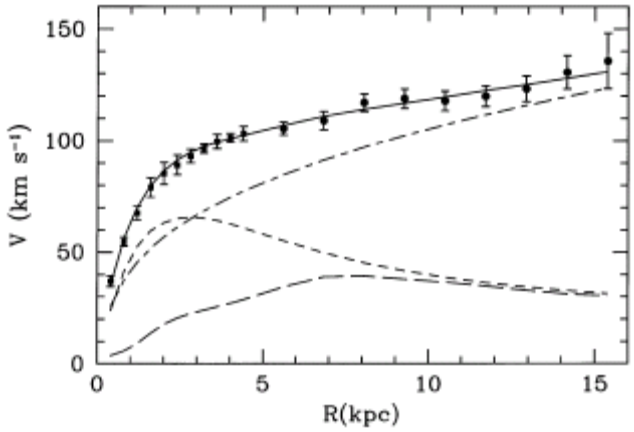

Figure 1.1 - Plot, from [12], showing the rotation curve for galaxy M33 with the data (points) and the best fitting model (continuous line). The dotted and dashed line is the halo, the short dashed is the stellar disk, and the long dashed line is the gas contribution.

1.2.2 Velocity dispersion in galaxy clusters

As galaxies move along their orbits in a cluster, their orbital velocities are balanced by the gravitational potential of the cluster. The Virial Theorem allows the average kinetic energy $\langle T \rangle$ of a system of N objects of mass m and average velocity v, bound by a potential energy V, to be related to the average total potential energy of the system $\langle V_{TOT} \rangle$.

$$\langle T \rangle = \frac{1}{2} N m v^2 = \frac{1}{2} \langle V_{TOT} \rangle .$$

Eq. 1.8

Therefore by measuring the velocities of galaxies within a cluster, an estimate can be made of the total mass of the cluster [3].

This was one of the earliest indications of dark matter, as Fritz Zwicky used measurements of galaxies in the Coma Cluster to infer the existence of some invisible matter. He found that the mass estimate from the virial theorem was almost ten times as large as the total mass of the galaxies.

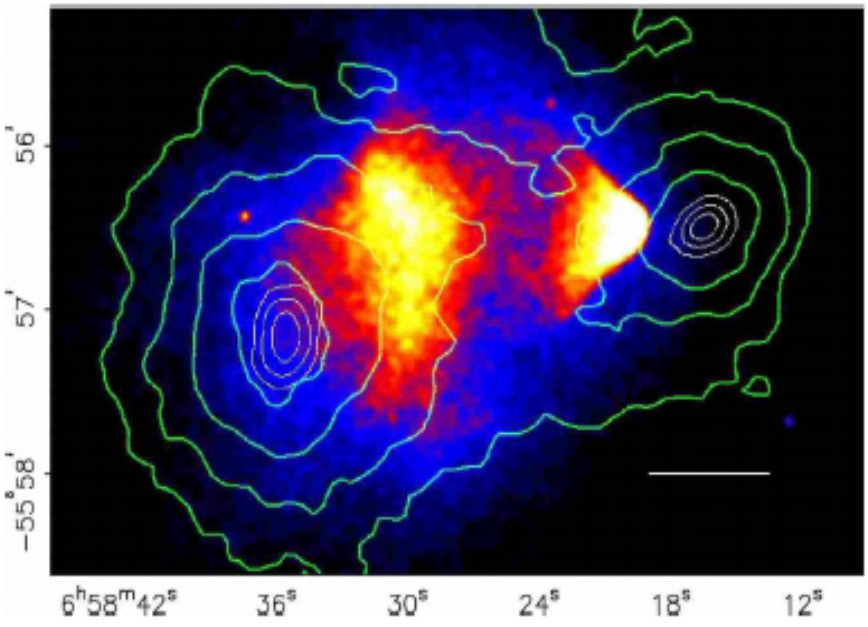

Figure 1.2 - An image of cluster 1E0657-558, from [13], showing the luminous mass distribution as a coloured image, while the total mass distribution is shown as the green contours.

1.2.3 X-ray emission in galaxy clusters

Between galaxies within a cluster, there is a cloud of hot gas known as the intercluster medium (ICM). This hot gas can be observed by its emission of X-rays. If it is assumed that the cloud is in hydrostatic equilibrium then the intensity of these X-rays may be used to estimate the mass of the cluster.

$$\frac{3}{2}k_B T = \frac{1}{2}\langle PE \rangle .$$

Eq. 1.9

This again finds that the estimated mass of the cluster is higher than would be expected given the luminosity of the cluster, but has also been used to find dramatic results for colliding galaxy clusters such as MACS J0025.4-1222 and the Bullet Cluster (merging cluster 1E0657-558), shown in figure 1.2. These consist of two clusters which are merging, leading to a spatial separation between the fluid-like X-ray emitting gas and the bulk of the total mass distribution (determined by gravitational lensing) [13, 14].

1.2.4 Cosmic Microwave Background

In the early universe, radiation and matter densities were coupled together electromagnetically, with their perturbations forming a series of acoustic oscillations in the density of the photon-baryon fluid. As the universe cooled and these decoupled from each other, these oscillations were left as an anisotropic distribution in the temperature of the photons. These photons from the surface of last scattering form the Cosmic Microwave Background (CMB), the anisotropy of which can be modelled and predicted using a number of parameter including the baryonic fraction of the total mass density.

Measurements of the temperature power spectra for the CMB give a series of peaks and troughs, the position and magnitude of which are sensitive to these parameters. Using measurements of the CMB from the Wilkinson Microwave Anisotropy Probe (WMAP) [15] some of these parameters were calculated to be

$$0.9821 < \Omega_{TOT} < 1.0081$$

$$\Omega_B = 0.0456 \pm 0.0015$$

$$\Omega_{DM} = 0.228 \pm 0.0013$$

More recently the Planck satellite [10] measured these and found improved values with higher mass, both for baryons and dark matter.

$$\Omega_B = 0.0496 \pm 0.0007$$

$$\Omega_{DM} = 0.269 \pm 0.0069$$

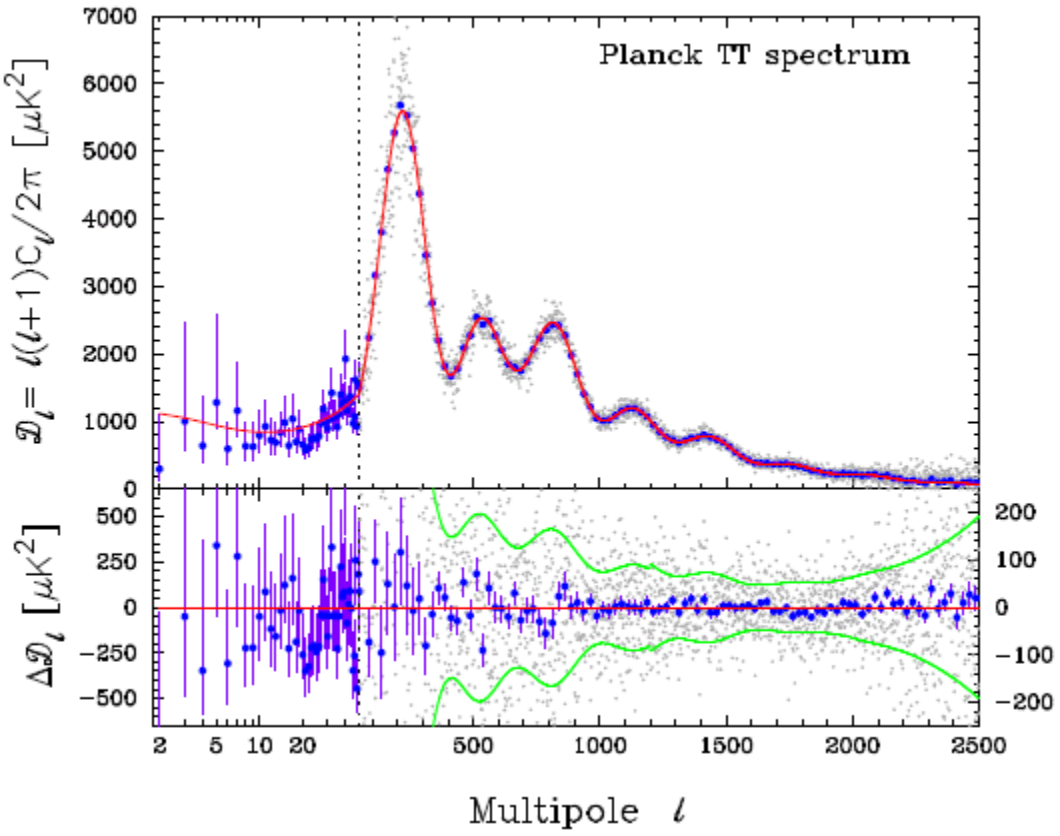

Figure 1.3 – Plot from [10] showing temperature (TT) and power spectra based on the Planck data.

1.2.5 Big Bang Nucleosynthesis

The fraction of the universe as baryons may also be constrained by creation of light nuclei during the early universe in a process known as Big Bang Nucleosynthesis (BBN) [16, 17]. The formation of these light elements can be modelled as a function of the baryon density, then using the abundances of different light nuclei in the current universe an estimate of the baryon density can be made. This gives $\Omega_B h^2 = 0.0226 \pm 0.0017$, and using a value for the Hubble constant this will give ~4.6% of the universe as baryonic compared to a further ~23% that must be some non-baryonic dark matter.

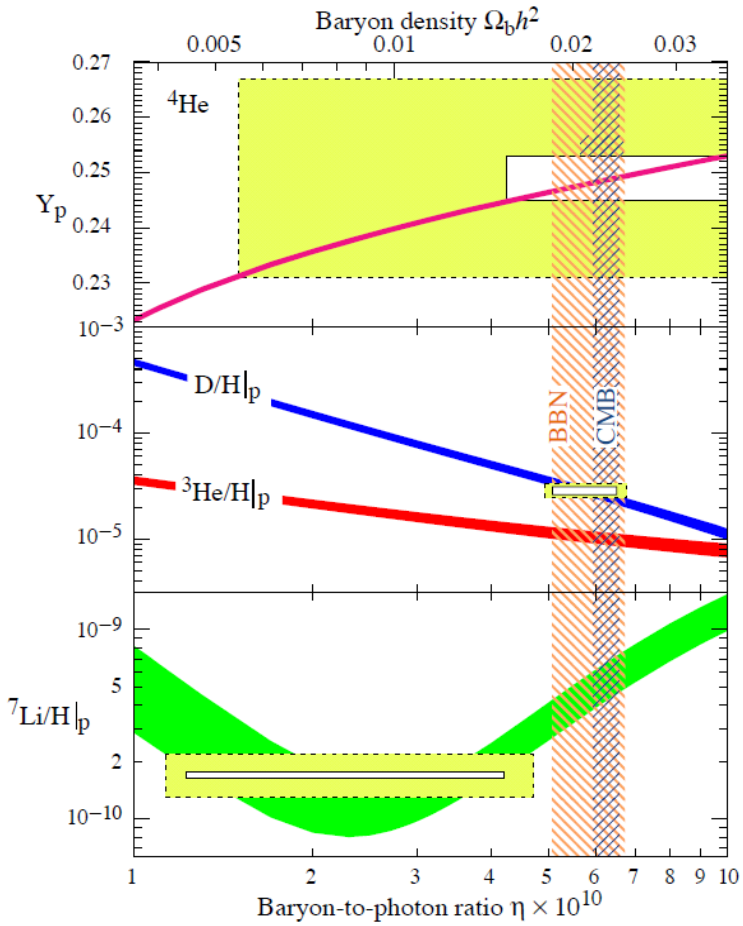

Figure 1.4 – From [18]. The solid bands show the relative abundance by mass of different light elements as predicted by BBN. The vertical bands show the BBN concordance range and the CMB value for baryon density (both at 95% CL) and the boxes show the observed light element abundances.

1.3 Dark Matter candidates

Astrophysical evidence for dark matter therefore exists on a range of scales, and there are a number of potential candidates [1]. These must firstly have very weak interactions with photons. They must also have weak baryonic interactions in order to fit the CMB power spectra. The candidate particle should also have a small self-interaction strength, otherwise the dense dark matter halos would quickly evaporate. There will be some baryonic dark matter objects – neutron stars, black holes, and brown dwarfs, collectively called MACHOs (Massive Compact Halo Objects) making up this extra mass. However, the density of these is not enough to give the complete

dark matter mass required by observations and evidence from big bang nucelosynthesis suggests that the majority of dark matter must be composed of non-baryonic material.

1.3.1 Weakly Interacting Massive Particles (WIMPs)

This is a term for a generic particle with masses, typically in the range from ~ 10 GeV to ~ 1000 GeV and with interactions of strength around the scale of the weak force [2]. For a type of particle to remain in thermal equilibrium in the early universe the interaction rate must be higher than the rate of expansion of the universe [1]. When the interaction rate falls below this the particles "freeze out" and the density (in co-moving coordinates) will remain constant. The cold dark matter density from observations is consistent with interaction strength at this level.

1.3.1.1 Supersymmetric WIMPs

A promising candidate for this kind of particle comes from the lightest particle in the theory of Supersymmetry (SUSY). SUSY aims to solve the hierarchy problem in particle physics by adding a new symmetry between bosons and fermions, and in the process brings a number of new particles – some of which are potential dark matter candidates. The Minimal Supersymmetric Standard Model (MSSM) brings in a new quantum number R and symmetry R-parity [19]. Every particle ($R = +1$) is provided with a super-particle with spin different by ½ and $R = -1$. This gives boson particles a fermionic super-partner and fermion particles a bosonic super-partner.

In many SUSY theories, the lightest supersymmetric particle (LSP) is expected to be stable, as R parity conservation prevents it from decaying into lighter particles, and thus it can only be destroyed by self-annihilation. There are a number of possibilities for what this LSP could be but one, the neutralino, forms one of the most promising dark matter candidates.

The neutralino is a SUSY particle made up of the supersymmetric partners for the electroweak and Higgs gauge bosons. It would be expected to be a Majorana particle with mass around 100 GeV and a spin independent interaction cross-section of 10^{-8} pb. With these properties, the neutralino as LSP would be a good candidate for a dark matter particle.

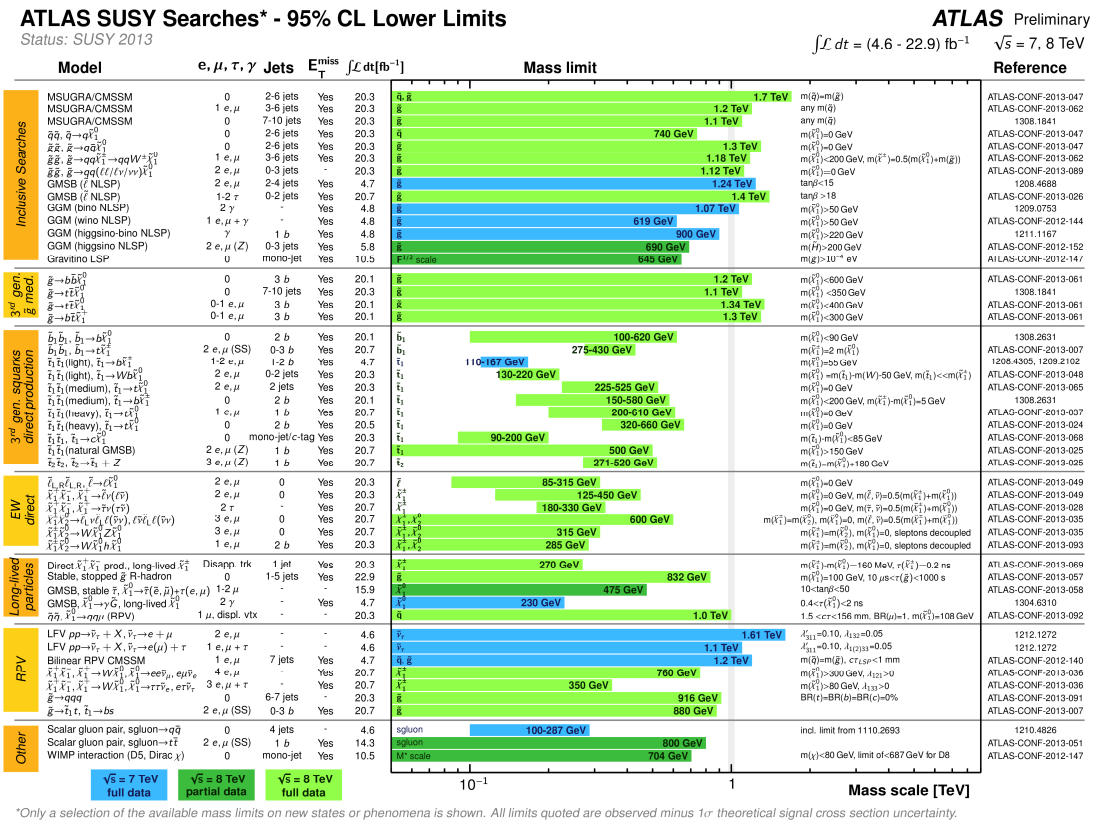

Figure 1.5 - Summary of exclusion limits set on supersymmetry by ATLAS data.

1.3.1.2 SUSY at the Large Hadron Collider

Searches for supersymmetric theories have taken place at collider experiments, including the Large Hadron Collider [20] and the Tevatron [21]. Typically these searches will produce jets with high transverse momentum and a large amount of missing energy corresponding to a pair of LSP particles which are left after a series of decays. These neutral, weakly interacting particles escape the detector leaving the missing energy.

At the time of writing, none of these searches have found significant excess over the standard model background, which places significant constraints on what supersymmetric models may exist [22, 23].

1.3.2 Axions

Quantum Chromodynamics (QCD) describes interactions of the strong nuclear force, however the theory allows some interactions which would violate the conservation of Charge Parity (CP). For QCD to remain valid, a solution must be found to this Strong CP problem – one such solution suppresses these interactions by the addition of a new particle, known as the axion. Current experimental evidence constrains the mass of these particles to be very low (~ 10 meV) [24] and they will interact very weakly with ordinary particles, but with the right relic density they can satisfy the parameters for cold dark matter.

Experiments looking to detect axions include CAST at CERN and ADMX, which use magnets to look for the conversion of axions into X-rays in a magnetic field. CAST look for solar axions, with a mass in the sub eV range around 0.5 eV [25], overlapping slightly with the range of hot dark matter axions. ADMX looks for much lower mass axions, with masses of a few μeV, in the dark matter halo [26]. This corresponds to the probable mass of cold dark matter axions.

1.3.3 Neutrinos

Another possible candidate for dark matter is the neutrino. In the past standard model neutrinos were considered to be a strong candidate for dark matter, but with the small neutrino mass they are simply not abundant enough to give the observed density of dark matter in the universe today.

Sterile neutrinos have also been proposed as dark matter and depending on their parameters could appear as either hot or cold dark matter [27]. They are currently

constrained by cosmological evidence such as measurements of the CMB which are able to measure the effective number of neutrinos (with the Planck satellite finding $N_{eff} = 3.30 \pm 0.27$ [28]) and limits on the sterile neutrino energy density for BBN.

1.4 Indirect searches for WIMPs

Indirect searches for dark matter involve the detection of the annihilation products of dark matter particles [1]. The self annihilation cross-section for WIMPs is proportional to the square of the local WIMP density, therefore it should be expected to occur in those regions where dark matter is most strongly concentrated – for example, the centre of the galaxy. However, there is still much uncertainty in this WIMP mass distribution.

As WIMP masses are relatively high, the annihilation should produce a range of possible particles for these indirect searches, including neutrinos, high energy gammas and various anti-particles.

1.4.1 Neutrinos

High energy neutrinos are used as the signature for several experiments. IceCUBE is based at the South Pole and uses an array of light detector distributed amongst the ice as a Cerenkov detector to search for the charged particles produced by neutrino interactions. These charged particles are likely to be produced by neutrinos or by muons and have a direction similar to that of the incident particle. Therefore an excess of neutrinos coming through the earth is searched for, to eliminate the background of cosmic muons in the other direction [29]. The signal for WIMP annihilation would be a monochromatic peak in the neutrino spectrum [30].

1.4.2 High energy gamma rays

The Fermi Space Telescope looks for a signal of gamma rays corresponding to the annihilation of dark matter particles into photons, or the photons produced by the Compton scattering of high energy electrons and positrons produced by the annihilation of dark matter [31]. This would give a signal with an annihilation peak and a cut off at the mass of the dark matter particle [32]. The Large Area Telescope used for detecting these gamma rays consists of alternating layers of thin tungsten foil, which converts the incoming photon into positrons and electrons via pair production, and silicon tracking detector. Finally the energy is measured in an electromagnetic caesium iodide calorimeter [33]. A segmented anti-coincidence detector made of plastic scintillating tiles surrounding the telescope is used to reject incoming charged particles.

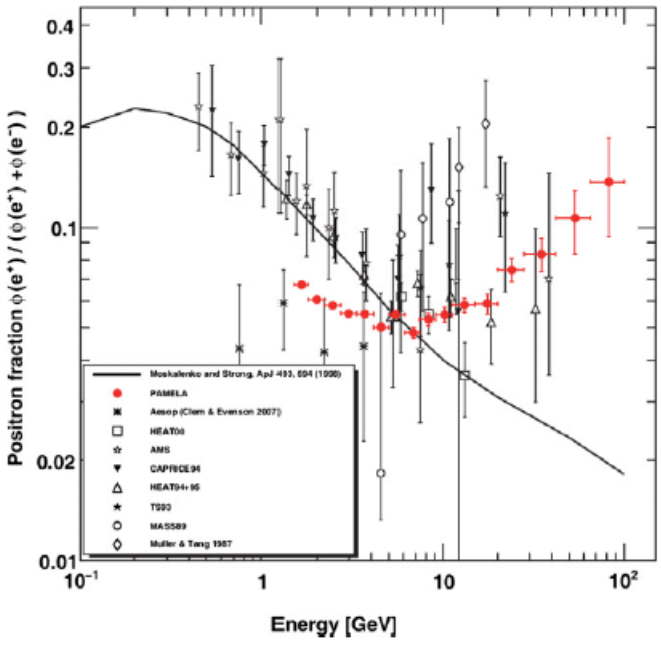

Figure 1.6 - Positron fraction observed by PAMELA. Plot from [34].

1.4.3 Anti-particle

Both the PAMELA and AMS experiments look for the production of anti-protons or positrons at energies of tens of GeV in WIMP annihilations in the dark matter halo

[34-35]. The positron fraction above ~10 GeV in PAMELA and AMS was observed to increase in energy, leading to some speculation of it as a dark matter annihilation signal. However, no such increase was seen in anti-protons, so the difference in the leptonic and hadronic channels may lead to difficulties in interpreting this in terms of a neutralino as dark matter.

1.5 Direct searches for WIMPs

Direct searches for WIMPs aim to detect these particles by their elastic scattering from target nuclei. By finding the interaction rate in the target and using an estimate of the local WIMP density, the interaction cross-section and the WIMP mass can then be calculated.

The interaction cross-section for WIMPs with ordinary matter is small but non-zero. The size of this interaction cross-section will depend on the properties of the nucleus, with the nuclear mass and spin impacting upon the spin independent and spin dependent parts of the cross-section. The spin dependent cross-section, given in eq. 1.10, comes from the axial-vector part of the interaction and has a value independent of the atomic number of the nucleus, *A*, but dependent on the nuclear spin, *J*.

$$\sigma_N^{SD} \propto \lambda^2 J(J+1)$$

Eq. 1.10

The spin independent cross-section, in eq. 1.11, meanwhile comes from the scalar part of the interaction and sums coherently over the nucleus giving a dependence on mass number.

$$\sigma_N^{SI} \propto A^2$$

Eq. 1.11

This then allows comparisons between different targets in the event that a spin independent WIMP signal is detected.

The cross-section may also be given in the form of the WIMP-nucleon cross-section

$$\sigma_n^{SD} = \sigma_N^{SD} \frac{\mu_n^2}{\mu_N^2} \frac{\lambda_n^2 J_n(J_n+1)}{\lambda_N^2 J_N(J_N+1)} \quad \sigma_n^{SI} = \sigma_N^{SI} \frac{\mu_n^2}{\mu_N^2} \frac{1}{A^2} \quad \text{and} \quad .$$

Eq. 1.12

The total cross-section is given by the sum of these two terms. For nuclei with $A \sim 30$ or higher spin independent is likely to dominate [36].

To calculate the interaction cross-section for the observed interactions in an experiment, a value for the local WIMP flux is required. To fit with astrophysical measurements, WIMPs should be gravitationally held in the galaxy with enough density to fit the rotation curve of the galaxy.

WIMP velocities are generally taken to have a Maxwellian distribution with velocities similar to that of stars relative to the centre of the galaxy, as in eq. 1.12.

$$f(v) = k(v_{esc}) \exp\left(-\frac{|v|^2}{{v_0}^2} \right), \; v < v_{esc},$$

Eq. 1.13

where $k(v_{esc})$ is a normalization constant based on the escape velocity. v_0 is the sun's circular velocity relative to the rest frame of the galaxy, 220 km/s. This is truncated at the galactic escape velocity, v_{esc} = 544 km/s [37]. With this velocity distribution the local halo density is normally assumed to be ρ_0 = 0.3 GeV cm^{-3}, from which the WIMP density will be given by $\rho_{WIMP} = \xi\rho_0$ with ξ as the fraction of WIMPs in the local halo density.

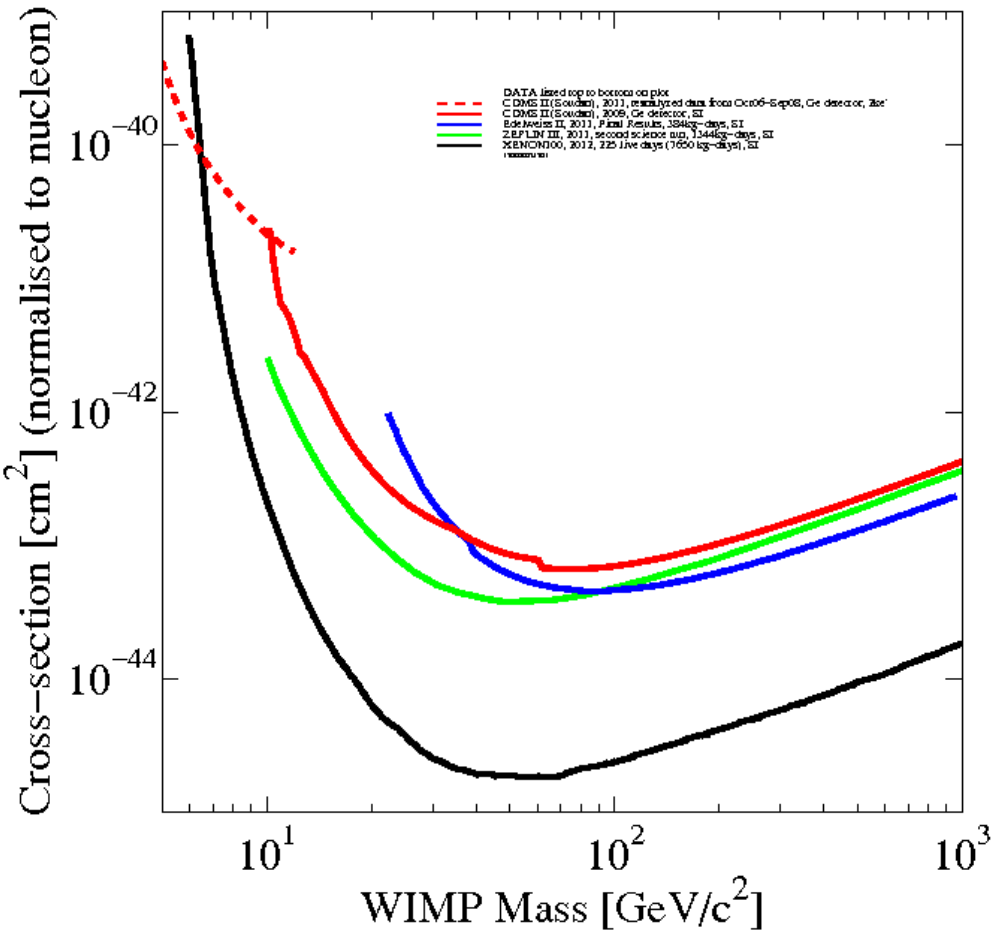

Figure 1.7 – The limits or signals found by the different experiments are usually presented on a plot showing the normalised WIMP-nucleon scattering cross-section on one axis and the WIMP mass on the other. This is known as an exclusion plot. This exclusion plot shows some of the most recent spin-independent limits for the Xenon 100 (in black) [39], CDMS (the red line showing the 2009 results, and the red dashed line showing a 2011 reanalysis) [40,41], Edelweiss (in blue) [42] and Zeplin III (in green) [43] experiments. Plot produced using [44]

Finally, the cross-section and mass of the WIMP, the model of the nucleus (through the nuclear form factor) and the model of the local WIMP distribution are combined to give the total expected interaction rate. For elastic scattering with a spin independent coupling, the differential event rate [38] is

$$\frac{dR}{dE} = \frac{\sigma_n \rho_0}{2\mu^2 m_X} A^2 F^2(E) \int \frac{f(v,t)}{v} d^3 v \,,$$

Eq. 1.14

where σ_n is the WIMP-nucleon cross-section, ρ_0 is the local WIMP density, $f(v,t)$ is the WIMP velocity distribution, μ is the WIMP-nucleon reduced mass, A is the mass number of the target nuclei and $F(E)$ is the form factor.

The interaction cross-sections calculated as a function of the WIMP mass with these standard assumptions about the WIMP distribution for a few of the current dark matter direct detection experiments are presented on the exclusion plot in figure 1.7.

1.5.1 Detection signal

For the expected WIMP masses in the range 10 GeV to 1 TeV, the energy deposited in nuclear recoils due to elastic scattering of WIMPs from nuclei will be ~10 keV. The shape of the energy spectrum will be dependent on the velocity distribution of the WIMP flux, as this is taken as a Maxwellian distribution the energy spectrum will be roughly exponential, as in equation 1.15.

$$\frac{dR}{dE_R} = \frac{R_0}{E_0 r} e^{-\frac{E_R}{E_0 r}},$$

Eq. 1.15

where E_R is the recoil energy and r is a kinematic factor depending on the mass of the dark matter particle and the mass of the nucleus:

$$r = \frac{4 m_\chi m_N}{\left(m_\chi + m_N\right)^2}.$$

Eq. 1.16

This exponential distribution means that low thresholds are particularly useful in dark matter searches as lowering the threshold will greatly increase the number of dark matter particles detected.

Further to this, there are several different detector signatures which are useful to dark matter experiments:

- the WIMP flux through the detector will vary in amplitude and direction with time (annual or diurnal modulation);
- events can be discriminated from background using the simultaneous measurements of a combination of heat, ionization or light given out in an interaction;
- the WIMP event rate will depend on the mass of the target nuclei, so a

combination of different targets can allow for the identification of a WIMP signal through scaling of rate with target mass number.

Experiments should also be designed as low background experiments to reduce events from other sources, such as neutrons, which may have similar signals in the detector.

1.5.2 Methods of Direct Detection

Using these different WIMP signals, there are several different styles of experiment that can be used to search for dark matter.

1.5.2.1 Annual modulation

Due to the movement of the earth through the dark matter halo, the WIMP flux will have a seasonal variation which can potentially be measured in a direct detection experiment. DAMA, an experiment using NaI crystals, [45] has measured an annually modulated signal. However the cross-section and mass have since been excluded by other experiments.

1.5.2.2 Directional

The rotation of the earth should produce daily modulations in the direction of the WIMP flux through the earth. The DRIFT-II experiment looked for nuclear recoil tracks in low pressure CS_2 gas to identify such a modulation, and plans are ongoing to scale up the experiment [46].

1.5.2.3 Liquid noble gas

Some direct detection experiments use liquid noble gases as a target (typically Xenon or Argon). These can be produced in large amounts with very high purity, allowing for large targets to be used. These experiments come in two main forms; single phase and double phase. In a single phase experiment, such as XMASS [47] or DEAP 3600 [48], a volume of the noble gas is surrounded by photomultiplier tubes (PMTs), and a measurement of the light made. Since no second measurement is made, these

experiments must use the pulse shape to discriminate between WIMP candidate events and the background. In a double phase experiment discrimination is carried out by the measurement of both scintillation light with PMTs and the ionization charge using a Time Projection Chamber. The chamber contains both a liquid and a gas phase. An electric field is applied across the chamber and any electrons produced drift upwards until the phase boundary, here the charge produces a second scintillation with size proportional to the total charge. The time difference of the two signals and the light pattern on the PMTs can be used to find the position of the original interaction [49,50]. Experiments of this kind include XENON 100, ZEPLIN-III and LUX-350 along with their planned successors XENON 1T and LUX-ZEPLIN [51].

1.5.2.4 Cryogenic Detectors

Another method of dark matter detection involves the use of cryogenic detectors [4]. These can achieve very good sensitivity when operating at low temperatures; the low heat capacity due to the T^3 dependence of the heat capacity for the dielectric crystals used as a target allows detectors to measure a temperature rise from an interaction that deposits a very small energy, and therefore gives the potential for detectors with good resolution and low energy thresholds.

The range of target materials that can be used for these cryogenic dark matter experiments also allows for several methods of discrimination between the background events, mostly caused by interactions with β and γ radiation, and potential dark matter events. This involves the simultaneous measurement of two signals from an interaction, which when combined allow the background events to be rejected. These measurements may be heat and scintillation light, as used in CRESST [7], or heat and ionization, as used in EDELWEISS or CDMS [52,40].

The ratio of these two energy measurements will be different for electron recoils and for nuclear recoils. Neutrons and WIMPs will interact and deposit energy via nuclear recoils, while electrons and photons will deposit energy via electron recoils.

With the signal size for an electron recoil given by keV_{ee} and the signal for a nuclear recoil given by keV_r then the energy for an electron recoil E_e to give the same signal size as a nuclear recoil of energy E_r is related by equation 1.17.

$$E_r(keV_r) = Q.F \times E_e(keV_{ee}), \qquad \textbf{Eq. 1.17}$$

where *Q.F.* is the quenching factor.

For example, with the CRESST calcium tungstate detectors the quenching factors were measured as in table 1.1 [53].

Nucleus	W	Ca	O
Q.F.	0.0391 ± 0.004	0.0638 ± 0.006	0.1109 ± 0.009

Table 1.1 - Quenching Factors for calcium tungstate.

Therefore, for the recoil of a tungsten nucleus, the ratio of the measured energy in the scintillation channel to the measured energy in the phonon channel will be ~4% of that for an electron recoil at a similar energy.

Even for electron recoils the amount of energy given out as scintillation, or ionization, is small compared to that given out as heat. This makes measurements of the second parameter difficult due to the small signal and provides even more motivation for the phonon-scintillation detectors to have a really low threshold especially for the light detector.

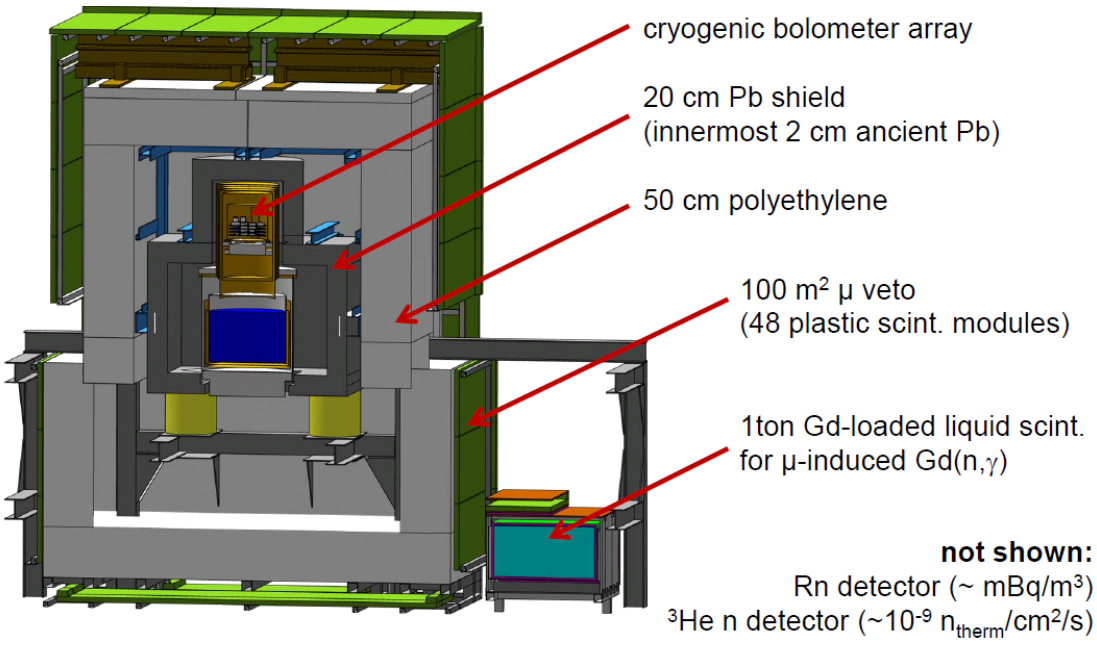

Figure 1.8 – The EDELWEISS II experimental setup. Taken from [54].

1.5.2.5 EDELWEISS

EDELWEISS uses an array of cryogenic detectors at the LSM underground laboratory near Modane in France. This underground location for the detectors, under 4800 m water equivalent of rock, helps to keep the background radiation for the experiment low, particularly the cosmic muon flux. In addition to this there is 20 cm thick lead shielding around the cryostat to shield gamma radiation from the detector, polyethylene shielding for neutrons, and a muon veto which tags muons in order to identify possible muon induced neutrons.

The EDELWEISS detectors consist of a pure germanium crystal, with an NTD Germanium sensor mounted to it in order to measure the heat channel of the detector and electrodes to measure the ionization channel. To provide the ionization measurement and define a fiducial volume for the detector, the surfaces were covered in a series of aluminium electrodes in the form of concentric rings. The rings are alternately connected together and used to create a fiducial volume surrounded by a guard region in which surface events can be identified thus removing spurious events

due to surface contamination [52]. The ability of this detector to discriminate between electron recoil, due to the lighter particles (γ,e), and nuclear recoils, due to WIMPs or neutrons, comes from the ratio of the heat measurement to ionization.

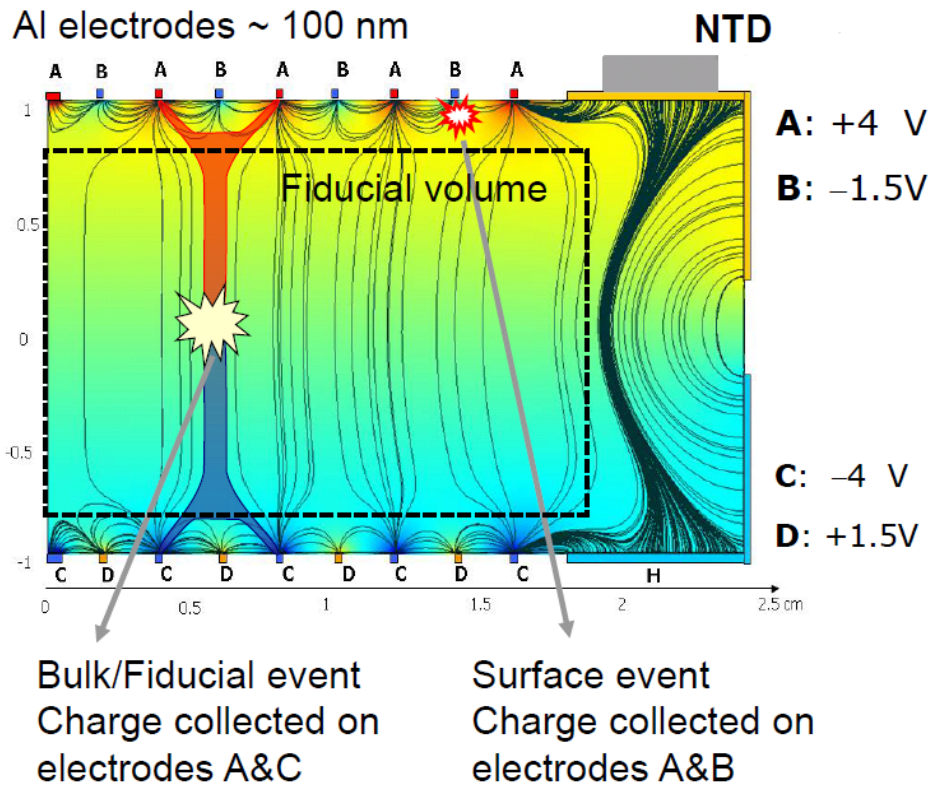

Figure 1.9 – Diagram of an EDELWEISS phonon-ionization detector. The Al electrodes around the surface may be used to reject events that occur near the surface of the detector and define an inner fiducial volume. Diagram from [55].

Each of the germanium FID 800 detectors have total mass of 800 g, with a fiducial mass of around 640 g defined by the electrodes. The average FWHM resolution of the baseline for the phonon channel is 1.2 keV. For the ionization channel it is 0.9 keV [42].

These detectors are operated at around 18 mK, a low temperature which allows NTD Germanium, which increases exponentially in resistance for decreasing temperature, to be used as a thermometer. The properties of such a thermometer will be described in detail in Chapter 4 of this thesis.

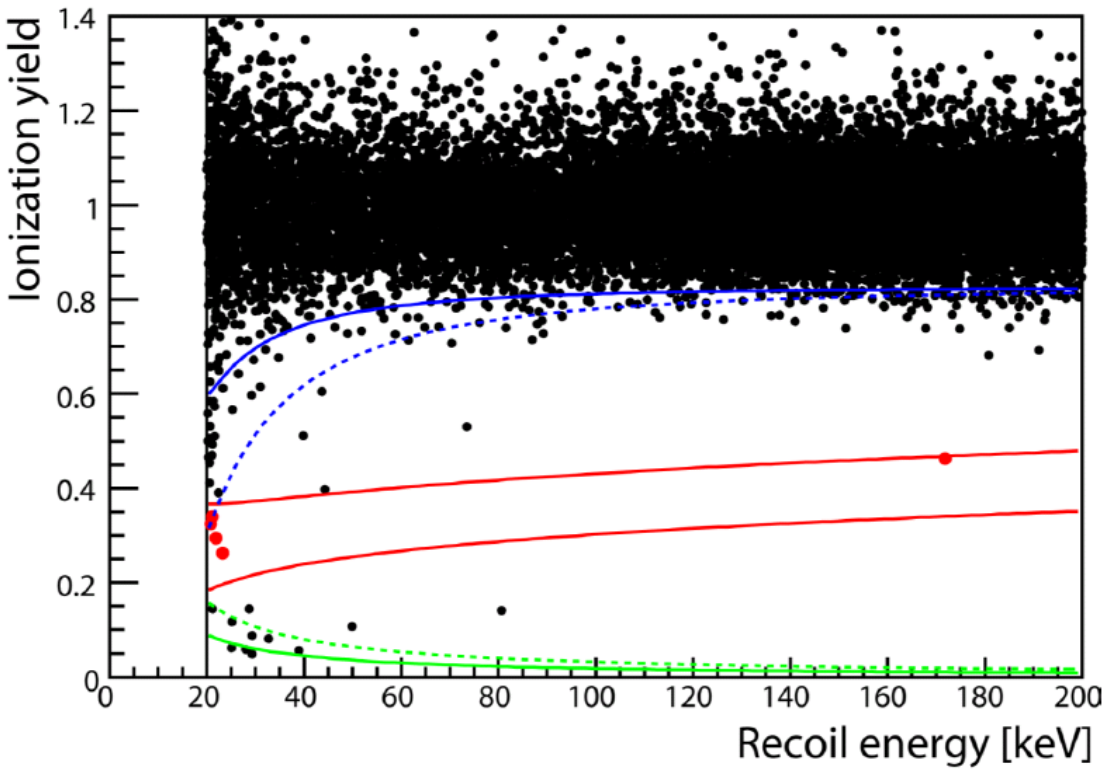

Figure 1.10 - Final yield plot for EDELWEISS II (2008-2010). Five events observed in the nuclear recoil (red) with a background of three events expected between 20 keV and 100 keV gives no indication of a WIMP signal. The ionization yield is the ionization signal divided by the heat signal and normalised so that it is around 1 for the gamma background. From [42]

1.5.2.6 CDMS

The CDMS collaboration, based at the Soudan Underground Laboratory in Minnesota, also uses heat and ionization measurements. [56-57] Pure germanium or silicon disks are used with metal electrodes on the two faces of the substrate. The phonon measurement is made with a Transition Edge Sensor; this is a narrow tungsten film stabilised so that it is kept within the superconducting to normal conducting phase transition. When a particle interacts with the detector, the athermal phonons produced are collected by superconducting aluminium films connected to the TES. This causes a rise in the temperature of the tungsten film and thus its resistance. The temperature of the tungsten film is held stable by the Joule heating due to the voltage bias applied. This process is known as electrothermal feedback. As the resistance

changes, the heating power required changes. The integral over time of the heating power change leads to a measure of the energy deposited in the tungsten film.

1.5.2.7 CRESST

CRESST uses detectors with the simultaneous readout of temperature and scintillation [7]. The temperature measurement is carried out using a Superconducting Phase Transition (SPT) thermometer, a thin film of tungsten which is held in the transition between the superconducting and the normal conducting phases and has a resistance that varies approximately linearly with temperature for small changes. The change in resistance of the thermometer is read out using a Superconducting Quantum Interference Device (SQUID). A constant bias current is applied to a parallel circuit configuration with the SPT in one branch and in the other branch, a series configuration of a reference resistors and the input coil of the SQUID. The magnetic field produced by this SQUID input coil is then converted to a change in voltage at the output of the SQUID with its electronics. The threshold and resolution that can be achieved by this are potentially very good, but the detector is only linear over a very narrow range and the operating point and response of the detector must be monitored and continually adjusted by sending heater pulses to the detector periodically to check the response and ensure the detectors are held at the same point in the transition. This is in contrast to the high impedance NTD germanium sensors, as used by EDELWEISS, where the operating point can be continuously measured using the resistance of the sensor and the detector response remains linear over a wide range of energies.

The thermometer is mounted on a scintillating crystal target. The light output by this can be measured and used for discrimination between different event types. The scintillation light is measured by absorbing it with a silicon light absorber, and then

the temperature change is read out using another SPT thermometer. The discrimination in CRESST occurs, as in EDELWEISS, with a ratio between the two measured energy values. The scintillating targets used by CRESST are Calcium Tungstate ($CaWO_4$) and Zinc Tungstate ($ZnWO_4$) crystals.

The CRESST collaboration found an excess of events which could be accounted for by light mass WIMPs at 25.3 GeV and 11.6 GeV [58], however this is in tension with other results [59.60].

1.6 Neutrinoless double beta decay (0νββ)

The mass of neutrinos has been shown to be non-zero by the results of neutrino oscillation experiments, however further work is still being carried out to determine the actual mass of the neutrino and its properties. Neutrinos may be either Dirac particles, with separate particles and antiparticles, or Majorana particles, for which particles and antiparticles are the same [6,61].

If neutrinos are Majorana then processes that involve the annihilation of a pair of neutrinos can take place, leading to the violation of lepton number conservation. These processes, such as neutrinoless double beta decay, would be forbidden for Dirac particles, so the observation of such a process would allow an experimental determination of the nature of neutrinos.

1.6.1 Double beta decay

Double beta decay is a second order weak process in which a nucleus decays by the emission of two electrons, increasing its atomic number by two while its mass number remains constant. There are three different paths through which double beta decay can occur. The first is the standard model process involving the production of two anti-neutrinos.

This has been observed in various isotopes with a halflife of ~10^{19} to 10^{21} yr [62,63]. The second is neutrinoless double beta decay, in which the two neutrinos act as Majorana particles and annihilate each other [6].

$$(A,Z) \rightarrow (A,Z+2) + 2e^{-}$$

This process violates lepton number conservation. The third involves the production of an exotic particle known as a Majoron, denoted here by χ.

$$(A,Z) \rightarrow (A,Z+2) + 2e^{-} + \chi$$

There are a range of different theoretical models in which this process may occur, some of which would violate lepton conversion and some of which would not. Both of these decays would require the existence of some beyond standard model physics, if they were to occur. The last process here has never been observed, and the second has only been observed in a disputed claim (which will be covered later) [64].

1.6.2 Mass of neutrinos

The mass of neutrinos has been shown to be non-zero by the results of neutrino oscillation experiments, giving values for the difference of the masses squared between different neutrino species. However, though a range of experiments have set limits on the mass, the actual mass of these species is yet to be determined. First, it is possible to determine the mass of a neutrino through the kinematics of a standard beta decay process and limits have been set by the Troitsk and Mainz experiments. Next, limits can be set by cosmological models and measurements of the structure of the universe, including WMAP and Planck. Finally, and of most relevance to this thesis, if neutrinos are Majorana particles it is possible to find their mass by searching for neutrinoless double beta decay and using the decay rate.

1.6.2.1 Beta decay

Massive neutrinos will impact upon the kinematics of normal beta decay processes, giving an end point to the beta decay spectra which is dependent on the neutrino mass. Experiments to determine this will usually involve the tritium decay spectra, due to the relatively low mass of the nuclei. In 2005, the Mainz experiment used this method with thin films of Tritium to give an upper limit on the $\bar{\nu}_e$ mass of 2.3 eV [65] and in 2011 the Troitsk experiment found an upper limit of 2.05 eV with a gaseous source of Tritium [66]. The KATRIN experiment is expected to improve upon these results with a new measurement in 2015 [67].

1.6.2.2 Cosmology

Further limits can be made on the scale of neutrino masses with cosmological results. The growth of perturbations in the early universe is dependent on the sum of the neutrino masses. The Planck satellite recently put a limit on the masses of

$\sum m_\nu < 0.98$ eV (95%, for Planck, WP and highL)

$\sum m_\nu < 0.32$ eV (95%, for Planck, WP, highL and BAO),

where WP denotes a polarization low-multipole likelihood from WMAP [68], highL the data from high resolution CMB experiments such as the Atacama Cosmology Telescope [69], and BAO baryon acoustic oscillation data.

1.6.2.3 Neutrinoless double beta decay

Neutrinoless double beta decay may give an opportunity to improve upon these limits if neutrinos are Majorana particles. The decay rate for a neutrinoless double beta decay source will be proportional to the square of the mass.

$$\Gamma^{0\nu} = G_{0\nu}(Q,Z)\left|M^{0\nu}\right|^2\left|m_{\beta\beta}\right|^2,$$

Eq. 1.18

where $G_{0\nu}$ is the phase space factor, $M^{0\nu}$ is the nuclear matrix element and $m_{\beta\beta}$ is an effective double beta decay mass [70]. The effective double beta decay mass contains the neutrinos masses along with the mixing matrix between the different eigenstates. With a calculation of the phase space and nuclear matrix elements, the neutrino masses can then be estimated. The nuclear matrix element provides the major source of error for this calculation, as a suitable model must be assumed. There are a number of models which could be chosen including, for example, the Interacting Shell Model, which includes all corrections to the matrix element but uses a reduced valence space [71], and the Interacting Boson Model, which models low lying states in terms of boson wave functions [72].

1.6.3 Isotopes

For a neutrinoless double beta decay experiment, the choice of candidate material for the experiment will be influenced by a number of factors. Most importantly, they must have a suitable nuclear binding energy. This must be such that neutrinoless double beta decay can occur, with

$$m(A,Z) > m(A,Z+2) + 2e^{-}$$

Eq. 1.19

and such that background processes such as single beta decay events, which would otherwise dominate the experiment, will be rare

$$m(A,Z) < m(A,Z \pm 1) + e^{-}$$

Eq. 1.20

A simple model of the binding energy may be given in the form of the Semi Empirical Mass Formula (eq. 1.21). This shows the nuclei masses (with fixed even mass number A) forming a parabola shape about a minimum due to the asymmetry term with a_a and this separating into two curves – one for even values of A and Z and one for Z odd, due to the pairing term with a_δ.

$$E_B = a_V A - a_S A^{2/3} - a_a \frac{(A-2Z)^2}{A} - a_C \frac{Z^2}{A^{1/3}} \pm \frac{a_\delta}{A^{3/4}}.$$

Eq. 1.21

The actual values for the mass will be more complicated to obtain than this, but the simple model already shows the differences in binding energy for even-even and odd-odd nuclei (with fixed mass number *A*) that make certain even-even nuclei the preferred candidates for neutrinoless double beta decay (as in Fig. 1.11).

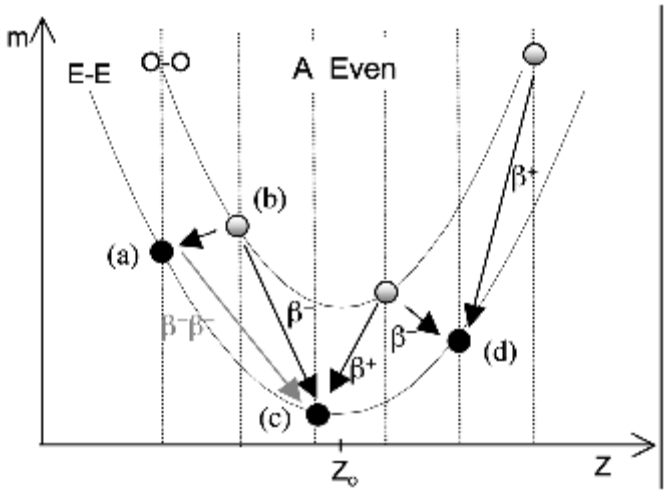

Figure 1.11 – The masses of various nuclei with a fixed even value of A. (a) is a potential candidate for double beta decay. From [61]

Along with this, the selection of the appropriate isotope for the experiment will also involve the experimental considerations such as the abundance of the isotope, the ability to enrich it in the material and the compatibility with the chosen detection technique.

The Q-value of the isotope will also be important. The typical signal for a neutrinoless double beta decay experiment will be a peak at the Q value, so it must have a value that can be easily separated from any features of the radioactive background sources in the experiment, which may have a much higher rate than the double beta decay process.

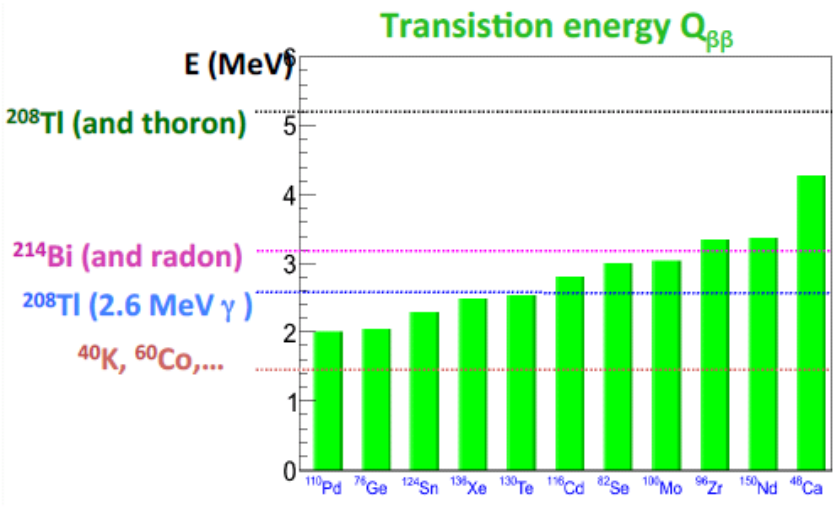

Figure 1.12 - Q value for potential neutrinoless double beta decay sources with the most promising notable background energies superimposed. Ge has a low Q value, but remains promising due to its ease of use in some experiments. From [73].

1.7 Searches for neutrinoless double beta decay

There are a number of different experiments currently searching for double beta decay, they use a range of different methods and target materials.

1.7.1 Germanium diodes (Heidelberg-Moscow and GERDA)

The Heidelberg-Moscow experiment, using on five Ge diodes enriched to 86% with the candidate ^{76}Ge, ran underground at Gran Sasso in Italy until 2001. It provided a lower limit on lifetime of 1.9 x 10^{25} yr and an upper limit on mass $<m_\nu>$ of 0.3 to 0.6 eV. A subset of the collaboration claimed to have identified 0νββ with a series of small peaks near the Q value for ^{76}Ge, giving a mass of 0.39 eV and a half life of 1.5 x 10^{25} yr [64].

The GERDA collaboration has used detectors with a similar ^{76}Ge source to check this claim [74]. So far they have observed no signal and placed a lower limit on the halflife of 3.0 x 10^{25} yr at the 90% confidence level.

1.7.2 SuperNEMO

The successor to Nemo3, SuperNEMO uses modules with source foils containing the double beta decay nuclei ^{82}Se or ^{150}Nd, and detects the particles produced using a tracking detector (drift chamber with magnetic field) and calorimeter (low Z scintillator) [75]. This class of experiment has the double beta decay source separated from the detector itself. It is expected to reach a sensitivity of up to ~ 2 x 10^{26} yrs.

1.7.3 Liquid Scintillator (KamLAND and SNO+)

These use a large mass of a liquid scintillator loaded with source nuclei. KamLAND used 13 tons of ^{136}Xe loaded liquid scintillator and found a lower limit for the half life of 3.4 x 10^{25} yrs [76,77]. SNO+ meanwhile will use nuclei of ^{130}Te as the source [78].

1.7.4 Cryogenic detectors (Cuore and Lucifer)

Cuore, the successor to Cuoricino, uses ^{130}Te as a double beta decay source [79]. It has a system of TeO_2 bolometers stacked in towers. These bolometers measure the energy released in a particle interaction as a change in temperature, which is read out with an NTD germanium thermistor. These detectors are operated at temperatures between 7 and 10 mK, for similar reasons as the cryogenic dark matter detectors. Cuore has a resolution of ~ 5 keV at 2.53 MeV. Cuoricino was able to set an upper limit of 300 to 710 meV on the effective neutrino mass, and Cuore would hope to improve on this limit.

Similar to the cryogenic dark matter experiments, simultaneous measurements in two channels can be used to reduce the background of the experiment. The signal of a neutrinoless double beta decay interaction can be separated from the background of alpha particles by using the ‘quenching factor’ of the material. As described in

1.5.2.4 the ratio of the energy converted into scintillation light and into phonons will depend on the type of particle that deposits the energy.

The Lucifer experiment [80] aims to use the combined measurement of scintillation light and phonons for such discrimination. There are suitable scintillating crystals for such a detector that would contain isotopes such as ^{100}Mo, ^{116}Cd, and ^{82}Se which would potentially decay through neutrinoless double beta decay. Lucifer uses crystals of ZnSe as the scintillating target material with NTD Ge sensors as readout for the phonon channel and a light-absorbing silicon wafer, also with a NTD Ge thermometer, as the readout for the light channel. However, other scintillating source crystals could be used including $CdWO_4$, $ZnMoO_4$ and $CaMoO_4$.

2. Detector layout and infrastructure

A large part of the work described in this thesis is that prototype cryogenic detectors with NTD Ge sensor readout and target materials suitable for dark matter or neutrinoless double beta decay searches were made, prepared and tested in the cryogenic detector laboratory at Oxford University. The layout of the detectors and the infrastructure used to run them are important elements, necessary to understand the detector response. This chapter describes these aspects and their implication for the operation of the detector and its use in future experiments.

The detectors are cooled down to their operating temperatures (around 10 mK) using a He-3 dilution refrigerator (Oxford Instruments K400). This equipment and the thermometers placed throughout it for calibration and operation of the detector are described in sections 2.1 and 2.2. In section 2.3, the general layout of the cryogenic detectors is presented.

The detectors are electrically connected to the readout circuit, and thermally connected to a temperature bath, via a pair of gold bond wires. Through their thermal characteristics these affect both the operating temperature and pulse shape of the detector's response. These are described briefly in 2.4, while a more complete thermal model is given in chapter 5. Following on from these wires in the readout system is a set of polyimide based cabling, designed and fabricated in Oxford for EDELWEISS / EURECA to provide low radioactivity levels and low electronic capacitance. For an independent test, before delivering to EDELWEISS, these cables, described in section 2.6, were made to fit the K400 cryostat.

The housing of the detectors provides a number of functions, acting as shielding to reduce the rate of background events in the detector due to natural radioactivity,

providing a large mass helping with stabilization of the detector operating temperature, and as mechanical support for the detector. Its effect and contribution is shown in section 2.5.

Next, the heat capacities of materials used in the detectors are investigated and its effect on the detector response discussed. Finally the scintillation properties and light collection efficiency of the light detecting module and its housing are described.

2.1 Cryostat

The detectors are cooled down in a Kelvinox 400 dilution refrigerator (K400), with a cooling power at the mixing chamber of 400 μW at 100 mK and a stable base temperature of below 7 mK [81]. The design of the cryostat and the components placed within (see Fig. 2.1) will affect the base temperature at which the detector can be operated and the temperature stability that can be achieved for the detector.

The cryostat is supported by a top plate which rests on a set of air dampers, which should minimize the transfer of physical vibrations of the cryostat and its immediate surroundings to the detector. These vibrations could otherwise severely affect the temperature stability of the detector and prevent the cryostat reaching the low temperatures required. This is cooled down in several stages. First the main bath is filled with helium, cooling the cryostat to 4 K, while helium exchange gas is present in the Inner Vacuum Chamber (IVC) to ensure all components within are efficiently cooled to ~4 K. Then, the IVC, which also contains the detector, is pumped out using a turbo molecular pump and by allowing a charcoal “sorb” to cool and absorb any remaining gas. Once a good vacuum has been achieved, the 1K pot of the cryostat is started – by filling the liquid helium from the main bath into the 1K pot and pumping on it, the cryostat can be cooled to ~1.5 K.

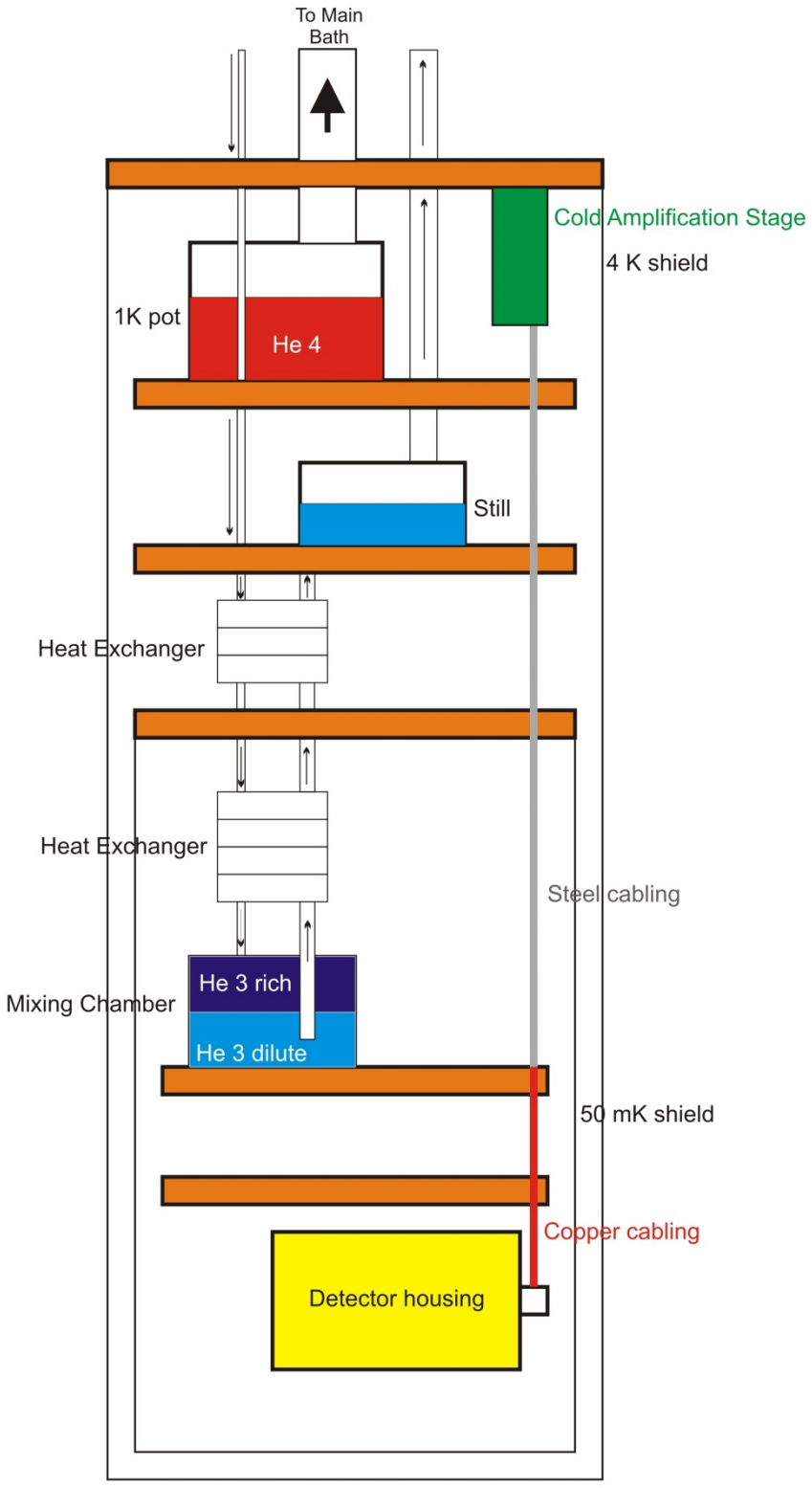

Figure 2.1 - Diagram of the Kelvinox 400 Inner Vacuum Chamber. The cryostat is cooled to a base temperature of ~7 mK at the mixing chamber. This allows the NTDs to be operated at these very low milli-Kelvin temperatures.

The filling of the 1K pot and the related physical vibrations within the cryostat is a potential source of microphonic noise. This is described further in section 5.8.

To achieve lower temperatures, a helium-3 and helium-4 mixture is condensed inside the dilution unit of the cryostat and circulated using another set of pumps. In the mixing chamber, the He-3 and He-4 in the mixture separates into a He-3 rich phase and a He-3 dilute phase. The dilute phase is pumped via the Still, which is itself heated to provide a constant flow of He-3 from this phase and has a temperature around 600 mK, leading to a flow of He-3 from the concentrated phase to the dilute phase. The process of crossing this boundary is endothermic and helps cool the mixing chamber to its base temperature of ~7 mK.

The detector and the temperature stabilisation levels are connected below the mixing chamber, and this cools them down to temperatures near the base temperature of the cryostat but decouples them slightly from temperature fluctuations at the mixing chamber level. Polyimide based cabling is then used to carry the signal from the detector to the cold electronics stage at the 4 K level of the cryostat – though this stage has its own heating, and will be kept at a temperature of ~120 K.

Preventing thermal radiation from these higher temperature levels reaching the lower levels is essential for the cryostat to cool down effectively. For this reason, a 50 mK copper shield surrounds the low temperature parts of the cryostat, blocking out thermal radiation from the higher temperature levels and from the outside of the IVC, which is at 4 K. Additionally a copper plate is also used at each temperature level and a brass box placed around the 120 K electronics to prevent radiation from getting to the lower levels.

2.2 Temperature measurements

In order to characterize the detectors and set their operating point, knowledge of the temperature of the detector is required. To measure the temperature of the heat bath used for the detector, a carbon Speer resistor and a Ruthenium Oxide thermometer were mounted nearby. Both of these are resistors with a resistance that increases as the temperature decreases. These act as secondary thermometers, which do not themselves give a direct measurement of the temperature, but must be calibrated using a primary thermometer from which the temperature can be directly found.

To calibrate these thermometers the primary thermometer used was a nuclear orientation thermometer [82] with a ^{60}Co source in an iron matrix. The decay of ^{60}Co produces several γ-rays, with a spatial anisotropy in the emission probabilities due to the angular momentum of the nuclear energy levels. With a collection of radioactive nuclei the total emission will be isotropic, unless the nuclei are orientated in a particular direction.

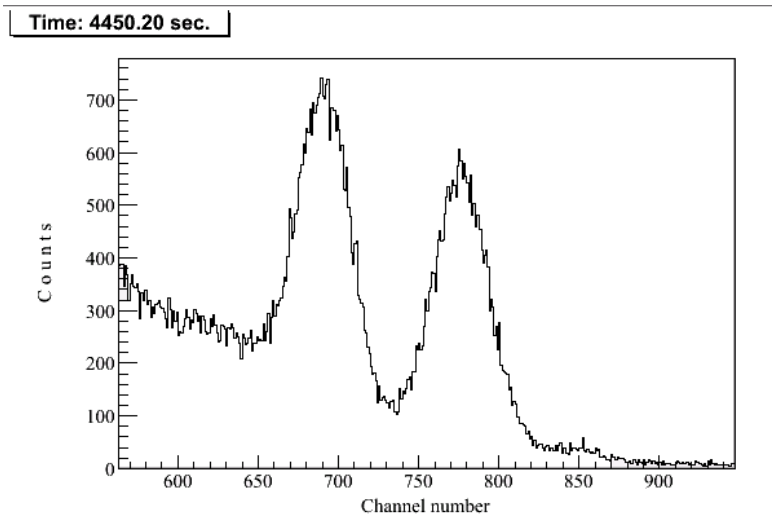

Figure 2.2 - part of a Nickel-60 spectrum, as used in the Cobalt-60 temperature calibration, that has been recorded for that purpose using a PMT. Clearly visible are the two energies of 1171 and 1333 keV from the 4+ → 2+ and 2+ → 0+ transitions.

The orientation of radioactive nuclei can be used as a thermometer by placing the source in a ferromagnetic matrix. When these are at room temperature the nuclei will

the randomly orientated and the emitted gamma ray intensity will be isotropic, but when the temperature becomes low (~40 mK or less) the nuclei start to orientate and the spectral anisotropy can be detected.

By placing a NaI scintillator with attached PMT (or similar detector) in the direction where the change in intensity is largest, one can then take a series of energy spectra at different temperatures (including room temperature) and fit to them to find the count rate of the peaks. Comparing the cold count rate of the anisotropic distribution and the warm count rate of the isotropic distribution then allows the size of the anisotropy to be measured and hence the temperature to be estimated. This allows a calibration to be made of the secondary thermometer resistance and the measured temperature.

In addition to this, mounted on several stages of the cryostat are thermometers provided by Oxford Instruments – at the still, the 50 mK shield and the mixing chamber. These can be used for diagnostics when running the cryostat.

2.3 Detector layout

A combined light detector module with two separate cryogenic detectors (see Fig. 2.3 and 2.4) has been used to make a simultaneous light and phonon measurement. The primary detector is a 'phonon detector' with a large scintillating absorber crystal; this would act as the target for a dark matter experiment or contain the source for the beta decay search. The scintillation light given out by this is contained by a shell of reflecting foil placed around the two detectors, and absorbed by a light absorbing layer on the secondary detector, the 'light detector'.

The energy deposited in each of these detectors causes a change in temperature, which is measured as a change in resistance for a NTD germanium thermistor glued on top of the substrate crystal. The NTD sensor is electrically connected to the readout

system via a pair of gold bond wires which attach to the side via two gold contact pads. These gold wires also provide a thermal connection between the detector and its housing, which acts as a temperature bath. From here, the signal is carried to the electronics via the polyimide cabling. Further descriptions of the gold bond wires and the cabling will be covered in sections 2.4 and 2.6 of this chapter. The details of the electronics in the readout system and of the NTD germanium thermistor will be given in Chapters 3 and 4.

The layout of the two detectors is shown in the diagrams below.

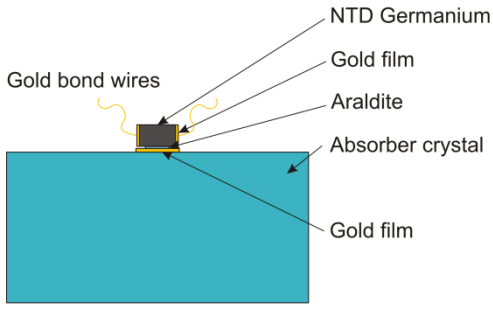

Figure 2.3 - The layout of the phonon detector.

The absorber crystal of the phonon detector is a scintillating crystal chosen for its properties that suit a dark matter or double beta decay experiment. On the first version of the light detector a calcium tungstate crystal of dimensions 10 mm x 20 mm x 5 mm was used. Calcium tungstate is useful for dark matter searches due to the high mass of the tungsten nuclei, and has been used on the CRESST dark matter experiment. The crystal used for these detectors is relatively small due to the limited space in the cryostat and the relatively high radioactive background in the laboratory, given the slow response of cryogenic detectors. However, similar detectors in CRESST have been scaled up and have even shown an improvement in the resolution in the process [83,84].

On the next version a calcium molybdate crystal with dimension (10 × 10 × 5) mm^3 was used. The ^{100}Mo nucleus is a potential double beta decay source, so this detector could be used for double beta decay searches.

The crystal has a 250nm thick gold metal film evaporated onto it that helps to thermalize the athermal phonons formed by a particle interaction. Using a small amount of Araldite adhesive the NTD germanium sensor is then attached to the top of this gold film, measuring its "temperature". The araldite is spread out at a known thickness using thin metal sheets of that thickness, and then a metal stamp is used to transfer a known area of the glue to the crystal. In this way, the volume of glue used can be estimated and reproduced for future detectors. A teflon fibre is placed in the glue between the sensor and the gold film to prevent the NTD sinking into the glue while it dries and making direct contact with the gold film and forming a short circuit across the thermistor.

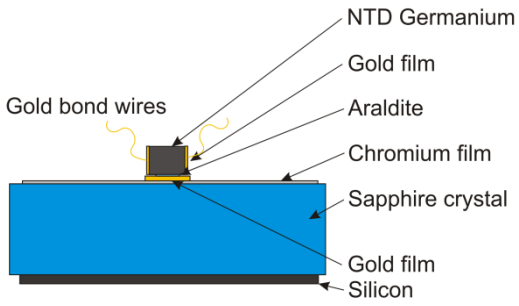

Figure 2.4 - The layout of the light detector.

The light detector layout is similar to the phonon detector. A 90 nm thick chromium adhesion layer was evaporated on top of the sapphire substrate, and then the gold film was placed on top of that. This layer provided extra adhesion between the sapphire crystal and the gold film. However, during the operation of the detectors, no difference in detector performance or durability was observed due to this layer, and the extra heat capacity meant this was not included in detectors fabricated later.

In order that this detector could absorb scintillation light from the phonon detector, a layer of Silicon was evaporated onto the opposite side of the sapphire crystal. The properties and specifications of this layer are described in more detail later in the chapter.

2.4 Bond wires

Gold bond wires are used to connect the gold contacts on either side of the NTD sensor to the connectors for the cabling (see Fig. 2.5). These provide two functions – firstly, an electrical connection to the signal tracks of the cable so that the resistance of the sensor can be readout by the electronics, and secondly a thermal link to the temperature bath of the detector holder.

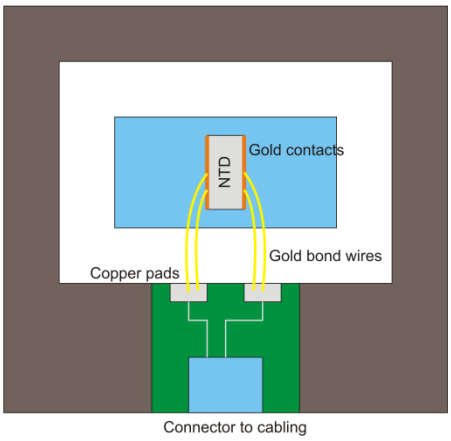

Figure 2.5 - Diagram showing the connection of the gold bond wires.

At one end they are bonded directly to gold contacts on either side of the NTD sensor and at the other end the wires are attached to copper pads on a p.c.b leading to the cabling. The bond wires could not be directly bonded to the pads due to restrictions imposed by the layout of the detector in the housing and the design of the wire bonding machine; however they could be attached by other means. Lead solder was found to provide a good electrical connection, but the thermal connection was

difficult to reproduce consistently due to the superconductivity of the solder at low temperatures (shown in Table 2.1). Silver paint was found to provide both a good electrical connection and a reliable thermal connection.

The thermal connection that these bond wires provide is vital, as it not only provides the primary way for the detector to cool down, but also determines the shape of any temperature pulses that may be observed in the detector. The temperature model of the detector is described in more detail in chapter 5, but a simple approximation would give the decay time constant of these pulses as

$$\tau = \frac{C}{G},$$

Eq. 2.1

where C is the heat capacity of the detector and G is the thermal conductivity between the detector and the heat bath. In reality, pulses are better characterized by two or even more decay time constants.

Therefore the decay time of pulses can be varied by changing the number and length of the gold wires used so as to change the value of the thermal conductivity G. For the prototype light detector consisting of NTD 38a on sapphire the results of several configurations are shown in the table below.

Connection Method	Number of bond wires	Time constant [ms]
Solder	2	81
Solder	4	54
Silver Paint	4	38

Table 2.1 – The time constant for different setups of the gold bond wires with NTD38a. Silver paint provided a consistent and strong thermal connection to the bond wires. Solder produced more inconsistent results due to its superconductivity.

As expected, increasing the number of bond wires will increase the thermal conduction and cause a drop in the decay time. However the solder provides an unreliable thermal connection at the contact pad each time the connection is remade, leading to the time constant being different (slightly higher in this case) than it should

be. This is explained by the volume and shape of the solder being different after each solder process (heating and solidification). The copper pads onto which the gold wires are connected through the lead, and the gold bond wires themselves, are normal-conducting metals and thus the lead, a superconductor with a bulk critical temperature of 7.2 K could be normal-conducting when the gap between the gold wires and copper pads are small (in the region of a coherence length - 83 nm). This however cannot be controlled reliably, as exemplified by the results in table 2.1. Thus, silver conductive paint (from electrolube) has been adopted for making a more reproducible connection of the gold bond wires to the copper pads. A small amount of the paint is applied to the pad and the bond wire pushed into it. It then dries quickly, in about ten minutes at room temperature. The solvent evaporates leaving the silver that was dispersed within it, producing good conductivity and adhesion to the pad and the wires.

2.5 Detector housing

Initially the detector was held in an open frame with a pair of brass clamps as the support (see Fig. 2.6). A high rate of pulses was observed in the signal from this detector, making the operation of the detector difficult. Therefore an investigation was carried out into the source of these pulses, with three potential sources:

- electronic interference
- mechanical effects of the clamps
- natural radioactivity

The first of these was ruled out by the lack of coincidences between pulses on different detectors. The other two required testing of the detector housing. The detector is held within a copper housing that provides several functions.

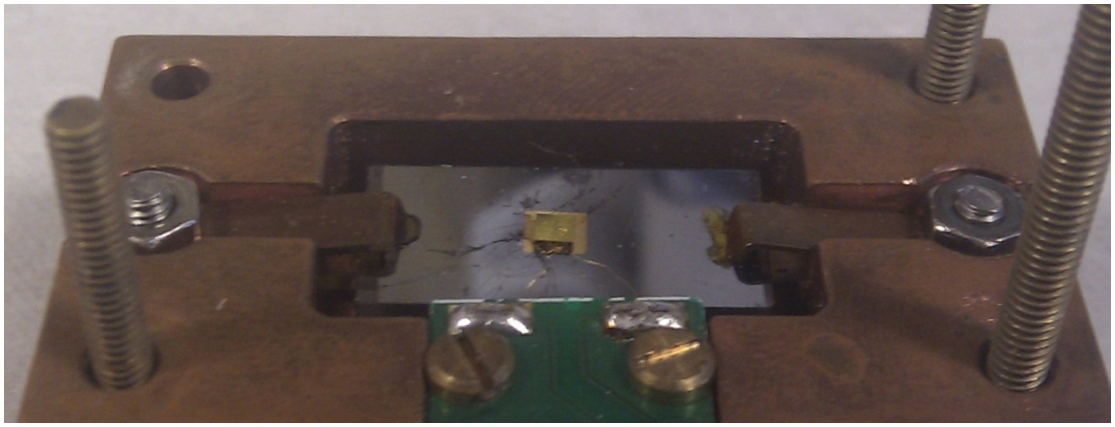

Figure 2.6 - NTD J1 glued to a sapphire substrate mounted in an NOSV copper frame, with brass clamps and GE varnish supporting the crystal. The gold wires from the NTD sensor are connected to the contact pads using solder.

2.5.1 Support

Firstly it allows the detector to be physically supported. This support should be thermally insulating, to help provide something close to the ideal detector model with the gold bond wires as the sole thermal link. As well as this, the method should be reproducible so that detectors can be replaced without significant changes in their support.

If the crystal was clamped too strongly then cracks or defects could occur [85]. If it wasn't strong enough, there was the potential for vibrations to occur between the clamp and the crystal producing temperature pulses similar to those expected from particle interactions. Several modifications were made to the brass clamps in an attempt to remove these possible vibrations as a potential source for the excess signal pulses. A small piece of nylon was inserted between the crystal and the tip of the clamp in order to reduce possible vibrations, and GE varnish was applied at the contact between the crystal and the clamp to provide a more even connection. However no change in the detector performance was observed.

This seemed to suggest that the brass clamps did not have a problem with vibrations; however the bending of these clamps that was required to insert the crystal and tighten

the clamps could lead to permanent deformation of the shape of the clamps. With this, even mechanical support was difficult to reproduce so the method of clamping was changed.

In the later versions of the housing, the two detectors are suspended within the copper block by two lengths of 100 μm thick Kevlar fibre. These are looped around the crystal at either end, then tensioned using a pair of screws. With these screws and with the flexibility of the fibre the risk of putting too much stress on the crystal was reduced.

2.5.2 Shielding

Other than the electrical interference or mechanical effects, there was the possibility that the high rate of events was due to the housing providing insufficient shielding from background radiation. For a cryogenic detector in use in a dark matter or neutrinoless double beta decay search keeping the radioactive background and the contamination of the detector low is crucial. This is why such detectors are operated in deep underground laboratories with sufficient shielding of copper, lead and typically polyethylene around.

In contrast, when operating such a detector in an above-ground laboratory the natural radioactivity in the surroundings will cause particle interactions in the detector, giving pile-up events (cryogenic detectors are slow, with typical time constants several 10 ms) and also contribute a background rate of temperature pulses measured by the NTD germanium sensor. These contributions are undesirable as pile-up in the detector leads to difficulties in extracting the true energy information of the interaction. The background could even be high enough to affect the temperature stability of the detector through the regular occurrence of temperature pulses in the

detector. They may also obscure some of the signal of interest if the signal rate is low compared to the background rate.

It thus provides a limitation on how far the detectors can be tested in the above-ground laboratory at Oxford. Cryogenic detectors for an actual dark matter search would be large to maximise the target mass of the detector and hence its exposure but the level of background radiation in the laboratory in Oxford is much higher than that of an underground laboratory so such a large absorber mass becomes impractical due to the high rate of background events.

Being able to only operate a relatively small detector (typical volume ~1 cm^3) is not necessarily a limitation or restriction. The calculations of heat capacity and development of similar detectors by the CRESST collaboration show that the absorber mass can be increased with little impact on resolution, so a prototype detector run in the laboratory can be scaled up to a larger mass in the right conditions.

The background rate can be reduced through extra shielding, and the desired signal to background ratio improved by the careful placement and collimation of the radioactive sources used to test the detector response.

Attenuation of background

The radioactive background for the detector is therefore reduced by additional shielding around the detector. There are several possible mechanisms by which gamma particles can interact with matter, and depending on the energy of the particle these can play a role in attenuating the number of background photons [86].

Photoelectric Absorption

In this process a photon interacts with an atom causing one of the bound electrons to be ejected as a photoelectron. The full energy of the photon will be absorbed in this process. The form of the probability for this interaction occurring will vary, but have

some dependence on the charge Z of the atom and the energy E_γ of the incident photon. This probability can be expressed in the form

$$\tau \sim \frac{Z^n}{E_\gamma^{3.5}},$$

Eq. 2.2

where n varies between 4 (at low energies) and 5 (at high energies).

Compton Scattering

This scattering process between the photon and a free or weakly bound electron in the material will deflect the photon and transfer some energy to the recoiling electron. Unlike photoelectric absorption, this leaves a scattered photon with part of the original photon energy. For an originally monoenergetic source of photons, this leads to a continuous distribution of energies.

Pair Production

If the photon energy is greater than twice the electron mass (1.022 MeV) then pair production may take place, with the photon converting to an electron-positron pair. The probability of this increases with energy and varies with atomic number as Z^2.

Attenuation coefficient

The effect of this scattering on a beam of gamma rays can be described by the linear attenuation coefficient μ. This is the sum of the interaction probabilities for each of the three processes. For an intensity I_0 incident upon a material of thickness L, the transmitted intensity I will be given by

$$I = I_0 e^{-\mu L},$$

Eq. 2.3

where μ is the attenuation coefficient. This coefficient depends on the atomic number (Z) and density (ρ) of the material and on the energy of the incident gamma ray. As the density of materials may vary, the drop off in intensity may also be described by the mass attenuation coefficient μ/ρ, the linear coefficient divided by the density. For

each of the processes, the scattering probability tends to increase for high-Z materials, so such a material would be the best choice for the shielding material. Therefore lead (Z = 82) bricks can be used as shielding outside the cryostat. Inside the cryostat however, lead would not be suitable as it becomes superconducting at low temperature and the resultant poor thermal conductivity would cause difficulties for cooling the cryostat. Copper can be made with higher purity and cooled down more easily. However, copper has a heat leak below 20mK due to the slow release of heat by the conversion of orth-para conversion of hydrogen molecules [82], which prevents the cryostat cooling down efficiently. NOSV copper (a degree of purity for copper, with low hydrogen content) is used in order to reduce this and allow the low temperatures required by the detectors to be reached.

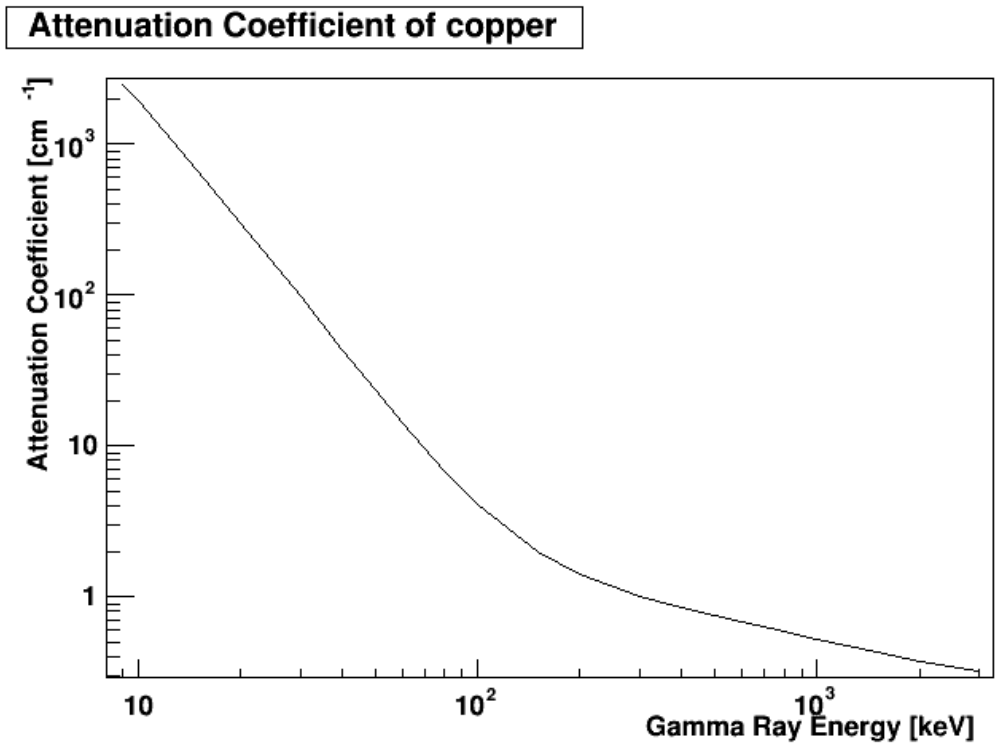

Figure 2.7 – The mass attenuation coefficient of copper for a range of gamma ray energies, for data from [87].

Shielding

The walls of the cryostat, the IVC and the 50 mK shield should already provide some shielding from external radiation, but this can still be improved further. There is also the possibility of some radiation from sources closer to the detector. After several prototypes the shielding of the detector was combined with the physical support of the detector in one NOSV copper structure.

This consisted of three components, a top plate of 10 mm thickness, a bottom plate of 15 mm thickness with an 8 mm diameter hole in the centre to allow radioactive sources to be used for testing, and a middle section with a cavity in the centre where the phonon and light detectors were suspended. The central section was 25 mm high and ~15 mm thick, with several small holes for the strings holding the detector and to attach the connector p.c.b. for the cabling. It also had a 10mm x 5mm opening for radioactive sources to be used for testing.

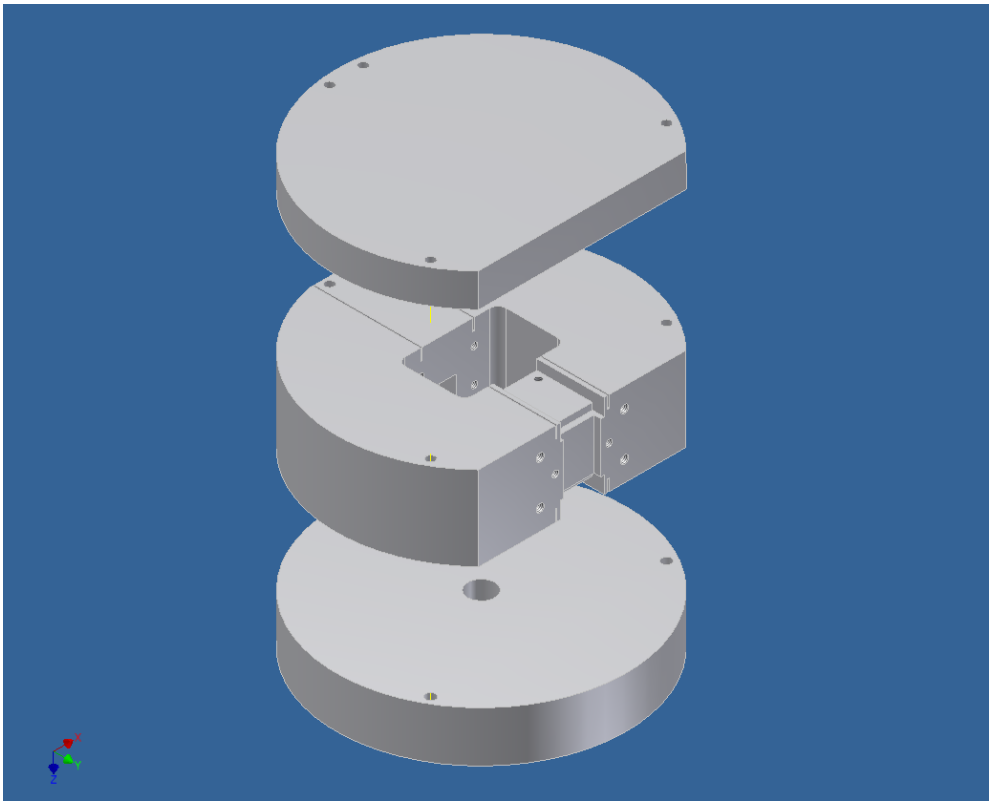

Figure 2.8 - The three components of the detector housing.

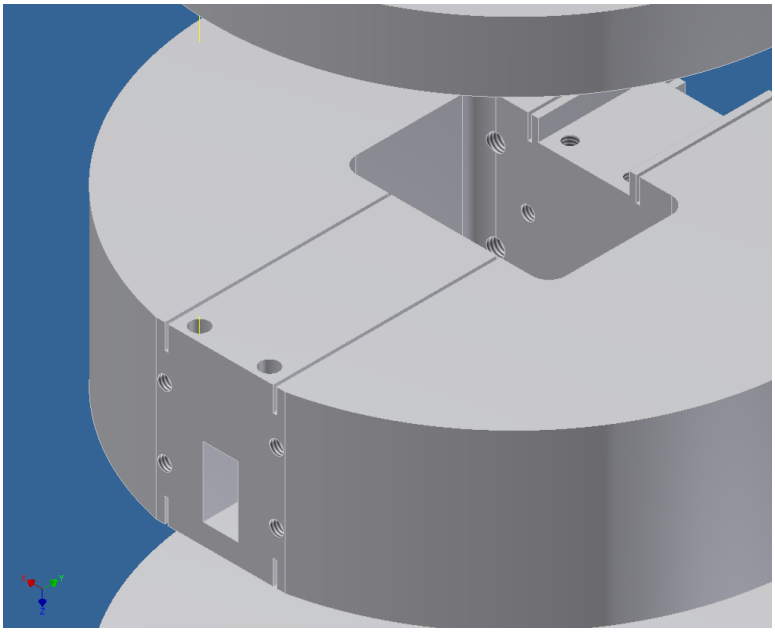

Figure 2.9 - A close up of the central component of the housing, showing the side opening to allow a gamma beam from a radioactive source through to the detector.

Before this final version of the housing several prototypes were tried (see Table 2.2), showing a variation in the measured background rate with the amount of shielding coverage around the detector, which gave confidence that the origin of the relatively high rate of particle interaction in the detector was due to external background.

As the shielding of the detector was improved through these modifications, so the background rate measured in the detectors dropped and the performance of the detectors improved.

Setup	Background Rate above 122keV [s^{-1}]	Solid Angle Coverage
Copper Frame	0.6 ± 0.1	~0.5x4π
Bottom Disk + Frame	0.45 ± 0.1	~0.7x4π
Full Setup	0.13 ± 0.01	~0.98x4π

Table 2.2 - The rate of pulses, with pulse heights greater than pulses from the 122 keV peak of a Cobalt-57 source, as the amount of shielding around the detector is varied.

The reduction in the error on the background rate for the full setup, compared to the earlier arrangements, comes about through the improvements in operating the detector and identifying pulses in such conditions.

The openings for the particles from radioactive sources allow for the collimation of beams from such a source. This will reduce the proportion of lower energy Compton scattered particles received by the detector compared to the full photo peak. These low energy events would add to the pile-up related problems in the detector. Additionally, an arrangement of brass plates with a central hole and lead bricks was used outside to align and collimate the beam already outside the cryostat.

2.5.3 Temperature bath

As well as the shielding and support provided by the housing, it acts as a temperature bath for the detectors, providing the stable temperature for the detector temperature to slowly decay back to after a particle interaction. This aspect is described in Chapter 6. The housing is made of NOSV copper to facilitate this, as the copper has good thermal conductivity and is free of heat leaks allowing the housing to be cooled down to 10 mK and below.

2.5.4 Reflecting cavity

Finally the housing provides a reflecting cavity to contain the scintillation light emitted by the phonon detector and allow for it to be collected by the light absorber. To achieving maximum light collection efficiency, and thus the greatest light detector signal size, VM2000 foil (from 3M) was placed around the two detectors for as close to 4π coverage as possible. Small gaps have to be left in the foil for the gold bond wires and the string supporting the detector. The foil has a very good reflectance on the inside with >98% reflectivity at frequencies between 400 nm and 700 nm – the region of the spectrum where the scintillation light is produced. The outer side of the

foil has an adhesive applied, allowing the foil to simply be stuck to the inside of the housing.

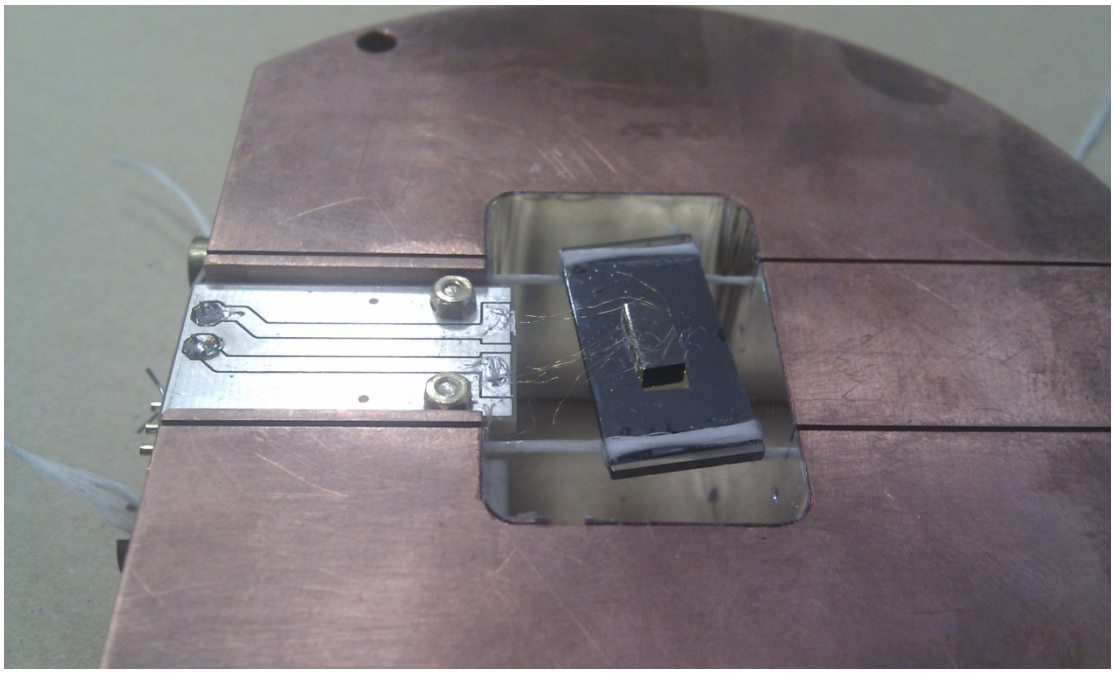

Figure 2.10 - NTD 38a glued onto the sapphire light detector inside the final version of the detector housing. The crystal is held in place using Kevlar fibres and the gold bond wires connected to the p.c.b. using silver paint. The reflecting foil can be seen around the inside of the cavity.

2.6 Cabling

The detector is connected to the cold amplification stage via etched metal foil on polyimide cables (see Figure 2.11). There are two different kinds of this cabling, copper cabling from the detector to the mixing chamber and steel cabling from there to higher temperatures. The relatively low thermal conductivity of the steel cable makes it suitable for bridging the larger temperature difference from ~10 mK to ~120 K without conducting too much of the heat down to the detector. This heat conduction is also reduced using sets of heat sinks, which divert heat to the fixed temperature levels rather than the detector, and by splitting the steel cabling into two parts with a copper heatsink for the individual tracks in the middle at 50 mK. The heat transfer to the detector level is described further in Chapter 6.

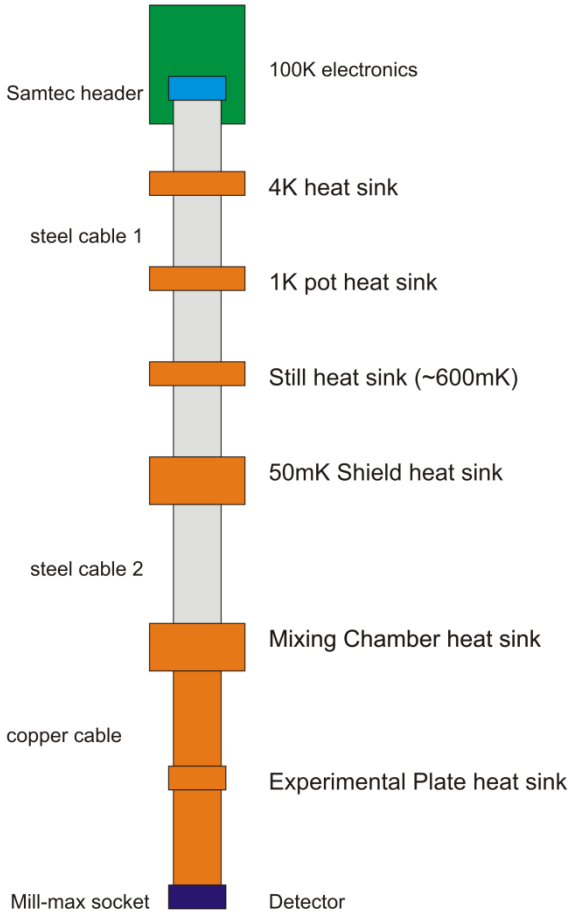

Figure 2.11 - Cabling scheme from the detector to the 100 K electronics.

Part of the motivation for this cabling is to test it for the EDELWEISS-III dark matter experiment. For such a low background experiment the use of radiopure materials in the cabling is very important, hence the copper cabling – with a lower natural radioactivity is used close to the detector.

At the cold amplification stage, relatively far from the detector, this is of less concern and the steel cable is connected to the circuit board with a 1 mm pitch Samtec connector. Radioactivity measurements showed that the radiopurity of this connector was not good enough – particularly due to the black dyed liquid crystal polymer used as insulated housing for the pins. Therefore custom made connectors were designed and made in Oxford with Mill-max pins and sockets held in a Delrin housing (as in

Fig. 2.12). For shielding against electromagnetic interference and for mechanical support some of these connections were then clamped inside brass housings.

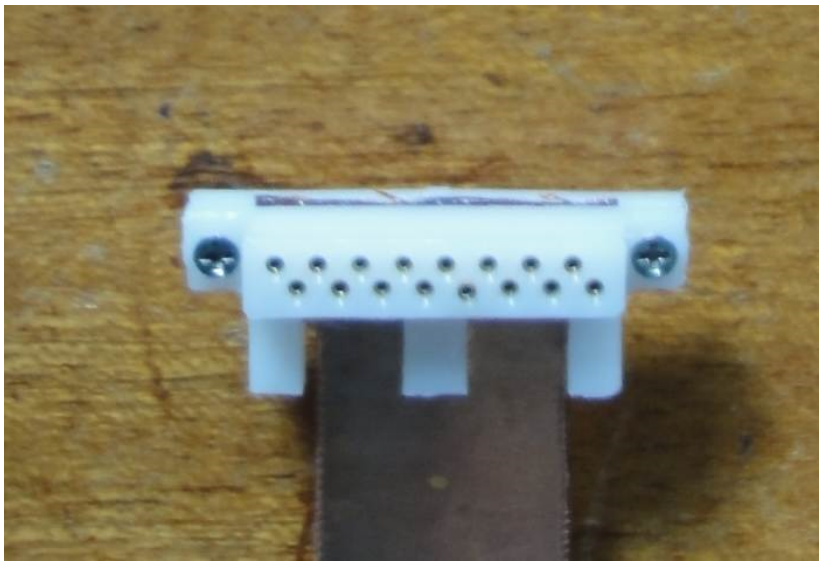

Figure 2.12 - Mill-max sockets inside a Delrin holder, on the end of one of the 16 track copper cables for use in EDELWEISS-III

The cables themselves consist of a layer of polyimide which has been laminated onto a metal foil (either copper or steel). The foil is etched into tracks using a photolithographic process [88] – a 'photoresist' layer is applied to the foil and then it is exposed to UV light. A 'phototool' is used to expose only the parts that will become the conducting tracks of the cable. Under exposure the photoresist becomes insoluble to developer solution so the rest can be washed away, leaving only the photoresist above the tracks.

Finally the etching is carried out, using FeCl (for copper) or HCl (for steel) the foil which isn't covered in the photoresist is etched away leaving the track design from the phototool. Next the cables are laminated for most of the length, leaving the ends so connectors can be soldered on, another layer of polyimide is added on to provide some extra thickness to the cable, as shown in Fig. 2.13. Then a shielding layer of copper or steel is added.

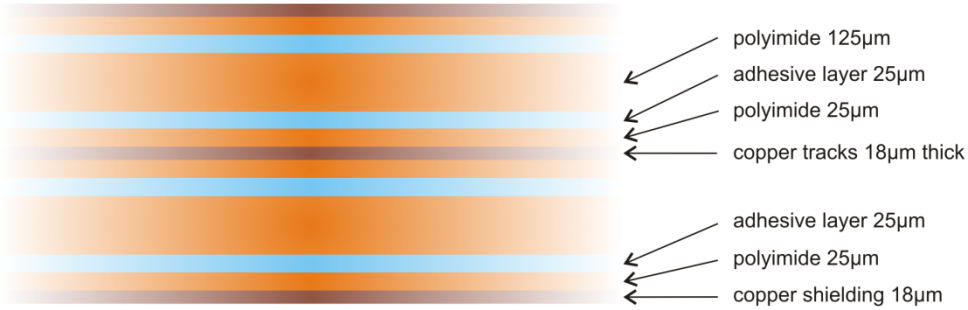

Figure 2.13 - cross-section of the copper cable.

There is an additional fabrication process for the steel cable. Soldering to steel would require the use of an aggressive flux, which is potentially problematic due to the risk of some residue remaining, which could cause some parasitic resistance or even eventually corrosion to the cable. Therefore the ends of the steel cables are copper plated so that connectors can be soldered to them.

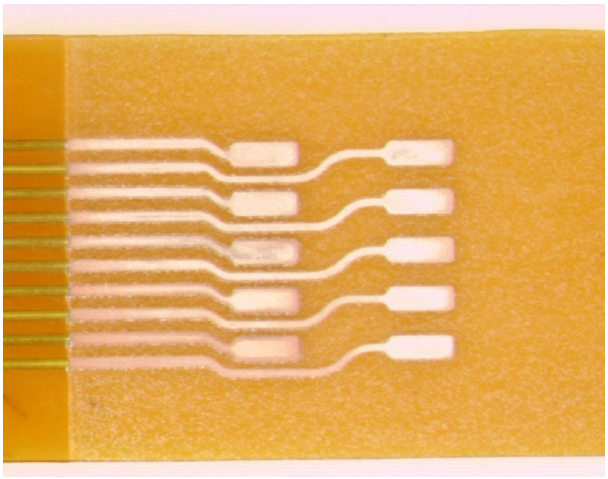

Figure 2.14 - Copper plated steel tracks. On the left of the picture the edge of the laminated polyimide cover layer can be seen.

The detector is read out first through a 20 cm long cable with ten copper tracks of width 0.1 mm and pitch 0.5 mm. This has a shielding layer of copper on either face for most of its length, and the custom connector, made of Millmax pins and a delrin connector, on either end. The copper foil has a thickness of 18 µm, and the polyimide

a thickness of 25 μm. The copper used as shielding layers is similar, but a thicker 125 μm layer of polyimide is added between the tracks and the cover layer – this provides some extra rigidity to the cable and further reduces the microphonic noise due to vibrations.

This is connected to the steel cabling, which comes in two sections, the first has delrin/Millmax connectors on both ends, while the second has this at one end and a 1mm pitch Samtec connector at the other. In between the two steel cables is a section at 50 mK of copper tracks on a polyimide base, which is used to provide extra heat sinking to the tracks. The steel cabling has a total length of 80 cm, a width of 10mm and similar dimensions for the tracks but with a foil thickness of 25 μm and a polyimide thickness of 75 μm rather than the 25 μm layer.

2.7 Heat capacity

The heat capacity of the detector will be important for the sensitivity of the detector as it will determine the size of the temperature change corresponding to an interaction of certain energy. It will also contribute to the noise via thermal fluctuations, and determine the characteristic time constants of the detector response.

The heat capacity will later be measured experimentally by looking at the response of the detector to pulses of known energy from a radioactive source. However, it may also be estimated theoretically to investigate what components of the detector provide the dominant contributions and what improvements could be made to future versions of the detector.

2.7.1 Lattice heat capacity

For the crystalline absorber the heat capacity will be dominated by the vibrations of atoms in the crystal lattice [89]. These lattice vibrations may be modelled as phonons

and, at low temperatures, this phonon contribution to the heat capacity can be calculated using the Debye model.

$$C_p = \frac{12\pi^4}{5} n_a k_B \left(\frac{T}{\theta_D}\right)^3,$$

Eq. 2.4

where n_a is the number of lattice atoms per mole, k_B is the Boltzmann constant, and θ_D is known as the Debye temperature of the crystal. The Debye temperature is a characteristic of the type of material used. The Debye frequency ν_D is calculated, using the speed of sound in the crystal v_s and the number density of atoms n, as a theoretical estimate of the maximum frequency of vibrations in the crystal.

$$\nu_D = \left(\frac{3n}{4\pi}\right)^{\frac{1}{3}} v_s$$

Eq. 2.5

This frequency is then converted into its corresponding temperature, θ_D, the Debye temperature.

$$\theta_D = \frac{h\nu_D}{k_B}.$$

Eq. 2.6

The detectors tested use dielectric crystals of calcium tungstate and calcium molybdate [90] for the absorber of the phonon detector, and sapphire for the substrate of the light detector.

Crystal	Al_2O_3	$CaWO_4$	$CaMoO_4$
Debye T (K)	1024	270	446

Table 2.3 – the Debye temperatures of the crystals used for the detectors.

The other components of the detector, the metal films and the NTD Germanium, will also have a phonon contribution to the heat capacity, but at low temperatures the T^3 dependence makes this relatively small compared to the specific heat contribution from electrons.

2.7.2 Heat capacity of metals

Unlike the absorbers, the presence of free electrons means that metals have a significant contribution to the heat capacity from these [89]. At low temperatures the electronic heat capacity can be described by the free electron model.

Electrons are fermions with spin 1/2 and obey the Pauli Principle, so each energy state will be occupied by two or less electrons with opposite spins. The electrons therefore fill up the energy states, from the lowest to a maximum limit known as the Fermi Energy E_F.

$$E_F = \frac{h^2}{8\pi^2 m}\left(\frac{3\pi^2 N}{V}\right)^{\frac{2}{3}}.$$

Eq. 2.7

The free electron model assumes that the electrons in a metal are completely separate from their atoms and ignores interactions between electrons, so that the electrons are modelled as an ideal gas. This has a density of states *g(E)*.

$$g(E) = \frac{V}{2\pi^2}\left(\frac{8\pi^2 m}{h^2}\right)^{\frac{3}{2}} E^{\frac{1}{2}}.$$

Eq. 2.8

With these and the Fermi-Dirac distribution function the electronic contribution to heat capacity is then found to be

$$C_e(T) = \frac{\pi^2}{2} N k_B \frac{T}{T_F},$$

Eq. 2.9

where T_F is the Fermi Temperature, related to the energy by $E_F = k_B T_F$. Adding in the smaller contribution from the lattice vibrations we now get the heat capacity described by

$$C = \gamma T + \beta T^3.$$

Eq. 2.10

The electronic contribution has been simplified into a single constant γ, known as the Sommerfeld constant. The linear dependence of the electronic heat capacity means

that it will be dominant at low temperatures when the lattice contribution drops off quickly.

In the detectors there are gold pads on the crystal below the NTD germanium wafers, and gold contacts on either side of the wafer. In addition to this, the light detector has a chromium film between the gold and the crystal to provide extra adhesion for the gold film. Gold has the Sommerfeld constant γ_{gold} = 0.689 mJmol^{-1}K^{-2} and the Debye Temperature θ_D = 162 K, while Chromium has γ_{chrom} = 1.40 mJmol^{-1}K^{-2} and θ_D = 630 K.

Germanium will have a lattice contribution to the heat capacity, with a Debye temperature of 371 K. However, like metals, the heat capacity at low temperature will be dominated by its charge carriers and can also be described by equation 2.10. The Sommerfeld constant may vary between NTD sensors due to the effect of the neutron doping and the metallization process [91,93], with γ for a similar NTD to the ones used being equal to 1.05x10^{-6} JK^{-2}cm^{-3} [94].

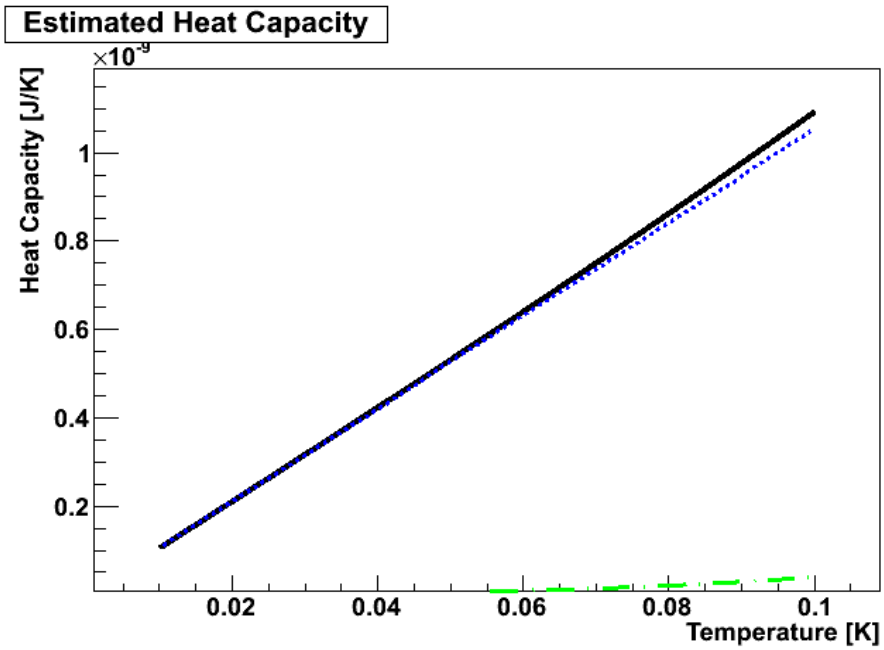

Figure 2.15 - the theoretical NTD Germanium heat capacity with the total heat capacity plotted in a bold black line, while the phonon and electron contributions are shown as the dashed green and dotted blue lines.

2.7.3 Heat capacity of Araldite

In amorphous solids such as araldite, the Debye model can no longer apply as the length of the homogenous material becomes shorter. This disorder provides extra vibrational modes (fractons [92]) by which heat can be transferred. This will give excess heat capacity, above what the Debye model would have provided. There will be an extra linear term in the heat capacity, along with the T^3 term that might have been expected.

$$C_a = aT + bT^3 \qquad \textbf{Eq. 2.11}$$

The values of the two constants, *a* and *b*, are 2.91 $\mu Jg^{-1}K^{-2}$ and 15.7 $\mu Jg^{-1}K^{-4}$ respectively.

2.7.4 Total heat capacity

These individual components all contribute towards the total heat capacity of the detectors. The combined result is shown in tables 2.4 and 2.5.

Part	Dimensions (mm^3)	Heat Capacity @ 20mK (J/K)	Heat Capacity @ 10mK (J/K)
NTD Germanium	2 × 7 × 1	2.9×10^{-10}	1.47×10^{-10}
Chromium film	10 × 16 × 0.00009	8.8×10^{-11}	4.4×10^{-11}
Araldite	2 × 2 × 0.025	1.4×10^{-11}	7.1×10^{-12}
Gold film (on crystal)	3 × 8 × 0.00025	8.5×10^{-12}	4.3×10^{-12}
Silicon	10 × 18 × 0.00025	7.4×10^{-12}	3.7×10^{-12}
Gold film (NTD sides x2)	1 × 7 × 0.00025	5.0×10^{-12}	2.5×10^{-12}
Sapphire (A)	10 × 20 × 0.5	1.7×10^{-13}	2.2×10^{-14}
Total light detector heat capacity (J/K)		4.2×10^{-10}	2.08×10^{-10}

Table 2.4 – the heat capacity of the light detector.

Part	Dimensions (mm^3)	Heat Capacity @ 20mK (J/K)	Heat Capacity @ 10mK (J/K)
NTD Germanium	3 × 8 × 1	5.0×10^{-10}	2.52×10^{-10}
Araldite	2 × 2 × 0.025	1.4×10^{-11}	7.1×10^{-12}
Gold film (on crystal)	3 × 8 × 0.00025	8.5×10^{-12}	4.3×10^{-12}
Gold film (NTD sides ×2)	1 × 8 × 0.00025	5.7×10^{-12}	2.9×10^{-12}
Calcium Tungstate	10 × 20 × 5	1.25×10^{-11}	1.6×10^{-12}
Total phonon detector heat capacity (J/K)		5.6×10^{-10}	2.68×10^{-10}

Table 2.5 – the heat capacity of the calcium tungstate phonon detector.

The dominant part of the detector's heat capacity is the NTD Germanium sensor (see Table 2.4 and 2.5). This means that the size of the absorber crystal for the phonon detector can be increased to provide a larger target mass, before having a significant effect on the overall heat capacity of the detector. The thermal fluctuation noise of the detector varies with a dependence of $\sqrt{CTk_BT}$, therefore at low temperature the target mass should be able to increase without much effect on the contribution of that to the resolution.

At a temperature of 20 mK the Calcium Tungstate crystal absorber should be able to increase by a factor of around forty before the heat capacity becomes equivalent to that of the NTD Germanium sensor, while at 10 mK it should be able to increase by over one hundred times before becoming equivalent.

However, for the light detector increasing the substrate crystal of the detector is not necessary as it only needs to collect the scintillation light from the phonon detector in its light absorbing layer. Therefore the dominating NTD heat capacity will severely limit the resolution of the detector, and a smaller NTD sensor should be found.

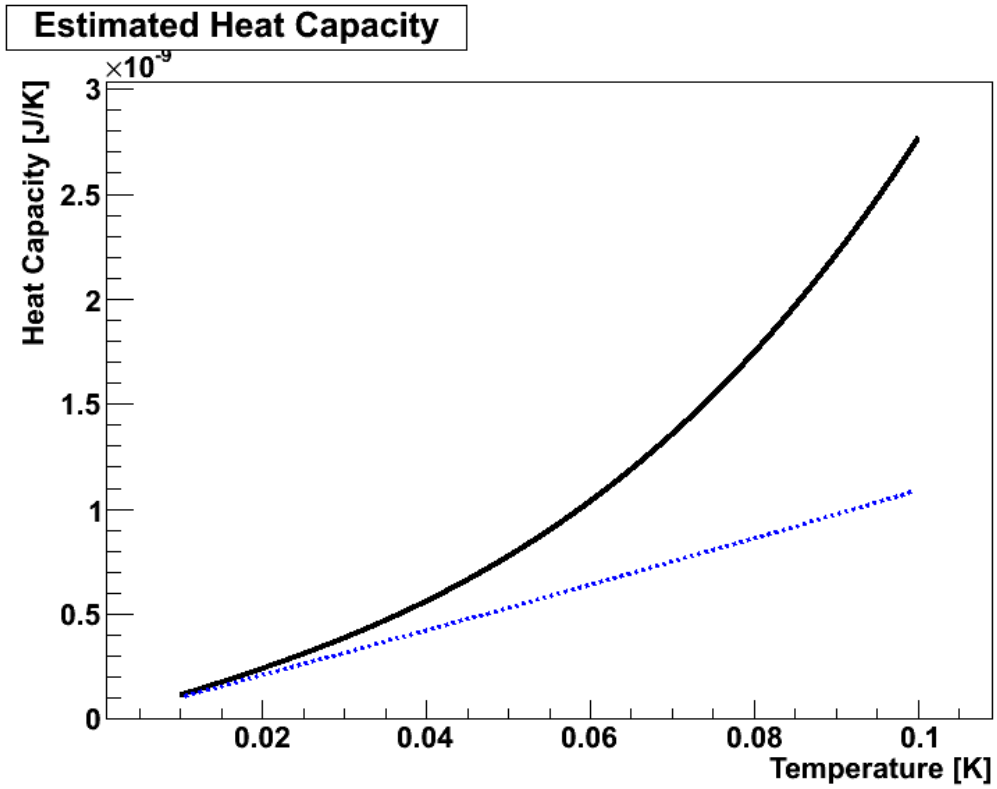

Figure 2.16 – calculated heat capacity estimate shown from 10mK to 100mK. The total is shown as a solid black line, and the contribution from the NTD germanium alone shown as a dashed blue line.

After the NTD Germanium, the next largest contributions to the heat capacity, particularly at low temperatures, are the Araldite and the Chromium film. The Chromium was added to the light detector to provide extra adhesion for the gold film on the sapphire. However, the phonon detector, which was made later without using the Cr film, shows that it is not necessary. Therefore in future versions of the light detector the Chromium should not be included.

The Araldite, on the other hand, is required and efforts were made to control and limit how much of the glue was used on the detectors (described in 2.3).

2.8 Scintillation

The scintillating crystal of the phonon detector should be chosen to suit the experiment, with nuclei of a high mass number for dark matter detection or high

levels of a suitable double beta decay nucleus for a neutrinoless double beta decay search.

In addition to this, the scintillator should have a high scintillation efficiency, to maximise the light collected, and should be produced with low intrinsic radioactivity, to reduce the background for the experiment [95].

Oxide crystal scintillators such as Tungstates and Molybdates are crystals which fit these specifications. With the high mass of the tungsten and molybdenum nuclei, they are suitable for WIMP searches, and with isotopes such as ^{100}Mo or ^{180}W they could be used for neutrinoless double beta decay searches [96].

Taking two potential crystals, calcium tungstate ($CaWO_4$) and calcium molybdate ($CaMO_4$) as a prototype; the scintillation spectrum for calcium tungstate peaks around 420 nm, and for calcium molybdate peaks around 540 nm.

The scintillation properties of these crystals have been measured over a range of temperatures, generally at temperatures significantly higher than the milli-Kelvin temperatures where the detectors will be operated. The properties may vary with temperature due to the interaction of the emission centre with lattice vibrations [97,98]. However, the results from these higher temperature studies (for example, figure 2.1 at 8 K) may still be applied at lower temperatures as the scintillation properties of the crystal do not change significantly at these low temperatures [99].

At low temperatures, the decay time constants for the scintillation light are small relative to the final time constants of a temperature pulse in the detectors, which are typically ~10 ms. Typically there would be a fast component of ~1 μs and a slower component of ~500 μs. Both $CaWO_4$ and $CaMO_4$ have similar time constants, with the slow decay at 9K for an α particle interaction being 360 μs for the tungstate and 380 μs for the molybdate.

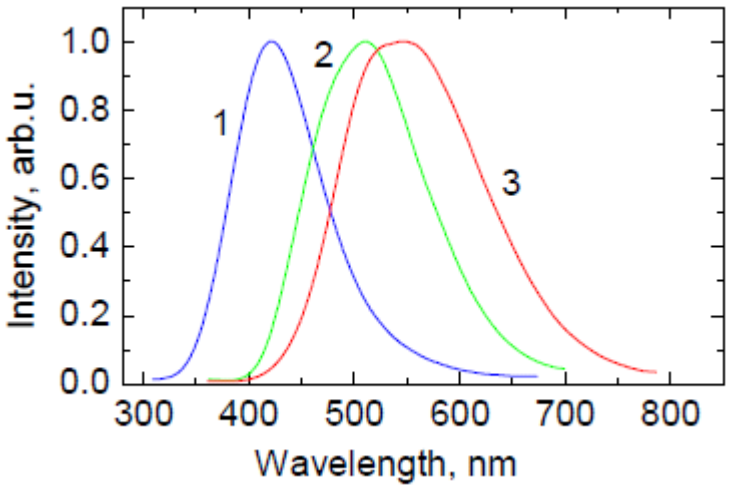

Figure 2.17 - Luminescence spectra of $CaWO_4$ (1), $ZnWO_4$ (2) and $CaMO_4$ (3) measured at 8 K for excitation with 31 eV VUV photons. From [100]

The relative light output of the two crystals is also rather similar. The room temperature light efficiency of calcium tungstate is given by 4.4 %, [101,102] but this increases at low temperatures so that the efficiency at low temperature (measured at 9 K) will be ~8.2 % [100]. At 9 K calcium molybdate will have an efficiency of 7.8 %.

2.9 Light Collection

The silicon layer on the light detector is present in order to act as an absorber for the scintillation light given off by the phonon detector. Two key considerations in the selection of this light absorber are maximising the amount of light absorbed and minimizing the heat capacity of the absorber layer, to reduce any adverse effects on the resolution of the detector.

The light absorber should therefore absorb as much of the light within this spectrum as possible, while the selection of the light absorber material and geometry should be made so as to minimise the heat capacity of the detector and increase the signal size.

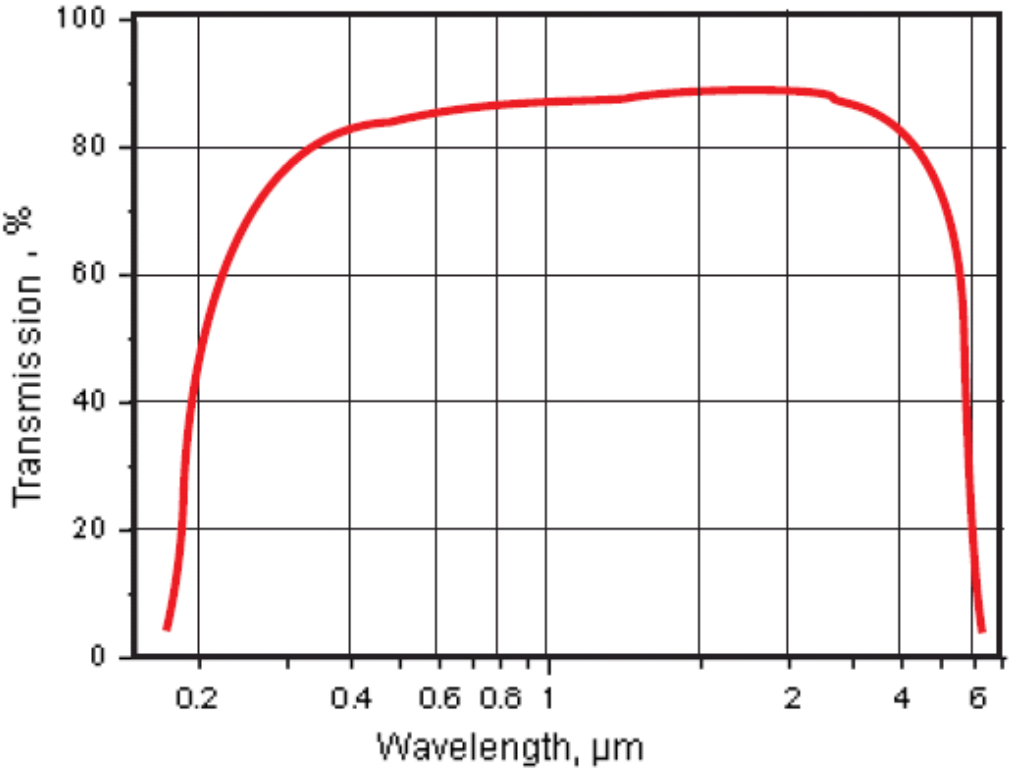

Figure 2.18 - Transmission Spectrum for Sapphire. At the optical wavelengths at which the Calcium Tungstate scintillates, this is mostly transparent [103].

The heat capacity of crystalline silicon is given by the Debye Model described previously with a Debye temperature of 645 K [104]. However, the sputtered amorphous silicon used for this light detector will be higher, with a heat capacity that can be modelled by a linear dependence with coefficient 3.2×10^{-6} J/gK^2 [105]. The heat capacity of the sputtered silicon layer used is presented in the table in 2.7.4. The value is significantly smaller than the NTD germanium, the dominant component of the heat capacity, so should not have too much impact upon the pulse size for the absorbed scintillation light.

The sapphire crystal, used as the substrate for the light detector, has a wide transmission band, which will be transparent to the majority of this scintillation light; therefore an additional light absorbing layer is required to collect the scintillation light, which would otherwise pass through undetected.

Silicon will absorb at these optical wavelengths, but the silicon layer needs to be thick enough to absorb the light.

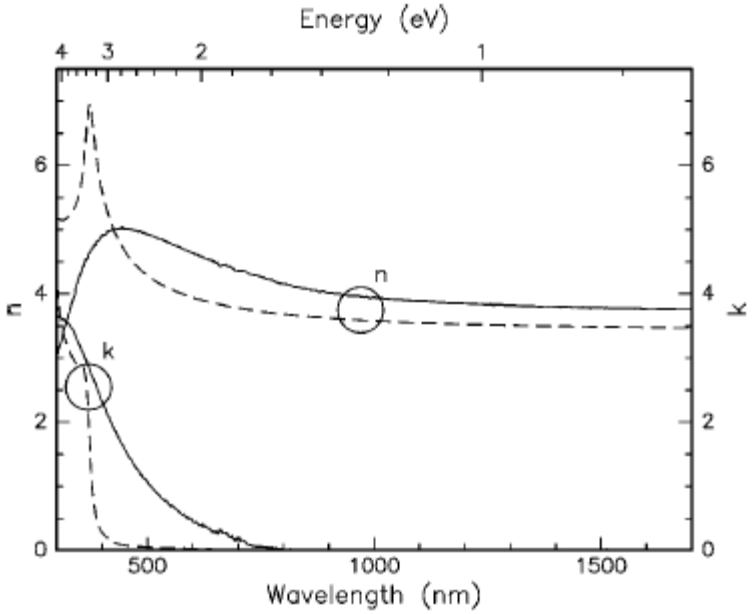

Figure 2.19 - The solid line shows the real and imaginary parts of the refractive index for amorphous silicon. The dashed line shows the same for crystalline silicon. The imaginary part, which described the absorption in the material, has a peak of 3.5 at ~300nm and falls off as the wavelength increases. From [106].

The opacity of a material to light can be described by giving the refractive index $\tilde{n}$ as a complex function

$$\tilde{n} = n + i\kappa .$$

Eq. 2.12

The two parts of this, n and κ, will give the phase speed and the level of absorption of the light in the material. Consider the wavenumber, k, of an electromagnetic wave in the medium.

$$k = \frac{2\pi n}{\lambda_0},$$

Eq. 2.13

with the electric field

$$E(z,t) = \mathrm{Re}(E_0 e^{i(kz-\omega t)}) .$$

Eq. 2.14

If the complex function for n is used, the two parts of the refractive index can be separated.

$$E(z,t) = e^{-2\pi\kappa z/\lambda_0}\,\mathrm{Re}(E_0 e^{i(2\pi n z/\lambda_0 - \omega t)})$$

Eq. 2.15

The term κ is known as the extinction coefficient and provides the exponential decay due to the absorption of light. The intensity of the light is proportional to the square of the electric field, so this can be given as an absorption coefficient a.

$$a = \frac{4\pi\kappa}{\lambda_0}$$

Eq. 2.16

At its peak, at a wavelength of around 300 nm, the silicon will have an absorption length of 127 nm. Therefore a thickness of 250 nm should be a suitable thickness for this absorbing layer. However, the scintillation peaks of $CaWO_4$ and $CaMoO_4$ are at higher wavelengths where the absorption length of the silicon layer is longer. For the calcium tungstate the absorption coefficient similar to that at its peak, corresponding to an absorption length ~135 nm, but for the calcium molybdate the absorption length is longer at ~ 240 nm.

For scintillation light from the calcium tungstate crystal passing through this layer an estimate of the amount of the light absorbed can be made using equation 2.17.

$$\int_{\lambda} I_{emission}(\lambda)(1 - e^{-a(\lambda)x})d\lambda$$

Eq. 2.17

Therefore, using the emission spectrum of Calcium Tungstate with a peak of 420 nm and FWHM of 90 nm, approximately 86% of the light will be absorbed. However, to consider the total amount of light absorbed by the light detector, one also needs to consider the reflecting foil that clads the inner walls of the detector housing. This does not give complete 4π coverage around the detector as some gaps were needed to allow in the string for holding the detector and the gold wires to the NTD sensor. There may also be reabsorption by the phonon detector, the amount of which will vary with the size and shape of the detector, as well as the how polished the surfaces

are and the presence of any defects in the crystal. Estimates of the collection efficiencies are calculated in chapter 7.11.

3. Readout electronics

The NTD germanium thermometers of the detectors are read out by measuring the resistance of the NTD sensor. This is achieved by voltage measurements across the sensor for a modulated bias current. This is carried out using an electronics system split into several sections; at room temperature there are two circuit boards, the first of which controls the bias sent (see Fig. 3.1 lower image) and reads out the detector with several amplification stages and the second of which is a DAQ board which filters and digitizes the data (see Fig. 3.1 upper image). Inside the cryostat, at ~120K, there is an additional cold amplification stage.

Figure 3.1 - The 12 Channel DAQ board (top) and the Pre-amplifier and Bias control board (bottom) used in the electronics chain at room temperature.

The bias current is modulated at a frequency ~1 kHz, with symmetric amplitude (+ve / −ve) with respect to no current. This modulation of the bias current allows the absolute value of the resistance of the NTD sensor to be measured at any given time and allows the readout to operate in a low noise frequency region. The bias is a superposition of a square wave component, which will give the main part of the

output signal, proportional to the resistance of the sensor, and an exponential component, which boosts the current at each transition to compensate for the RC time constant of the detector and wiring. The production of this modulated excitation will be described in sections 3.1 and 3.2.

With this bias current sent down to the NTD sensor, the resistance can then be found by a measurement of the voltage across the sensor. This begins with a differential amplification stage with cascoded FETs. The input stage of this contains a pair of FETs operating at 120K, to reduce noise, followed by a second pair of FETs in the room temperature electronics. Following this, a summing amplifier stage combines the voltage outputs from the previous stage to give the voltage drop across the detector.

At this point a compensation voltage may be added to the signal to reduce the signal size and prevent it exceeding the maximum voltage, as limited by the supply rails. Ultimately the temperature pulses will be found as a change in voltage of the signal, so this allows more gain to be applied to the signal if necessary to give a better signal to noise ratio. These stages of the electronics are described in section 3.3.

Finally the signal is filtered or anti-aliasing, with a loss pass filter, to remove frequencies about the Nyquist frequency. A Bessel filter is used for this to prevent distortion in the signal. It is then digitized using a 16 bit ADC and the continuous stream of data is stored as a series of 32768 point long sections. These elements of the DAQ chain are described in sections 3.4 and 3.5.

3.1 Modulation

The use of a modulated signal, as opposed to a d.c. readout with constant current, has two major advantages. Firstly, it allows a direct measurement of an absolute value of

the NTD-sensor resistance at any given time through eliminating common mode voltage offsets. Secondly, it allows the readout to operate in a frequency region with as low noise as possible, typically above the 1/f corner frequency [107].

A 10 V reference, together with an inverter and a fast switch, is used to create a signal that periodically switches between positive and negative values. An FPGA on the circuit board produces a modulation which is then connected to the logic input of a CMOS device, containing a single pole, double throw switch [108], with +10 V and −10 V voltages on its two inputs. The frequency of this modulation can be selected by sending commands to the FPGA – with a range from a few Hertz to a few kilohertz. The selection of this frequency will be discussed in section 3.1.3.

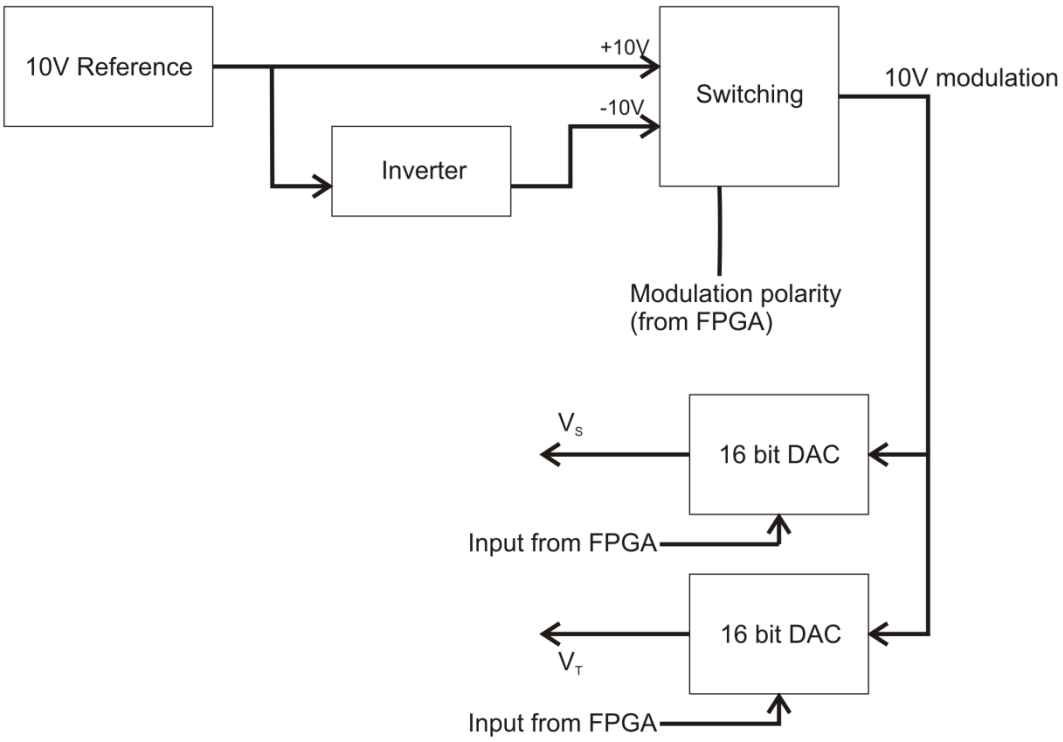

Figure 3.2 - The modulation voltage is created using a switch modulated by an input from an FPGA. The modulation then goes to a set of DACs where it is used as the reference for the components of the modulated bias current. The amplitude for each component is adjusted through sending appropriate commands from the FPGA to each individual DAC.

3.1.1 Offsets

There is the potential for d.c. offsets to appear in the signal, due to the offsets inherent to any active electronics components (op-amps, DACs etc.) or due to thermopower in the cryogenic wiring between the room temperature electronics and the milli-Kelvin temperature levels near the detector. The offset voltage of op amps may typically be up to a few milli-volt in size, similar to the signal variations expected for a particle interaction in one of the detectors. Thermopower, the voltage induced across material due to a temperature gradient across it, could also have a size up to a milli-volt due to the material in the cabling from room temperature [135].

The electronic component offsets could have time dependence due to temperature fluctuations at the room temperature circuit board, while the thermopower introduced in the cabling connecting the room temperature electronics to the detectors operating at milli-Kelvin temperatures inside the dilution refrigerator will also be time dependent with variations in the fill level of the main bath or the 1K pot causing changes in the temperature profile of the cabling. As these offsets produce a d.c. signal,without modulation these changes in offset would be difficult to distinguish from changes in thermometer resistance. Using the modulation allows variations of the d.c. component to be cancelled and the alternating signal due to the resistance to be extracted.

These offsets from zero may have typical values in the final signal of around ten milli-Volt, with variations of a similar magnitude occurring on a timescale of ~1 s. The size and speed of the drift was independent of the temperature scale of the detector – similar fluctuations were observed when operating the setup at 77 K, and at room temperature.

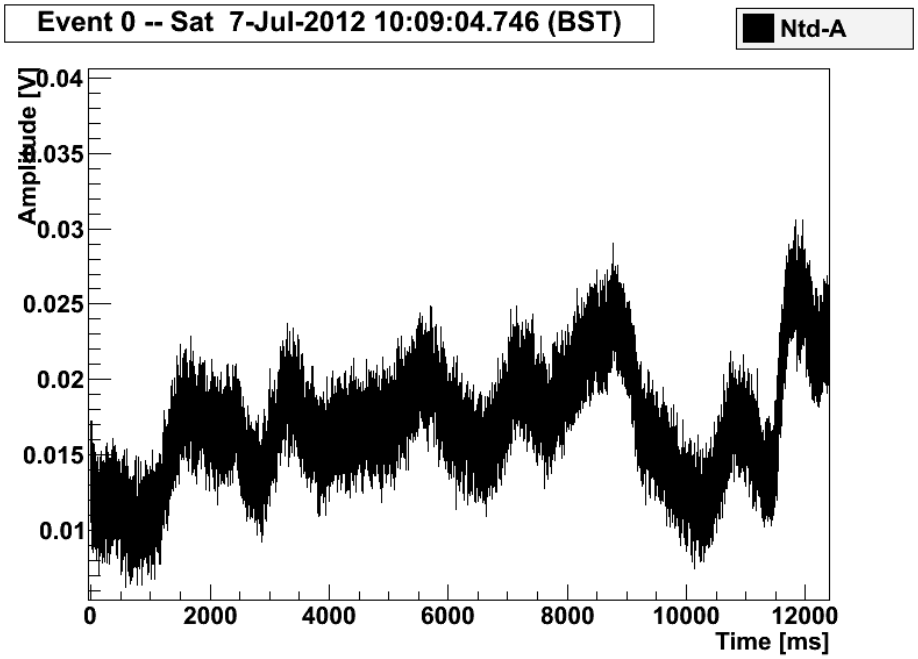

Figure 3.3 - The drift of the zero offset for the detector signal at 10mK with no excitation applied.

The behaviour of offsets produced in the different sections of electronics will be slightly different, with some having a size proportional to the NTD resistance and some being independent of resistance. Both sections, however, will produce a d.c. contribution to the signal which can be removed by the modulation. If an offset is introduced in the readout section of the electronics (described in 3.3), it will produce such a d.c. offset, independent of the NTD sensor resistance.

Offsets introduced in the bias section however will add to the excitation current (described in 3.2) and produce an additional signal proportional to the NTD resistance. However, unlike the modulated bias signal these roughly constant offsets will not change polarity at the modulation frequency, therefore they will provide another d.c. offset (albeit one with a dependence on the NTD resistance) that can be removed by the de-modulation process during the analysis of the data.

3.1.2 Stability of the modulation

It is important that the frequency of the modulation remains constant over time; variations in the modulation in a single detector could be misinterpreted as a change

in the absolute voltage of the signal, while variations between different detectors could lead to mismatches in timing between different pulses – particularly important as discrimination with the detectors requires simultaneous measurements.

The period of the modulation may vary slightly over time due to variations in the temperature of the room temperature electronics; however this effect is very small – with fluctuations in the order of 10^{-4} of the period, as in Fig. 3.4. The period will typically be ~1 ms, while the temperature pulses in the detector are of length ~10 ms.

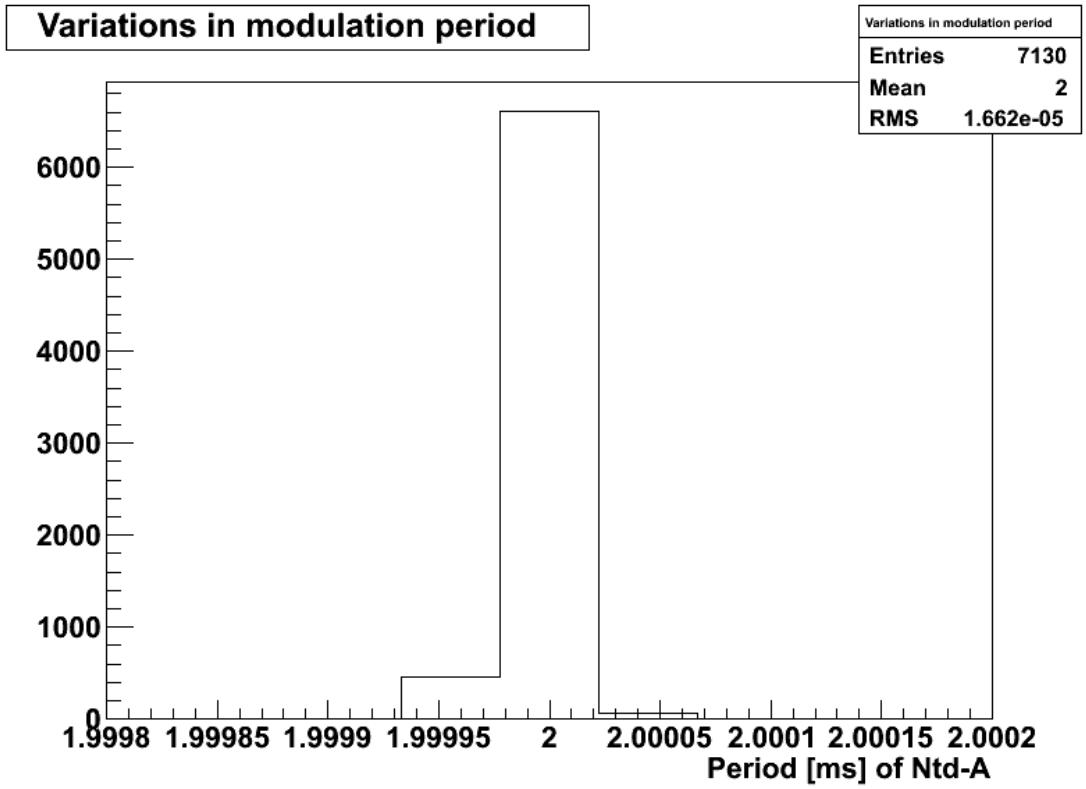

Figure 3.4 - Measured values for the period of the modulation, with it set at a frequency of 500 Hz.

3.1.3 Limits on the modulation frequency

For the lower limit of the modulation frequency, it should be faster than the variations in the common mode offsets. However, as these variations are relatively slow, the upper limit is more important. There will be an upper limit on the useful range for the choice of the modulation frequency; it will be limited by the parasitic capacitance across the detector (giving rise to an RC time constant, typically C ~ 50pF), and by

naturally limited capability of the pole cancellation circuit that is included in the readout electronics to compensate for this RC time constant of the voltage read across the NTD-sensor. Ideally the highest frequency possible would be used.

3.2 Bias

There are two parts to the excitation for the bolometer – a square wave component, V_S, that provides the main part of the bias current and an exponential component, V_T, that provides an extra component to boost the signal soon after the polarity switch. The voltage across the NTD due to V_S will not be a pure square wave – due to the RC time constant arising from the parasitic capacitance there is a significant rise time seen, as well as a downward slope on the top (and upward at the bottom) due to the high pass filter in the electronics. The rise can be made steeper by adding the exponential component V_T to help charge the parasitic capacitance quicker.

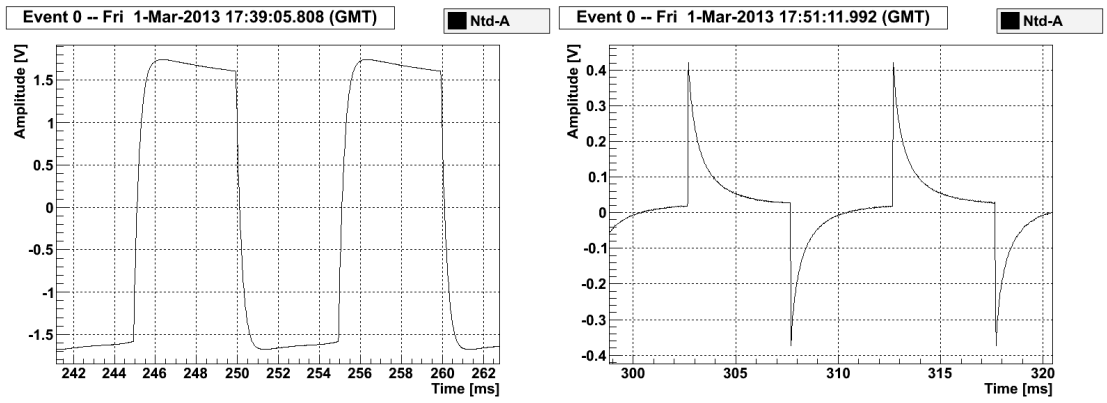

Figure 3.5 – voltage measured across the NTD sensor due to (a) the main part of the bias current V_S; and (b) the exponential boost V_T.

Both of these come from the DACs as square waves but, as shown in Figure 3 section A, V_S goes to the sensor via an integrator, with a series resistor R_{IN} and parallel capacitor C_F. This integrates the square, with a factor $1/(j\omega R_{IN}C_F)$. Meanwhile V_T is input via a series capacitor C_{IN} which leaves the signal as a square but provides a

factor C_{IN}/C_F in amplification. These two components add and are sent to bolometer stage (section C in Fig. 3.6).

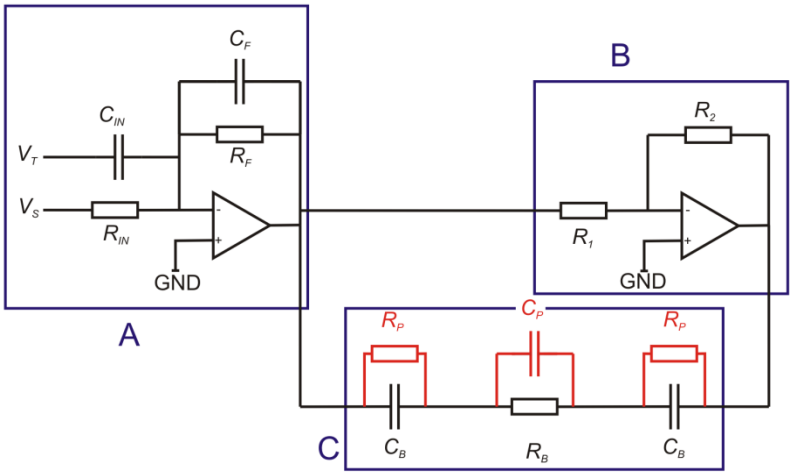

Figure 3.6 - the bias section of the readout electronics, showing the circuit for excitation (A) and the inverter (B) that provides the inverse modulation. The elements below (C) show the NTD-sensor (with parasitic capacitance) and the d.c. blocking bias capacitors (with parasitic resistance).

The bias current reaches the bolometer sensor resistance R_B through a pair of series blocking capacitors C_B, which provide d.c. isolation for the sensor. These capacitors also differentiate the bias currents. thus the main part of the excitation V_S, which was integrated in the last section, is then differentiated back to a square. The boost V_T, which had been left as a square, is differentiated to give its exponential shape.

This is complicated slightly by the resistor R_F which provides a d.c. path in the feedback circuit in A. This feedback provides a high pass filtering effect to keep the output tied to a value around zero and prevent it from drifting and hitting a supply rail. The time constant for this effect is ~30 seconds, much longer than the length of the modulation (which is typically ~1 ms) and the length of pulses due to particle interactions (which are typically ~100 ms).

The resistance of the NTD-Ge sensor R_B is kept in series with two capacitors C_{B1} and C_{B2}, but the bolometer and the capacitors may have some parasitic capacitance or parasitic resistance in parallel.

The parasitic resistance across each of the capacitors forms a high pass filter, however the time constant of this, $C_{B1}R_{P1,}$ will be very high so the bias only really undergoes the differentiation due to these capacitors. However the parasitic capacitance, C_P, across the resistor, R_B, will affect the shape of the signal. It creates the low pass filter type effect with a time constant $R_B(C_P+C_B/2)$ which slows down the rise of the signal after each polarity switch. It is this effect which the exponential boost V_T is designed to counteract. With a carefully selected ratio of the two excitation voltages the terms in the signal should cancel and produce a square wave. This square wave, and any non-periodic effects due to variations in resistance, can be expressed as the sum of many sinusoidal components with different frequencies in a Fourier transform, and hence the circuit can be described using complex impedances.

$$\Delta V_B = V_S \frac{1+ j\omega R_{in} C_{in} V_T / V_S}{1+ j\omega R_B (C_P + \frac{1}{2} C_B)} \frac{j\omega C_F R_F}{1+ j\omega C_F R_F} \frac{C_B}{C_F R_{in}} R_B .$$

Eq. 3.1

Equation 3.1 shows the $\left(1+ j\omega R_B (C_P + \frac{1}{2} C_B)\right)^{-1}$ term from the parasitic capacitance, it is this part which would create a potentially slow exponential rise for the signal. If the bolometer resistance and the parasitic capacitance become too high, the signal will take too long to rise and flatten out. This will provide an upper limit on what modulation frequency can be used.

The exponential boost part of the bias circuit multiplies this with the extra term $1+ j\omega R_{in} C_{in} V_T / V_S$ as the numerator of the fraction to introduce pole-zero cancellation. The "zero" is the numerator introduced by the additional part of the bias circuit and it is used to cancel the "pole" in the denominator due to the parasitic capacitance. The two terms will cancel when

$$R_B\left(C_P + \frac{1}{2}C_B\right) = R_{in}C_{in}\,V_T/V_S \ .$$

Eq. 3.2

Therefore V_T and V_S can be fine tuned to solve this equation, and remove the low pass behaviour of the parasitic capacitance.

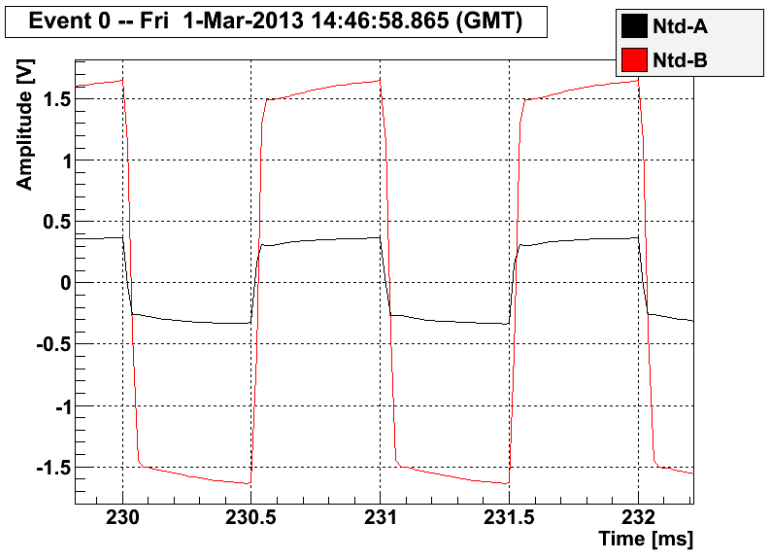

Figure 3.7 – Two NTD signals with the pole zero cancellation applied. This will correct for the slow rise, but in practice there may be additional effects which have not been included in this model.

Along with this exponential boost, the problem also requires that the parasitic capacitance across the detector is kept low, as the size of the bias current that can be used is limited by the supply rails of the amplifier. The shape of the signal will also be limited by the slew rate of the electronics, so if the RC time constant becomes too large then the full correction for it will not be possible. The extra Joule heating effect on the detector from this current is also undesirable. The parasitic capacitance is covered in more detail in Chapter 4.

3.3 Amplification

The voltage signal across the NTD-sensor is then read out with a differential amplifier stage with two cold (~120 K) JFETs at a cold electronics stage in the cryostat (see Fig. 3.8). This is a cascode circuit containing two more FETs at room temperature (one in each branch). They are connected such that one acts as a common source, and the other as a common gate. This gives a two stage amplifier with the first part acting as a transconductance amplifier, which outputs a current signal proportional to the input voltage, and the second part acting as a current buffer. This improves the isolation between the input and output of the amplifier by removing any direct coupling between the two.

The bias signal at either side of the detector is connected to the gate of the two JFETs. The drain of these transistors goes to the source of another transistor on the room temperature electronics, while the source voltage goes to the gate input of this warm transistor.

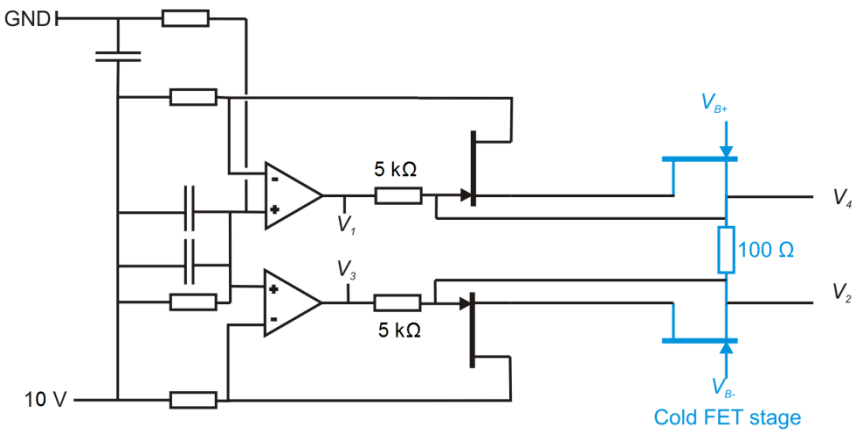

Figure 3.8 - the differential amplifier stage, including the cold FETs.

The current flowing into the drains of these two transistors is fixed by the two op amps. A 10 V supply and voltage divider gives a constant voltage at the positive input of the op amps (measured for two of the signal channels, with an error of less

than 0.01 V). Each op amp then adjusts its output to fix the negative input, resulting in a current flow across the 5 kΩ resistor which gives the four output voltages $V_{1,2,3,4}$. The two cold transistors with the 100 Ω resistor between them act as a source follower and convert the bias current input through the NTD sensor into a voltage signal that can be readout by the rest of the circuit.

In this circuit there is no d.c. path to the inputs of the JFETs. The bias point would therefore normally drift, but the parasitic resistance of the capacitors C_B provides such a d.c. path. This is enough to accommodate the leakage current of the JFET and has the beneficial effect of keeping the transistor at a suitable operating point. The usual voltage at the input to the JFET is established through this parasitic resistance. When the input to the JFET was changed from this value by grounding and then left to float back to the original value the time constant of the drift back was ~8 seconds. This requires that the parasitic resistance is TeraOhm or even larger. This then allows the approximation in section 3.2 that R_P is negligible.

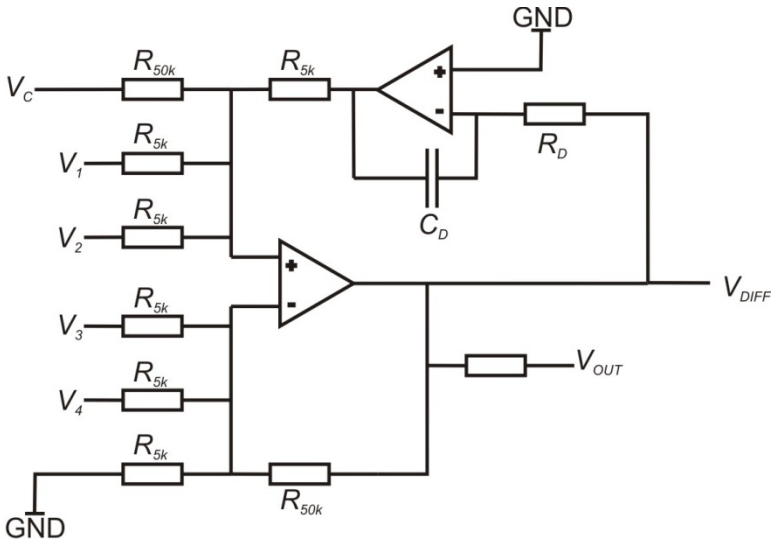

Figure 3.9 - the final summing amplifier stage.

Before entering the next stage V_2 and V_4 are buffered to prevent parasitic current from any further loading to the circuit. Finally the four output voltages from here are then

combined to give the difference in the voltage drops across the resistors. This then shows the amplified version of the voltage across the bolometer.

$$V_1 - V_3 + V_2 - V_4 = -100(V_{B+} - V_{B-}).$$

Eq. 3.31

In addition to this, a "compensation" voltage, V_C, is added, so a "null" output signal can be produced when the bolometer is fixed at its operating resistance (and no pulses are present). Since the main interest is in the small changes of sensor resistance, this allows the nominal operating resistance to be subtracted from the signal before the next amplification by a factor of ten (as well as any subsequent gain) is applied. The signal will then be small with just the departures from the nominal value, and can be easily amplified without exceeding the linear range of the amplifier block or hitting the supply rails.

Once the compensation is added, a final amplification by a factor of ten takes place so that the output signal V_{DIFF} becomes

$$V_{DIFF} = \frac{j\omega R_D C_D \left. R_{5k} \middle/ R_{50k} \right.}{1 + j\omega R_D C_D \left. R_{5k} \middle/ R_{50k} \right.} \left[V_C + \frac{R_{50k}}{R_{5k}} (V_1 - V_3 + V_2 - V_4) \right]$$

$$V_{DIFF} = \frac{j\omega R_D C_D \left. R_{5k} \middle/ R_{50k} \right.}{1 + j\omega R_D C_D \left. R_{5k} \middle/ R_{50k} \right.} \left[V_C - 1000(V_{B+} - V_{B-}) \right]$$

Eq. 3.42

Including the form of ΔV_B from earlier, shows further the frequency dependence of the output. This form of the equation can then be converted to one in the time domain.

$$V_{DIFF} = \frac{j\omega R_D C_D \left. R_{5k} \middle/ R_{50k} \right.}{1 + j\omega R_D C_D \left. R_{5k} \middle/ R_{50k} \right.} \left[V_C - 1000 \left(V_S \frac{1 + j\omega R_{in} C_{in} \left. V_T \middle/ V_S \right.}{1 + j\omega R_B (C_P + \frac{1}{2} C_B)} \frac{j\omega C_F R_F}{1 + j\omega C_F R_F} \frac{C_B}{C_F R_{in}} R_B \right) \right]$$

Eq. 3.5

$$V_{DIFF} = A(V_S, R_B)\left[f_d e^{-t/t_D} + f_F e^{-t/t_F} + f_b\left[1 - \frac{t_{pzc}}{t_{Cp}}\right] e^{-t/t_{Cp}} \right] + V_C e^{-t/t_D},$$

Eq. 3.6

where the amplitude A is a term proportional to the bolometer sensor resistance and square voltage, and the terms f_d, f_F and f_b are constants with values depending on the components of the circuit.

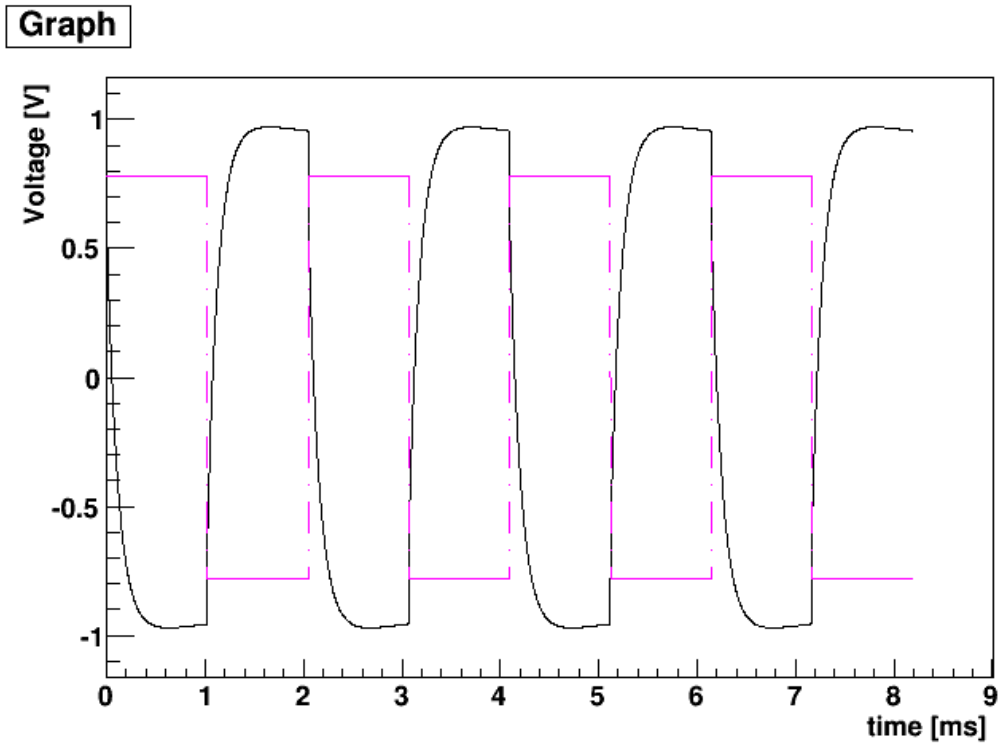

Figure 3.10 - a simulated NTD signal with the t_D signal shown as a purple dotted line.

The first of these is the sum of the "compensation" voltage, V_C, and a square wave term proportional to R_B and V_S. These have an exponential component with a time constant given by

$$t_D = R_D C_D \, R_{5k} / R_{50k},$$

Eq. 3.7

which has a value around ~3 s. This gives a square signal, as shown in figure 3.10. The second term contains the $R_F C_F$ high pass filter from the bias circuit acting on the square wave with R_B and V_S. This time constant has a value around ~30 s.

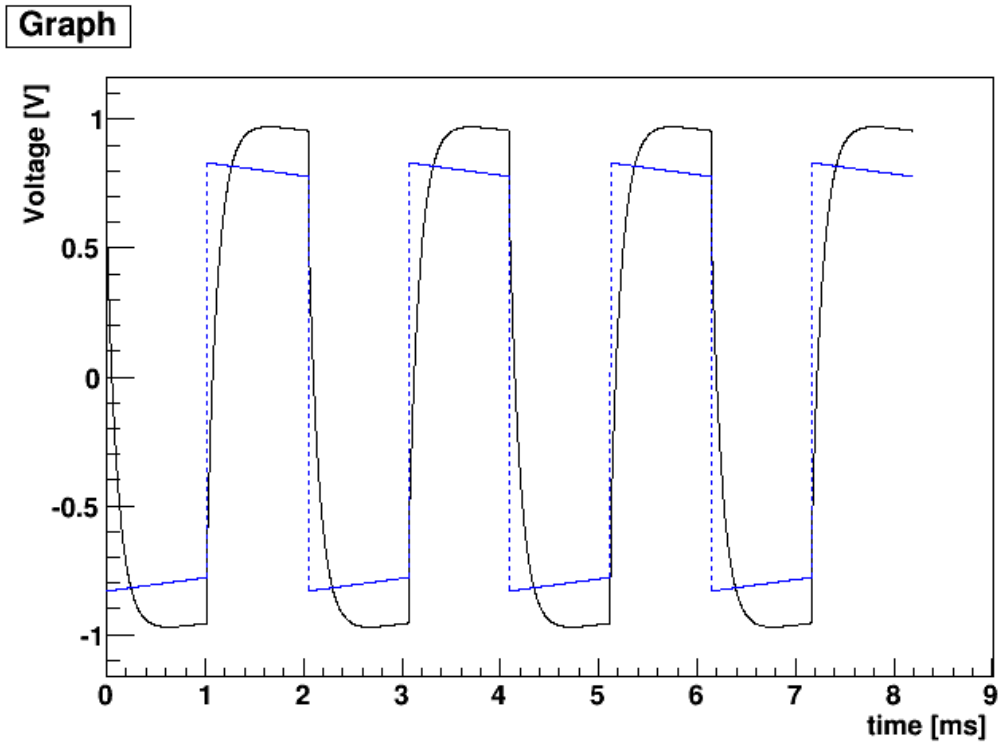

Figure 3.11 - a simulated NTD signal. The t_F exponential term, shown in blue, has a high pass filtering effect, and is the source of the downwards slope of the top of the square.

Finally the third term contains the low pass filter from the bias circuit due to parasitic capacitance. This has a time constant of

$$t_{Cp} = R_B\left(C_P + \frac{1}{2}C_B\right).$$

Eq. 3.8

However, this term can be cancelled using the pole zero cancellation described in the bias section, if the values of V_S and V_T are set such that

$$t_{pzc} = R_{IN}C_{IN}\,V_T/V_C = t_{Cp}$$

Eq. 3.9

The formula has two free parameters in it – the resistance of the bolometer, R_B, and the parasitic capacitance across the bolometer, C_P. Of these parameters, the parasitic capacitance (described in more detail in chapter 4) for a given setup will be constant at low temperatures. Therefore it can be determined independently and treated as a known parameter, leaving the NTD resistance R_B to be found.

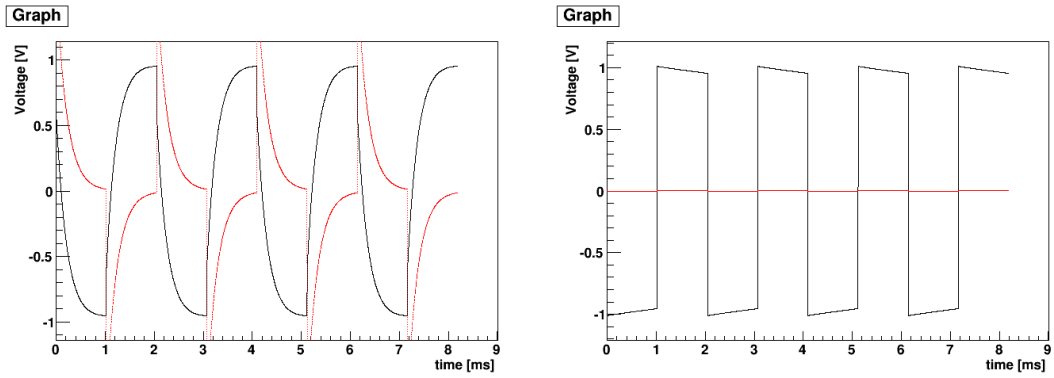

Figure 3.12 - Simulated plots of the signal for a 1 MΩ resistor with a very large parasitic capacitance of 100 pF; the exp(-t/t_{Cp}) term shown as a red dotted line, and the total signal as a solid black line. (a) V_S = 1 V, V_T = 0: the parasitic capacitance causes an exponential term to be subtracted from the signal (b) V_S = 1 V, V_T = 1.4 V: the effect of the capacitance is cancelled.

3.4 Filtering

The analogue signals from the four bolometer signal channels are fed from the readout board to an ADC board, along with the PT100 and heater voltage monitoring channels for controlling the temperature of the cold amplification stage. The signal now has another gain applied. This has a value between 1 and 100, and can be selected from a set of preset values with a command sent to an FPGA. According to the Nyquist-Shannon sampling theorem [109] the signal should have its frequency band upper limit at no more than half the sampling rate used. If the upper limit is higher than this, aliasing may occur when the signal is reconstructed. Therefore, to avoid aliasing, the signal is filtered using a four pole LTC1563 low pass Bessel filter. These have unity gain and a cut off frequency of 25.6 kHz.

Bessel filters have a maximally flat group delay, so in the pass band the output signal is not distorted. This characteristic makes it the ideal choice for working in the time domain.

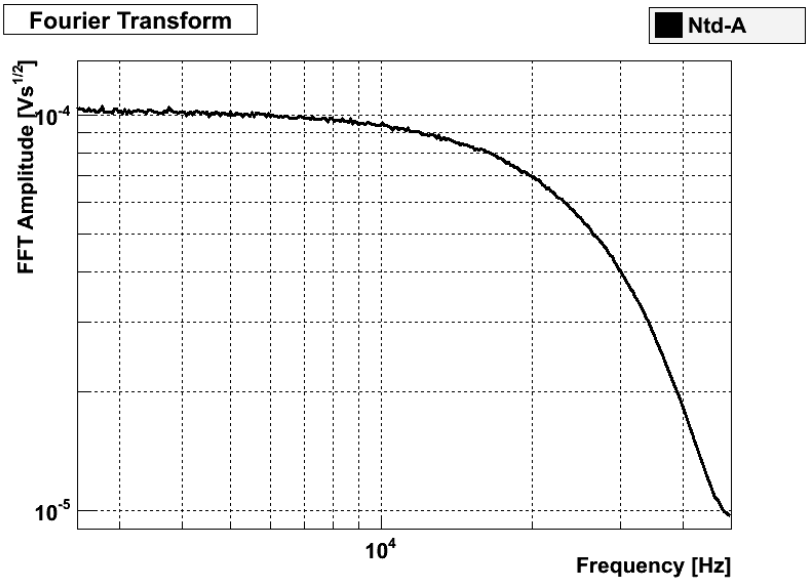

Figure 3.13 - the Bessel filter roll off at 25.6 kHz. This plot is with the cryostat at room temperature, so otherwise the spectrum should be approximately white as the Johnson noise dominates.

On an earlier version of the electronics, an eight-pole LTC1564 elliptical filter was tested. The high frequency cut off was sharper and may have been useful for work on frequency analysis, but due to the unsuitability in the time domain it was not pursued.

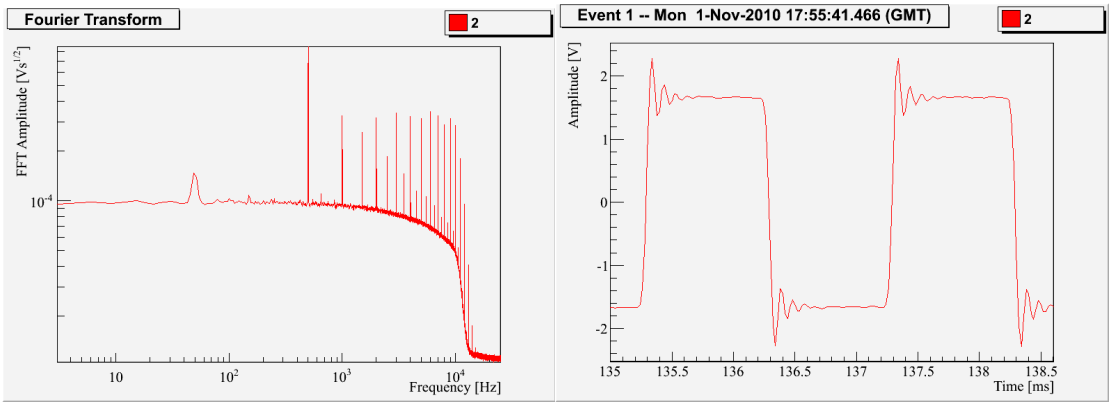

Figure 3.14 – a frequency spectrum and square wave signal with the elliptical filter. The roll off of the spectrum is much sharper than that of the Bessel filter, but the ripple it introduces on the square is not desirable for the type of time-domain signal processing envisaged.

3.5 ADC

Next the filtered signal is fed to a 16 bit ADC. With a range from +10 V to −10 V this gives a resolution of ~0.3 mV, on the signal it receives. With a gain of 1000 applied at earlier stages in the readout electronics, this will correspond to ~300 nV. In

addition, a variable gain (7 values between 1 and 100) can be engaged, improving the resolution of the readout system even further.

The digitised signal is sent, via an FPGA and optical fibre, to a nearby computer where the data is recorded. This data can have a sampling timebase of as fast as 10 μs, and is sampled continuously. It is stored in records of up to 32768 data points – however there is no dead time between the records and these can be lined up to create a continuous stream of data.

4. NTD Germanium sensor

The temperature sensors used for the cryogenic detectors are made of Neutron Transmutation Doped Germanium (NTD Ge). These have a resistance that increases to large values as they are cooled, making them useful as thermometers. The first sections of this chapter will discuss the form of this resistance with temperature and how this affects the sensitivity of the detector.

Following this, the measurements and characterization of NTD Ge thermistors are described. These measurements provide a value for both the resistance of the sensor, and the parasitic capacitance across the detector (as described in the previous chapter). The resistance measurements allow different sensors to be characterised and the optimum sensor to be chosen for the detectors, while the capacitance measurements allow aspects of the cabling near the detector to be tested for future use in the EDELWEISS experiment.

4.1 Resistance

Neutron Transmutation Doped Germanium is germanium that has been doped by exposure to a neutron source [110]. The neutron absorption that occurs causes the germanium to become an n-type doped semiconductor as Arsenic and Selenium are implanted in the lattice. One advantage of neutron transmutation doping is that it tends to provide a very uniform level of doping and allow very low concentrations of the dopants.

The resistance of NTD Ge rapidly increases to values around a MegaOhm upon cooling to milli-Kelvin temperatures. This makes it a good choice for the

thermometer of a cryogenic detector, which is operated at low temperatures in order to have the benefit for the energy resolution of low heat capacity.

Lightly doped semiconductors, like Germanium, have typical binding energies of milli-electron volts and so are completely ionized at room temperature. As the temperature decreases, this ionized portion of the material will also decrease, leading to a rise in the resistance of the material. When the temperature becomes low enough, the thermal ionization of the impurities becomes negligible.

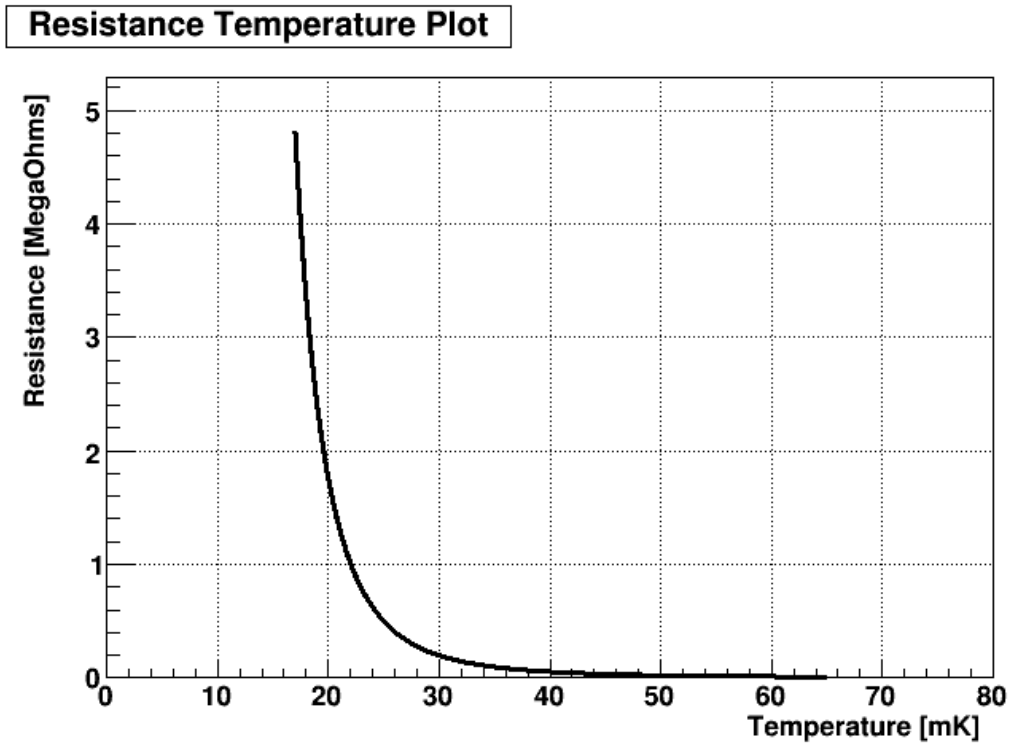

Figure 4.1 - Resistance versus temperature plot for Neutron Transmutation Doped Germanium

For very low temperatures, conduction is described by a process called variable range hopping [93,111]. In this the doping is low enough that the charge transport takes place by phonon-assisted tunnelling between impurity sites. The energy difference required to tunnel is made up by the absorption or emission of a phonon with the required energy. At low temperatures, high energy phonons are rare so longer hops are needed in order to find an unoccupied site with a similar enough energy to the original site. The resistance given by this theory is

$$R(T) = R_0 \exp\left(\frac{T_0}{T}\right)^p .$$

Eq. 4.1

In the theory by Mott, the constant p was 0.25, but the introduction of Coulomb repulsion into the density of states modifies the formula to make $p = 0.5$ [112].

The resistance increases exponentially at very low temperatures; this makes it a very good thermometer at these temperatures where a very small change in temperature can be quite a large change in resistance.

4.2 Sensitivity

One part of calculating the theoretical signal to noise ratio for a detector, and therefore finding the best operating point, will be the sensitivity of the NTD sensor to changes in temperature. This will ultimately be combined with the heat capacity of the detector to find a signal response for a given energy, and then the noise itself to give a signal to noise ratio.

When energy is deposited in the detector by an incident particle there will be an increase in the temperature of the NTD Germanium thermistor. In a naïve estimate this temperature rise would be

$$\Delta T = \frac{E}{C}.$$

Eq. 4.2

The change in the temperature of the thermistor corresponds to a change in its resistance.

$$\frac{dR}{dT} = -\frac{R_0}{2T_0}\left(\frac{T_0}{T}\right)^{\frac{3}{2}} \exp\left(\frac{T_0}{T}\right)^{\frac{1}{2}}.$$

Eq. 4.3

From this formula it seems like the largest change in resistance, and hence the largest signal size for a given energy, will occur at the lowest possible temperature but the heat capacity of the detector, C, also needs to be taken into account.

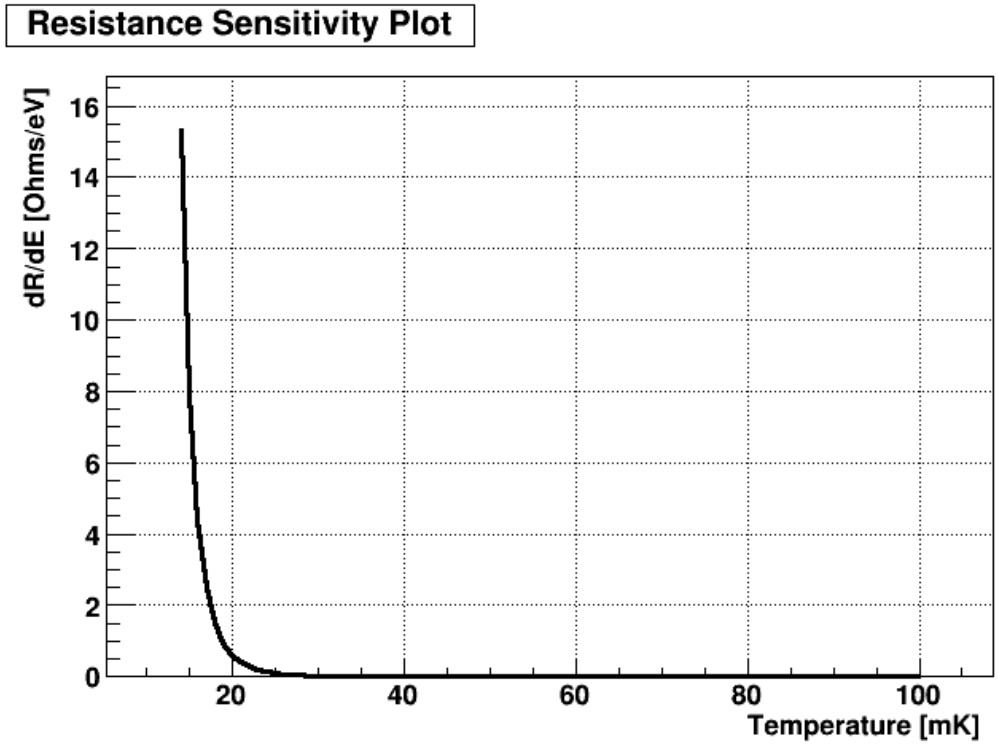

Figure 4.2 - The rate of change of resistance with energy for a range of NTD temperatures, using the estimated heat capacity from the previous chapter.

Taking account of the heat capacity, the change with energy is

$$\frac{dR}{dE} = \frac{dR}{dT}\frac{dT}{dE} = -\frac{1}{C}\frac{R_0}{2T_0}\left(\frac{T_0}{T}\right)^{\frac{3}{2}} \exp\left(\frac{T_0}{T}\right)^{\frac{1}{2}}$$

Eq. 4.4

Therefore the responsivity of the NTD sensor for a given energy will increase as the temperature is lowered, giving a larger signal. However for a full description of the detector response and the best operating temperature, the noise must also be considered.

4.3 Resistance measurement

The resistance of the NTD can be measured by fitting the theoretical function from the previous section to the signal from the readout. As described in the previous section, the signal can be modelled as a series of three exponentials with the resistance, R, and the parasitic capacitance, C_P, as free parameters:

$$f = [F_1(V_S, t_{Cp})e^{-t/t_D} + F_2(V_S, t_{Cp})e^{-t/t_F} + F_3(V_S, V_T, t_{Cp})e^{-t/t_{Cp}}] \times R + V_C e^{-t/t_D}.$$

Eq. 4.5

This theoretical form, described in more detail in Chapter 3, contains the parasitic capacitance in the form of the time constant t_{Cp} where

$$t_{Cp} = R_B\left(C_P + \frac{1}{2}C_B\right)$$

Eq. 4.6

with C_p the parasitic capacitance and C_B a fixed component on the electronics. V_S, V_T and V_C are the square wave voltage, the pole cancellation voltage and the compensation voltage respectively.

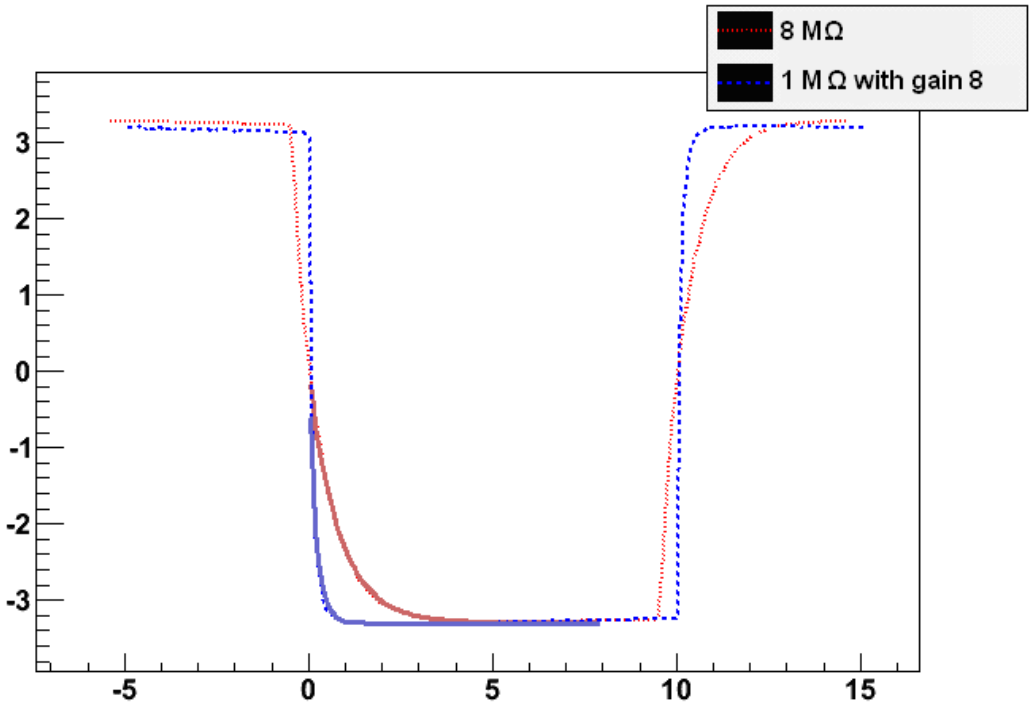

Figure 4.3 - Two signals from the same NTD at different resistances. The blue is at roughly 1MΩ and the red at roughly 8MΩ (a gain of 8 was applied to the blue so they are of comparable size).

The shape of this signal, as well as the amplitude, varies with changing resistance as shown in figure 4.3. As covered in the previous section, the parasitic capacitance and the bolometer resistance provide a "missing" exponential part of the square wave with time constant t_{Cp}. As the resistance (or the capacitance) change, this time constant increases and the signal takes longer to flatten out.

Therefore, the measurement of the resistance must take into account both the change in amplitude with resistance and the change in signal shape with resistance. To ensure a good measurement of resistance, the quality of the data is monitored and a good region of data selected. By treating the signal in this region as a series of periodic segments that occur at the modulation frequency chosen, a number of periods of the signal can be averaged to create a standard form for the signal shape. This is done and the resulting shape used to fit the region of data it was taken from – in this way the quality of data in the region can be tested and a clean standard signal obtained.

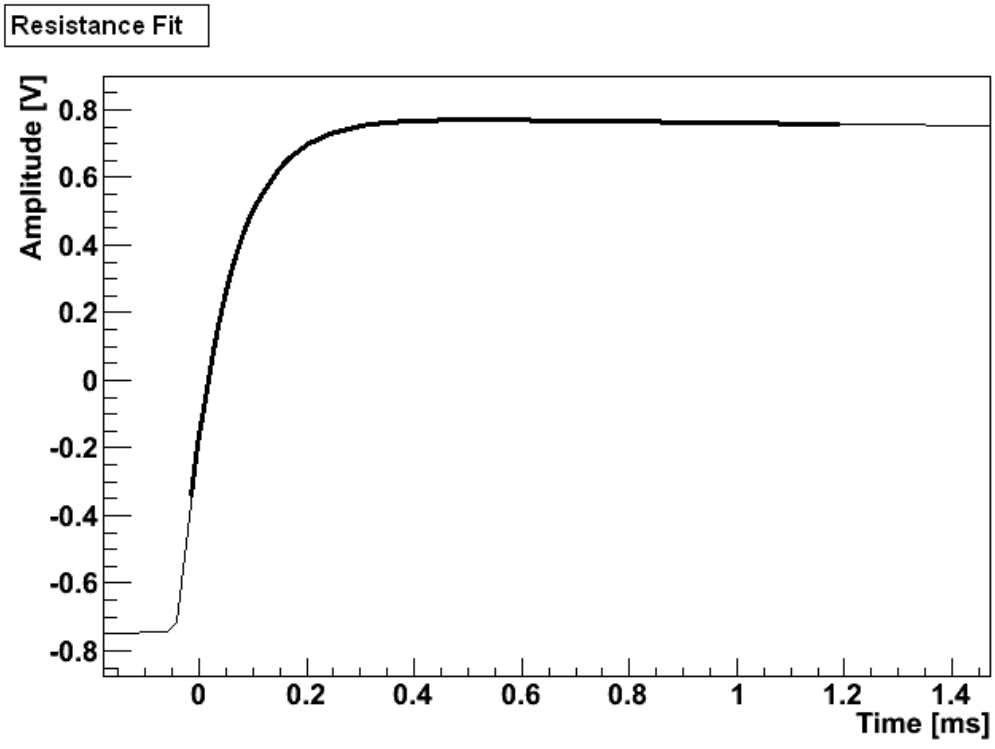

Figure 4.4 - a signal being fit to find the resistance. The fit is shown in bold.

This standard shape is then fit using the theoretical form of the signal with the bolometer resistance R and the parasitic capacitance parameter t_{Cp} as free parameters. The parasitic capacitance should be roughly constant, but may vary between runs and detectors due to changes or differences in the detectors or the cabling.

This time averaging of the signal will remove the effects of small instabilities in the resistance of the detector, or of pulses, particularly when the average is taken over longer periods. This means that the resistance measurement in this way is only directly useful for longer term measurements – rather than calculating the size of temperature pulses.

However some of the information obtained from these average measurements will be vital to the development and operation of the detector. The parasitic capacitance and NTD resistance and their variations with temperature help determine the characteristics of the NTD and estimate the contribution of various noise sources to the total noise of the detector.

4.4 Resistance – Temperature relations

Three NTD Germanium sensors have been tested: NTD 38a (which was ultimately used on the light detector), NTD 73a (which was ultimately used on the phonon detector) and NTD J1. The three NTDs have different geometry, with NTD 38a and 73a being long with dimensions of (2 × 1 × 7) mm^3 and of (3 × 1 × 8) mm^3 respectively. For these sensors the gold contact pads where along the long sides of the NTD. NTD J1, on the other hand, was smaller at (2 x 2 x 1) mm^3, and had its contacts on the two 2 mm x 2 mm faces. Each of the sensors also had its own characteristics for resistance, with the small NTD J1 operating at the highest temperature and NTD 73a operating at the lowest.

The detector, mounted on the experimental plate was stabilised at various temperature points (with temperature measured via the calibrated Speer resistor described in Chapter 2) and measurements of resistance taken. The resistance of the NTD was measured by choosing a small excitation, to reduce any self-heating effect due to the bias current sent through the resistor, and fitting to the output signal.

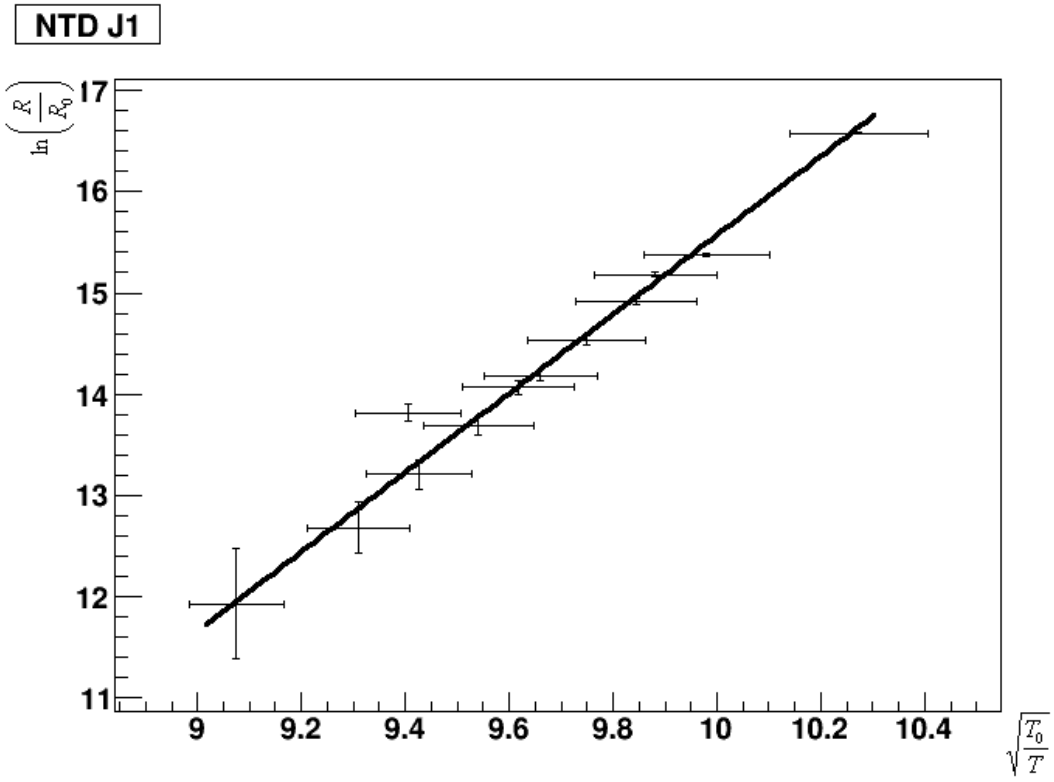

Figure 4.5 – A plot of resistance versus temperature where R_0 and T_0 are the NTD characteristic constants. The individual data points are plotted along with a line of best fit.

This was done for all three NTD Germanium sensors, giving the results in table 4.1.

NTD	R_0 [Ω]	T_0 [K]
38a	11.724	1.6854
73a	0.0933	2.5198
J1	0.6105	4.0872

Table 4.1 – The NTD characteristic constants for three different NTDs.

The resistance temperature curves corresponding to these three sets of characteristic constants are plotted in figure 4.6, showing the different optimum operating temperatures for the three different NTD sensors.

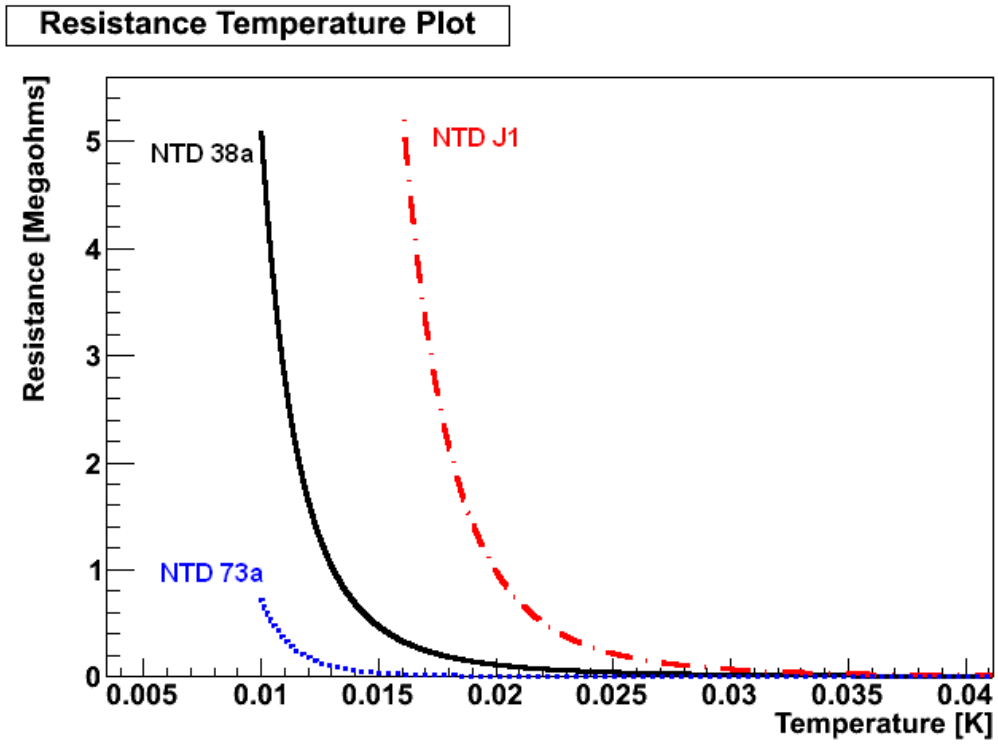

Figure 4.6 - the resistance temperature relations for the three NTD sensors.

NTD J1 becomes resistive at a much higher temperature than the other two, and so will be less suitable for use in a detector due to the higher heat capacities at these temperatures. However NTD 38a and NTD 73a become resistive at lower temperatures, and should actually be sensitive enough for use as a detector at around the same temperature. There is therefore the potential to use these two NTD sensors combined as a composite phonon - light detector module – with one of them attached to a scintillator and the other to a light absorber.

4.5 Parasitic Capacitance

The detector will have a parasitic capacitance across it, typically with a size ~50 pF, with contributions to this from the polyimide cabling, the connectors, the bond wires

and the NTD itself. The parasitic capacitance may provide an upper limit to the range of modulation frequencies that can be used. As described in Chapter 3, the parasitic capacitance causes the signal to have a time constant at each polarity switch of $R_B(C_P+C_B/2)$, where R_B is the NTD Resistance, C_P is the parasitic capacitance and C_B is the capacitance of a component in the cold electronics.

This can be helped by the use of an exponential boost in the bias current, but it also requires that the parasitic capacitance is kept low through the design of the detector and its readout circuit. By reducing the parasitic capacitance across the detector the problem can be reduced, but to identify what improvements could be made to this, and to test out the possible solutions, measurements of the parasitic capacitance are needed.

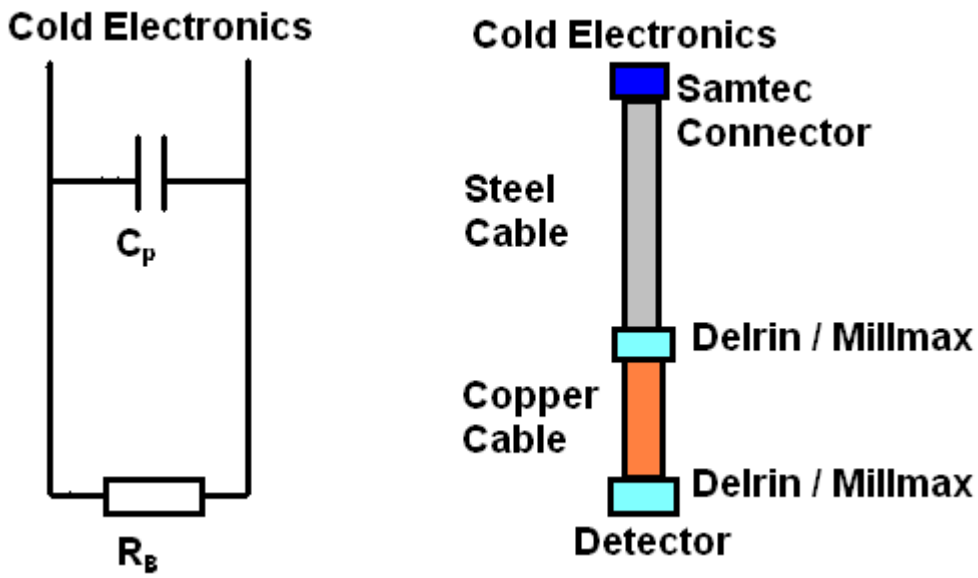

Figure 4.7 - Schematic diagram of the cabling from the high impedance NTD Ge detector to the cold amplification stage.

The parasitic capacitance occurs between the two signal tracks before they reach the cold amplification stage. As described in Chapter 2, this begins with a steel cable connected to the cold electronics with a 1mm pitch Samtec connector. The steel cable then connects to a copper cable via the delrin and Millmax connector. This copper

cable then connects to the p.c.b. at the detector via another delrin and Millmax connector, and finally the tracks are connected to the NTD germanium via the gold bond wires.

Another channel in the same cables had a 1MΩ resistor soldered to the p.c.b. in place of the detector, which allows the effect of the parasitic capacitance of the bond wires and the detector itself to be estimated. In this setup the extra heat sink at 50 mK had yet to be added with instead a single steel cable running from the cold amplification stage to the mixing chamber.

The connectors can be modelled by using the geometry of parallel infinite length wires surrounded by delrin for the Millmax pins and a liquid crystal polymer for the Samtec connector, as in the formula

$$C = \varepsilon_r \varepsilon_0 l \frac{\pi}{\cosh^{-1}(d/w)},$$

Eq. 4.7

where w is the diameter of the wires, d is the distance between them, ε_r is the relative permittivity of the insulator and l is the length of the wire. At room temperature delrin has ε_r of 3.7 and the liquid crystal polymer 3.16 [113].

If the NTD sensor, with its gold films on either side, is considered as a parallel plate capacitor; an estimate of its contribution to the capacitance can be made. These gold films have area 1 mm × 8 mm and are 2 mm apart, therefore with

$$C = \varepsilon \frac{A}{d},$$

Eq. 4.8

and an ε_r for germanium of 16, the capacitance of the NTD sensor will be 0.56 pF.

For the gold bond wires from the NTD sensor, the gold wires are 25 μm in diameter, roughly 10 mm in length and around 2 mm apart.

$$C = 2\pi l \varepsilon \frac{1}{\ln(d^2/t^2)},$$

Eq. 4.9

where *t* is the thickness of the wires, *d* is the distance apart and *l* is the length. The capacitance is 0.05 pF.

The cabling is slightly more complicated, but considering each part simply as parallel wires of 0.1mm diameter, set 0.5 mm apart and surrounded by polyimide (relative permittivity ~3) for a copper cable of length 30 cm and a steel cable of length 88 cm. These give values of 45.6 pF and 15.6 pF respectively.

Component	Calculated Room Temperature Capacitance (pF)
Delrin Connector (x2)	0.22 (×2)
Samtec Connector	0.31
Copper Cable	15.6
Steel Cable	45.6
NTD Germanium	0.56
Gold Bond Wire	0.05

Table 4.2 – The estimated capacitance at room temperature for different components.

Measurements of the cabling at room temperature found a track to track capacitance of 61.9 pF/m for the copper cable, and 62.7 pF/m for the steel cable. Track to ground capacitance was found to be higher at 147.6 pF/m and 130 pF/m for the copper and steel cable respectively. The copper cable used was 20 cm long, and the steel cable was 75 cm, therefore there is a combined track to track capacitance of 59.4 pF. At low temperatures the dielectric constant of polyimide films is smaller than that at room temperature. Therefore this room temperature capacitance is expected to be larger than that for the cables during the operation of the detector at milli Kelvin temperatures [114].

These measurements agree with the estimated values of the track to track capacitance of ~60 pF for cabling characterized at room temperature. The contributions to the

parasitic capacitance from sources other than the polyimide cabling are negligible in comparison to the capacitance of the cabling itself.

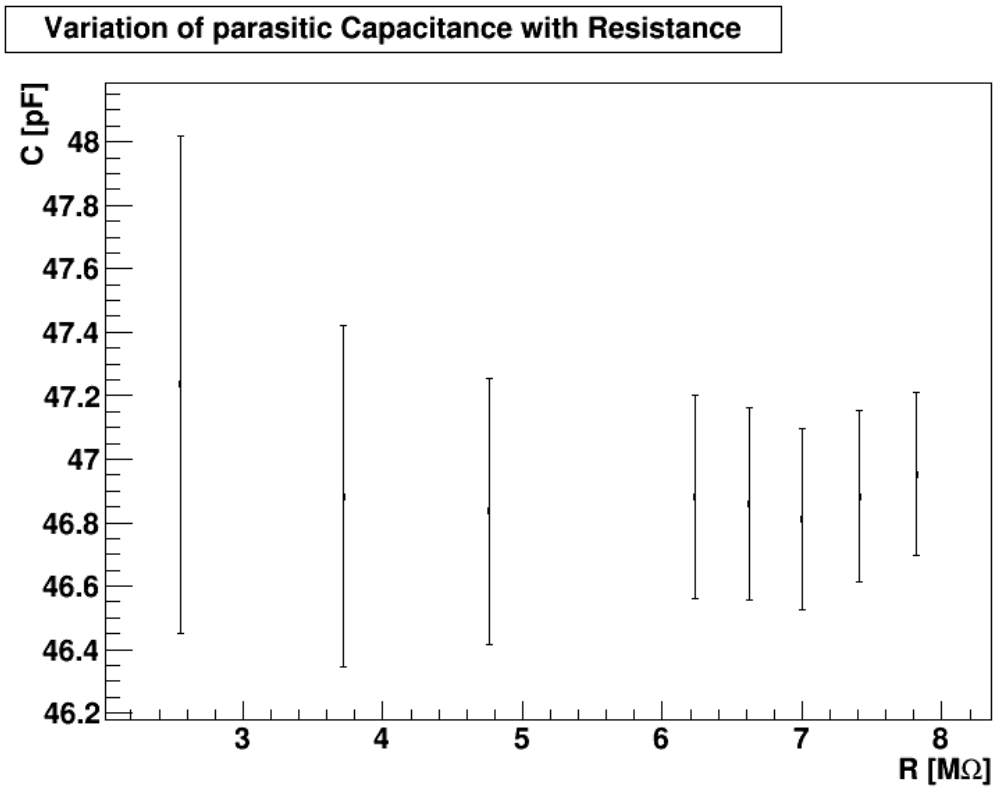

Figure 4.8 - measurements of the parasitic capacitance across detector B for a range of resistance values.

The parasitic capacitance of the cabling at low temperature cannot easily determined by direct measurement without changing the set up of the cryostat. Instead, the fitting method of finding the NTD resistance also produces a value for the parasitic capacitance across the detector and cold cabling, this time at the low temperatures where the detector will be operated. The fit values for the parasitic capacitance are around 47 pF with a resistance of ~1 MΩ on the NTD and remain roughly constant with temperature over the operating range of the NTD sensor.

The effect of the gold bond wires to the detector was investigated by taking measurements with a ~1 MΩ resistor connected to the end of the cable via the Mill-max pins. This also gave values of around 47 pF for the parasitic capacitance. Since the cabling and the Mill-max connectors remained the same in both cases, this

suggests that there is a relatively small parasitic capacitance contribution from the gold bond wires and the NTD germanium itself. The reduction in the capacitance compared to the room temperature measurements and calculations is likely due to the reduction in the permittivity of the polyimide at lower temperatures.

5. Pulse formation

When a particle interacts in the dielectric crystal target of the detector, some energy will be deposited in the detector. After a number of conversions this energy is thermalized in the NTD germanium thermistor. By measuring the resistance change of the germanium, the change in temperature due to the incident particle can be determined. In addition, if the target is a scintillator, a small proportion of the total energy will be emitted as scintillation light, and this can be absorbed by another crystal and itself measured as a temperature change with an NTD sensor.

Section 5.1 of this chapter describes a simple model of the cryogenic detector, with a simple absorber crystal connected to a heat bath via a thermal link. 5.2 and 5.3 describe the implications of this model for the detector response. Using the ideal model, calculations of the noise can be made for a variety of sources and compared to the real data.

Next the model can be extended by first considering the decoupling of the electron system and the phonon system in the detector. This changes the behaviour of the detector response to depositions of energy, while also providing extra thermal noise due to the fluctuations between these systems. Then, in section 5.6, the model can be expanded further by considering other conversion processes and systems within the detector.

Finally, to give a complete description of the response from the detector and the noise sources that impact upon the resolution, the linearity of the detector response is considered and measurements of microphonic noise in the detector are described.

5.1 Ideal Model

A model to describe the temperature pulses in the detector may be built up by first considering an ideal calorimeter consisting of three parts – an absorber which absorbs the incident power and thermalizes the energy, a thermometer to measure the temperature of the absorber, and a thermal link to a heat sink to return the absorber to some stable temperature value [4].

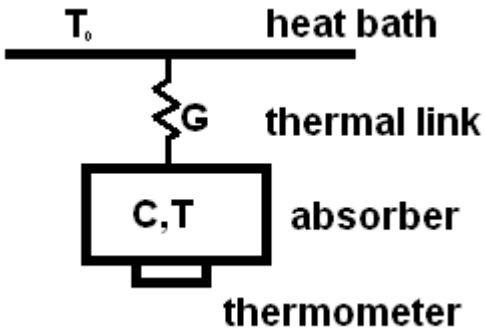

Figure 5.1 - Schematic diagram of an ideal calorimeter.

The absorber has a heat capacity *C*, the thermal link has a thermal conductivity *G*, and the heat bath of temperature T_0. Generally the thermal conductivity of this thermal link will have the form of a power law given in equation 5.1 [115].

$$G = G_0 T^{\beta}.$$

Eq. 5.1

The sensitivity of the thermometer will be defined as α in equation 5.2 [115].

$$\alpha = \frac{T}{R}\frac{dR}{dT}.$$

Eq. 5.2

The thermometer will be read out by a bias current, which produces a Joule heating effect for the detector with a power $P_J(T)$. This heating will cause the detector to stabilise at equilibrium with a higher temperature, *T*, than that of the heat bath, T_0.

$$\int_{T_0}^{T} G(T')dT' = P_J(T).$$

Eq. 5.3

If some external power P_X is added to the detector, for example, by a particle interaction, it will leave equilibrium with a new temperature T_D, [115] that varies according to the differential equation in eq. 5.4.

$$C\frac{dT_D}{dt} + \int_{T_0}^{T} G(T')dT' = P_X + P_J(T).$$

Eq. 5.4

For the small signal limit it is useful to substitute into this equation so that $T_D = T + \Delta T$, where T is the equilibrium temperature from equation 5.3.

$$C\frac{d(T+\Delta T)}{dt} + \int_{T_0}^{T} G(T')dT' + \int_{T}^{T_D} G(T')dT' = P_X + P_J(T+\Delta T).$$

Eq. 5.5

Now using that result from the equilibrium case (eq. 5.3), and defining a small signal limit change in power $\Delta P = P_J(T+\Delta T) - P_J(T)$. With these small variations in temperature, it can be assumed that $G(T)$ is constant over the temperature range T to T_D. This gives equation 5.6.

$$C\frac{d(\Delta T)}{dt} + G(T)\Delta T = P_X + \Delta P$$

Eq. 5.6

The Joule heating from the bias will vary with temperature as the resistance changes; this produces an effect known as electrothermal feedback [116]. This may be represented in the formulae as an effective thermal conductivity. Using the thermometer sensitivity α from earlier, the change in the Joule heating power can be converted as in equation 5.7.

$$\Delta P = \frac{dP}{dT}\Delta T = I^2\frac{dR}{dT}\Delta T$$
$$\Delta P = \frac{P\alpha}{T}\Delta T \quad ,$$
$$\Delta P = -G_{ETF}(T)\Delta T$$

Eq. 5.7

with an effective thermal conductivity G_{ETF} due to the feedback. This can be combined with the thermal conductivity of the thermal link G to give equation 5.8.

$$C\frac{d(\Delta T)}{dt} + (G + G_{ETF})\Delta T = P_X$$

Eq. 5.8

This equation shows that the ideal bolometer has a low pass filter effect on the incident power P_X, with a time constant of

$$\tau_{eff} = C/(G + G_{ETF}) = C/G_{eff} \ .$$

Eq. 5.9

The time constant depends on the heat capacity of the detector, the thermal conductivity and the electrothermal feedback, which may have a different effect depending on the sign of α. For the NTD Germanium sensors α is negative, and so the Joule heating will produce negative feedback and shorten the time constant for the detector. In the frequency domain this behaviour may be expressed in the form

$$\Delta T(\omega) = \frac{1}{G_{eff}} \frac{1}{1 + j\omega\tau_{eff}} W(\omega),$$

Eq. 5.10

where $W(\omega)$ is the external power applied to the detector.

5.2 Responsivity

Now consider the read-out of the detector. To fully describe the detector one must consider how this temperature change is measured. The temperature change gives a corresponding change in the resistance of the NTD germanium temperature sensor. A bias current is applied to the sensor so that the resistance can be measured as a voltage.

The output signal, in this case the voltage, can be related to temperature by eq. 5.11.

$$\frac{\Delta V}{V} = \alpha A_{tr} \frac{\Delta T}{T},$$

Eq. 5.11

where A_{tr} is a dimensionless parameter known as the transducer sensitivity, and α is the thermometer sensitivity.

The thermometer sensitivity is given by equation 5.2 and the resistance of the NTD germanium varies exponentially with temperature as in equation 4.1 so the sensitivity is given by

$$\alpha = -\frac{1}{2}\sqrt{\frac{T_0}{T}}\,.$$

Eq. 5.12

The minus sign indicates that the resistance of the NTD Germanium decreases as the temperature increases. For a typical NTD, such as the NTD 38a used on the light detector T_0 is 1.685 K therefore at the operating temperature of the detectors, around 10 mK, the sensitivity will be −6.5.

The transducer sensitivity meanwhile is defined as in equation 5.13.

$$A_{tr} = \frac{R}{V}\frac{dV}{dR}\,.$$

Eq. 5.13

For the signal with pole cancellation applied (as described in Chapter 3) the voltage has the form shown in equation 5.14. This has an output voltage that is linear with resistance, so the transducer sensitivity is equal to one.

$$V_{DIFF} = \frac{i\omega R_D C_D \,{R_{5k}}/{R_{50k}}}{1 + i\omega R_D C_D \,{R_{5k}}/{R_{50k}}}\left[V_C - 1000\left(V_S \frac{i\omega C_F R_F}{1 + i\omega C_F R_F}\frac{C_B}{C_F R_{in}} R\right)\right].$$

Eq. 5.14

The signal size at a particular operating point can be expressed in terms of the responsivity of the detector. This is defined in equation 5.17.

$$S(\omega) = \frac{\Delta V(\omega)}{W(\omega)}\,.$$

Eq. 5.17

Therefore for the ideal model, using equations 5.10 and 5.11, the responsivity of the detector is given by

$$S(\omega) = \frac{1}{G_{eff}}\frac{1}{1 + j\omega\tau_{eff}}\frac{V\alpha A_{tr}}{T}$$

Eq. 5.18

Using the typical values of α and A_{tr} for a detector at around 10 mK with pole cancellation, and taking G_{eff} as ~10 nW/K, the responsivity will therefore be

$$\frac{65\times10^{9}}{1+j\omega\tau_{eff}}\ \text{V/W}$$

Eq. 5.19

with the time constant τ_{eff} being ~50 ms.

5.3 Electrothermal feedback

Electrothermal feedback will occur in the detector due to Joule heating [86]. The bias current to the NTD Germanium sensor will heat the detector due to its resistance, which then causes the resistance of the sensor to change. The thermometer sensitivity α is negative, so the resistance decreases due to the bias current. For a fixed temperature value for the heat bath, the detector will therefore settle at an equilibrium temperature dependent on the size of the bias current applied.

As this equilibrium temperature (and thus the resistance) will be different to the temperature due to the heat bath, it is useful to define the dynamic impedance of the thermometer. This is the resistance of the sensor at a particular operating point, this is the rate of change of the voltage across the thermometer with the bias current sent through the thermometer.

$$Z(\omega)=\frac{dV(\omega)}{dI(\omega)}$$

Eq. 5.20

This takes into account the electrothermal feedback effect of the bias current and its impact on the equilibrium temperature of the thermometer. For the ideal case [87] described, this becomes

$$Z(\omega) = R\frac{1+\frac{P\alpha}{GT}+j\omega\tau}{1-\frac{P\alpha}{GT}+j\omega\tau}$$

Eq. 5.21

Figure 5.2 shows the measured values of resistance for a range of different bias currents as the temperature of the detector housing, which acts as the heat bath, was kept constant. This shows the behaviour effected from equation 5.21.

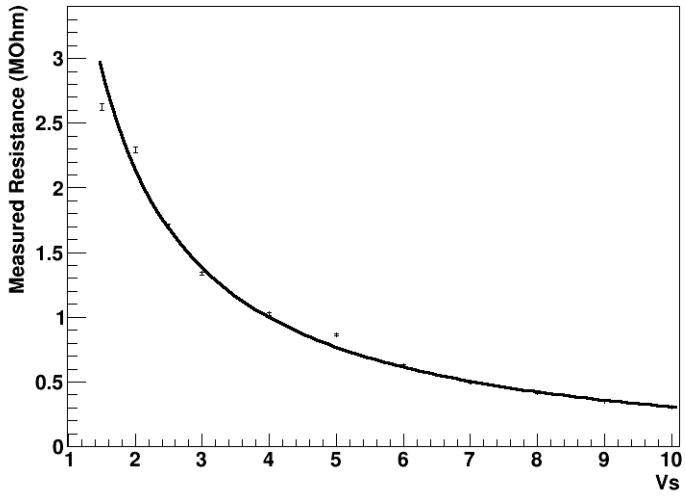

Figure 5.2 - The measured value of resistance against the bias current, with the bias current displayed as the square voltage Vs used to set its value.

Electrothermal feedback must be taken into account when selecting an appropriate bias current for the detector. Although increasing the bias current would be expected to increase the signal size relative to some forms of noise, it can have the negative effect of raising the temperature of the detector and reducing the sensitivity of the NTD sensor with a detrimental effect on the signal to noise ratio.

5.4 Ideal noise

Now that a value for the responsivity of the detector has been found, the output voltage noise should be determined so that the resolution of the detector can be estimated for the detector operating in different configurations.

The noise from various sources can be expressed as the Noise Equivalent Power (NEP), the power $W(\omega)$ that would have to be input to give an equivalent response $\Delta V(\omega)$ to the noise output. It can be calculated as the ratio of the output noise voltage and the responsivity of the detector [117].

5.4.1. Thermal Fluctuation Noise

This fundamental source of noise is due to the random movement of phonons causing an exchange of energy between a piece of material and its surroundings [118].

For a heat capacity C at a temperature T the size of these fluctuations will be given by

$$\delta E = \sqrt{k_B T^2 C} \,. \qquad \textbf{Eq. 5.22}$$

For the estimated heat capacity of these detectors, this would give a possible limit for the energy resolution of ~3.8 eV at 10 mK for the phonon detector and ~ 3.3 eV for the light detector.

These fluctuations give a noise equivalent power, for a detector at temperature T connected to a heat bath via a thermal link with conductance G, that is independent of frequency as in equation 5.23 [118].

$$(NEP_{TFN})^2 = 4 k_B T^2 G \,. \qquad \textbf{Eq. 5.23}$$

This can be converted into a voltage noise for the output signal using the responsivity of the detector.

$$v_{TFN}(\omega) = NEP_{TFN} S(\omega) \,. \qquad \textbf{Eq. 5.24}$$

5.4.2. Johnson Noise

This is the noise due to the random movement of charge carriers causing thermal fluctuations. As these charge carriers have a very small relaxation time, the noise distribution can be approximated as white except at frequencies well above what we need to consider here.

For materials with higher resistance the number of collisions involving the charge carriers will be higher, leading to an increase in noise. Therefore for a high impedance temperature sensor, like the NTD germanium, this may be a significiant source of noise.

For a resistance R at temperature T it has a noise equivalent power of

$$(NEP_J)^2 = \frac{4k_B TR}{|S(\omega)|^2}$$

Eq. 5.25

and a spectral output voltage noise of

$$v_J = \sqrt{4k_B TR}\,.$$

Eq. 5.26

The large resistance of the NTD germanium will obviously provide a major contribution to the Johnson noise, however other components in the readout circuit may also have a resistance. Of particular importance is the kapton cabling running from the cold electronics stage to the detector, this occurs before any amplification of the signal and would provide a resistance in series with the detector. The resistance of the cabling at low temperatures will be relatively small (~100 Ω) compared to that of the NTD (~1 MΩ), however the higher temperature of parts of the cabling means it still causes significant Johnson noise.

With the cable running from a temperature of ~100 K down to the milli-Kelvin stage of the detectors, there will therefore be some of the cable at higher temperatures, due

to the need to stabilise the FET temperature at these values. This may therefore influence the choice of operating temperature for the FET.

The Johnson noise due to the cabling with various FET stage temperatures can be estimated if assumptions are made about the temperature profile of the cable. In general for a cable of length l with resistivity ρ and a temperature profile $T(l')$ the noise will be given by Eq. 5.27

$$e_v^{\,2} = \int_{l'=0}^{l} 4k_B T(l') \frac{\rho}{A} . dl'$$

Eq. 5.27

By assuming a linear temperature profile for the cable with FET stage temperature, T_F, and detector temperature, T_D, this equation can be written as Eq. 5.28.

$$e_v^{\,2} = \int 4k_B \left(\frac{(T_F - T_D)}{l} l' + T_D \right) \frac{\rho}{A} . dl'$$

Eq. 5.28

Assuming that the resistivity of the cable is constant over its length, the integral can be done and the total resistance of the cable, R, can be substituted in to get Eq. 5.29.

$$e_v^{\,2} = 4k_B \frac{(T_F - T_D)}{2} R$$

Eq. 5.29

For a 100 Ω cable leading to a 1 MΩ sensor at 10 mK,

FET Temperature, T_F [K]	Johnson Noise due to cable [nV Hz $^{-0.5}$] (estimated for a linear profile)
80	0.47
100	0.53
120	0.58
140	0.62
NTD Temperature, T_D [mK]	Johnson Noise due to NTD [nV Hz$^{-0.5}$]
10	0.53

Table 5.1 – Estimated values of Johnson nouse due to the cable for a few different FET temperatures, and an estimate of the Johnson noise due to the NTD germanium sensor for comparison.

In practice, the temperature profile of the cable will not be linear, and will instead depend of the location of the cabling heat sinks. This simplified calculation is

therefore an overestimate of the Johnson noise. The majority of the noise will occur between the FET stage and the first heat sink (at 4K). Considering instead only this ~15 cm section of the ~ 88 cm cable, the Johnson noise will be closer to 0.1 $nVHz^{-0.5}$. While this may be smaller than the Johnson noise for the NTD Ge itself, ideally the FET temperature should be kept as low as possible to minimize this contribution. The positioning of heat sinks may also be used to optimize the temperature profile. Other sources of noise however require that the FET stage is stabilised at temperatures around 120 K.

Alternatively the cold amplification stage using JFETs, which have an optimum temperature around 120 K, could be replaced by one using HEMT instead, which may be used at much lower temperatures [119]. This would greatly reduce the Johnson noise due to cabling in the pre amplification stage.

5.4.3. Amplifier Noise

The noise in the first amplification stage of the signal can also be very important in determining the resolution of the detector. These detectors are read out with a cold amplification stage containing a pair of JFET amplifiers.

JFET readout has a negligible current noise (but does have voltage noise). The noise model for a JFET is normally that there is a voltage noise source at the input of the JFET in series with the signal path and a current noise source from the JFET input to ground (and hence parallel to the source or detector impedance). The white noise is therefore $\left\langle V_{ser}{}^2 \right\rangle + R_{source}{}^2 \left\langle I_{par}{}^2 \right\rangle$.

So for a high impedance sensor it will be especially important to have a readout with I_{par} negligible.

Typically this has a noise equivalent power of

$$(NEP_{amp})^2 = \frac{v_a^{\,2}}{|S(\omega)|^2} + i_a^{\,2}\frac{|Z(\omega)|^2}{|S(\omega)|^2}$$

Eq. 5.30

and a spectral voltage noise of

$$v_{amp} = \sqrt{v_a^{\,2} + i_a^{\,2}|Z(\omega)|^2}\ .$$

Eq. 5.31

This noise of the JFETs is dependent on their temperature. Using a pair of PT100 thermistors to measure the temperature and a pair of 100 Ω resistors as heaters, the cold electronics stage was stabilised at a range of temperatures and the noise on the NTD sensors measured at various frequencies by a Fourier transform of the signal as displayed in figure 5.3.

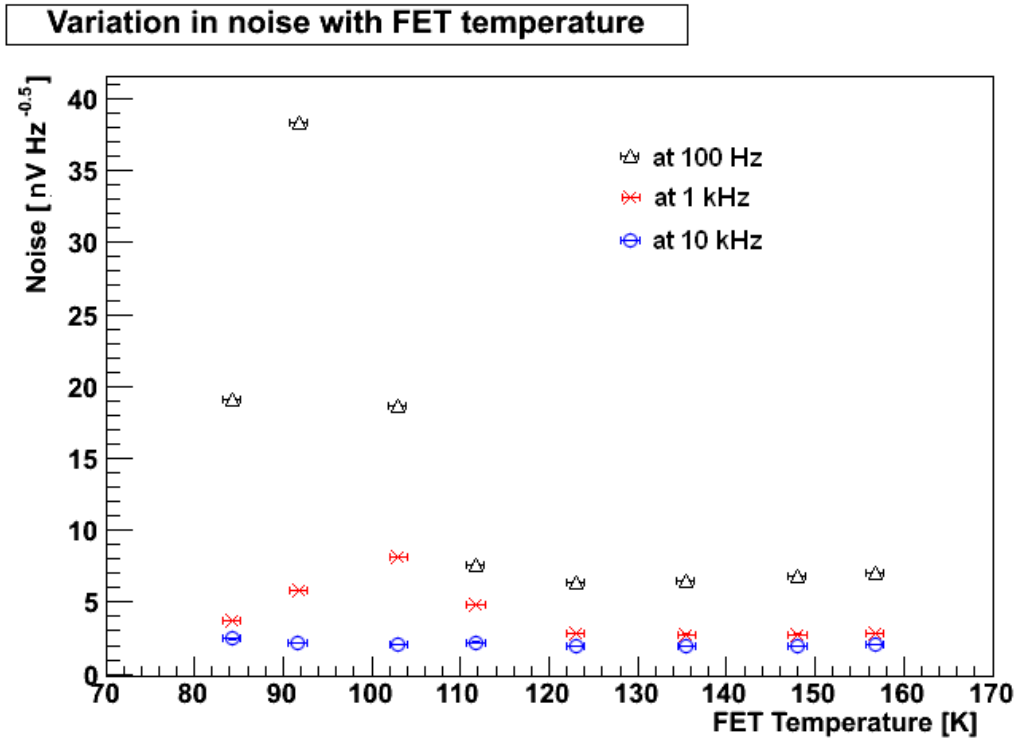

Figure 5.3 – The variation of noise with FET temperature at 0.1, 1 and 10 kHz as measured for an NTD sensor.

The amplifier noise seems to have two minima – one at low temperatures, below 80 K and the other at higher temperatures above 120K. However, at the lower temperatures the performance of the amplifier suffers and the signal size will drop along with the noise. The ideal temperature, in terms of the signal to noise ratio, will therefore be

~120 K since at higher temperatures there may be excess noise from the Johnson noise of the cabling. The LSK 389 JFETs used should have a voltage noise at 1 kHz of v_a = 0.9 nV/√Hz [120]. The size of the voltage noise however is larger than that of the estimated Johnson noise from the NTD germanium and the cable.

5.4.4. 1/f noise

Excess low frequency noise may also occur due to fluctuations in the size of the a.c. signal – for example due to change in the operating temperature of the detector. Such changes could be given as a spectral intensity $S_R(\omega)$ [121] which allows the noise to be written as

$$(NEP_f)^2 = \frac{I^2 S_R(\omega)}{|S(\omega)|}.$$

Eq. 5.32

This dominates at lower frequencies and provides the $1/f^{\,a}$ shape in the low temperature frequency spectrum. The 1/f noise is characterised by its corner frequency, f_C, this gives the boundary between the low frequency region, where the 1/f noise is large and gives the spectrum the sloping shape, and the high frequency region, where the 1/f noise is smaller than the white noise and the frequency spectrum flattens out. The frequency will typically depend on the temperature of the detector as the noise contributions from various noise sources vary. For the noise of the NTD sensors at temperatures around 15 mK, the corner frequency is approximately 2 kHz, as shown in figure 5.4.

However, these slow changes in the resistance should be taken care of by the temperature controller and faster changes reduced by the thermal low pass filter. Any remaining fluctuations could be removed by the use of a high pass filter. Fluctuations in the d.c. operating point of op-amps and FETs in the readout system could be another source of low frequency noise, but these should be removed by the modulation of the signal.

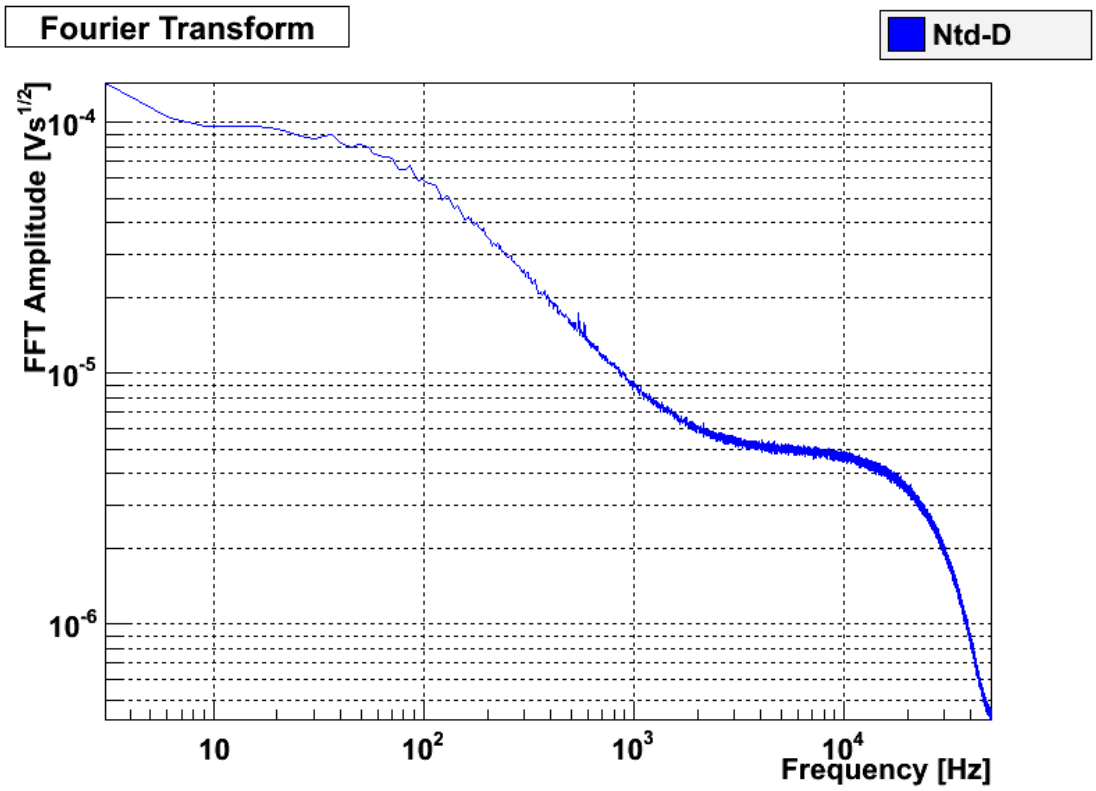

Figure 5.4 - Frequency spectrum for an NTD at 15 mK showing the 1/f slope at low frequencies and the white noise at higher frequencies, with the corner frequency between the two at around 2 kHz.

The 1/f noise will be particularly important when choosing the bandwidth of the readout; as the noise tends to increase below the corner frequency it will therefore be best to choose the minimum frequency of the band at a value above this.

5.4.5 Photon Background Noise

The photon background absorbed by the detector may also have a heating effect on the detector, changing the operating temperature and producing shot noise similar to the thermal fluctuation noise [122].

For the thermal photons from the surroundings of the detector the noise equivalent power may be given as

$$(NEP_{photon})^2 = 4\frac{A\Omega}{c^2}(k_B T_S)^5 \int \frac{x\,dx}{e^x - 1}\left(1 + \frac{\alpha\varepsilon f}{e^x - 1}\right)\alpha\varepsilon f$$

Eq. 5.33

where $x = \frac{h\nu}{k_B T_S}$.

However, at the energies in the range needed for these detectors this thermal phonon noise is not significant.

5.5 Electron-phonon decoupling

The next step in building a useful model of the detector response is to introduce a theory known as the hot electron model – in this the thermal coupling between electrons and phonons in the detector is not as strong as the coupling between the electrons. This leads to the electrons and the phonons acting as two different temperature stages of the system connected by a thermal conductivity, G_{ep}, with the time needed for the temperature to equalise in the two systems becoming significant. This model is illustrated in figure 5.5. The thermal connection between the phonon system and the heat bath will be relatively weak, $G_{pb} << G_{ep}$, and can be neglected in the following calculations.

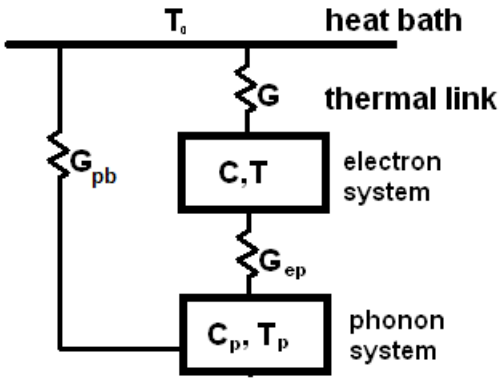

Figure 5.5 – The thermal model of the detector in the hot electron model.

The Joule heating of the bias will be dissipated in the electron system, while the heat deposition due to a particle interaction will occur in the phonon system. As with the ideal model, taking the equilibrium case

$$\int_{T_0}^{T_e} G(T')dT' + \int_{T_P}^{T_e} G(T')dT' = P_J(T_e)$$
$$\int_{T}^{T_P} G(T')dT' = 0$$

Eq. 5.34

This will give the same equilibrium temperature as in equation 5.3 of the ideal model, for the case with no external power added. Now bring in the external power P_X to the phonon system of the detector, and call the new non-equilibrium temperature of the electron system T_e.

$$C_e \frac{dT_e'}{dt} + \int_{T_0}^{T_e'} G(T')dT' + \int_{T_P'}^{T_e'} G(T')dT' = P_J(T_e')$$
$$C_p \frac{dT_P'}{dt} + \int_{T_e}^{T_P'} G(T')dT' = P_X$$

Eq. 5.35

With $T_e' = T_e + \Delta T$ and $T_l' = T_l + \Delta T_l$, and using the same methods as before, these equations become

$$C_e \frac{d(\Delta T_e)}{dt} + G(T_e)\Delta T_e + G_{ep}(T_e)\Delta T_e = \Delta P_J + G_{ep}(T_p)\Delta T_p$$
$$C_p \frac{d(\Delta T_p)}{dt} + G_{ep}(T_p)\Delta T_p = P_X + G_{ep}(T_e)\Delta T_e$$

Eq. 5.36

Defining the change in the Joule heating, ΔP_J, in terms of the effective thermal conductivity due to electrothermal feedback (from equation 5.7) the electron temperature equation becomes equation 5.37.

$$C_e \frac{d(\Delta T_e)}{dt} + G(T_e)\Delta T_e + G_{ep}(T_e)\Delta T_e + G_{ETF}\Delta T_e = G_{ep}(T_p)\Delta T_p .$$

Eq. 5.37

This gives the low pass filter effect, similar to the ideal model, with a time constant now containing the electronic heat capacity divided by the sum of the thermal conductivities of the heat link, the electron-phonon decoupling and the Joule heating, with this filter acting on the temperature change of the phonon system.

In the frequency domain these equations become

$$j\omega C_e \Delta T_e + G(T_e)\Delta T_e - G_{ETF}\Delta T_e + G_{ep}(T_e)\Delta T_e = G_{ep}(T_p)\Delta T_p$$
$$j\omega C_p \Delta T_p + G_{ep}(T_p)\Delta T_p = W(\omega) + G_{ep}(T_e)\Delta T_e$$

Eq. 5.38

The size of the thermal conductivity term due to electron-phonon decoupling, G_{ep}, is relatively small compared to the thermal conductivity of the link between the electron system and the heat bath, G. Therefore combining these and using this to neglect small terms due to the decoupling, gives Eq. 5.39.

$$\Delta T_e(\omega) \approx \frac{1}{(1+j\omega\tau_p)(G+G_{ETF})(1+j\omega\tau_{eff})} W(\omega),$$

Eq. 5.39

which is similar to that of the ideal model, with an additional time constant in eq. 5.40.

$$\tau_p = C_p \Big/ G_{ep}(T_p).$$

Eq. 5.40

The electron phonon thermal coupling can be described using Pippard's free-electron model giving a thermal resistance between the electrons and phonons of the gold film with a T^5 temperature dependence [123]. With 3.3×10^5 $Wcm^{-3}K^{-6}$, and the dimensions of the gold described in section 2, this gives a thermal conductance at 10 mK of 0.2 nW/K. This may be compared to the thermal conductivity G of the gold bond wires that connect the detector to the heat bath. At 10 mK this is ~10 nW/K. The two time constants can therefore be estimated using the phonon and electron heat capacities of the detector. For the phonon detector at 10 mK these are estimated at ~1.6 x 10^{-12} and ~2.7×10^{-10} J/K respectively. This gives a fast time constant of 8 ms from the phonon system and a slower time constant of 27 ms from the electron system.

This decoupling will also provide an extra source of noise, as thermal fluctuations across the electron-phonon boundary contribute. According to Boyle and Rodgers (1959) [124] the noise equivalent power of these fluctuations is

$$NEP_{ep} = \sqrt{2k_B G_{ep} \frac{T_e^{\,5} + T_p^{\,5}}{T_e^{\,3}}} \,.$$

Eq. 5.41

Assuming the temperatures is around 10 mK and that G_{ep} and G have the values given above, this additional noise equivalent power will be ~14 % of the thermal fluctuation noise in the ideal model.

5.6 Finite rise time and other time constants

The rise time of the detector temperature has so far been considered to be instantaneous, but in practice this will be finite. This requires the energy conversion processes and the energy transfer between different components of the detector to be considered in more detail.

In the dielectric absorber ionising radiation will mainly deposit its energy via inelastic interactions with electrons. These excited electrons quickly lose their energy by transfer to other electrons or through the excitation of electron-hole pairs until their energy is less than twice the energy gap of the dielectric. For Calcium Tungstate this energy gap is 5.2 eV [98]. From this point the electrons cannot lose energy by these methods, and the energy is mostly transferred by the emission of optical phonons, a mode of lattice vibrations with the neighbouring atoms out of phase with each other, with a timescale of ~10ps. In scintillating material there may be a small amount of relaxation by the emission of photons.

On a time scale of ~100ps the optical phonons decay into two acoustic phonons, a mode of lattice vibrations with conherent movement between neighbouring atoms, with about half the Debye frequency, leading to an almost monoenergetic phonon distribution. These high frequency phonons have an athermal distribution and will

now start to thermalize. The energy of these phonons is down converted through anharmonic decay to lower energy phonons.

The phonons will also enter the gold film beneath the thermometer and quickly thermalize and interact with the free electrons producing a thermal electron distribution. The thermal resistance they encounter when crossing the boundary between the dielectic crystal and the gold film can be described by its thermal boundary conductance G_K. This reaches the electron system of the NTD Germanium and provides a temperature change and a corresponding change in resistance for the sensor.

The conversion of the initial electrons in the absorber, produced by the particle interaction, into acoustic phonons is relatively quick – with a total time of ~100 ps, compared to a typical pulse length of ~10 ms. Therefore for the model below, these steps are assumed to be an instantaneous change with the energy arriving as acoustic phonons in the absorber.

The rise time will be limited by the thermal conductivity between the different internal systems of the calorimeter, and by the thermalisation time within the detector. Therefore the rise time of the detector can be modelled as a term with an exponential time constant τ_R such that the pulse shape can be given by equation 5.42, with the two decay time constants τ_1 and τ_2.

$$V(t) = \left(1 - e^{-t/\tau_R}\right)\left(e^{-t/\tau_1} + e^{-t/\tau_2}\right). \qquad \textbf{Eq. 5.42}$$

The next step will be the transfer of the phonons across the boundary to the gold film, with some thermal boundary resistance. At the boundary between the two different materials, many of the phonons moving towards the boundary will be reflected back due to the differences in the vibrational properties of the materials.

5.7 Linearity

When a particle interacts with the detector a temperature pulse occurs. This has a rapid rise time followed by a slower decay containing several components. However this temperature change is not directly observed in the detector as a temperature change, but instead as a change in the resistance of the NTD Germanium sensor which is read out as a change in voltage using a bias current. Despite the exponential relationship of NTD resistance and temperature, they can still be shown to have a linear response for small signals.

The change in resistance for the temperature change ΔT will be ΔR where

$$\Delta R = R(T+\Delta T) - R(T) = R_0 \exp\left(\frac{T+\Delta T}{T_0}\right)^{-1/2} - R_0 \exp\left(\frac{T}{T_0}\right)^{-1/2}$$

$$\Delta R = R_0 \exp\left(\frac{T}{T_0}\left(1+\frac{\Delta T}{T}\right)\right)^{-1/2} - R_0 \exp\left(\frac{T}{T_0}\right)^{-1/2}$$

$$\Delta R \approx R(T)\left(\exp\left(-\frac{1}{2}\frac{\Delta T}{T}\right)-1\right)$$

Eq. 5.43

Therefore in the limit that $\Delta T << T$ the resistance response to a change in temperature will be linear, with a scale factor related to the stabilised resistance and temperature of the detector. For a detector operating around 10 mK, an energy deposition of 1 keV would lead to a temperature change of the order of one micro-Kelvin, therefore this linear approximation is suitable when looking at relatively small pulses.

5.8 Microphonics

Microphonic noise is caused by the physical vibrations of some component near the detector. During the operation of the cryogenic detectors at milli-kelvin temperatures, excess noise peaks were observed at frequencies around 500 Hz to 1 kHz when the

1K pot of the cryostat was filling. The extra vibrations of the 1K pot [125,126] caused this noise to appear at the detector, which is shown in figure 5.6.

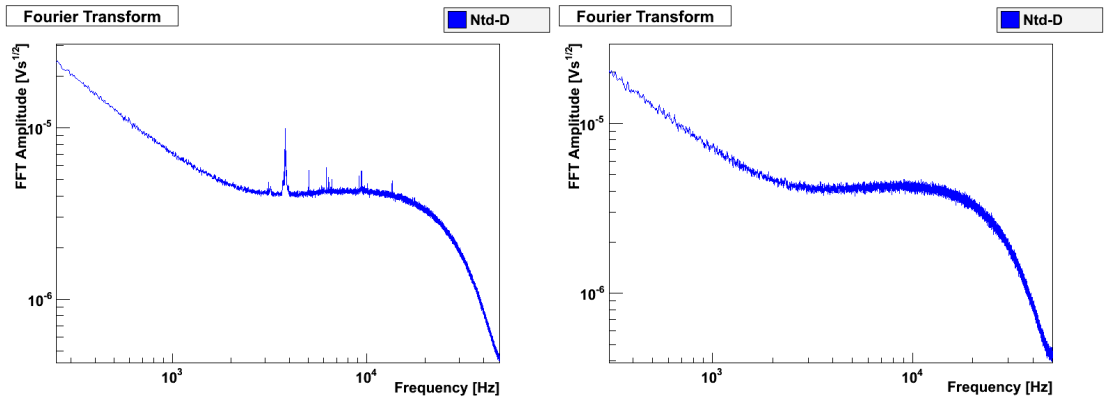

Figure 5.6 - Fourier spectrum with the 1K pot needle valve open (left) and closed (right). Excess high frequency noise appears when the 1K pot is filling.

These vibrations were picked up at some point in the read out chain of the detector, with two main possible suspects – the etched kapton cables or the gold bond wires to the detector. Using the a similar set of cabling, a 1 MΩ resistor and a detector with NTD germanium sensor, both mounted on the same level of the cryostat, were read out simultaneously. The resistor was directly connected to the end of the cable, while the NTD sensor was connected via the gold bond wires.

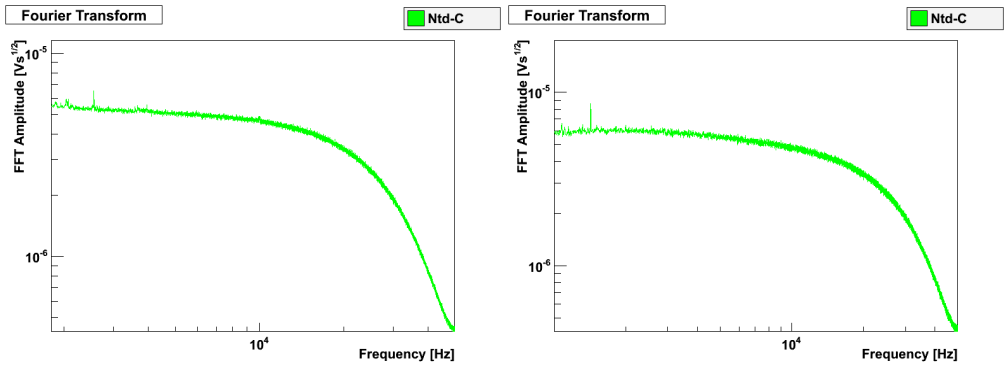

Figure 5.7 - section of the frequency spectrum for a 1 MΩ resistor with the 1K pot needle valve open (left) and closed (right).

In this case, no microphonic noise was observed on the resistor signal with the 1K pot in either state. Therefore the cables are adequate and the noise must appear via the thinner gold bond wires which were not present for the 1 MΩ resistor.

6. Temperature stability

Any fluctuations of the operating temperature of the detector will have an effect on the output signal of the detector. As the operating temperature changes, the responsivity of the detector will also change, in part due to the changing resistance of the NTD germanium and in part due to the temperature dependence of the heat capacity of the detector components.

These fluctuations at the detector could be due to a number of sources. As in section 2.1, vibrations or movement of the cryostat can raise the temperature at the detector. This effect is minimized by supporting the cryostat on air dampers. Resistive heating due to the signal and bias currents sent to the detector can also have some effect on the temperature level of the detector. Heat may also be transferred from higher temperature stages in the cryostat, the temperature of which may vary during the operation of the cryostat due to the level of helium in the main bath or the filling of the 1K pot.

For small variations in temperature the change in detector response is linear and can easily be dealt with during the analysis process. Larger variations, however, will introduce non-linear effects which require more complicated analysis. If these temperature variations are fast enough (on a timescale similar to that of the pulses induced by particle interactions), they may also produce distorted pulse shapes due to changes in the baseline position. These distorted pulses could then provide unreliable measurements of the energy deposited.

Therefore it is important to provide a stable temperature bath for the detector and keep the variations in the temperature small and slow. To achieve this the temperature is stabilized using an arrangement of heater resistors and thermometers along with a

number of different temperature levels, as described in sections 6.1 and 6.2. This helps to reduce the size and speed of the fluctuations.

Care is also taken to prevent a heatload from other sources being introduced close to the detector. Sections 6.3 and 6.4 describe the impact of thermal radiation from higher temperature levels in the cryostat and the conduction of heat through the cabling. Finally section 6.5 describes the effect of Joule Heating in the cabling.

6.1 Thermal model

The layout of the experimental plate of the cryostat can be described in a simplified model like figure 6.1.

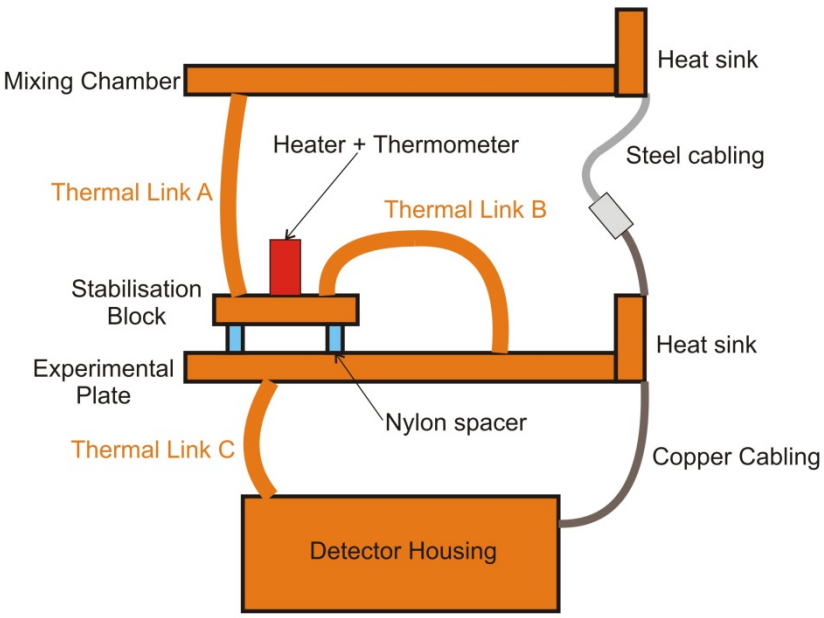

Figure 6.1 - Schematic drawing of the thermal connections to the detector. This is thermally connected to the mixing chamber only by the copper cable, and any additional link added alongside this.

The temperature stabilisation block has a RuO resistor (as a thermometer) and a 400Ω resistor (as a heater). The thermometer was tested by Lakeshore as being 1007 Ω at 305 K, 1077 Ω at 77 K, and 1467 Ω at 4.2 K in open dewars. The stabilisation block was stabilised using a Picowatt AVS-47 temperature bridge to read the resistance of

the thermometer and a corresponding Picowatt TS-530 temperature controller to maintain the temperature of the stabilisation heatsink.

Copper strips, with dimensions given in table 6.1, connect each of the temperature levels, providing a thermal path for the transfer of heat between them. The cabling will also provide this as well, but to a lesser extent – with the steel cable and brass connections to the copper cable giving a low conductivity between the mixing chamber and experimental plate.

	Length (mm)	Width (mm)	Thickness (mm)	No. of links
A	70	5	0.4	1
B	60	5	0.4	1
C	20	10	0.4	6

Table 6.1 – The dimensions of the copper links between the temperature stages shown in figure 6.1.

The thermal link between the experimental plate and the detector is relatively strong, so for the following model they can be considered to be at a similar temperature. The thermal link provided in parallel between the mixing chamber and the experimental plate via the cabling is relatively weak, so it will be ignored in this model.

The thermal model of the experimental plate can then be described by the set of coupled differential equations 6.1 and 6.2.

$$C_{EP}\frac{dT_{EP}}{dt} + G_{SE}(T_{EP} - T_S) = 0 \qquad \textbf{Eq. 6.1}$$

$$C_S\frac{dT_S}{dt} + G_{SM}(T_S - T_M) + G_{SE}(T_S - T_E) = P_{htr}(t), \qquad \textbf{Eq. 6.2}$$

where C_{EP} and C_S are the heat capacities of the experimental plate and the temperature stabilisation block; T_{EP}, T_S and T_{MC} are the temperatures of the experimental plate, stabilisation block and mixing chamber; G_{SE} and G_{SM} are the thermal conductivities between the levels; and P_{htr} is the power delivered by the heater, with the current provided by the temperature controller.

Taking the equation 6.1 on its own - the solution (equation 6.3) is an exponential with the time constant $\tau_{SE} = C_E / G_{SE}$. Therefore with a relatively large mass on the experimental plate, so the heat capacity becomes large, and a relatively small thermal link, so the thermal conductivity becomes small, the time constant will be large and the temperature response to temperature fluctuations at the stabilisation block will be slow.

$$T_E = (T_{E0} - T_S)e^{-t/\tau_{SE}} + T_S$$

Eq. 6.3

Considering both equations, similar exponential behaviour is found, with a weak heat link decoupling the stabilising level from the fluctuations of the mixing chamber level, and the experimental plate further decoupled from the stabilising level.

By substituting the form for T_S from equation 6.1 into equation 6.2 and rearranging one can get the combined equation, 6.4.

$$\frac{C_S C_E}{G_{SM} G_{SE}} \frac{d^2 T_E}{dt^2} + \left(\frac{C_S}{G_{SM}} + \frac{C_E}{G_{SE}} + \frac{C_E}{G_{SM}} \right) \frac{dT_E}{dt} + T_E = T_M + \frac{P_{htr}(t)}{G_{SM}} .$$

Eq. 6.4

For now, assume that the mixing chamber temperature T_M and the heater power to the temperature stabilisation level are constant. With a change of variables

$$T_E = T + T_M + \frac{P}{G_{SM}}$$

Eq. 6.5

the equation is simplified further to give equation 6.6.

$$\frac{C_S C_E}{G_{SM} G_{SE}} \frac{d^2 T}{dt^2} + \left(\frac{C_S}{G_{SM}} + \frac{C_E}{G_{SE}} + \frac{C_E}{G_{SM}} \right) \frac{dT}{dt} + T = 0 .$$

Eq. 6.6

This second order differential equation has a solution which is the sum of two exponentials, giving the form of the experimental plate temperature as equation 6.7.

$$T_E = Ae^{-at} + Be^{-bt} + T_M + \frac{P}{G_{SM}} ,$$

Eq. 6.7

where *A* and *B* give the amplitude of the two exponential decay components, and *a* and *b* give the time constants of the change in temperature. The amplitude will depend on the initial conditions of the temperature levels, while the time constants provide an exponential change in temperature down to a constant value given by the mixing chamber temperature and the stabilisation heating power. These time constants will be a sum of several terms containing a ratio of heat capacities and thermal conductivity – similar to the simple case described in equation 6.3.

With the heater power term, there is a dependence on the thermal conductivity between the stabilisation level and the mixing chamber. This will therefore provide a change in the equilibrium temperature for a given power, if the thermal link between these two stages is altered.

For the more realistic case, where the mixing chamber temperature may vary with time and there may be some heating power applied to the stabilisation level, these terms may be combined into one generic time varying function *f(t)*. This gives the non-homogeneous differential equation 6.8.

$$\frac{C_S C_E}{G_{SM} G_{SE}} \frac{d^2 T_E}{dt^2} + \left(\frac{C_S}{G_{SM}} + \frac{C_E}{G_{SE}} + \frac{C_E}{G_{SM}} \right) \frac{dT_E}{dt} + G_{SM} T_E = f(t)$$

Eq. 6.8

The solution to this will depend on the form of this time variation.

However, things will not be quite this ideal in reality, with additional heating due to thermal radiation from higher temperature levels, Joule heating due to the bias current for the thermometer, and possible heat leaks in some of the material used.

Considering the thermal link between the experimental plate and the detector housing will also give further decoupling of the detector response and the heater input. There may also be heating of the detector itself by Joule heating and by the gamma particles of the radioactive background.

6.2 Time response

As described in the previous section, the time response of the temperature of the detector housing can be explained in terms of the heat capacity of the housing and of the stabilisation block, along with the thermal conductivity of the copper link that connect these and provide a thermal connection between them. Typically with the form $\tau = C/G$.

For equation 6.7, assuming a constant mixing chamber and heater power, the time constants are

$$a,b = \frac{-(\tau_S + \tau_E + C_E/G_{SM}) \pm \sqrt{(\tau_S + \tau_E + C_E/G_{SM})^2 - 4\tau_S\tau_E}}{2\tau_S\tau_E}, \qquad \textbf{Eq. 6.9}$$

where τ_S is C_S/G_{SM} and τ_E is C_E/G_{SE}.

The time constants due to the thermal links can be estimated by applying a sudden change in temperature and fitting an exponential curve to the response.

In a stripped down version of the setup (as shown in figure 6.2), the TS-530 temperature controller was used to heat up the experimental plate, and then the heating removed so that the detectors cool down slowly by the flow of heat to the mixing chamber. For equation 6.4, this provides a sudden change in P_{htr} from an approximately constant non-zero value to zero. This will lead to an exponential decrease in temperature, as in figure 6.3, until it settles at a new, lower point.

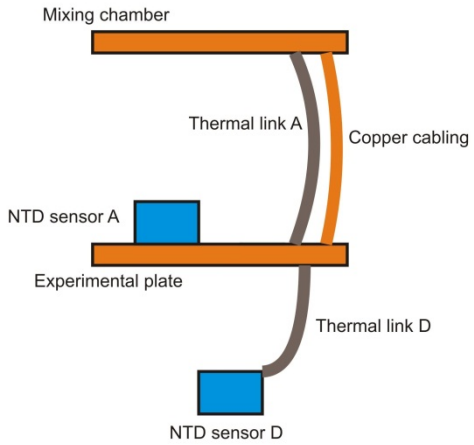

Figure 6.2 - The setup used to test the temperature response due to the thermal links.

This was carried out first with the thermal link provided only by the copper cable and thermal link D, and then with thermal link A added between the mixing chamber and the experimental plate. The time constants obtained are presented in table 6.2.

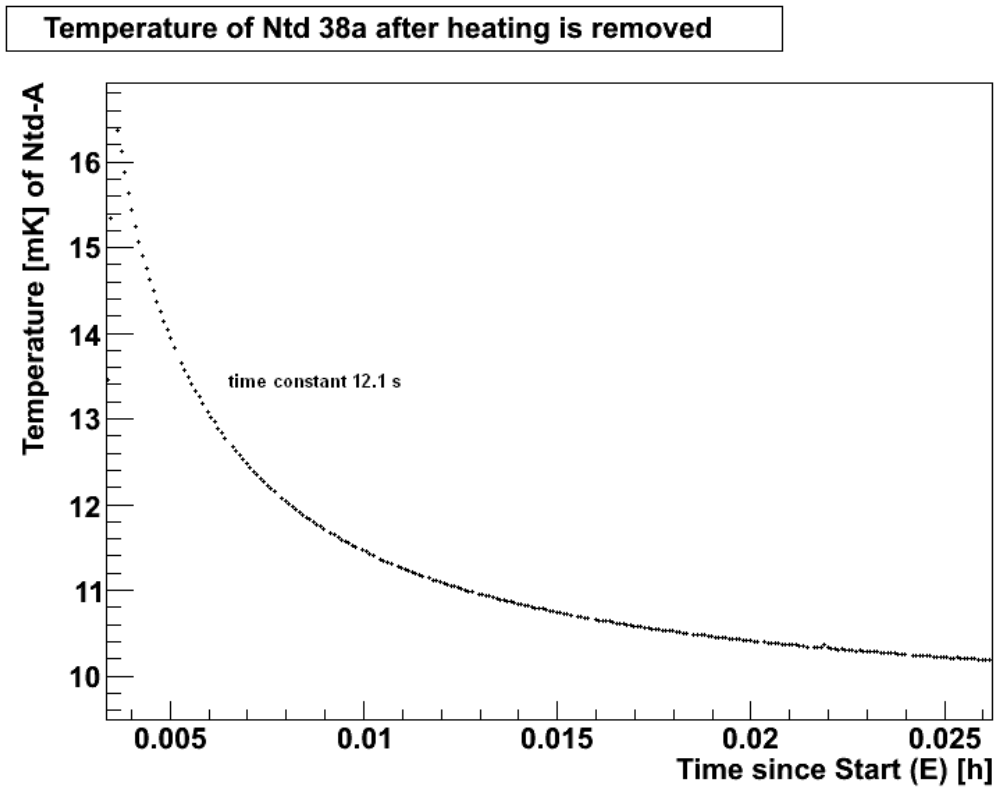

Figure 6.3 - The response of Ntd A when the heating provided by the temperature controller was suddenly stopped. An exponential curve was fit and a time constant for the recovery found.

Time constant (s)	Cables only	Cable + Copper Link
NTD A	211	12.1
NTD D	390.9	270.5

Table 6.2 – the time constants for different thermistors either with the cables as the sole thermal connection between the experimental plate and the mixing chamber, or with an additional NOSV copper link added alongside the cable.

The cable by itself provides some thermal connection between stages, predominantly along the copper shielding, but the addition of another copper strip running alongside the cable provides some extra thermal connection and therefore decreases the time constant for the experimental plate response. Since Ntd-D is suspended beneath the experimental plate there is an extra stage in the thermal model, giving the detector a longer time constant than for Ntd-A.

The thermal link has a low pass filter type effect, reducing the size and speed of the temperature fluctuations coming from the mixing chamber.

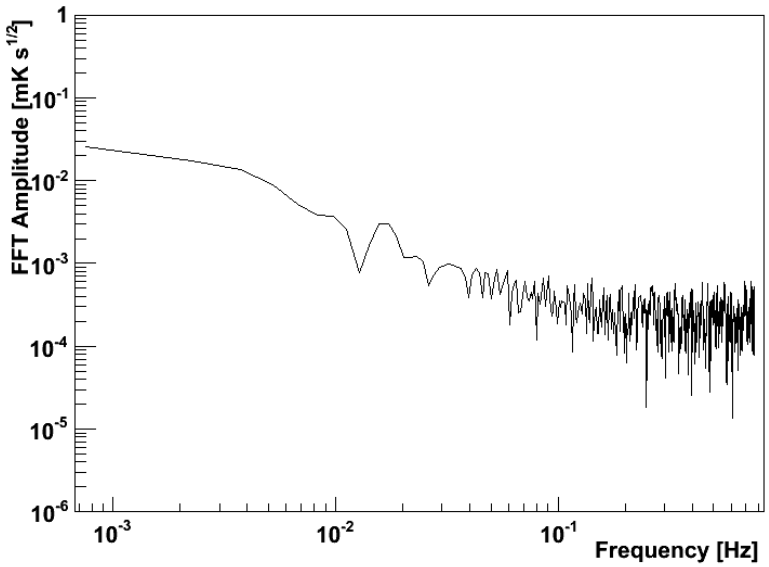

Figure 6.4 - Fourier Transform of the NTD temperature.

A Fourier transform of the temperature at the detector, such as figure 6.4, shows the amplitude initially decreasing at low frequencies, as would be expected with a low pass filter. However the temperature levels off at higher frequencies rather than continuing this low pass filter behaviour. This suggest the presence of some extra

source of heat fluctuations directly applied to the experimental plate or detector – such as heating from the many low energy depositions present from the radioactive background.

The time constant that sets this low frequency decrease can be varied as in table 6.2 by using the thermal conductivity between various stages. However, the same effect could also be achieved by increasing the heat capacity at one of the stages. As the experimental setup inside the cryostat was developed, new larger detector housing was necessary to provide shielding for the detector from the radioactive background. This had the additional effect of providing a large mass of copper suspended below the experimental plate, in which the detectors were held. This increased mass provided a larger heat capacity, thus increasing the time constant of the detector response. In this new configuration the cryostat was heated and stabilised using the AVS bridge and temperature controller system, then the heating was suddenly removed so that the temperature fell back down to its base value.

This fall in temperature was fit to with the sum of several exponential terms, so that.

$$T = T_0 + Ae^{-at} + Be^{-bt} .$$

Eq. 6.10

The results of a fit using this form are given in table 6.3, showing values for the time constants larger than the previous values.

T_0 [mK]	A [mK]	B [mK]	a [/hr]	b [/hr]
8.9535	0.569	0.241	22.782	2.3095

Table 6.3 – Results of a fit to a change in detector temperature using the form in eq. 6.10.

The larger mass and increased heat capacity therefore give an increase in the size of the time constants. However, there may still be the effect of some source of thermal fluctuations being applied at a stage closer to the detector, where this filtering will have less effect. This may be due to low energy depositions from the radioactive

background, but thermal radiation from other higher temperature and heat transfer through the cable must also be considered.

6.3 Radiation

The JFETs on the cold amplification stage are kept at a relatively high temperature of around 120 K to provide the best noise performance from them. This is achieved by a carefully adjusted thermal link from the board to 4 K, and by a temperature stabilisation setup with a pair of PT100 thermistors and a pair of heater resistors. However the introduction of this warm material into the IVC provides a potential problem for the temperature of the detectors. If the heat from the board is not dissipated properly, it could prevent the detector getting down to a low enough temperature to function or have adverse effects on the temperature stability of the detector.

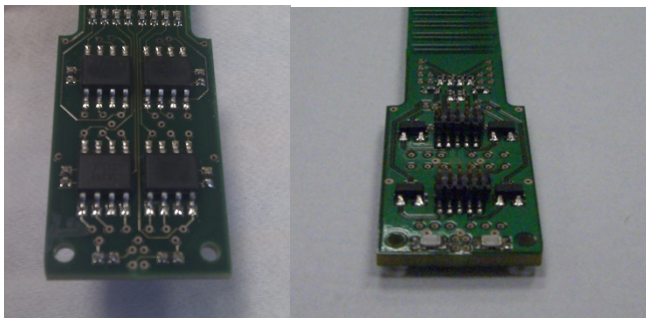

Figure 6.5 - the 100K electronics board. The two samtec connectors allow for the cables from the detector to be connected.

If the temperature of the p.c.b. varies from T_1 to T_2 the difference in the heat radiated out will be given by

$$P = \sigma \varepsilon A\left(T_2^4 - T_1^4\right), \qquad \textbf{Eq. 6.11}$$

in which σ is the Stefan-Boltzmann constant [127], ε is the emissivity of the material and A is the area of the p.c.b. This radiation should be contained within a brass box (shown in Fig. 6.6) which surrounds the board, and is thermally connected to the 4 K

level of the cryostat. In addition to this, the different temperature stages of the cryostat (as in Fig 2.1) prevent radiation from the high levels of the cryostat reaching the lower temperature stages.

The dimensions of the end of the p.c.b. are 26 mm × 16 mm, therefore if the board warms up from 100 K to 120 K the thermal radiation from the board (assuming $\varepsilon = 1$) will increase from 2.32 mW to 4.83 mW.

This radiation should be prevented from reaching the detector by the shielding box around the electronics, and the radiation shielding at each successive stage of the cryostat. This shielding was tested using thermometers, from Oxford Instruments, on various stages of the cryostat, the 1 K pot, the still and the 50 mK stage. The sensitivity of these thermometers is poor (~10 mK for the 1 K pot thermometer), but no response was observed on these when the JFET temperature was increased.

Figure 6.6 - The box used to shield the lower levels from the 100K radiation. This is also wrapped in aluminium foil for extra protection.

For the 1K pot level, the temperature of the stage can typically vary between 1.2 K and 1.5 K during the operation of the cryostat, depending on whether the 1K pot is filling or not. This variation in temperature should produce a change in the amount of thermal radiation being transmitted to the stage below. The 1K pot level is a

copper plate of diameter 10 cm, so assuming the emissivity as 0.87 (that of oxidised copper, polished copper will be much lower around 0.03), an upper limit on the variation of the radiative heatload from this level to the still is calculated as 0.81 mW and 2.0 mW. These heatload variations of ~mW from the 1K pot do not noticeably affect the temperature of the experimental plate.

6.4 Conduction

There may also be a heat load from higher levels through the conduction of heat along the cabling. Fig. 2.13 shows the cross-section of the cabling. The layers of polyimide have low thermal conductivity and will not contribute much to the conduction compared to the metal tracks and metal shielding of the cable.

Steel tracks and shielding rather than copper tracks and shielding were chosen for the cabling from higher temperatures to reduce this conduction; the lower thermal conductivity of the steel provides a smaller heatload than the copper. The conduction through the cables can be divided into two separate components – heatload through the tracks and heatload through the shielding. These two components are heatsunk separately, the shielding through a series of copper clamps at each temperature stage, while the tracks initially had none but later had one added at the 50 mK stage. This model of heat transfer for the cable will however neglect the heat transfer through the layers of polyimide which would provide additional heat sinking to the tracks.

6.4.1 Tracks

For the version of the cable with no heat sinking for the tracks, the extra heating through the tracks of the cable will be given by Eq 6.12

$$P = \int_{T_D}^{T_1} \kappa(T)\left(\frac{a}{l}\right)dT \ ,$$

Eq. 6.12

where κ is the thermal conductivity of the material, a is the cross-sectional area and l is the length. The cable has ten steel tracks, each of width 0.1 mm, thickness 35 μm and length 80 cm. These steel tracks have a resistivity of $\rho = \alpha + \beta T^2$ where α = 7.14×10^{-7} Ωm and β = 3.13×10^{-12} ΩmK^{-2} [88]. This can be converted to a thermal conductivity using the Wiedemann Franz law [89],

$$\frac{\kappa}{\sigma} = L_0 T \,. \qquad \textbf{Eq. 6.13}$$

For the detector at 10 mK, the heating from the cable increases from 7.3 μW to 10.4 μW if the temperature changes from 100 K to 120 K. This change in heatload is a much lower value than the potential change due to thermal radiation, but it appears directly at the detector and thus may have more effect on the detector.

To reduce this heat load, a heat sink, shown in Fig. 6.7 was added at the 50 mK stage containing copper tracks with a number of larger copper pads, to provide more surface area for heat transfer, clamped between two copper layers to provide extra heat sinking between the tracks.

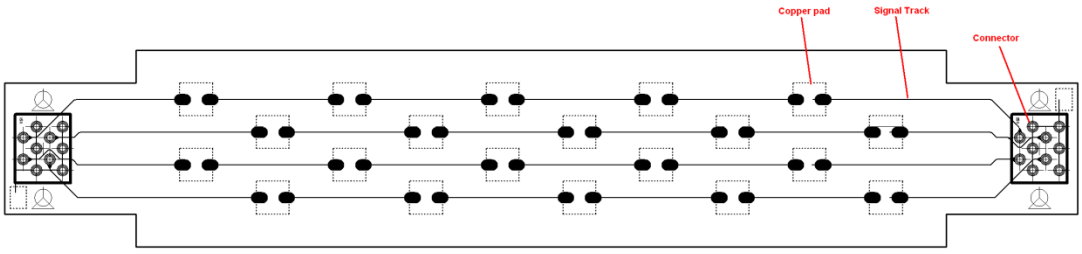

Figure 6.7 - This shows the layout of the tracks in the heat sink for the tracks. The heat sink has copper tracks, with several larger pads, on a polyimide layer clamped between two copper cover layers.

6.4.2 Shielding

For the heatload through the shielding of the cables, the calculation is, but with two shielding layers of width 12 mm, thickness 35 μm, and total length 80 cm. These are heatsunk at various stages between the p.c.b. and the detector – at 4 K, the 1K pot

level, the Still, the 50mK shield and the mixing chamber. With 10 cm from the electronics to the first heatsink, at 4 K, the heatload on this level will increase from 67.6 μW to 96.5 μW if the temperature changes from 100 K to 120 K. Even if a second steel cable is added to operate more detectors or thermometers, the heatload due to conduction through the shielding is still considerably smaller than the radiative heatload from the JFET stage. The cable is heatsunk at each temperature level in the cryostat.

6.4.3 Polyimide

The thermal conductivity of polyimide is $4.64\times10^{-3}\,\boldsymbol{T}^{0.5678}$ W/mK [129], so ignoring any heat sinking effects from the tracks or shielding, the heatload due to conduction at 100 K along it will be ~5 μW. This will have a relatively small effect compared to any conduction down the steel shielding layers.

6.5 Joule heating

With the bias current sent down to the detector there may also be heating due to components with a significant resistance. First consider the cabling: each cable contains four signal tracks which carry a bias current to the two detectors on the other end. This current is typically ~10nA, with an optimum value chosen according to the detector sensitivity at that excitation size, and will provide a heating effect due to the resistance of the cables.

$$P_{res} = \int_{T1}^{T2} \frac{I^2}{A}\rho(T)\frac{dl}{dT}dT \qquad \textbf{Eq. 6.14}$$

For the steel tracks of length 80 cm, width 0.1 mm, thickness 35 μm, and assuming a constant temperature gradient through the cable, the extra heatload is 16.7 fW per track. As discussed in section 5.4.2, the temperature profile of the cable will not be linear, so the actual heatload will be even smaller than this. This heating power is tiny

in comparison to the heatload from other sources and, though the JFET temperature may affect the temperature profile of the cable, and thus its resistance, the amount of Joule heating will not be significant.

The effect of Joule heating on the detector itself has already been covered as part of the thermal model in chapter 5. The NTD sensor has a relatively high resistance, typically in the range of MegaOhms at its operating point, therefore the Joule heating of the detector due to the bias current will have a significant effect on the temperature of the bolometer and its response due to electrothermal feedback.

$$P = I^2 R$$

Eq. 6.15

With a bias current of ~10 nA, and an sensor resistance of ~ 1 MΩ, the additional heating effect on the detector will be ~ 100 pW.

As described in sections 7.9, any slow, small changes in temperature can be corrected for during analysis in the conversion of voltage pulse heights to energies. Larger, or faster, changes introduce non-linear effects so care has been taken to provide a stable environment for the detector where temperature fluctuations have been reduced and the effect of other sources of heat minimized.

7. Detector tests and Analysis

This chapter describes measurements and results obtained from two detector modules, each with two low-temperature calorimeters using an NTD Ge sensor as a thermometer for precise energy measurements. One of the calorimeters in a detector module was equipped with a calcium tungstate or a calcium molybdate absorber and the other designed as a scintillation detector. Energy deposited in these detectors is read out as a voltage pulse which can then be analysed. The size of these pulses can be calibrated to energy, and the detector used to measure with high precision the energy deposited by a photon or particle. A main advantage of cryogenic calorimeter is the relatively wide choice of possible absorber materials, an important aspect when addressing the physics goals of an experiment. For example, such a detector with a suitable resolution and choice of detector material could be used for dark matter or neutrinoless double beta decay experiments.

The signal as it is recorded is a continuous stream of modulated data, subdivided into 327.68 ms long segments known as 'records'. In order to recover the energies of particle interactions the signal is first processed to remove the modulation introduced by the a.c. bias. A software filter can then be applied to the data to reduce the size of low frequency fluctuations in the operating point of the detector, or to smooth out the data by removing high frequency noise. These are described in sections 7.2 and 7.3. Section 7.4 describes the triggering algorithm that is used to identify the locations of the voltage pulses and to select the sections of the continuous data stream to be analysed.

To find the amplitude of these pulses and identify any pulses which may give an unreliable measurement of the amplitude, typically pile up or triggers on baseline fluctuations, the pulses are fit with a exponential pulse shape and cuts made on the

quality of the fit. In order to do this an accurate model of the pulse shape must be found. To achieve this initial parameters describing the shape of the pulse are calculated, as in section 7.5, and a shortlist of good pulses selected based on these parameters. Then, using this shortlist, a fit is made to the data and a set of parameters is extracted that better models a pulse containing multiple exponential terms, as described in equation 5.42. This pulse shape is then fit to the full list of pulses and the maximum of the pulse found, which may then be used a measure of the energy deposited in the detector.

Finally this voltage pulse height measurement is converted into an energy measurement by taking account of the operating point of the detector and adjusting for the heat capacity of the detector and the sensitivity of the NTD sensor at this temperature. By testing the detector using a radioactive source that produces particles with a narrow range of energies, an energy spectrum can be recorded that shows the spectral features expected. These features, including the narrow full energy peak, allow the performance of the detector to be tested over a range of energies and the resolution of the detector to be determined.

7.1 Spectral features

For assessing the performance of the detectors in this thesis, several gamma-emitting nuclei have been used (see Tables 7.2, 7.3 and 7.4). Gamma particles from these sources that are fully absorbed by the detector will produce a photo peak at the full energy of the photon. However, there will also be other features in the energy spectrum [130] associated with these photons due to interactions in the detector and its surroundings, as discussed in the following. These sources are placed outside the cryostat and must pass through the walls of the cryostat and layers of shielding, so these interactions can be quite significant.

7.1.1 Characteristic X-ray escape peaks

In photoelectric absorption, when the energy of the photon is greater than the binding energy of the electrons, one of the electrons from the inner shells of the atom may be freed, leaving a vacancy in this shell. An electron from one of the outer shells may fill the vacancy, emitting an x-ray in the process [131].

The energy of these x-rays is given by the difference in the energy levels. For tungsten the transition of an electron from the L shell to fill a vacancy in the K shell will give energies of $K_{\alpha 1}$ = 59.3 keV and $K_{\alpha 2}$ = 57.9 keV. For an M shell electron filling the K shell the x-rays have energies $K_{\beta 1}$ = 67.2 keV and $K_{\beta 2}$ = 69 keV.

	$K_{\alpha 1}$ [keV]	$K_{\alpha 2}$ [keV]	$K_{\beta 1}$ [keV]	$K_{\beta 2}$ [keV]
W	59.32	57.98	67.2	69.1
Mo	17.48	17.37	19.6	20

Table 7.1 – K shell energies for tungsten and molybdenum, data from [129].

These x-rays may be reabsorbed into the crystal, giving the full energy peak, or they may escape giving a peak in the detector of the full energy minus the x-ray energy.

7.1.2 Compton Scattering

A Compton scattering interaction produces a recoil electron and a scattered photon with an energy dependent on the scattering angle.

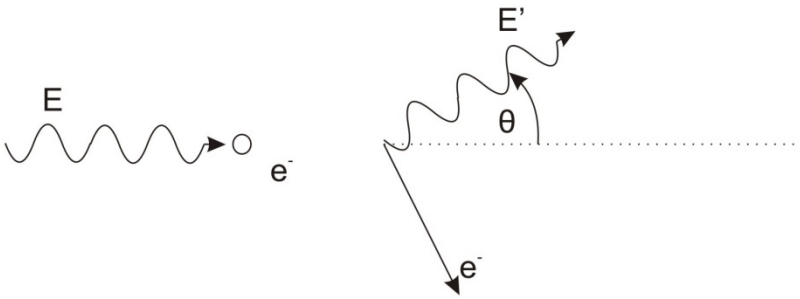

Figure 7.1 – A photon Compton scattering from an electron.

For an incident photon of energy E which scatters by an angle θ, the final energy of the photon will be given by E'.

$$E' = \frac{E}{1 + \frac{E}{m_e c^2}(1 - \cos\theta)}$$

Eq. 7.1

This formula gives a minimum energy for the scattered photon when the photon is deflected back in the direction it came from with $cos\theta = -1$, and a maximum when $cos\theta = 1$, equivalent to an unscattered photon.

For a photon of energy E that scatters in the detector the scattered photon may be reabsorbed within the detector giving the full energy peak, or it may go on to escape the detector. In the second case the detector will only measure an energy E_m

$$E_m = E - E'$$

Eq. 7.2

This produces a feature in the spectrum known as the Compton Edge with energy given by Eq. 7.3, corresponding to the highest deposited energy with an escaping scattered photon. This should give a gap between the photo peak and the edge, with a continuous distribution of energies below the edge.

$$E_C = \frac{2E^2}{m_e c^2 + 2E}$$

Eq. 7.3

However, this edge will be softened as multiple scattering of the photons leads to energies deposited in the detector with values between the edge and the photo peak. This is not the only effect of Compton scattering on the measured energy spectrum. Before the photons reach the detector they may scatter in the material surrounding it – for example, the walls of the cryostat or the shielding around the detector. Using Eq. 7.3 again to consider particles that have been scattered once, the photons reaching the detector will have a minimum energy of

$$E'_{\min} = \frac{E}{1 + \frac{2E}{m_e c^2}}.$$

Eq. 7.4

These back-scattered photons, which have been scattered in a direction opposite to their initial one, produce a spectral feature known as the reverse Compton shoulder near this energy. However there will once again be the possibility of multiple scattering, which would leave the scattered photons with energies below this. Scattering by smaller angles will produce a continuous range of photon energies up to the energy of the peak. The size of these effects on the spectrum depends on the arrangement of the source, the detector and its surroundings, and is best described using simulations of the layout. Such simulations are carried out in section 7.1.6.

7.1.3 Pair production escape peaks

For most of the sources used in this thesis pair production will not be important, as a minimum energy of twice the electron mass is required to create an electron-positron pair. Thus, pair production requires incident gamma particles of over 1.02 MeV, and in this work, this is only true for gammas from a ^{60}Co source. As the kinetic energy of the positron reduces through multiple scattering, eventually it will annihilate with

an electron, producing two annihilation photons of energy equal to the electron mass, 511 keV. For a small detector these photons may escape giving a single and a double escape peak at $m_e c^2$ and $2m_e c^2$ below the full energy peak.

7.1.4 Test sources

In this thesis, a number of radioactive sources have been used. For example, in a dark matter search with cryogenic detectors the nuclear recoils associated with WIMP scattering are expected to typically have values of ~10 keV. For neutrinoless double beta decay the Q-value is in the region of several MeV. The detector is tested and calibrated by using several sources, placed outside the cryostat, with a range of energies from within this range, and appropriate for its physics use. The following sections describe the gamma emissions from the sources used in this thesis.

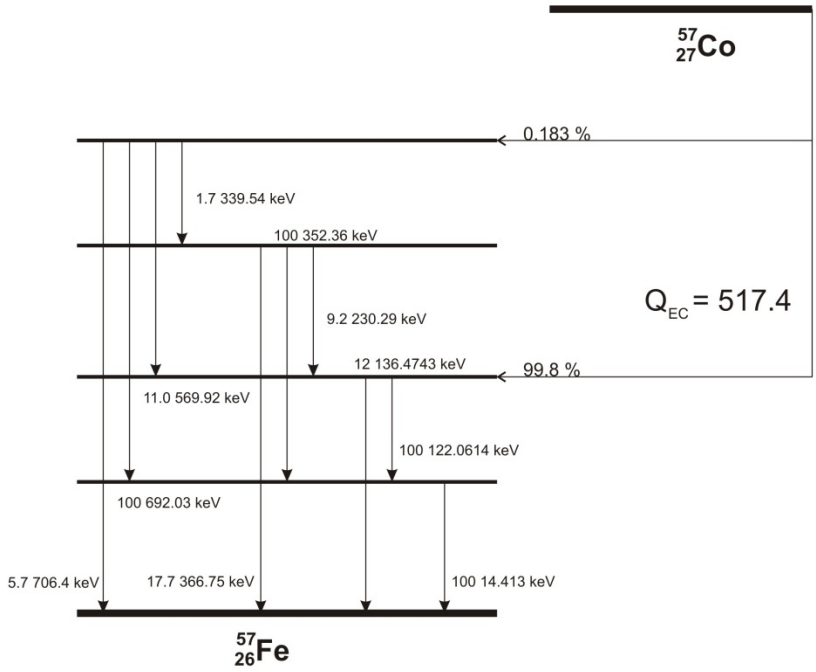

Figure 7.2 - Decay scheme for Co-57 using data from [129].

7.1.4.1 Cobalt 57

This undergoes electron capture to an excited state of ^{57}Fe, producing gamma particles with 136 keV or a pair with 122 keV and 14.4 keV [129,130] as shown in figure 7.2.

Cobalt 57 Peak [keV]	W Escape Peak $K_{\alpha 1}$ [keV]	W Escape Peak $K_{\alpha 2}$ [keV]	W Escape Peak $K_{\beta 1}$ [keV]	W Escape Peak $K_{\beta 2}$ [keV]	Mo Escape Peak $K_{\alpha 1}$ [keV]	Mo Escape Peak $K_{\alpha 2}$ [keV]	Mo Escape Peak $K_{\beta 1}$ [keV]	Mo Escape Peak $K_{\beta 2}$ [keV]	Compton Edge [keV]	Backscatter E_{min} [keV]
136.47	77.2	78.5	69.3	67.4	119.0	119.1	116.9	116.5	47.5	89.0
122.06	62.7	64.1	54.9	53.0	104.6	104.7	102.5	102.1	39.5	82.6
14.41									0.8	13.6

Table 7.2 - Spectral features for the Co-57 source and further energies produced through interaction in specific detector materials [129].

The features expected in the detector from these peaks are listed in table 7.2. The most prominent features of this spectrum will be the 122.1 keV peak, with a smaller 136.5 keV peak nearby – the relative abundance of these peaks are approximately 9:1, not taking into into account the difference in scattering within the materials surrounding the detector. There would also be a large 14.4 keV peak, but this will be greatly reduced compared to the higher energy peaks by the shielding around cryostat, including the walls of the IVC and main helium bath. This change in the ratio of the peaks is shown in Geant simulations in 7.1.6.

Of the escape peaks, the Kα lines with be the most prominent, particularly those from the 122 keV gammas. Due to their low count rate the β lines are likely to be negligible, but they are included here for completeness. The Tungsten escape peaks will be well separated from the full energy peaks and can be clearly measured, but the Molybdenum peaks will be closer to the full energy peaks and in some arrangements may be mixed in with the broadened low-energy shoulder of the 122 keV peak, as in the simulation shown in Fig. 7.1.6.

7.1.4.2 Cobalt 60

^{60}Co undergoes beta decay to ^{60}Ni, producing mostly1.173 MeV and 1.333 MeV gamma rays, as in the decay scheme in figure 7.3..

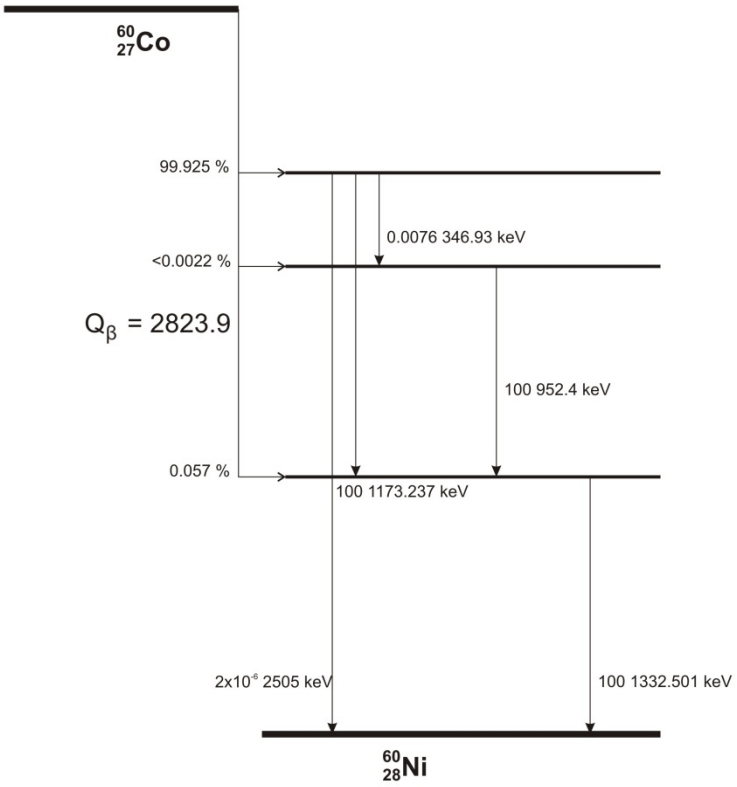

Figure 7.3 - Decay scheme for Co-60 using data from [129].

Cobalt 60 Peak [keV]	W Escape Peak $K_{\alpha 1}$ [keV]	W Escape Peak $K_{\alpha 2}$ [keV]	Mo Escape Peak $K_{\alpha 1}$ [keV]	Mo Escape Peak $K_{\alpha 2}$ [keV]	Single Pair Prod. Esc. Peak [keV]	Double Pair Prod. Esc. Peak [keV]	Compton Edge [keV]	Backscatter E_{min} [keV]
1332.5	1273.2	1274.5	1315.0	1315.1	821.5	310.5	1118.1	214.4
1173.2	1113.9	1115.3	1155.8	1155.9	662.2	151.2	963.4	209.8

Table 7.3 – Spectral features for the Co-60 source and further energies produced through interaction in specific detector materials [129].

The spectrum for this source will mostly consist of the two large peaks, with the other possible decay modes having extremely low rates. As with the escape peaks for

molybdenum with Cobalt-57, the escape peaks for tungsten and molybdenum for gamma from a Cobalt-60 source, both have energies relatively close to the full energy peaks of the source, and they may be difficult to resolve due to scattered photons from the material around the detector with energies close to the peaks. However, unlike the other sources, the higher energy of the gammas gives the possibility for pair production to occur. This could lead to two extra peaks – corresponding to one or both of the annihilation photons produced by the positron escaping the detector. However the energy is still relatively low so the probability of pair production will not be high, therefore these peaks may be difficult to measure.

7.1.4.3 Barium 133

This undergoes electron capture to ^{133}Cs, producing a numbers of peaks around 400 keV and below, predominantly at 356 keV as shown in the decay scheme in figure 7.4.

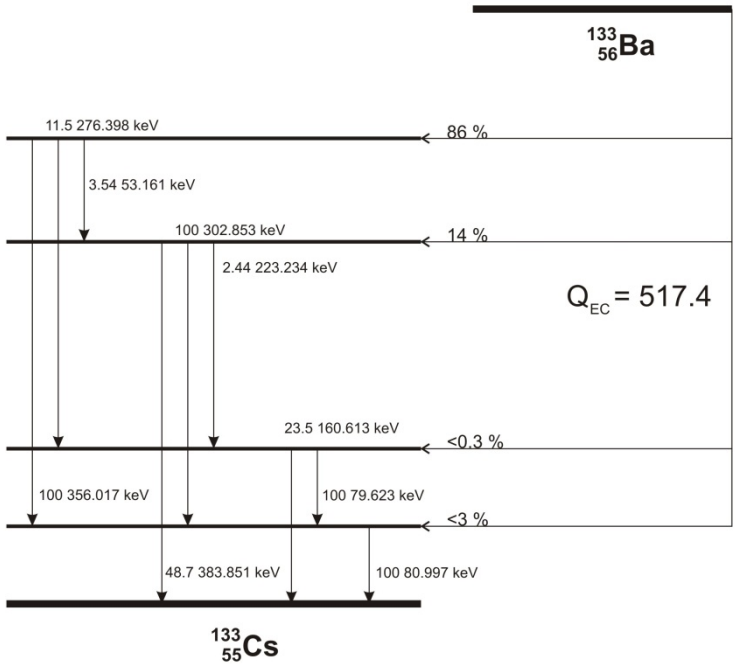

Figure 7.4 - Decay scheme for Ba-133 using data from [129].

Barium 133 Peak [keV]	W Escape Peak $K_{\alpha 1}$ [keV]	W Escape Peak $K_{\alpha 2}$ [keV]	Mo Escape Peak $K_{\alpha 1}$ [keV]	Mo Escape Peak $K_{\alpha 2}$ [keV]	Compton Edge [keV]	Backscatter E_{min} [keV]	Relative rate
383.9	324.5	325.9	366.4	366.5	230.5	153.4	0.054
356.0	296.7	298.0	338.5	338.6	207.3	148.7	0.748
302.9	243.5	244.9	285.4	285.5	164.3	138.6	0.110
276.4	217.1	218.4	258.9	259.0	143.6	132.8	0.086
223.2	163.9	165.3	205.8	205.9	104.1	119.1	0.003
160.6	101.3	102.6	143.1	143.2	62.0	98.6	0.017
81.0	21.7	23.0	63.5	63.6	19.5	61.5	0.858
79.6	20.3	21.6	62.1	62.3	18.9	60.7	0.072
53.2			35.7	35.8	9.2	44.0	0.026

Table 7.4 - Spectral features for the Ba-133 source and further energies produced through interaction in specific detector materials.[129].

The relative rates of the peaks estimated from their branching ratios are given in table 7.4, but interactions between the source and the detector may change that rate significantly, with lower energy gammas being attenuated more. In this case the 81 keV line is the largest, but with the presence of the material around the cryostat this may drop below the rate of the higher energy 356 keV peak.

7.1.5 Simulations

To assess the contributions from the materials comprising the cryostat and the immediate detector surroundings, a Geant4 simulation was carried out for the detector inside the cryostat with a Cobalt 57 source placed outside the cryostat, as more material was added around the detector.

With an arrangement with a detector, a source and no background particles, the spectrum is clear with the two large photopeaks. A simulated detector resolution as in Eq. 7.5 was used, with values similar to those determined from the experiment (section 7.10).

$$\sigma = \sqrt{1.5^2 + 10^{-3}E + 10^{-6}E^2}\ ,$$ **Eq. 7.5**

where both the resolution and the energy are given in keV. The results of this simulation are presented in figure 7.5.

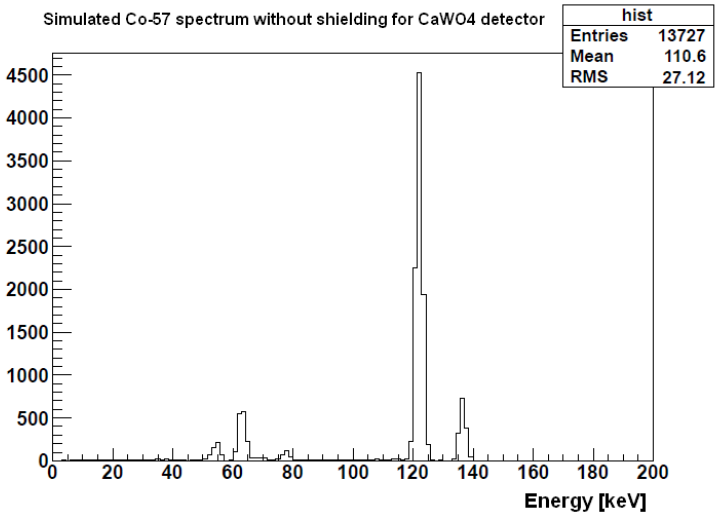

Figure 7.5 - Energy spectrum simulated in Geant4 with just the detector and a Cobalt-57 source. The peaks at 122 keV and 136 keV can be seen with their expected 1:9 ratio. At lower energies, there are the tungsten escape peaks for the 122 keV at ~63 and ~54 keV as well as the Kα escape at ~78 keV for the 136 keV peak.

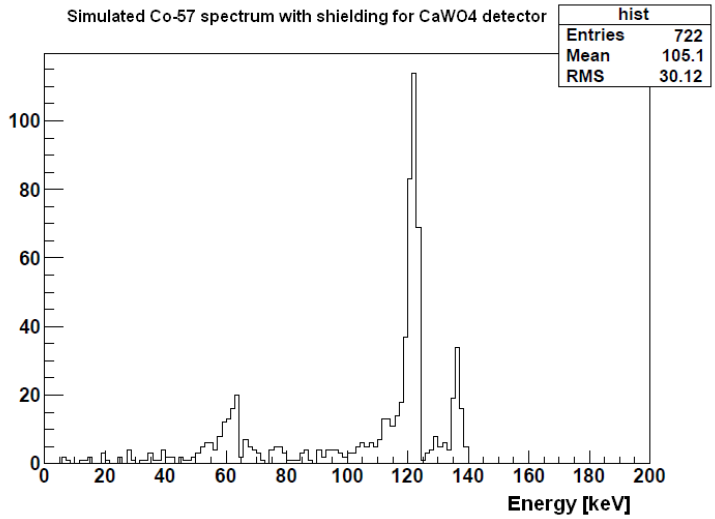

Figure 7.6 - Energy spectrum simulated in Geant4 with the experimental plate, calorimeter housing, cables and additional thermometry added. The relative rates of each of the peaks has changed, with the 136 keV peak now more prominent than before, while the higher amount of scattering in the material around the detector leads to a broad shoulder at the low energy side of each peak.

When copper shielding was placed around the detector, the rate of events decreased and the lower energy side of the peaks broadened out due to the higher proportion of scattered particles. The results of this simulation are shown in figure 7.6. The largest

effects on this coming from the detector housing and the IVC can. However, the peaks remained well defined therefore the detector can have shielding placed around it to reduce the background rate without ruining the resolution of the peaks from the Cobalt-57 source.

7.2 Detector Bias Modulation

The signal from the detector is recorded as a continuous modulated voltage signal of the form described in chapter 3. For further data processing, this modulation should be removed to give a processed signal proportional to the amplitude of the voltage across the NTD sensor.

The alternating signal can be divided into periodic units based on the switching points of the modulation. For each of these periods an amplitude value depending on the resistance of the NTD-Ge sensor can be determined, and the modulation thus removed. Taking a central baseline value, the modulus of the signal with respect to this baseline is summed up to give the area between the signal and the baseline.

For each pair of consecutive data points the algorithm calculates the area under the curve using the trapezium rule.

$$I = s \times \frac{|y[i] - c| + |y[i+1] - c|}{2}, \qquad \textbf{Eq. 7.6}$$

where s is the time between each sample in the signal.

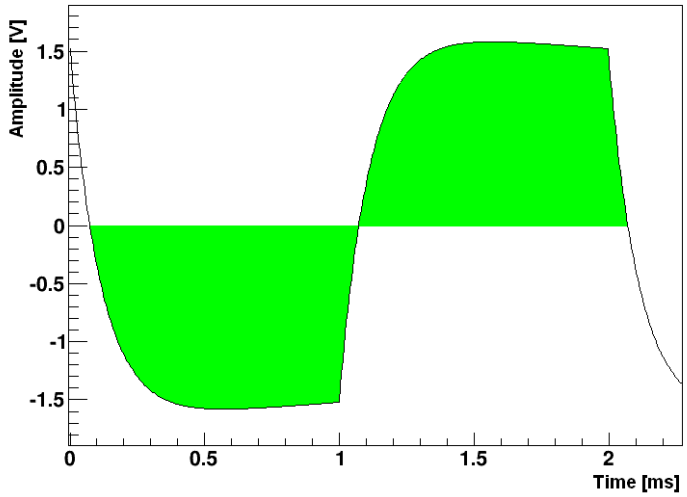

Figure 7.7 - the area between the signal and the baseline for a single period is shown in green for simulated data with a central value at zero.

At the switching points where the signal *y* crosses the central base line value, *c*, the crossing time, t_s, is estimated

$$t_s = t[i] + \frac{|c - y[i]|}{|y[i+1] - y[i]|} \times s \,.$$

Eq. 7.7

Then it is used with the trapezium rule to take account of the parts of the signal above and below the central value.

$$I = (t_s - t[i]) \times |y[i] - c| + (t[i+1] - t_s) \times |y[i+1] - c|$$

Eq. 7.8

The sum of these area slices is then divided by the time of the period to give the average amplitude for that section of the signal.

7.2.1 Central value

The value selected as the central baseline value *c* will have some effect on the output amplitude, increasing the calculated value beyond the actual size of the signal. This could cause problems when relating a change in the size of the signal to a change in the resistance of the detector.

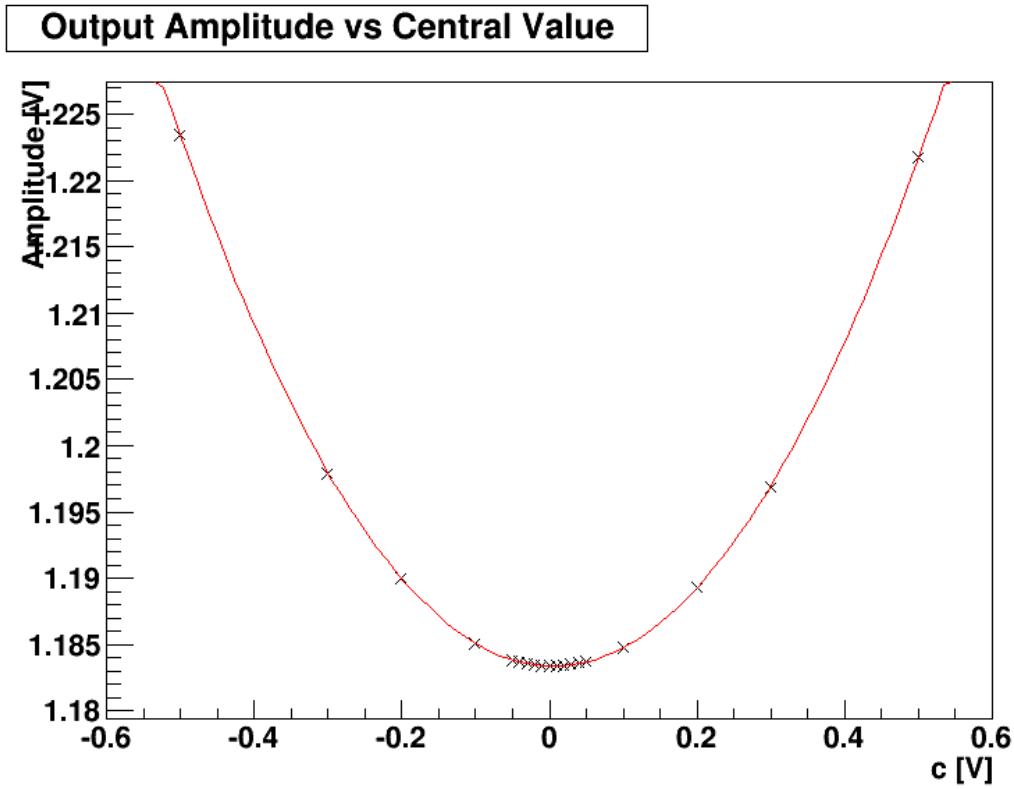

Figure 7.8 - The output amplitude calculated for a range of input central values. A quadratic function, shown as the red line, was fit to the data. The amplitude has a minimum value when the central value is equal to the d.c. offset on the signal, in this case c = 5.398 mV.

The optimum value of the central value will be when *c* is equal to the d.c. offset of the signal, as shown in figure 7.8. Offsets from the earlier stages of the readout will be reduced due to the hardware high-pass filter of the summing amplifier, but offsets from the final stages of the readout electronics will still be present. Typically this offset has a value around 10 mV or less.

These offsets may vary slowly over time, as in figure 7.9, so choosing a fixed value is not appropriate, as these variations in offset could be presented as variations in the NTD resistance. With the symmetric signal one could simply average over a number of periods and let the contributions from either half of signal cancel to give the d.c. offset, but this method also has issues – the presence of a pulse within these periods will cause the signal to become asymmetric, dragging the average away from the true

d.c. offset. Taking a longer segment of data for this average reduces the distorting effect of these pulses, but includes more of the offset fluctuations.

However, the fluctuations of the offset are slow compared to the ~328 ms long records in which the data is stored. Therefore a single calculation of the d.c. offset can be made for each of these records by finding a short region within the record which is free of pulses and other distortions. A set of six periods is averaged and the r.m.s of the signal about the average is found. The region with the lowest r.m.s is selected to give the value of *c* for that record.

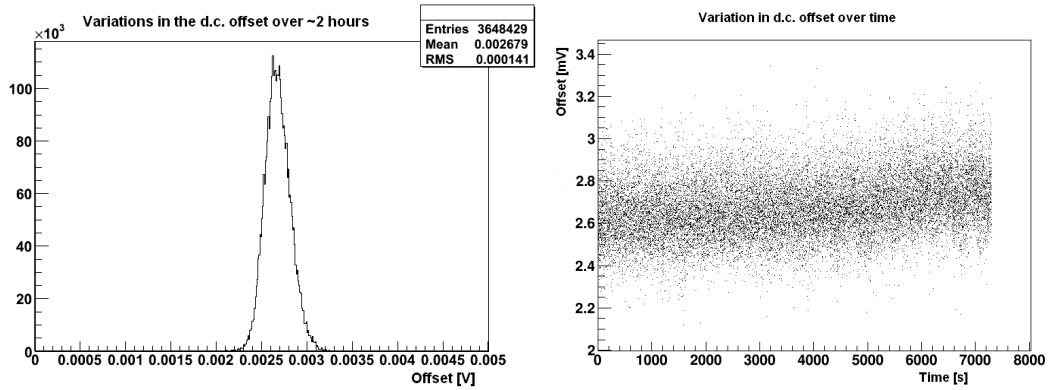

Figure 7.9 – a typical example of the distribution of d.c. offset values over a period of approximately two hours.

7.2.2 Amplitude

The amplitude output by the integration does not depend linearly on the resistance of the sensor, but instead has some dependence on the shape of the signal. This is particularly affected by the RC time constant of the NTD resistance and the parasitic capacitance, as in figure 7.10 which shows the results of simulations for different capacitance values. Therefore, for an accurate measurement of the operating resistance (and hence operating temperature), the method described in section 4.3 is best – using a fit to take account of the time constant.

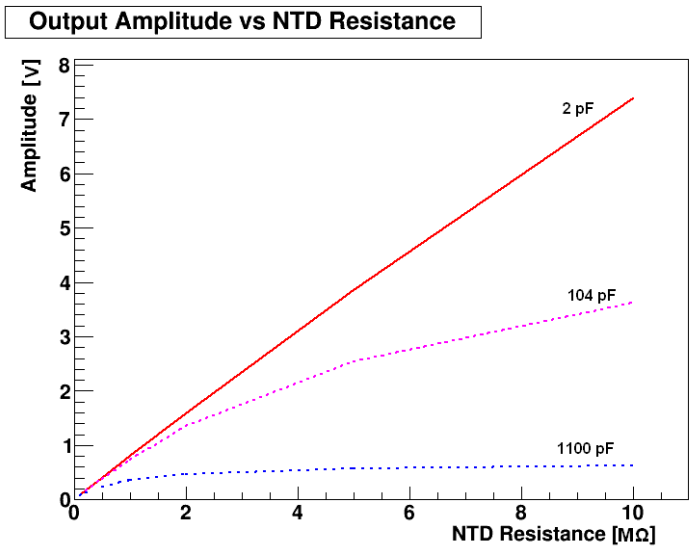

Figure 7.10 - the amplitude of the integration for simulations of a range of resistance and parasitic capacitance values.

7.2.3 Pulse heights

For small changes, like the pulses from the ~100 keV test sources which typically give a voltage change ~ 5 mV, the variation will be linear, as in figure 7.11.

This linearity for the amplitude and the pulse heights can be improved by reducing parasitic capacitance and by using the pole cancellation method to adjust for the time constant, as described in chapter 2.

7.2.4 Sampling frequency

The demodulated signal created by this process will occur at a much lower frequency (the modulation frequency (~ 1kHz) than the sampling frequency of the original signal (~ 100 kHz). Therefore the resolution in time that can be achieved will be decreased, and identifying short timing parameters such as the rise time, which have values similar to that of the new sampling period, may become difficult. To improve the timing resolution as high a modulation frequency as possible should be used, taking into account the limitations due to the parasitic capacitance.

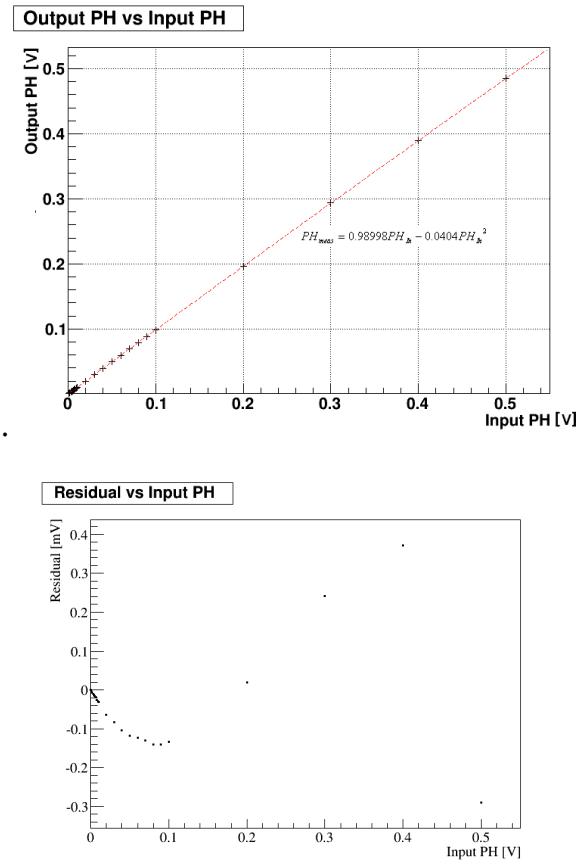

Figure 7.11 - the measured pulse height versus the input pulse height for simulations with a 1MΩ resistor and 100 pF parasitic capacitance. A polynomial fit was carried out; giving a result that was close to linear for the pulse heights from the sources used to test these detectors.

7.3 Filtering

There are electronic filters built into the hardware. These include the low pass Bessel filter with a cut off frequency at 25.6 kHz for anti-aliasing, and the high pass filter in the summation stage of the read out with a relatively long time constant (~30 s).

Once the modulation has been removed from the signal, further filters can be applied to the data using the analysis software.

7.3.1 Low pass filter algorithm

In the frequency domain, a simple low pass filter has the form

$$O(\omega) = \frac{1}{1 + j\omega\tau} \times I(\omega).$$

Eq. 7.9

This has an exponential impulse response; the output signal for a delta function on the input will be an exponential decay with a time constant of τ. In the time domain the filter can be written as

$$O(t) + \tau \frac{d}{dt} O(t) = I(t),$$

Eq. 7.10

where the solution is

$$O(t) = I(t) e^{-t/\tau}.$$

Eq. 7.11

For a series of discrete data points (such as the signal from the detectors), the form of the filter can be given by a convolution of the input signal and an exponential weighting function α related to the sampling frequency of the signal

$$\alpha = e^{-\Delta S/\tau},$$

Eq. 7.12

where the time interval between consecutive points is ΔS and the time constant of the filter is τ. So that, with the input of the filter as $I[i]$ and the output as $O_{LP}[i]$, the output of the low pass filter is

$$\begin{aligned} O_{LP}[i] + \frac{O_{LP}[i] - O_{LP}[i-1]}{\omega \Delta S} &= I[i] \\ O_{LP}[i] = I[i] \frac{\omega \Delta S}{1 + \omega \Delta S} &+ O_{LP}[i-1] \frac{1}{1 + \omega \Delta S} \end{aligned}.$$

Eq. 7.13

This form can be expressed as the recurrence relation

$$O_{LP}[i] = (1 - \alpha) I[i] + \alpha O_{LP}[i-1].$$

Eq. 7.14

7.3.2 High pass filter algorithm

In the frequency domain, the formula for a high pass filter is similar to that of the low pass filter. They can be related by

$$\frac{j\omega\tau}{1 + j\omega\tau} = 1 - \frac{1}{1 + j\omega\tau}.$$

Eq. 7.15

This allows for the low pass filter algorithm to be adapted into an algorithm for a high pass filter.

$$O_{HP}[i] = I[i] - O_{LP}[i]$$

Eq. 7.16

7.3.3 Application

The application of a high pass filter to the signal will reduce the effects of low frequency fluctuations of the signal, providing a more stable baseline for the pulses, as in Fig 7.12. However, this may remove the fluctuations of the baseline due to changes in the operating temperature of the detector. The change in the responsivity of the detector will still need to be taken into account, so some measure of the NTD Ge resistance from the unfiltered data will be required – hence why the de-modulation and filtering is carried out in software as opposed to hardware.

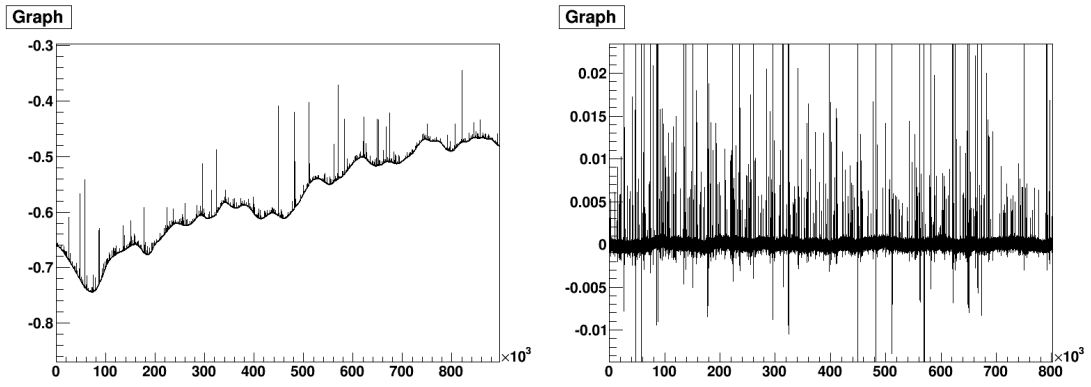

Figure 7.12 – On the left is the unfiltered signal for a section of data, while on the right is the same data after a high pass filter with a time constant of 1000 ms is applied. The longer term change in the signal is removed, just leaving the pulses on a relatively flat baseline.

The high pass filter will also change the shape of the pulses, giving a narrower peak followed by an overshoot, as in Fig 7.13. For a simple pulse of the form described in Chapter 5, with a rise time constant and two decay time constants, the high pass filter changes this with the addition of another time constant to the form.

$$y = A_1 e^{t/\tau_1} + A_2 e^{t/\tau_2} + A_3 e^{t/\tau_3}$$
$$y = \frac{A_1}{1 + j\omega\tau_1} + \frac{A_2}{1 + j\omega\tau_2} + \frac{A_3}{1 + j\omega\tau_3}$$

Eq. 7.17

Applying the high pass filter with a time constant τ_h to get a new signal *y'*.

$$y' = \left(\frac{A_1}{1 + j\omega\tau_1} + \frac{A_2}{1 + j\omega\tau_2} + \frac{A_3}{1 + j\omega\tau_3}\right)\left(\frac{j\omega\tau_h}{1 + j\omega\tau_h}\right)$$
$$y' = \left(\frac{A}{1 + j\omega\tau_1} + \frac{B}{1 + j\omega\tau_2} + \frac{C}{1 + j\omega\tau_3}\right)\left(1 - \frac{1}{1 + j\omega\tau_h}\right)$$

Eq. 7.18

Taking each part of this separately, for example with the first term in equation 7.19, the high pass filter term can be rearranged using partial fractions.

$$y'_A = \left(\frac{A}{1 + j\omega\tau_i}\right)\left(1 - \frac{1}{1 + j\omega\tau_h}\right)$$
$$y'_A = \frac{A}{1 + j\omega\tau_i} - \frac{A}{(1 + j\omega\tau_i)(1 + j\omega\tau_h)}$$
$$y'_A = \frac{A}{1 + j\omega\tau_i} - \frac{A_2}{1 + j\omega\tau_i} - \frac{A_3}{1 + j\omega\tau_h}$$

Eq. 7.19

where the constants A_2 and A_3 are given by

$$\frac{A_2}{1 + j\omega\tau_i} + \frac{A_3}{1 + j\omega\tau_h} = \frac{A_2 + A_3 + j\omega(\tau_h A_2 + \tau_i A_3)}{(1 + j\omega\tau_i)(1 + j\omega\tau_h)}$$
$$= \left(\frac{\tau_i}{\tau_i - \tau_h}\right)\left(\frac{1}{1 + j\omega\tau_i}\right) + \left(\frac{\tau_h}{\tau_h - \tau_i}\right)\left(\frac{A_3}{1 + j\omega\tau_h}\right)$$

Eq. 7.20

Therefore, as in equation 7.21, the high pass filter leaves the original exponential time constants (with some change in amplitude) and adds an additional term with the time constant of the filter.

$$y'_A = \left(1 - \frac{\tau_i}{\tau_i - \tau_h}\right)\left(\frac{A}{1 + j\omega\tau_i}\right) - \left(\frac{\tau_h}{\tau_h - \tau_i}\right)\left(\frac{A}{1 + j\omega\tau_h}\right).$$

Eq. 7.21

This will be important later in the chapter, when pulses (both raw and filtered) are fit to such exponential forms to find their pulse height. Understanding the effect of the filter on this form allows for the different fitting parameters to be compared between different fits and treatments of the data.

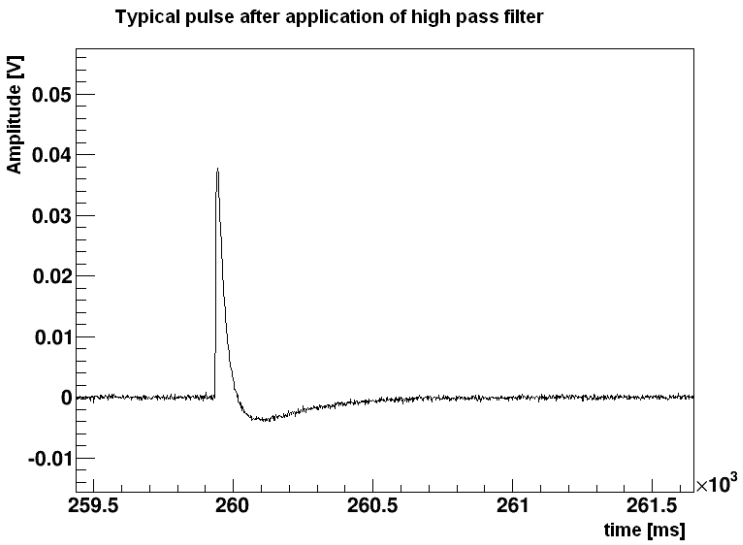

Figure 7.13 – 122 keV pulse in a high pass filter of 1000 ms.

A low-pass filter can be used to limit the bandwidth and reduce the contribution from high-frequency noise on calculations of amplitude or other pulse parameters. The implications of this for different methods of measuring the pulse height will be covered in more detail later in the chapter.

7.4 Trigger

With the raw data converted into a new form by the removal of the modulation and by filtering, the next step in the analysis is to identify where pulses are in the data so that their energies can be determined. The data is recorded without a trigger in the hardware, so it is stored as a continuous stream of data separated into consecutive records of fixed length. An offline trigger in the analysis software must therefore be used instead. For a full analysis of both the light detector and the phonon detector the triggering of both should be combined so that a correlated analysis can be carried out. The small amount of scintillation light emitted by the absorber crystal in the phonon detector means that the corresponding pulses in the light detector will be small and

could be missed, therefore the time of these events should be identified using the phonon detector.

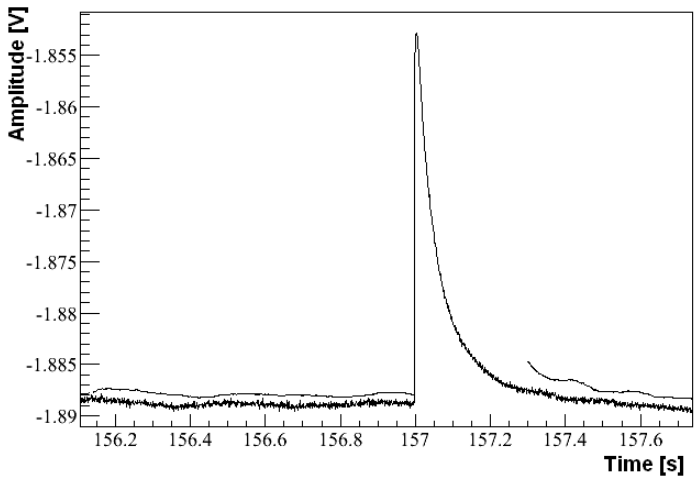

Figure 7.14 - a section of the signal with the threshold also plotted. This threshold was set as the calculated baseline plus five times the r.m.s of the baseline. When the pulse at 157.0s triggers a section of the data 300ms long is selected, to calculate the pulse parameters in.

The trigger for the phonon detector is done by setting a threshold above the level of the baseline and looking at the region of the signal between when it crosses this threshold and either falls back below a second threshold or remains above for a fixed amount of time, as in Fig. 7.14. The level of the trigger threshold is set by calculating the average position of the baseline and the size of the baseline noise in the previous data – a 70 ms section of the data that ends 15 ms before the point of interest is used. A least squares fit is carried out using a linear function for the baseline (described further in 7.5.1) giving a value for the position of the baseline and the r.m.s of the baseline noise.

Two cut-off values are then set; one for the beginning of a pulse where the signal rises above the first threshold value *th1* and a second at the end where the signal falls back below the second threshold value *th2*. Typically *th1* and *th2* might be set to 5 and 3 times the r.m.s above the baseline value. If the signal does not fall below *th2*, then the

pulse is ended after 300 ms. This section of data is then used to calculate the initial estimates of the pulse parameters, as in section 7.5.

7.5 Initial parameters

The final estimate of the energy for each pulse will be made with the fitting of a function to the pulse. However an initial estimate of the pulse amplitude and other parameters describing the pulse shape can be calculated by looking for where the signal meets various threshold values. This allows for any unreliable or spurious pulses (typically due to pile up or instabilities in the operating point) to be removed from the shortlist used to find the fitting parameters.

Firstly the baseline in the region of the pulse can be characterised with the values calculated in the previous section, by a least squares fit of a linear function to the baseline in a 70ms region before the pulse. The result of this fit can be extrapolated to estimate the baseline throughout the pulse and the r.m.s of the fit can be used as a measure of the baseline noise.

Next, a measure of the size of the pulse can be made. The simplest method for this is to find the maximum point of the signal and use the difference between this and the baseline. However, this will be dependent on the noise of the signal and is likely to give an over-estimate. Alternative methods include an integral over the entire pulse and using a low pass filter to smooth out the data, but these also have limitations and may not give a suitably accurate value of the amplitude.

To remove pulses for which the calculated amplitude may not be a good indication of the energy, the shape of the pulse can be investigated and used to exclude pulses which do not show the expected form.

7.5.1 Baseline

A section of the baseline from 15 ms before the maximum of the pulse is used to calculate the baseline of the signal, as in figure 7.15. This should be roughly constant, but may vary slowly due to fluctuations of the temperature bath or the tails of earlier pulses.

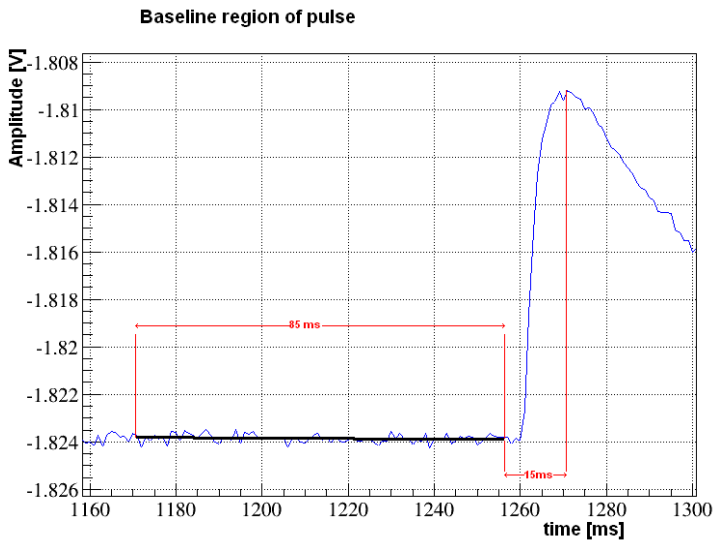

Figure 7.15 - The baseline fit for a pulse.

A constant value would therefore give an overestimate of the baseline noise, as in figure 7.16, through its r.m.s value, and lead to miscalculated pulse parameters if extrapolated through the rest of the pulse. With the exponential tails of earlier pulses being so common, the baseline should have an exponential shape, however the variation of the baseline should be small enough that a linear fit to the baseline is sufficient.

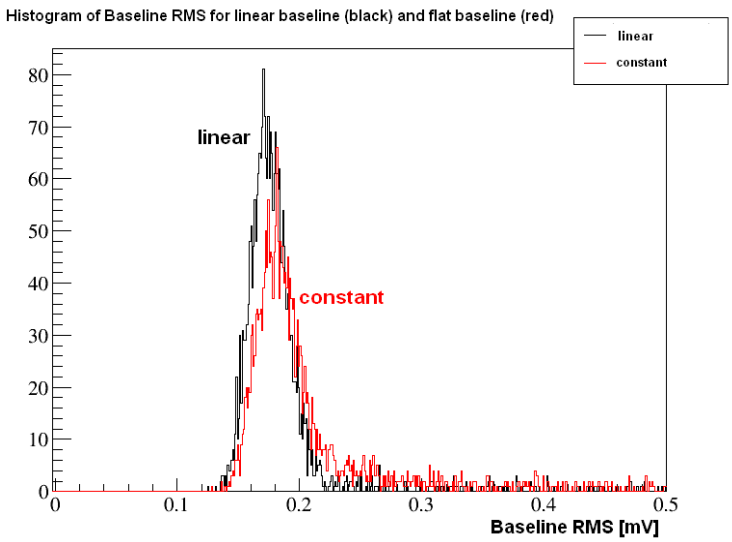

Figure 7.16 - Histogram of Baseline RMS values for a list of pulses, first calculated with a flat baseline (plotted in red) then for a linear baseline (in black).

The Baseline RMS naturally has a Gaussian distribution due to the noise, but due to the assumption of the baseline shape there will also be a tail of large values, where the baseline has been poorly modelled due to its fluctuations. Using the linear fit instead of the flat value reduces the number of these high RMS events.

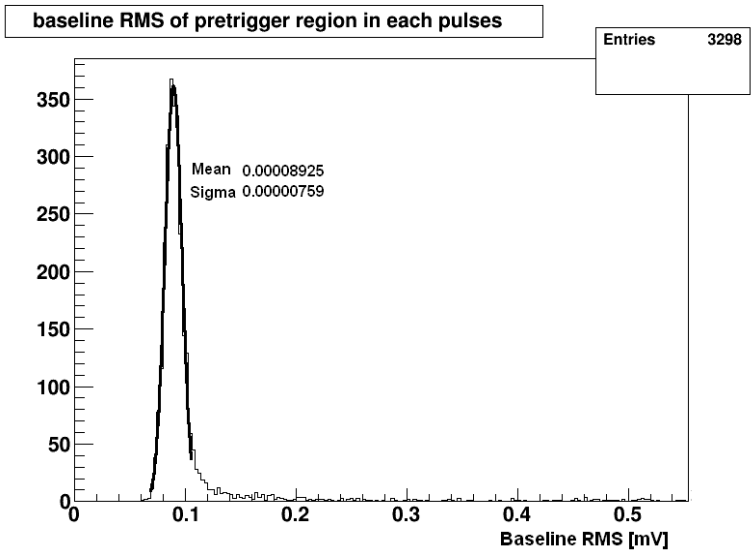

Figure 7.17 - The RMS of the linear fit to the baseline region. It gives a Gaussian peak at 0.089 mV, with a tail extended to high energies, due to pile up or other instabilities in the baseline region before the pulse.

The change in the baseline level across the data may also be calculated by taking the average of a 15ms region at the start and at the end of the triggered data, and using the difference between the two.

7.5.2 Amplitude

The energy deposited in the detector to form the temperature pulse can be estimated using the maximum value of the pulse. To calculate this, the maximum point of the signal is found and the estimated baseline value at that time subtracted – hence the importance of including any gradient in the fit of the baseline. If the maximum of the raw data is taken, the calculated value of the pulse height will be dependent on the noise and the positions of single data points near the peak leading to overestimations of the pulse height. This effect could be reduced by using a low pass filter or moving average to smooth out the noise fluctuations, but this has the effect of underestimating the pulse height, as in figure 7.18.

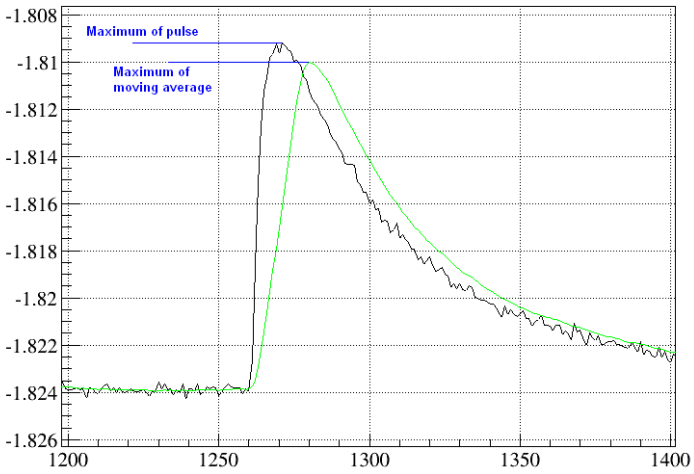

Figure 7.18 - the demodulated signal for a pulse with and without a sixteen point moving average applied. Without this, the pulse height may be overestimated due to the noise of the signal, while with it, the pulse height may be underestimated due to the relatively narrow peak.

Alternatively the size of the pulse can the estimated by calculated the area between the pulse and the baseline. This too will describe the amplitude of the pulse, but it has a different dependence on the shape of the pulse.

Ultimately the amplitude will be estimated using an exponential fit of the pulses, but this will require a clean set of pulses of similar height to calculate the initial parameters of the fit, hence these methods with obvious limitations remain useful.

7.5.3 Timing

To look for coincident pulses in the light detector and the phonon detector, such as figure 7.19, the timing of the pulses in each channel can be compared. To achieve this, the position of the peak in each detector is recorded and compared.

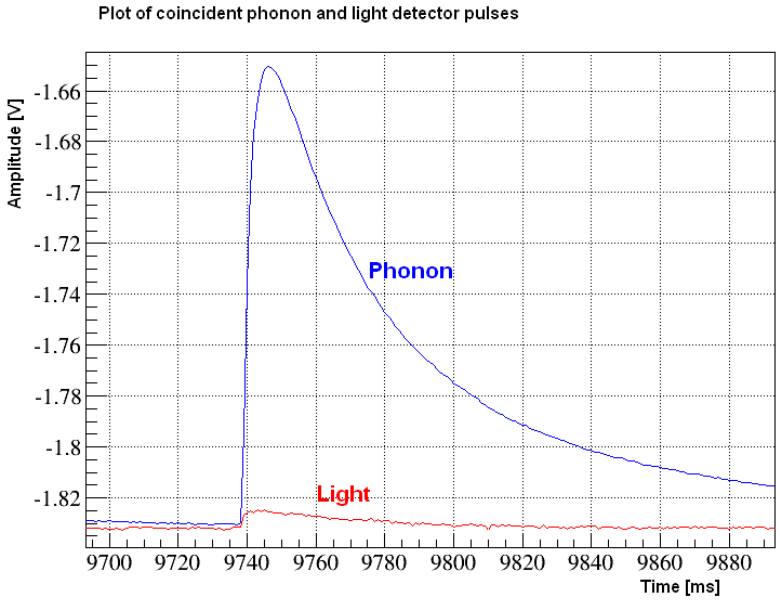

Figure 7.19 - Coincident pulses on the phonon and light detectors for an interaction with energy of several MeV.

The amount of scintillation light given out is relatively small compared to the energy that can be measured as phonons, so the pulse on the detector will be small compared to that on the phonon detector. As such, the trigger is set on the phonon detector and the initial analysis is independently carried out on the selected region for both detectors.

This gives the pulse height and position, and the other parameters described in this section. However, the pulse height on the light detector channel is small and could be hidden by the noise of the detector, or ignored if the maximum on the signal belongs to another source, such as a fluctuation of the baseline or a direct hit on the light detector. To remove these, the time difference between the two pulses can be investigated. If the difference between the two times is within one or two ms (the

time resolution set by the demodulation prevents further precision) the pulses are accepted as a coincidence and plotted.

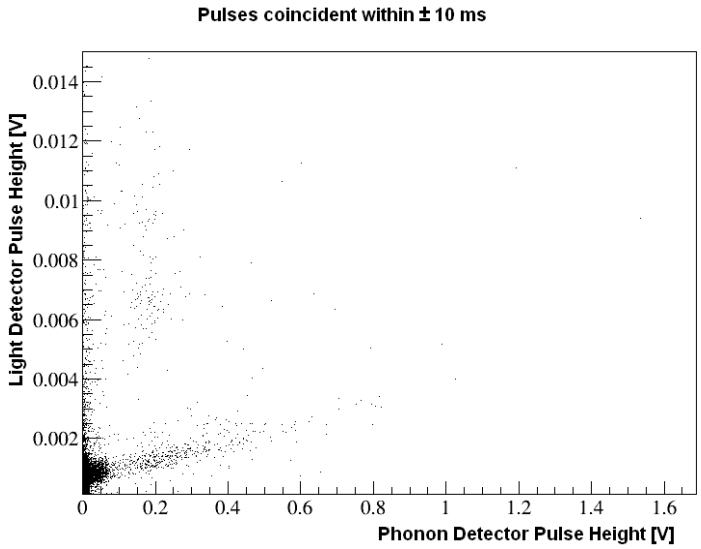

Figure 7.20 - Plot showing pulses coincident on the light detector within ± 2 ms.

The small pulse height of the light detector is greatly affected by the overestimating of the pulse due to noise fluctuations, as described in section 7.5.2. This gives an offset in the pulse height measurements of the light detector, as shown in 7.20, and prevents the relation between phonon detector pulse height and light detector pulse height going through zero. The pulse fitting in the next stage of analysis gives improved the determination of pulse height and solves this issue.

7.5.4 Pulse shape

To identify pulses where a calculation of the amplitude may not provide an accurate energy value for a real particle interaction, the shape of the pulses can be investigated. For now it is assumed that the pulse has a simplified two exponential form,

$$y = A\left(1 - e^{-t/\tau_R}\right)e^{-t/\tau_F}. \qquad \textbf{Eq. 7.22}$$

Time constants can then be calculated for the rise time τ_R and the decay time τ_F of the pulse by setting threshold levels at 1/e of the pulse height, as in figure 7.21.

The decay time threshold is set at

$$threshold_D(t) = baseline(t) + \frac{1}{e}\, pulseheight\ ,$$

while the rise time threshold is set at

$$threshold_R(t) = baseline(t) + \left(1 - \frac{1}{e}\right) pulseheight\ ,$$

with their initial times taken as the peak position and the trigger respectively.

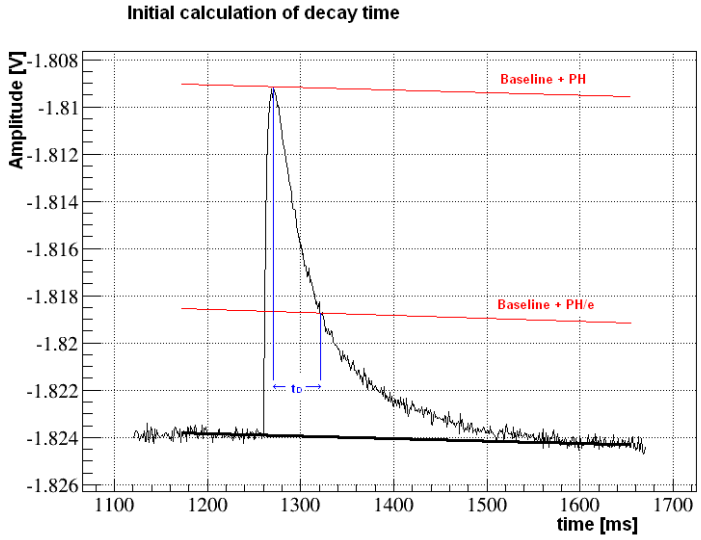

Figure 7.21 - Plot of a pulse showing the extrapolated linear baseline (black) with the decay time constant threshold in red.

The calculations of these time constants are limited by the time resolution of the de-modulated data and, as in Chapter 5, the pulses will be properly described by a more complex model containing additional exponential terms, but these quick estimates will allow for the easy identification of spurious events before a more complete analysis is carried out.

The area underneath the signal and the pulse height may also be compared to give another indication of the pulse shape. The ratio of the area under the signal to the pulse height can also be measured, giving another indication of the pulse shape.

$$IOPH = \frac{\sum_{i=i_{\max}-n2}^{i_{\max}+n3} y[i] - baseavg}{y[i_{\max}] - baseavg},$$

Eq. 7.23

where i_{max} is the peak position, *n2* is 15 and *n3* is 300.

Another parameter, known as the pile up ratio, is used to find secondary peaks within the event. Moving away from the peak (in either direction), local minima are searched for and the size of the secondary peak which follows them recorded. In an event with no pile up the size of this apparent secondary peak will simply be the size of the noise on the signal, therefore the size of this peak is given in a ratio with the baseline r.m.s.

7.6 Cuts

So that the exponential fit can be carried out, a clean set of pulses needs to be found by using the calculated pulse parameters as criteria for the removal of pulses from the data set. These pulses, which may give a misleading result for the energy of the interaction, may be

1. Baseline fluctuations – in which the fluctuations in the level of the baseline, for example due to the tail of an earlier pulse, may cause inaccuracies in the pulse height estimation and changes in the responsivity of the detector.

2. Baseline noise – in which the trigger occurs on the noise of the baseline.

3. Pile up – in which multiple interactions have occurred close together, giving a superposition of the pulse shapes.

Each of these problems can be reduced by other methods – reducing the background rate and the decay time constant of pulses, setting a higher trigger level, and the

temperature stabilisation of the detector, but they cannot be removed entirely. To remove these from the shortlist of pulses, cuts are therefore essential.

7.6.1 Baseline gradient

The fit to the 85 ms long baseline region before the pulse provides a value for the gradient of the baseline. This parameter provides one criterion for identifying fluctuations of the baseline level.

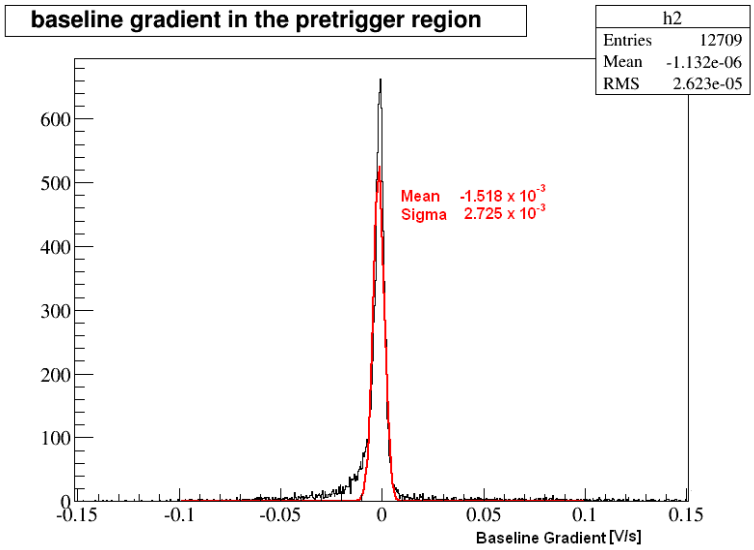

Figure 7.22 – Histogram of the baseline gradient with a Gaussian fit overlaid in red.

The distribution, shown in figure 7.22, has a roughly Gaussian shape, with a tail of negative values due to the tails of earlier pulses. The mean value will be close to zero, but is likely to be slightly negative for these detectors due to the rate of pulses. By making a cut at one sigma about the mean value of the gradient many of these pulses can be removed.

7.6.2 Pile up ratio

This finds secondary peaks within the pulse and can therefore be used to find events than contain pile up. Th distribution, in figure 7.23, shows a large peak at low values corresponding to the noise on the signal, with a broad range of larger values corresponding to pile up events. A cut at three sigma about zero is used to remove the pile up.

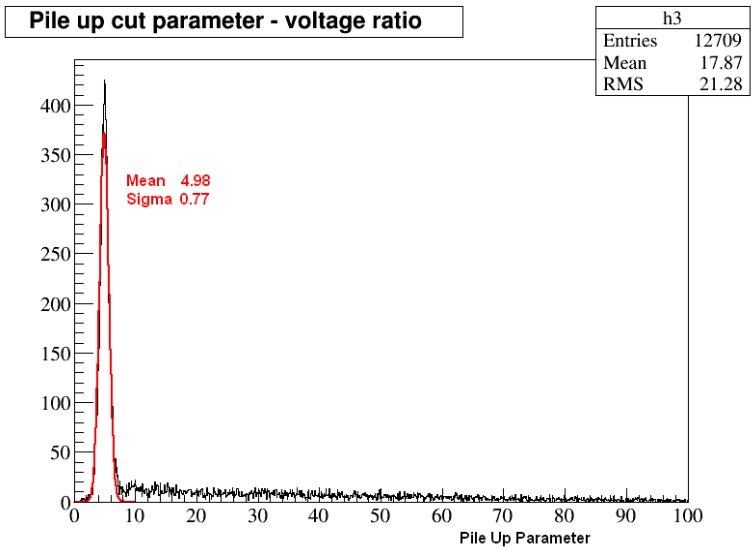

Figure 7.23 - Histogram of the pile up parameter.

7.6.3 Rise time

The rise time of good pulses will be small, with a typical value ~4 ms as in Fig 7.24, but distorted pulse shapes may provide values much larger than this while triggers in the baseline noise may give smaller values. A cut is made at two sigma on either side of the mean.

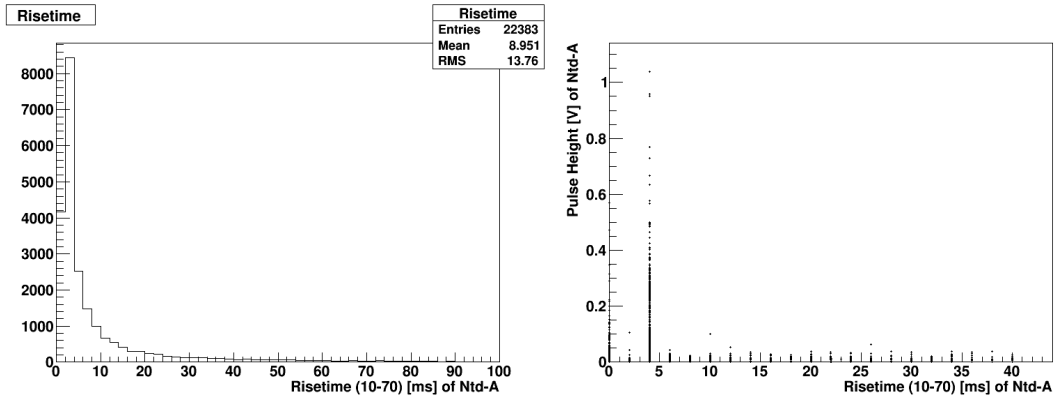

Figure 7.24 - A histogram of the rise time and a plot of the rise time versus pulse height.

The rise time seems to be more or less constant with pulse height, with the values outside of the narrow peak at ~4 ms belonging to events where noise or other distortions have affected the pulse shape.

7.6.4 Right minus left

Similar to the baseline gradient, this allows events with large fluctuations of the baseline to be found. The average value of the signal is calculated at both ends of the selected region, and the difference between the two values found. A cut can be made to the distribution, such as figure 7.25, at two sigma on either side of the mean to remove these events.

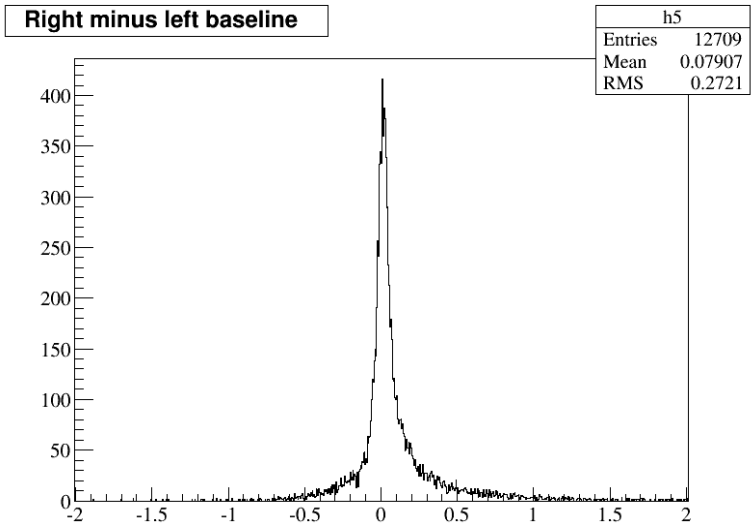

Figure 7.25 - Histogram of Right - Left of Baseline

7.6.5 Baseline rms

The baseline r.m.s is described in section 7.4.1, and using this result – events with a poorly fit baseline can be removed. These might include events with pile up or with excessive baseline fluctuations. Events with a baseline r.m.s of more than two sigma above the mean are removed.

7.6.6 Integral over pulse height

This is the ratio of the area under the pulse to the maximum pulse height. For the standard pulse shape this should have roughly the same value regardless of the amplitude of the pulse, therefore this can be used to identify pile up events, where the area under the signal should be larger than expected for that pulse height. The

distribution in figure 7.26 shows a peak at ~60 with a broad range of other events about this. A cut is made at three sigma above the mean.

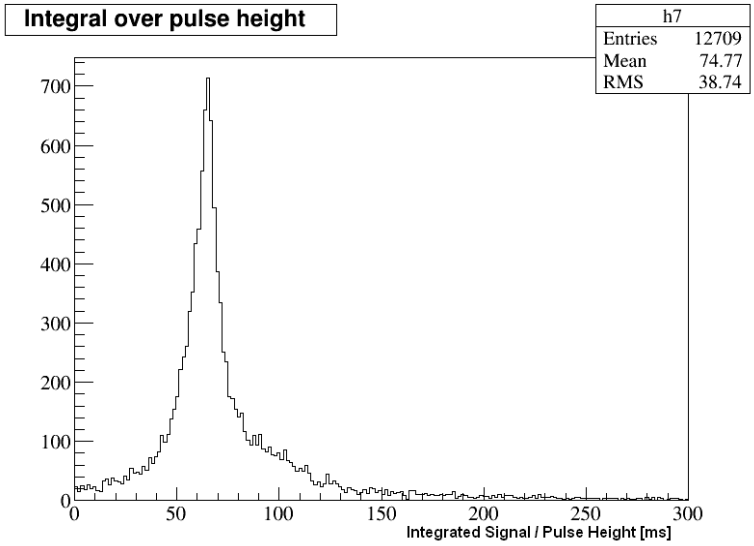

Figure 7.26 - Histogram of the integral over the signal divided by the pulse height for a complete list of events.

7.6.7 Decay time

As in equation 7.24 the pulses are best described by multiple exponential decay times, but a first approximation can be made by calculating a single decay time constant for the pulse. Using threshold levels, as in Fig. 7.21, this single measurement gives the time for the pulse to drop from its maximum pulse height to 1/e of that value. The time constant allows for the separation of good pulses, which will give accurate measurements of the energy, from distorted pulses, baseline fluctuations or noise which will not.

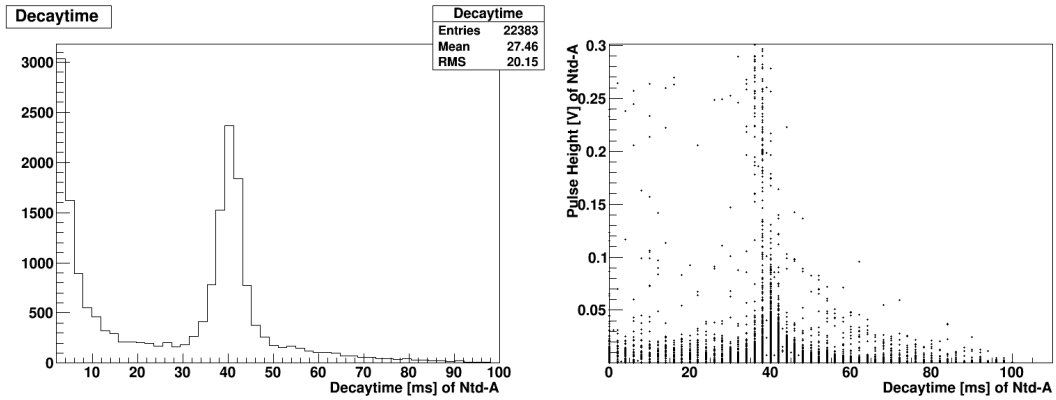

Figure 7.27 - A histogram of the decay time, and a plot of the decay time versus pulse height.

Fig. 7.27 shows the distribution of decay times with two maxima – one exponentially dropping off from zero, and the other around 40 ms. As with rise time the second peak remains roughly constant with pulse height and broadens out for the low amplitude pulses where noise and other effects start to distort the pulse shape.

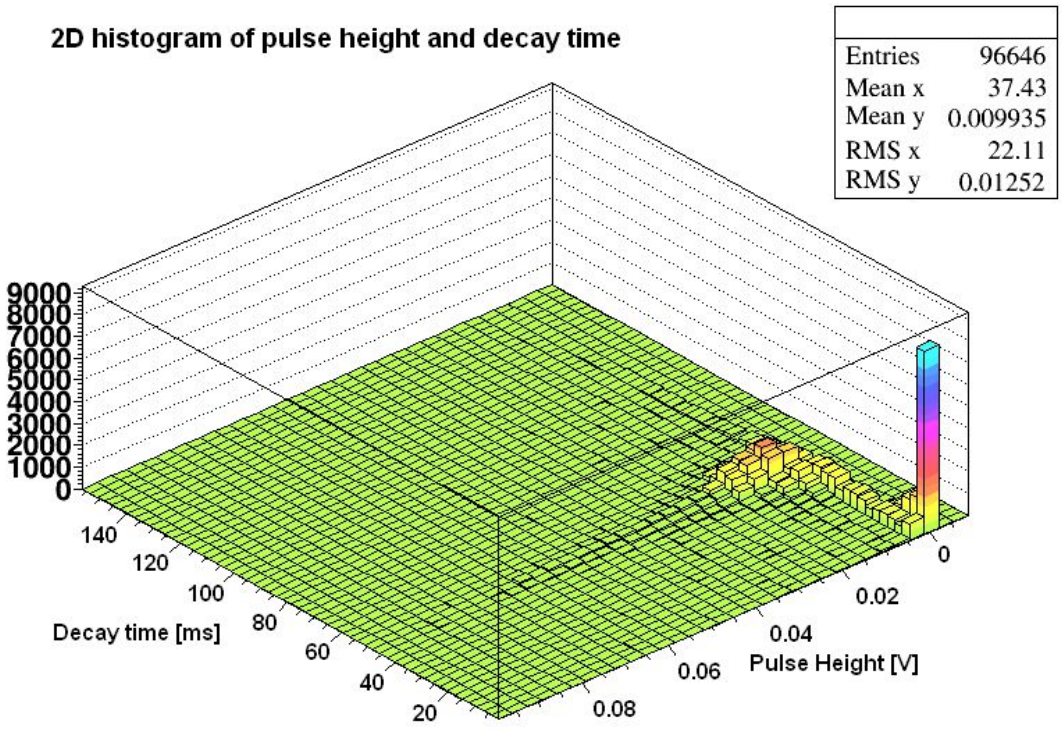

Figure 7.28 – 2D histogram of pulse height and decay time for the data shown in Fig. 7.27.

7.6.8 Effect of cuts

Cuts on these parameters, as in the list of cuts in table 7.5, are used to create a clean list of events from which a template fit can be made. The distribution of each of these parameters is similar for both the light detector and the phonon detector, but the light detector events are considerably smaller in amplitude. This relatively low signal to noise ratio means that the light detector cuts are relatively strict – this is not a problem for making the template fit, but these events should be reinstated for the final pulse fitting. By removing these non-ideal pulses, the spectrum of energies produced by the analysis will be a more accurate reflection of the true energies and the pulse template formed from the list of pulses will be improved.

Cuts	Lower	Upper
Baseline gradient	$-\sigma$	σ
Pile up parameter	N/A	$\mu + 3\sigma$
Rise time constant	N/A	$\mu + 2\sigma$
Right - left of baseline	$\mu - 2\sigma$	$\mu + 2\sigma$
Baseline r.m.s	N/A	$\mu + 2\sigma$
Integral / Pulse Height	$\mu - 3\sigma$	$\mu + 3\sigma$
Decay time constant	$\mu - 3\sigma$	$\mu + 3\sigma$

Table 7.5 – the cuts used to form the template pulse list.

A histogram of pulse height without these cuts, such as figure 7.28, shows the major features expected, but these features may be broadened due to these various problematic pulses and show a resolution worse than that expected from the baseline noise of the signal.

With the application of these cuts to the data, many of the events with poorly calculated parameters are removed giving much narrower peaks as in figure 7.29. The number of these pulses may be significant, as in Table 7.6, reducing the list of pulses to almost a quarter of its original length. However the removal of these events is required to make a very clean list of pulses so that a good template pulse can be made and initial fitting parameters calculated for the full list of pulses.

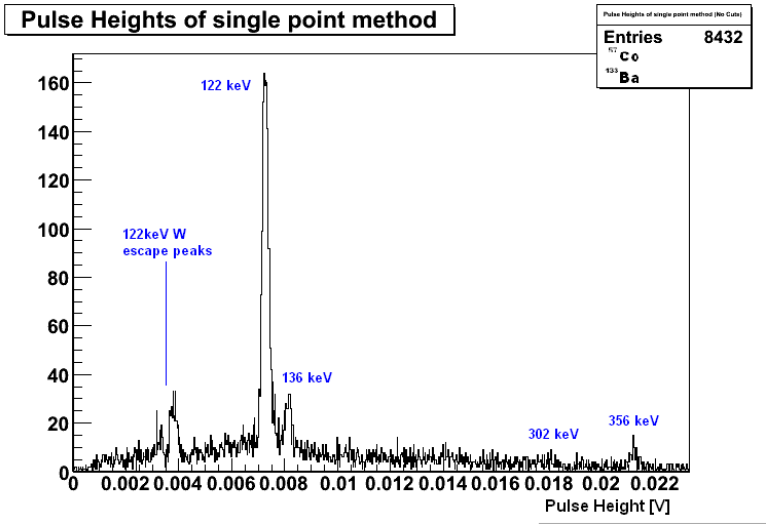

Figure 7.28 - Pulse Height spectrum before cuts have been carried out, with some of the most prominent peaks labelled. At this point, the resolution at 122 keV is ~7 keV.

For the fitting to individual pulses so that the energy can be calculated, some of these cut pulses may be reinstated. Some pulses, particularly those with large baseline gradients may produce a distorted template pulse and need to be removed for that purpose, but could still give an accurate measurement when the pulse is individually fit and the slope of the baseline accounted for. Events for which the fit is poor can then still be cut by using the quality of the fit.

Cuts	Phonon Detector		% remaining
	Lower	Upper	
Baseline gradient	$-\sigma$	σ	48.7%
Pile up parameter	N/A	$\mu + 3\sigma$	59.3%
Rise time constant	N/A	$\mu + 2\sigma$	92.9%
Right - left of baseline	$\mu - 2\sigma$	$\mu + 2\sigma$	54.4%
Baseline r.m.s	N/A	$\mu + 2\sigma$	78.0%
Integral / Pulse Height	$\mu - 3\sigma$	$\mu + 3\sigma$	58.2%
Decay time constant	$\mu - 3\sigma$	$\mu + 3\sigma$	84.9%
Combined			26.5%

Table 7.6 – the cuts used with a phonon detector and their effect on the amount of events for a typical set of data. Some of these events may be removed by more than one of the cuts.

Some of the cuts may remove similar types of pulses – for example, 'right – left of baseline' and the 'baseline gradient' cuts provide a similar function by removing events with excessively sloping baselines, while the ratio of the integral over the pulse

to the pulse height and the pile up ratio both remove pile up events where the presence of a secondary peak distorts the pulse shape.

Few events are cut on the 'rise time' cut, as it only considers the upper limit. This would mostly just act on some pile-up events, where a smaller pulse provides the trigger and a second larger pulse provides the peak position. This is only a small amount of the pile-up events detected.

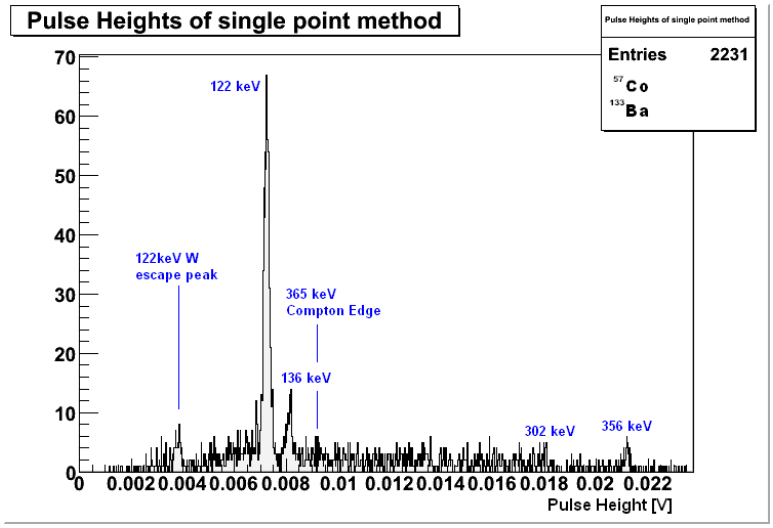

Figure 7.29 - Pulse Height spectrum after cuts have been carried out, with some of the most prominent peaks labelled.

7.7 Pulse template

With the list of pulses cleaned up by the cuts in section 7.6 and a rough estimate of the pulse height made, an average pulse shape can be determined for a particular energy and used to find rough values of the time constants for the exponential pulse shape. These will later be used as initial parameters for a complete fit of individual pulses over the full range of energies.

The pulses in the small energy range selected are averaged together to give an average pulse shape, as in figure 7.30. To ensure a large number of events are used, a histogram of the pulse height is made and the peak bin chosen as the energy range.

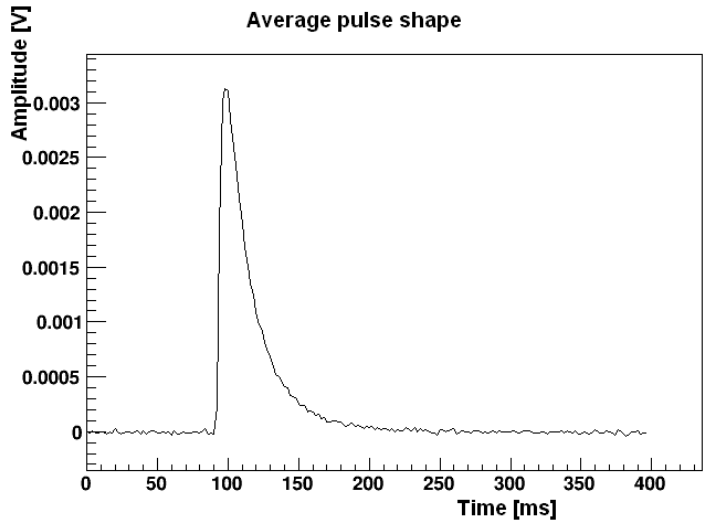

Figure 7.30 - the averaged pulse shape for events with energies near 122 keV (in the bin 3.125 mV to 3.150 mV).

This average pulse shape can then be fit using the theoretical form of the pulse shape. This has an amplitude of y as

$$y = (p_6 + p_9 \times i) + p_8 \times \left(-e^{p_0 + p_1 \times i} + e^{p_2 \times p_3 \times i} + e^{p_4 + p_5 \times i}\right) \text{ for } i \geq p_7$$

Eq. 7.24

with

$$y = (p_6 + p_9 \times i) \text{ for } i < p_7$$

Eq. 7.25

where the parameters $p_{0 \ldots 9}$ are free parameters which are fit. Parameters p_6 and p_9 describe the baseline of the pulse, p_1, p_3, p_5 give the three time constants of the pulse, while p_0, p_2, p_4 give the relative amplitudes of the time constant terms, and finally p_8 sets the amplitude of the pulse. The fit parameters from this may be used in the next step of the analysis to fit individual pulses.

Due to the steepness of the rise of the pulse, the fit to the rise, as shown in Fig 7.31 is not as good as the fit to the rest of the pulse. Uncertainty in the rise time and onset of the pulse both contribute to this. Assuming that the time constants and relative amplitudes of the three exponentials do not vary with the interaction energy, this may be used as a template to fit pulses at other energies. By using this function and fixing the values of the parameters zero to six, such a template fit may be carried out. For

such a fit, with fixed pulse shape, to provide an accurate fit to the pulse the shape of the pulse (both the size of the time constants p_1, p_2 and p_3 and the ratio of their coefficients p_0, p_2 and p_4) should remain constant over the range of energies and pulse heights analysed. Such correlations are checked in section 7.8 and found to be a good assumption.

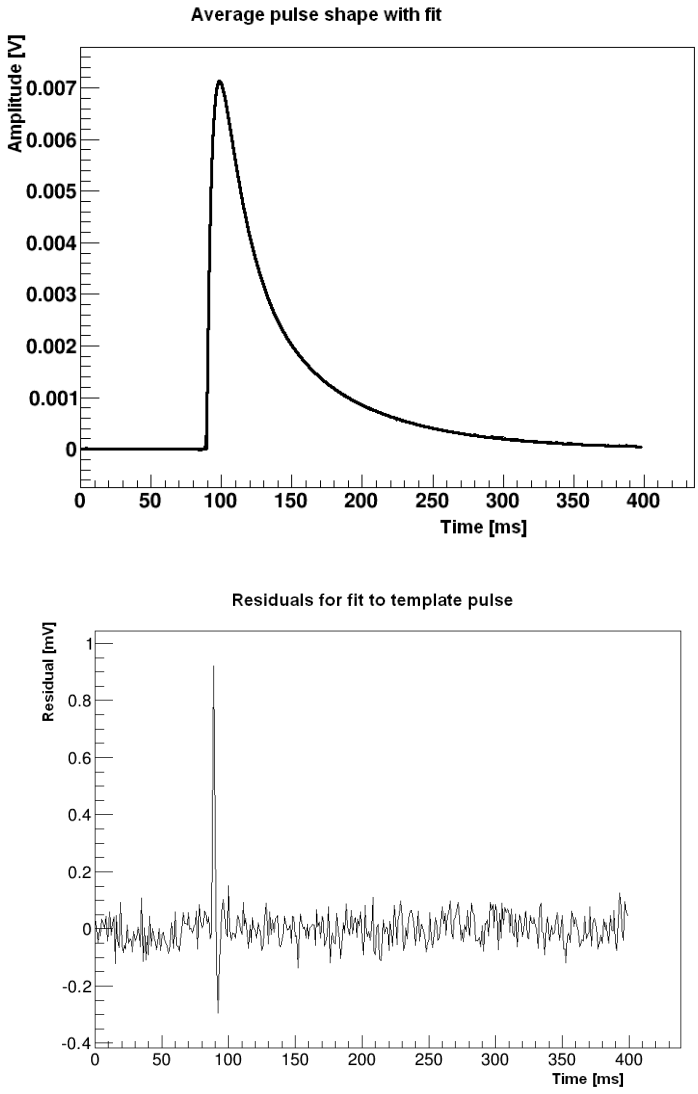

Figure 7.31 - The average pulse shape with the pulse shape function fit to it.

7.8 Pulse fitting

Next the complete list of pulses is fit to using the function in equations 7.24 and 7.25, with the previously calculated time constants as initial parameters. Poorly fitting

pulses, which might provide a misleading value of energy, can be rejected with a cut on the r.m.s of the fit.

For the potentially less regular pulse shape of these, the fit will require good estimates of the initial values. The exponential terms have their six parameters p_0 to p_5 taken from the fit of the average pulse. The pulse onset p_7 is also taken from the average fit. The baseline parameters p_6 and p_9 are taken from the earlier linear fit of the baseline. The final parameter p_8 should give the amplitude of the pulse for a fixed pulse shape (parameters zero to five). The initial value of this is set by taking ratio of the previously calculated pulse height for the pulse and the pulse height for the average pulse and multiplying the parameter of the average pulse (here labelled as $\overline{p}_8$).

$$p_8 = \overline{p}_8 \frac{PH}{PH_{avg}} .$$

Eq. 7.26

This function is now fit using ROOT Minuet to the entire list of pulse and the final parameters and goodness of fit recorded.

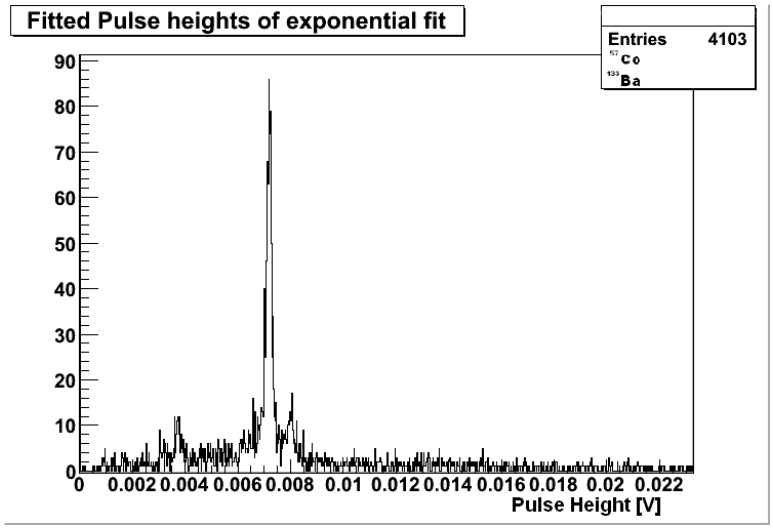

Figure 7.32 - Histogram of pulse heights for the exponential fits of a collection of pulses.

7.8.1 Pulse Height

The pulse height of the fit can be found by taking the maximum of the fit and subtracting off the baseline at that point as extrapolated from parameters p_6 and p_9. The three time constants of the fit can be found by converting the parameters p_1, p_3 and p_5 into units of time.

A final cut can be made using the quality of fit to remove any pulses where the pulse height may have been miscalculated, improving the spectrum from figure 7.32 to figure 7.33. This is measured using the chi squared value of the fit to the pulse. However, this varies with the size of the pulse and separate cuts must be made for low energy and high energy pulses; and this is described further in section 7.8.3.

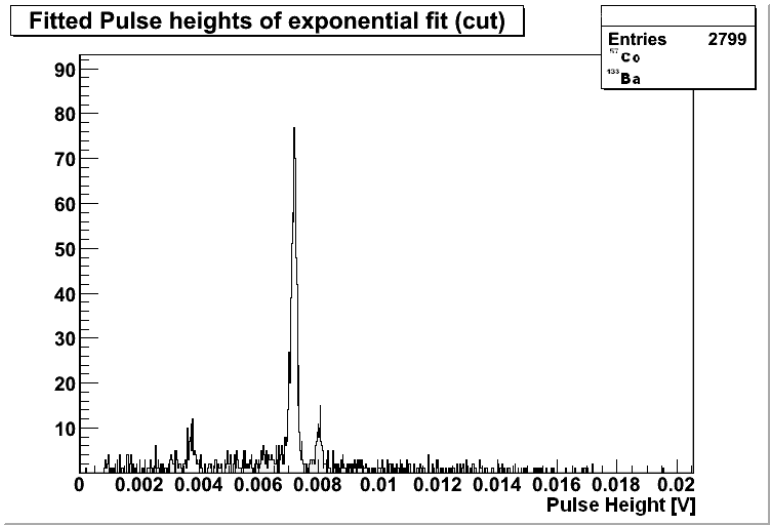

Figure 7.33 - Histogram of pulse heights for the exponential fits of a collection of pulses with a cut on the Chi Squared of the fit.

7.8.2 Time constants

The nine parameter fit gives three time constants associated with the pulse shape. One of these will be associated with the rise of the pulse, while the other two will be associated with the decay. The values from the fit will be improved compared to the previous calculations, which were limited by the period of the modulation and the much simplified model used to calculate them.

7.8.2.1 Variation of pulse shape

Each of these time constants is constant over the small range of temperatures at which the detector operates.

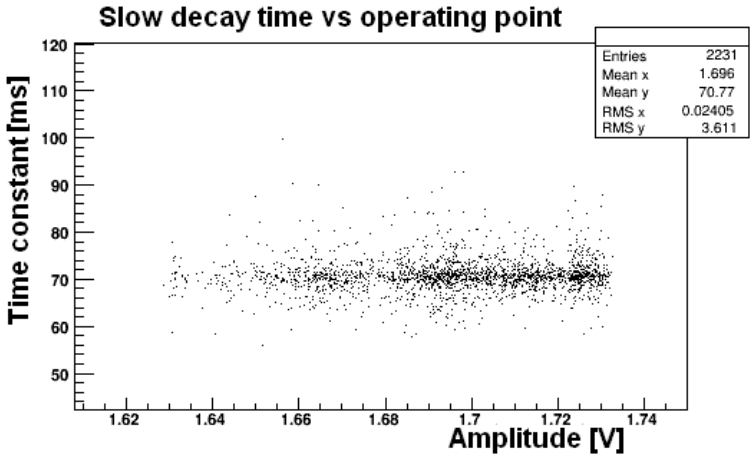

Figure 7.34 - Plot of the slow decay time constant against the amplitude of the baseline.

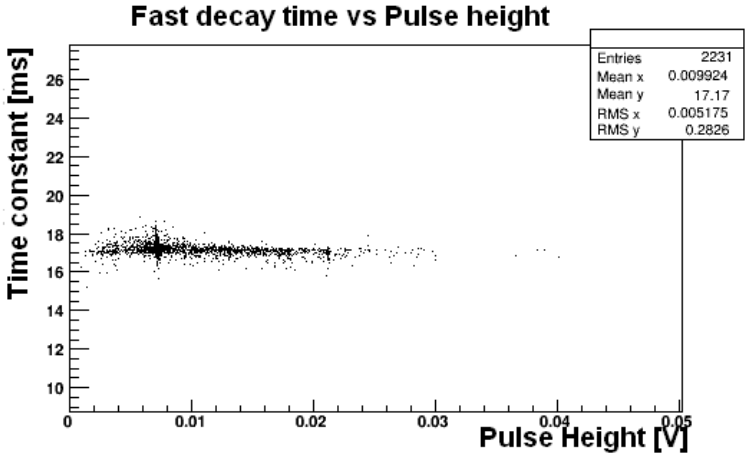

Figure 7.35 - Plot of the fast decay time constant against the pulse height of the fit.

This lack of variation in the time constants shown in figures 7.34 and 7.35 means that no adjustment is needed for different pulse shapes at different operating temperatures or with different pulse heights, and thus the pulse height remains a good measure of the energy deposited in the corresponding interaction.

As the shape of the pulse does not change with operating temperature or pulse height, a full 9-parameter fit of the pulse is unnecessary. The template pulse may be used to

provide the six parameters describing the shape of the pulse, with p_8 varied to fit to the amplitude of the pulse.

7.8.2.2 Time Constants

The previous calculations of rise time and decay time in sections 7.5 and 7.6, with precision limited by the sampling of the demodulation (~1 ms) gave a rise time of 4 ms and a decay time of ~40 ms. The results of the three time constant exponential fit, shown in figure 7.36, are similar for the rise time, but with the improvement in precision showing the time constant to be 4.1 ms. The single decay time was clearly inadequate to describe the signal and gave a results part way between the two decay time constants measured using the fit – at 17.3 ms and 60.6 ms.

The fast decay time is given by the decoupling of the electron and phonon systems in the detector. These have a thermal conductance between them G_{ep} which forms the time constant

$$\tau_p = C_p \Big/ G_{ep}(T_p), \qquad \textbf{Eq. 7.27}$$

where C_p is the heat capacity of the phonon system. Both of these terms will depend on the layout of the particular detector. This measured value of 17.3 ms is twice the size of the estimated value of ~ 8 ms from Chapter 5. The thermal model for that estimation assumed that the phonons in the absorber thermalize in the gold film and transfer heat to the electron system in the NTD germanium sensor, the temperature of which is readout out by a measurement of the resistance.

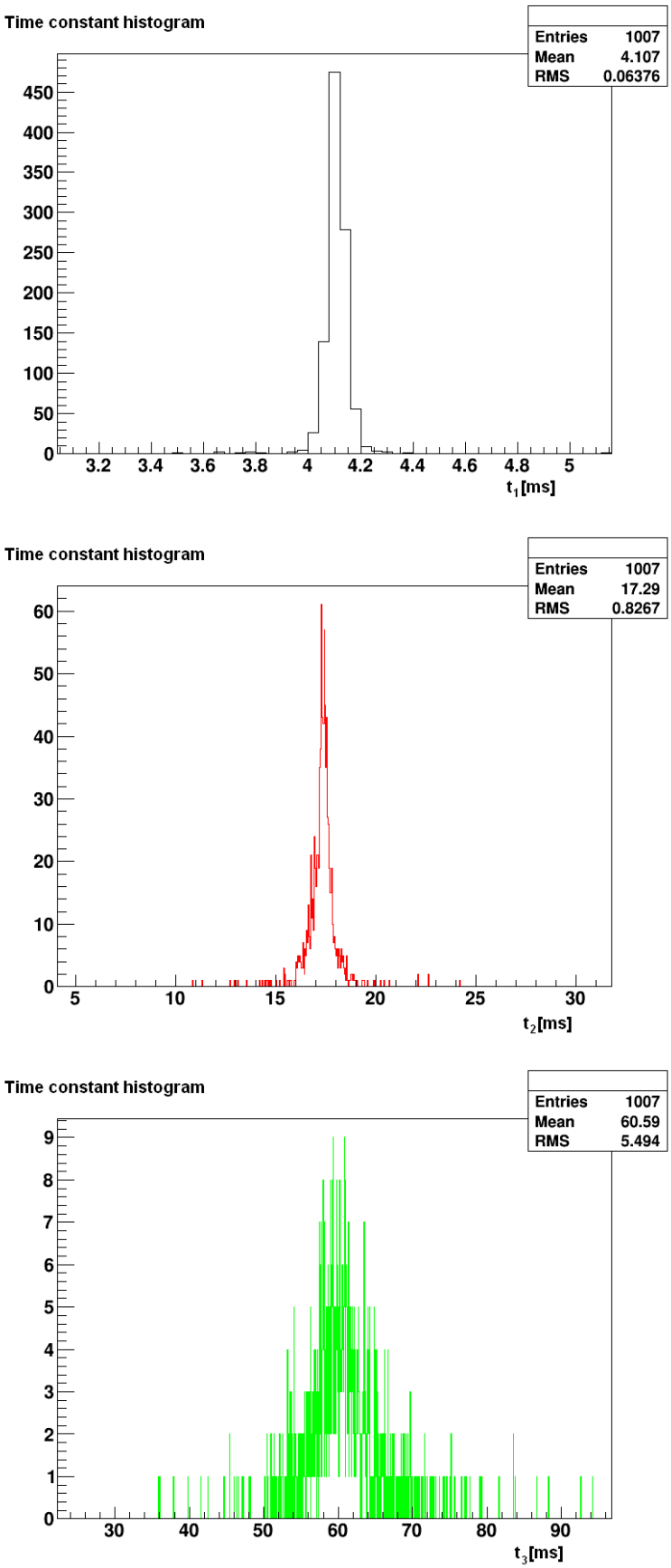

Figure 7.36 - Histograms of the three time constants, the rise t_1, the fast decay time t_2 and the slow decay time t_3.

In practice the detector layout is more complicated, with a layer of araldite attaching the NTD germanium to the gold film. The thermal resistance of this layer, and the kapitza resistance between the layers would cause a larger value for the time constant. The slow decay time constant described the transfer of heat from the detector through the gold bond wires to the copper detector holder that acts as a temperature bath. This should have the form given in Chapter 5 of

$$\tau_{eff} = C/(G + G_{ETF}) = C/G_{eff} \ ,$$

Eq. 7.28

where C is the heat capacity of the detector, G is the thermal conductance of the gold wires and G_{ETF} is the effective thermal conductance due to the electrothermal feedback of the Joule heating. This heating of the bias current has the effect of reducing the decay time constant from its intrinsic value; however a measurement of the decay time constant can be used to make an estimate of the heat capacity of the detector.

In chapter 5, the slow decay time constant was estimated as ~27 ms at an operating temperature of 10 mK using the heat capacity estimate from section 2.7 and an estimate of the thermal conductivity of the gold bond wires that provide the thermal connection to the heat bath. The measured value of the time constant is three times larger than this. There are several possible reasons for this, firstly this heat capacity is expected to be dominated by the electronic heat capacity of the NTD germanium sensor, which has a linear temperature dependence. The value used for this was based on the heat capacity of a similar NTD sensor, but as in section 2.7.2 this will vary between the different sensor types depending on their doping level and characteristics. The electronic component of the heat capacity therefore may be higher than the estimate used.

There will likely be other smaller corrections to this, for example, with the Joule heating of the detector there may be a temperature gradient along the gold bond wires from the colder temperature bath to the Joule heated NTD sensor. In the calculation the gold wires were assumed to be entirely at the temperature of the NTD. If part of the wire is in fact at a lower temperature than this then the thermal conductivity of the wires will be lower, contributing to the higher than expected time constant.
Ignoring these corrections and using the simple calculation to estimate the heat capacity of the detector for the 60.6 ms time constant in Figure 9, and assuming that the Joule heating is negligible, the heat capacity will be ~ 600 pJ/K at 10 mK.

7.8.3 Goodness of fit

The quality of the fit to the data will be measured by the chi squared of the fit to the data. This measure can then be used to cut out inferior fits with miscalculated energy values from the results. Such a cut can be done instead of, or as well as, the previous cuts in section 7.6. The parameters calculated in section 7.6 offered a basic measure of the pulse shape and could be used to remove pulses where there might be a problem with the energy measurement.

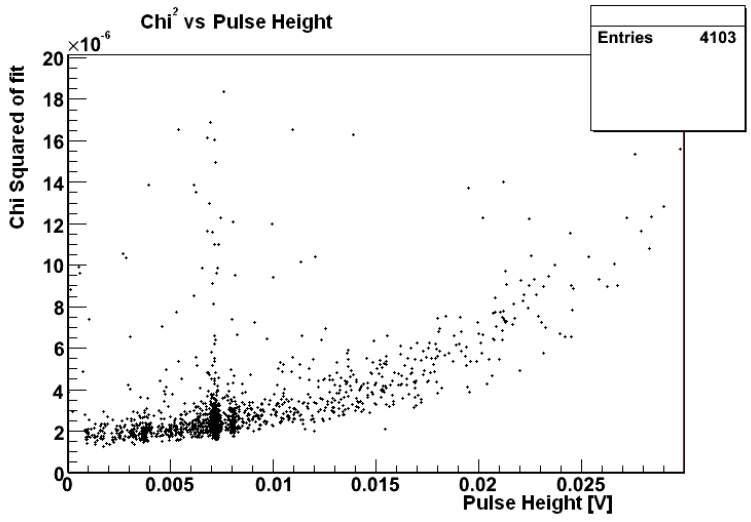

Figure 7.37 - Plot of the chi squared of fit against the Pulse Height. A 57-Co source was present, giving several dense regions in the plot at various pulse heights. For larger pulse heights the chi squared increases.

Using the quality of fit provides a method of applying the same procedure, using a better model of the pulse shape.

For smaller pulses the chi squared of the fit may be used. As in Fig 7.37, as the pulse height increases, the quality of the fit will get worse as position dependence and other effects have a greater impact. For these larger pulses, considering the ratio of the chi squared to the pulse height (Fig 7.38) gives a way of cutting out poorly fit higher energy pulses.

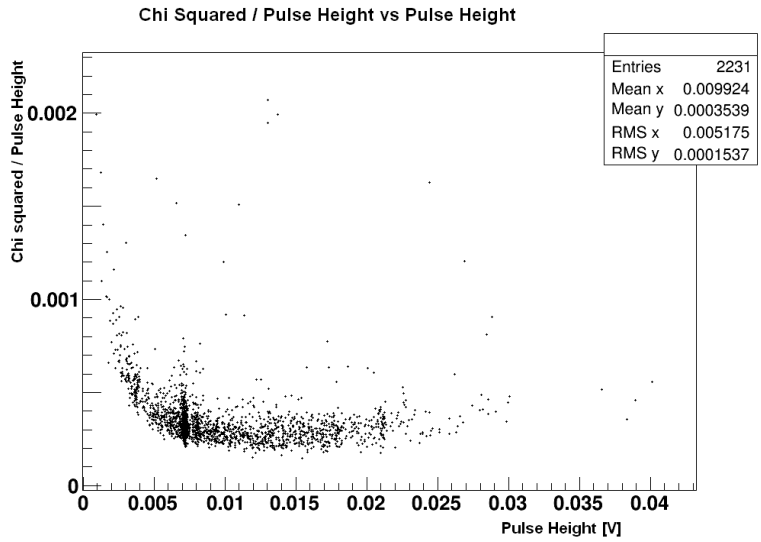

Figure 7.38 - Plot of the Chi Squared of fit divided by pulse height against the pulse height.

The form of the energy resolution in the detector as a function of energy is described further in section 7.10, but the form has a constant baseline level with additional energy dependent terms, which begin to dominate a high energies.

For pulse heights below 10 mV a cut is made on a chi squared value of 8×10^{-4} while for pulse heights above this a cut is made at a chi squared to pulse height ratio of 6×10^{-4}. The resulting spectrum following such a cut are shown in Fig 7.33.

7.8.4 Correlation with light detector

The pulses in the light detector should have a similar form, but the pulses from the collection of scintillation will be small in size compared to those on the phonon detector. The relatively larger noise means that finding the correct start point of the

pulse, p_7, may be difficult. The fit can therefore be improved by correlating it with the phonon detector and using the value for the onset of the pulse from the fit of the phonon detector.

A template fit is created for both detectors, with a list of pulses set by the cuts in section 7.6.8. Due to the lower signal to noise ratio of the light detector, these cuts are less strict for the light detector. A fit is then carried out for individual pulses, first using the nine parameter fit for the phonon detector. This allows the onset of the pulse to be determined as *p7*, and then used for the onset as a fixed parameter for a fit of the light detector.

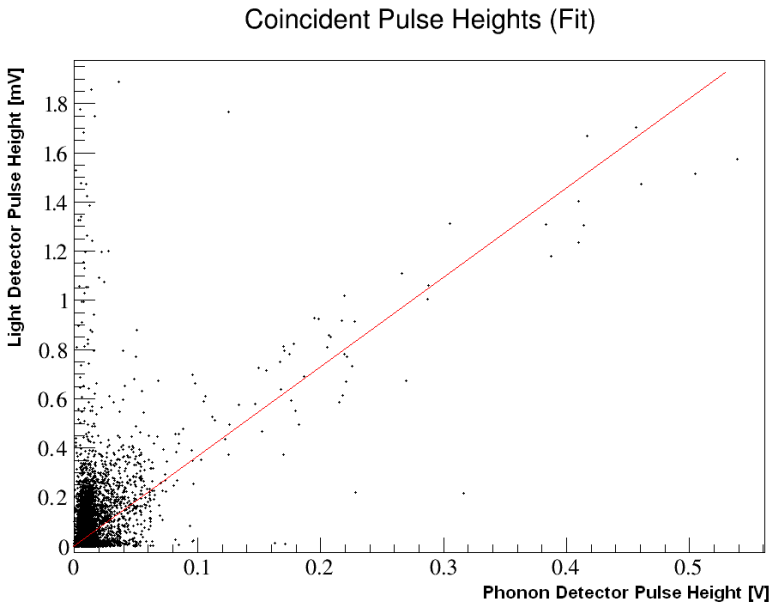

Figure 7.39 - Plot of the pulse height in the light detector versus the pulse height in the phonon detector, with the red line added to show the linear relationship between these for the scintillation events.

As Fig 7.39 shows, the relationship between the light detector pulse height and the phonon detector pulse height gives a straight line through zero; with the issue of an offset in the amplitude measurement (as in Fig 7.30) has been fixed. Fixing the pulse onset will reduce the number of pulse heights obtained from secondary peaks or baseline fluctuations in the light detector. The properties of the light detector are described further in section 7.11.

7.9 Energy conversion

So far, the signal has been kept as a voltage signal and the pulse heights so far represent a change in voltage. To convert these into their corresponding energy deposition values several factors need to be taken into account. The readout electronics and demodulation algorithm provides a conversion between this voltage and the resistance of the NTD germanium sensor, the operating point of the detector and the NTD characteristics provide the conversion between the resistance and the temperature of the sensor, and the heat capacity of the detector gives the conversion between temperature and energy.

$$\Delta V = \frac{dV}{dR}\frac{dR}{dT}\frac{dT}{dE}\Delta E$$

Eq. 7.29

Some of these factors will remain constant throughout the data but others, particularly the operating point, may vary or be unknown.

As in figure 7.41, this dependence on the operating point will have the effect of shifting any peaks in the voltage pulse height spectrum, leading to an apparent worsening of detector resolution. By converting the pulse heights into the energy deposited in the detector this effect should be removed.

7.9.1 Heat capacity

The heat capacity of the detector varies with temperature and directly effects the size of the temperature change when energy is deposited in the detector.

$$\Delta E = C(T).\Delta T$$

Eq. 7.30

Therefore, using the heat capacity allows for the conversion of a pulse height in terms of temperature into a pulse height in terms of energy.

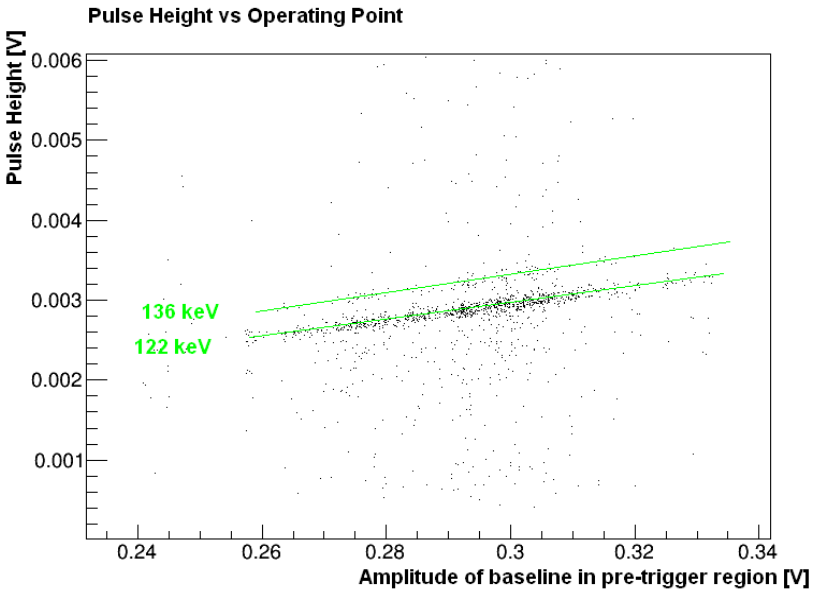

Figure 7.41 - Plot of the pulse height in Volts against the amplitude of the signal in the pretrigger region, for the $CaMO_4$ phonon detector with a ^{57}Co source present. Similar behaviour is observed with the $CaWO_4$ detector (not shown). The 122 and 136 keV lines show a dependence on the operating point of the detector, as expected.

When the heat capacity was estimated in chapter 2, the result was dominated by the electronic heat capacity of the NTD germanium sensor, but other components on the detector also contributed with both electronic contributions proportional to the temperature and phonon contributions proportional to the temperature cubed.

$$C = aT + bT^3$$

Eq. 7.31

where a and b are constants. For the $CaWO_4$ phonon detector, these constants were estimated in chapter 2 to be a ~25 nJ/K^2 and b ~ 1 μJ/K^4, while measurements of the slow decay time constant suggest values slightly larger than this (a ~ 60 nJ/K^2). However, the estimation of the NTD contribution was quite rough and a better value of the heat capacity is needed for this conversion.

7.9.2 NTD sensitivity

The response of the NTD Germanium sensor to the energy deposition and subsequent temperature pulse will also vary with temperature. As previously noted, the resistance of the NTD germanium will vary with the form given in Eq 7.32.

$$R = R_0 \exp\left(\frac{T_0}{T}\right)^{\frac{1}{2}}$$

Eq. 7.32

Therefore the rate of change of resistance of the NTD Ge with temperature is

$$\frac{dR}{dT} = -\frac{R_0}{2T_0}\left(\frac{T_0}{T}\right)^{\frac{3}{2}} \exp\left(\frac{T_0}{T}\right)^{\frac{1}{2}}.$$

Eq. 7.33

Using this formula, the pulse height in its form as a change in the resistance of the NTD germanium can be converted into a pulse height in terms of temperature. This can be calculated using the NTD characteristic constants calculated in chapter 4. However, for small changes in resistance, as in section 5.7, the resistance will vary linearly with temperature and thus the sensitivity will be constant. In the conversion of pulse heights for a sufficiently stabilised pulse, with $\Delta T << T$, it simply requires a multiplication by the constant sensitivity value.

7.9.3 Readout

The conversion between the voltage signal and the resistance of the NTD germanium requires the form of the readout used in chapter 3 and the demodulation described in section 7.2. The relationship between the amplitude of the demodulated data and the resistance on the NTD germanium will depend on the modulation frequency and the effect of the parasitic capacitance (or the compensation of parasitic capacitance). Therefore, the actual resistance of the NTD germanium is determined using the method of fitting to the raw modulated signal shape. This requires an averaged square signal shape, and is so unsuited for directly calculating the change in resistance for a pulse. However it can be used to determine the resistance corresponding to the operating point of the detector.

For small changes in resistance, such as the pulses resulting from a particle interaction in the detector or the small changes in operating point for a well stabilised detector,

the relationship between amplitude and resistance will be linear. Therefore, in the conversion of pulse heights to energy, the amplitude of the signal can be converted into a resistance by multiplying with a constant scaling factor determined by the fits of resistance.

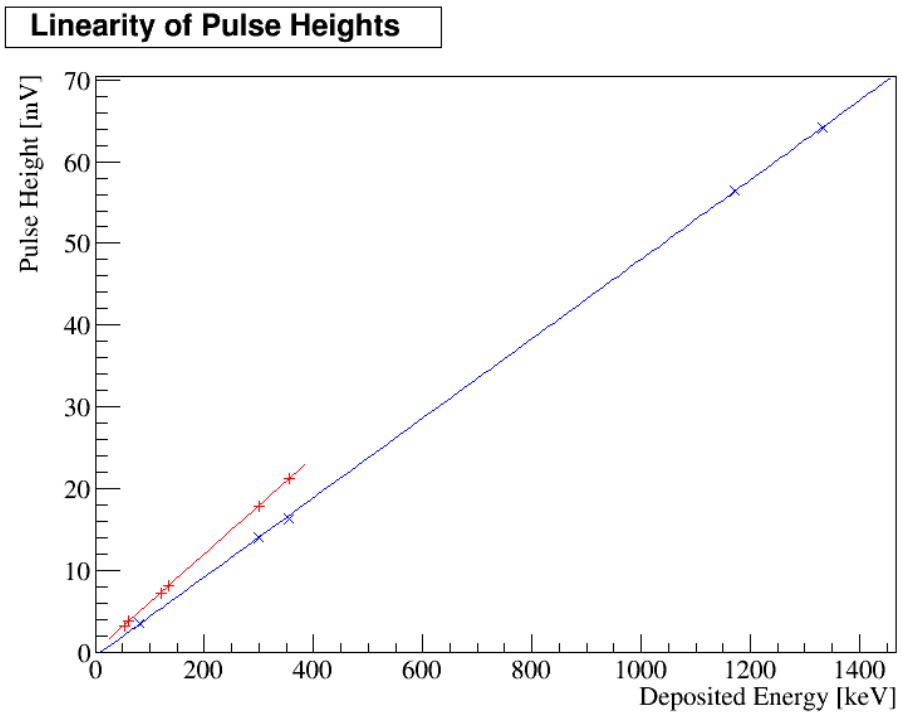

Figure 7.42- Plot showing the pulse height in volts against the energy for a number of peaks and features. The plot is shown for (red) the Calcium Tungstate detector at 1.6 MΩ and Vs = 1 with a ^{57}Co and ^{133}Ba source present, and (blue) the Calcium Tungstate detector at 1.2 MΩ and Vs = 1.5 with the ^{133}Ba and ^{60}Co sources present.

7.9.4 Linearity

As described in the previous three sections, for small changes in signal the response of the detector can be simplified. The readout and the NTD sensitivity give a constant scaling factor, and the heat capacity gives a scaling factor that varies linearly with temperature (and hence linearly with the amplitude of the baseline, for the small changes used here). Therefore the determined pulse height in volts for a given energy varies linearly with the amplitude of the baseline.

As in Fig. 7.42, this approximation is valid over a large range of pulse energies and the detector response remains linear. As shown in Fig. 7.43 the response also remains linear over a large range of operating points.

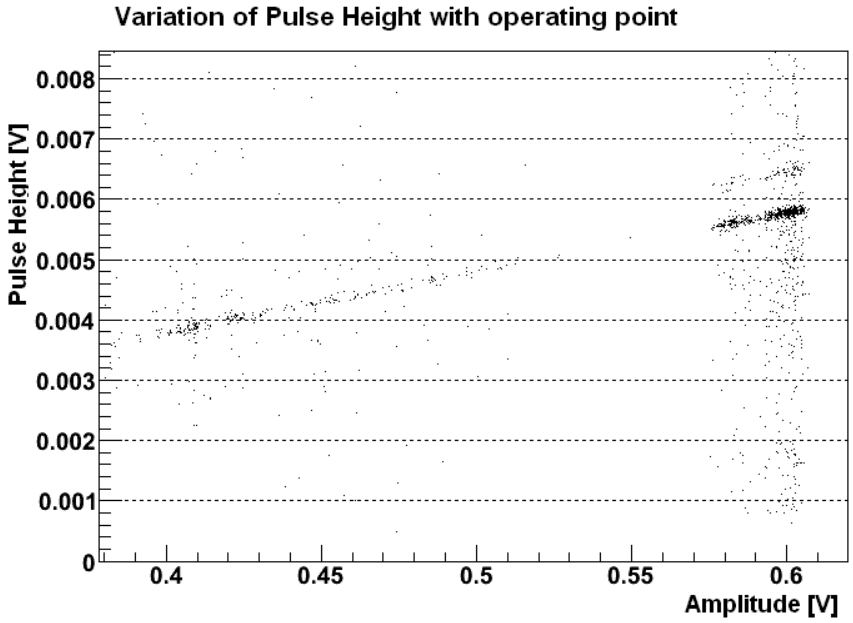

Figure 7.43 - The variation of pulse height with operating point for the Calcium Molybdate phonon detector.

With such a response, the pulse height can be converted into energy by dividing by the baseline position and multiplying by a suitable constant, determined from a calibration with pulses of known energy. The plot of pulse height in volts against amplitude shown in Fig 7.43 shows a large variation in the pulse height for the 122 keV peak, but when it is given as a ratio of pulse height to baseline position, as in Fig 7.44, the variation is removed.

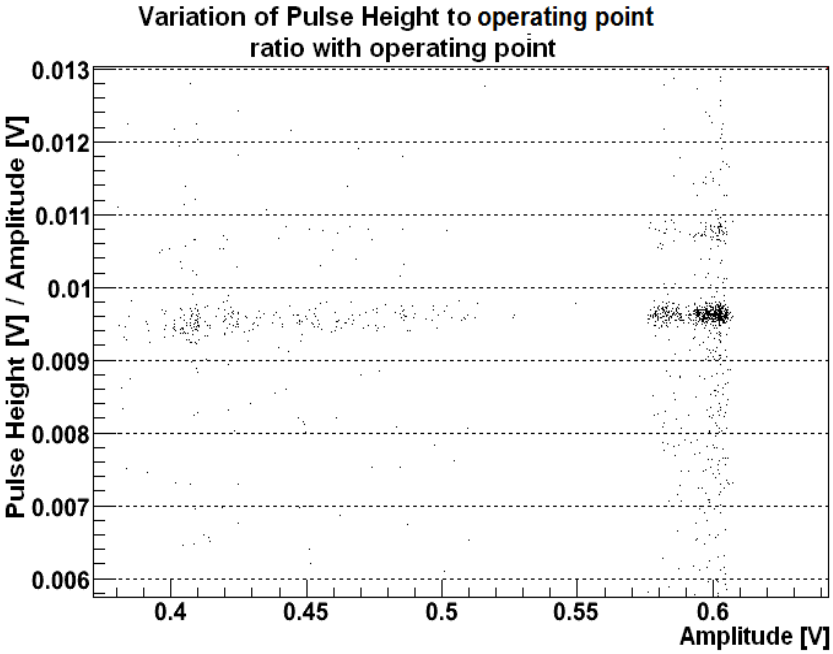

Figure 7.44 - The variation of the pulse height / amplitude ratio with operating point for the Calcium Molybdate phonon detector.

The conversion has a significant effect on the pulse height spectrum, removing the issues that are associated with the changing operating point.

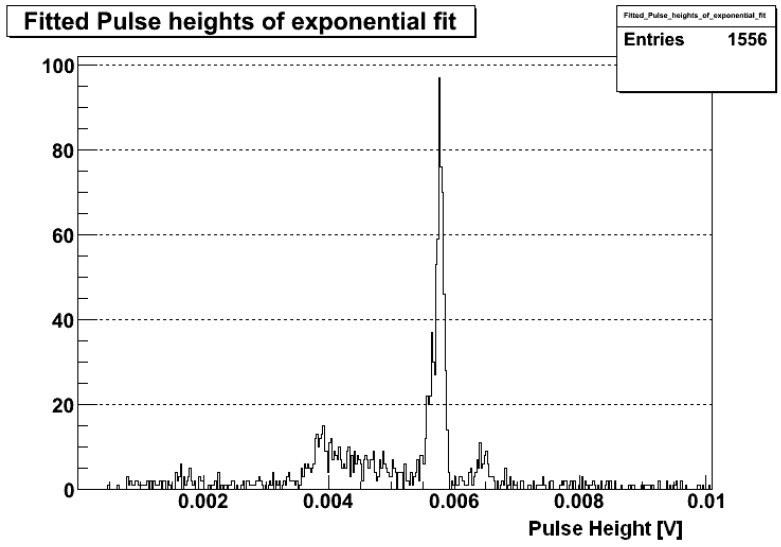

Figure 7.45 - The pulse height spectrum for the calcium molybdate data shown in Fig 7.43. The variation in operating point shifts the peaks, forming a second peak of 122 keV pulses around 4 mV.

Fig 7.45 shows the pulse height spectrum for the data in Fig 7.43. The spread of operating temperatures leads to a shifted set of peaks, but when the pulse height is adjusted using the baseline position, the variations in pulse height due to the change in

operating point are removed. The spectrum now features a narrow set of peaks with the features expected for this source.

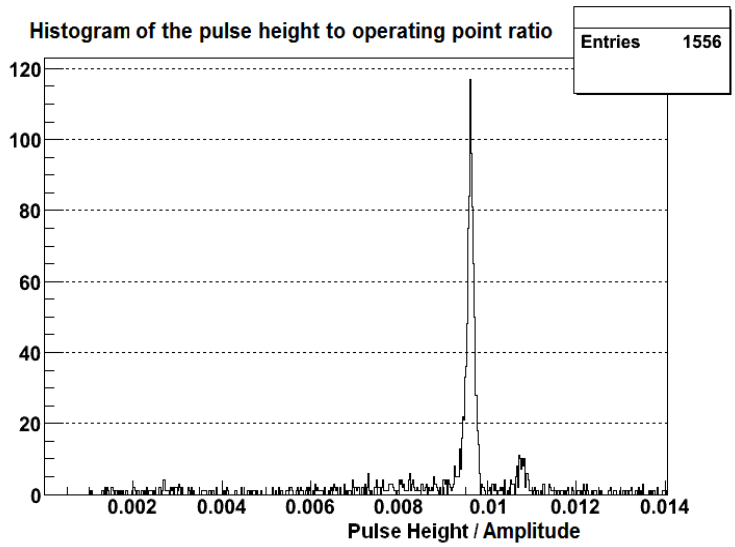

Figure 7.46 - the peaks narrow and the extra features disappear. Energy resolution at 122 keV of 2.05 keV.

The data shown in Figures 7.43-7.46 was deliberately sent through a range of operating points to test the detector response; the stabilisation process described in chapter 6 will prevent fluctuations on this scale occurring, but for the smaller fluctuations that do appear in the data this method allows for the pulse height measurements to be corrected and accurately converted into energy values.

7.10 Resolution

In general the resolution of the detector for a particle interaction of energy *E* can be expressed as

$$\sigma = \sqrt{(\sigma_0)^2 + (\sigma_1\sqrt{E})^2 + (\sigma_2 E)^2} \ .$$

Eq. 7.34

The first term, the baseline resolution is determined by the electronic noise, Johnson noise and others described in chapter 5. The second term, proportional to the energy is related comes from Poissonian statistics for the number of events in the peak. The

third term, proportional to the square of the energy, is common to all cryogenic detectors and includes position dependence and other effects. [132,133,134]

The size of the each of these terms can be determined by measuring the size of the baseline noise, when no pulses are present, and the resolution at several different values of energy then fitting to fit the form of the resolution with energy.

7.10.1 Baseline noise

By looking at regions of the data without any pulses present the baseline resolution, σ_0 can be estimated. The size of the baseline noise therefore provides a measure for the size of the non-energy dependent part of the resolution and hence the minimum possible resolution. The simple measure of the baseline noise is to take the FWHM of a stretch of data. However, fluctuations in the level of the baseline may also contribute to this and give an overestimate of the noise. To adjust for this, the baseline can be fit with a polynomial function and the r.m.s of the fit estimated as in figure 7.47. Using the energy conversion from the last section, this can be converted into energy. The best resolution obtained corresponded to a FWHM in energy of 1.85 keV.

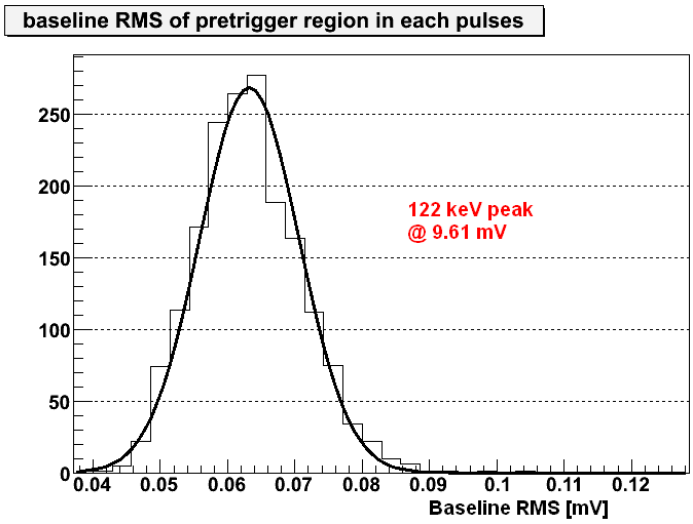

Figure 7.47 - Baseline noise for the calcium molybdate phonon detector.

The size of the baseline noise will ultimately determine the threshold of the detector and hence what trigger level can be set in the software for identifying pulses, if the level is too low then fluctuations in the baseline noise may be misidentified as particle interactions.

7.10.2 Peak width

As described in section 7.1, the incident particles from a radioactive source produce a number of different features in the detector. These features allow the resolution of the detector to be measured at a range of different energies. The resolution of a peak found as the full width at half maximum of that peak.

For a relatively clean spectrum this may be found for a Gaussian fit of the peak. However, Compton scattering can lead to a broadened shoulder on the low energy side of the peak, like 7.48, so a more accurate measure is to use the half width at half maximum of the peak. Other peaks, such as the Mo escape peaks for the calcium molybdate detector, may also make such measurements difficult – the escape peaks for 136 keV occur around 119 keV.

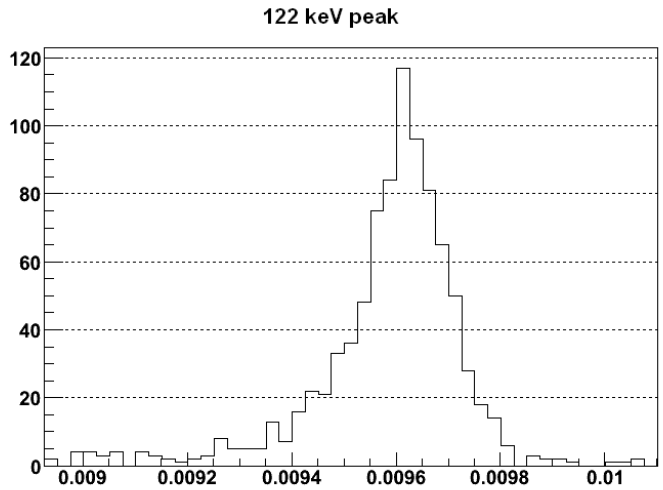

Figure 7.48 – 122 keV peak from a cobalt 57 source.

The energy resolution was determined for a range of different features in the detectors, first with the calcium tungstate phonon detector, with the results presented

in table 7.7, then with the calcium molybdate phonon detector, with the results presented in table 7.8.

Calcium Tungstate		
Peak Energy (keV)	FWHM (keV)	Error on FWHM (keV)
1332	15.5	3.5
1173	14.7	4
356.9	4	2
136	3.18	0.4
122	3.11	0.3
0	2.86	0.2

Table 7.7 – FWHM at different energies for the calcium tungstate phonon detector.

The resolution measured for the calcium molybdate detector was even better.

Calcium Molybdate		
Peak Energy (keV)	FWHM (keV)	Error on FWHM (keV)
136	2.76	0.5
122	1.91	0.3
0	1.79	0.2

Table 7.8 – FWHM at different energies for the calcium molybdate phonon detector. With the smaller crystal for the calcium molybdate, the number of events in some peaks (such as the 136 keV peak) is too small to obtain a meaningful, good resolution.

The crystal size for the calcium molybdate detector was smaller than that for the calcium tungstate detector, at almost half the volume. For these detectors, operating above ground in the laboratory in Oxford, the high rate of events from the radioactive background was a significant issue contributing to fluctuations of the baseline of the signal – either from the tails of earlier pulses, or from the presence of low energy pulses. This was likely to be a contribution to the difference in resolution between the two crystal sizes.

For the use of such detectors in future experiments in properly shielded underground laboratories this background would not be an issue and the size of the absorber could be increased without any detrimental effect to resolution.

7.10.3 Energy Dependence

The form of the resolution with energy is given by Eq 7.34. The baseline noise σ_0 can be estimated as in 7.10.1 while the energy dependent terms σ_1 and σ_2 can be found via

the measurements of 7.10.2. The range of radioactive sources available for testing allows the resolution to be measured at several energies up to the almost 2 MeV. By plotting these results, with the square of the full width half maxima as the square of the resolution against the energy deposited in the detector, the form of Eq 7.34 is fit to find the three coefficients.

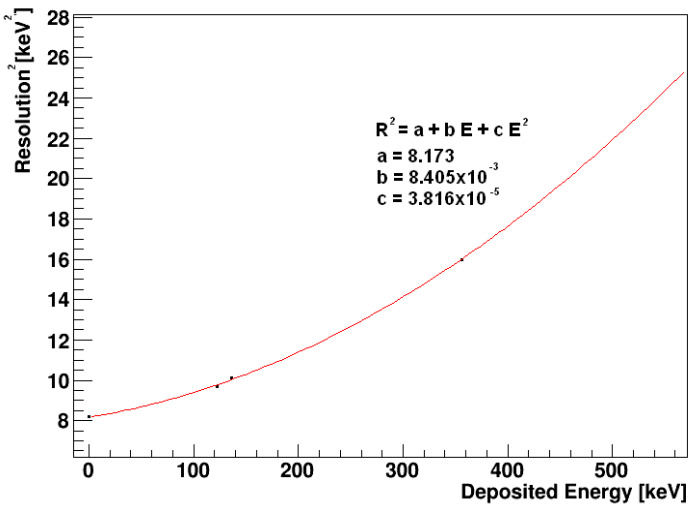

Figure 7.49 - Fit to the resolution squared of the calcium tungstate phonon detector.

This fit in Fig 7.49 gives a baseline resolution of σ_0 = 2.85 keV, with the energy dependent parts σ_1 = 0.0917 keV$^{1/2}$ and σ_2 = 0.00618. Though initially the energy independent term is the dominant contribution, for energies of ~400 keV and above the quadratic term $\sigma_2 E$ becomes dominant.

7.11 Light Collection

When energy is deposited in the absorber crystal of the phonon detector, the majority of it is converted into phonons and measured as a temperature rise using the NTD Ge thermometer. However, a small amount of the energy will be emitted by the crystal as scintillation light.

This light is contained and collected by using a second detector with a light-absorbing substrate and placing both detectors within a cavity, lined with reflecting foil, to form a phonon-scintillation detector module. By looking at the ratio of the coincident pulse heights in each detector, the light collection and scintillation characteristics of the detector can be estimated.

For a deposited energy of E_0 the energy emitted as scintillation light by the phonon detector is given by

$$E_S = KE_0 ,$$

Eq. 7.35

while the energy measured by the phonon detector is

$$E_P = (1-K)E_0 ,$$

Eq. 7.36

where K is the scintillation efficiency of the crystal.

However, not all this light will be absorbed by the light detector. Some amount of it may be reabsorbed by the phonon detector and some may be absorbed by the surroundings of the detector module. The aim of the reflecting foil lining the cavity is to keep this absorption by surroundings to a minimum, but the foil does not have complete 4π coverage around the detectors. It is necessary to leave gaps for bond wires to the detector and the detector supports to pass through. The energy absorbed by the light detector is therefore

$$E_L = (1-\delta)KE_0 ,$$

Eq. 7.37

where $1\text{-}\delta$ is the collection efficiency of the module.

Fig 7.50 shows a number of coincident events with light detector energies higher than would be expected from the scintillation output and light collection efficiency of the phonon-scintillation detector. These correspond to direct hits on the light detector due to the high rate of pulses in the detector. There may also be events in which a particle Compton scatters in one detector depositing some energy before being absorbed in the

other detector. The light detector used is a (10 × 20 × 0.5) mm^3 sapphire crystal as the substrate for the light absorbing silicon layer and the NTD germanium to be attached to. This crystal is 10% of the size of the calcium tungstate crystal used for the phonon detector, and ~13% of the size of the calcium molybdate, so although there will be less particle interactions occurring directly in the light detector compared to the phonon detector, there will still be a considerable number of interactions.

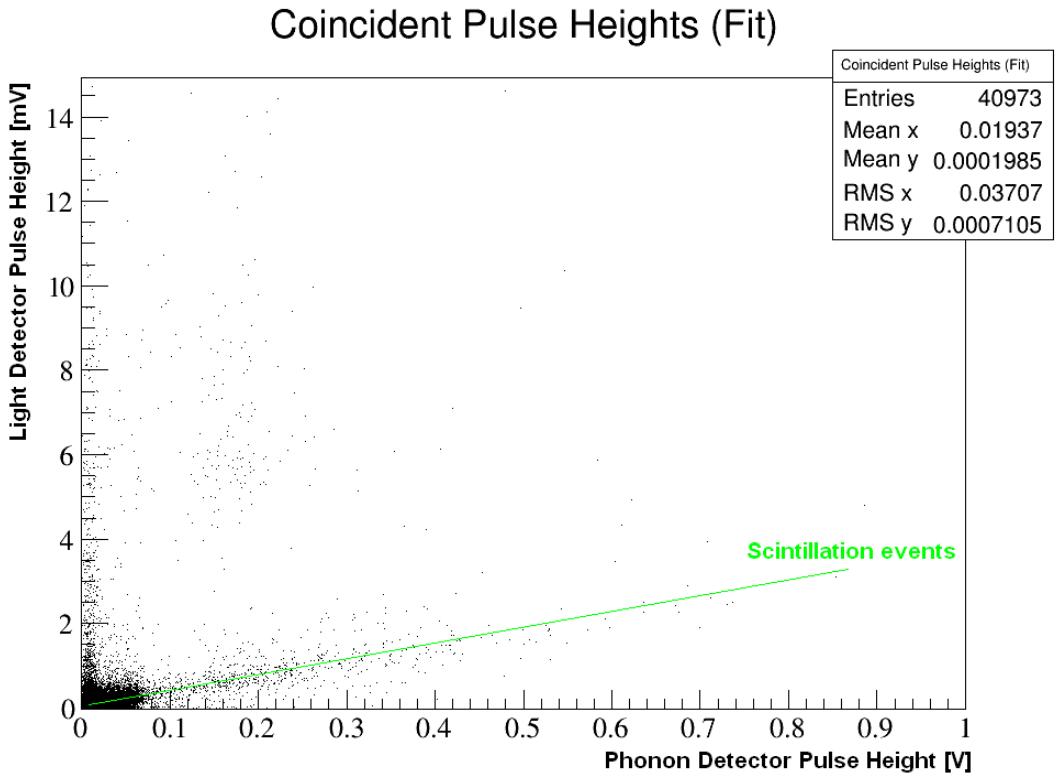

Figure 7.50 - Plot of pulse heights in light detector and in the phonon detector evaluated using the correlated template fit. A straight line of scintillation events, where the pulse in the light detector corresponds to the scintillation from a larger pulse in the phonon detector, is highlighted on the plot.
There is a peak of events in the phonon detector at ~150 mV, and in the light detector at ~6 mV due to direct . There are also a small number of coincident events on both detectors, due to the high rate of pulses in the detector. These produce a cluster of coincident events above the line of scintillation events near the peak energies.

With improved shielding to the detector to reduce the rate of background events and a smaller substrate crystal for the light detector these could be reduced in future versions. The yield plot shown in figure 7.51 gives a constant ratio of the voltage pulse height in the light detector and the voltage pulse height in the phonon detector. These voltage pulse heights can be converted using the formulae in the previous

section, 7.10, to find the ratio of the pulse heights in energy by using the details of the bias current and a resistance measurement of each detector to find the respective temperature.

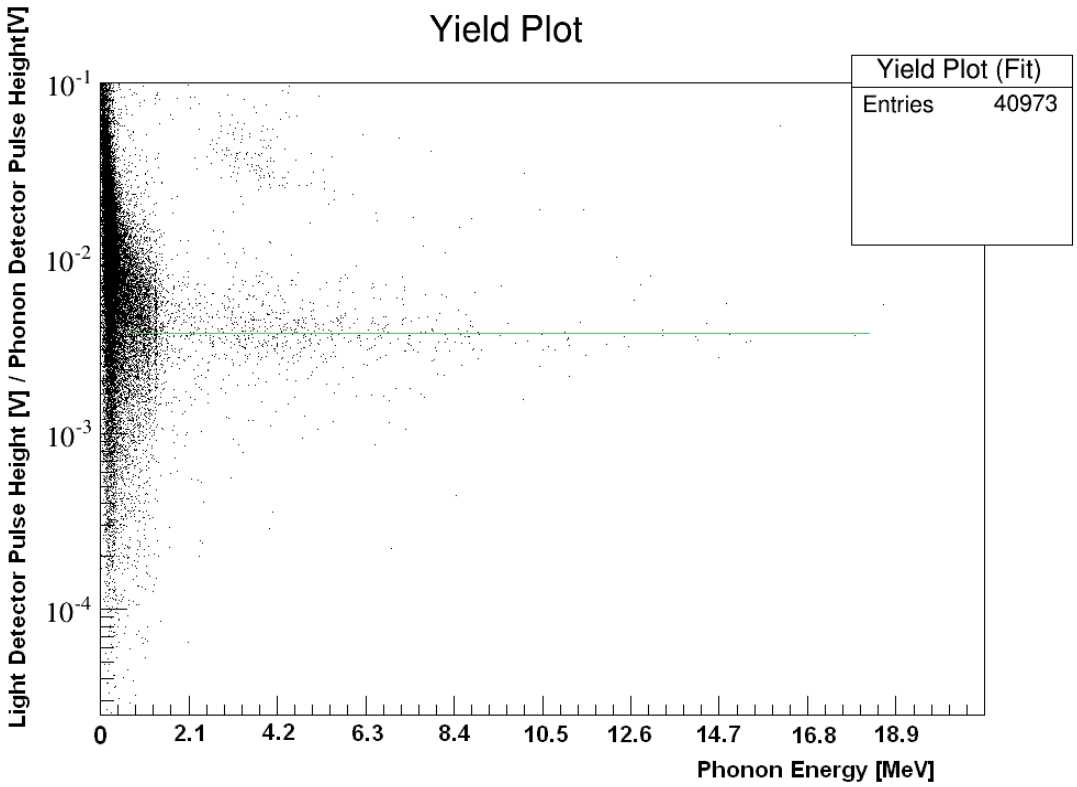

Figure 7.51 - Yield Plot. Similar to that produced by cryogenic detectors in dark matter experiments such as CRESST or EDELWEISS (Fig 1.10). The vertical axis shows the ratio of pulse heights in the light detector and phonon detector while the horizontal axis shows the energy deposited in the phonon detector.

For figure 7.51 the phonon detector had a bias of V_S = 2 V, while the light detector had a bias of V_S = 1 V plus some exponential boost for pole cancellation. The resistance measurements then gave temperatures of 9.02 mK and 9.07 mK for the phonon and light detectors respectively, with the exponential boost raising the temperature of the light detector through Joule heating.

In the conversion between the voltage pulse height and deposited energy, a value for the heat capacity of the detectors must be used. These heat capacities will be dominated by the contribution of the NTD germanium, and be linear with

temperature. By assuming that both NTDs have similar contributions to heat capacity the ratio of heat capacities can be given as a ratio of temperatures. Using this and the characteristic constants of the NTDs, the sensitivity of the NTD sensors at these temperatures (given in Eq 4.4) can be used to convert the pulse heights to energy. The ratio of voltage pulse heights of ~ 3.5×10^{-3} converts to a ratio of energies of 1.08×10^{-2}, ie. approximately 1% of the energy deposited in the phonon detector is measured as scintillation light in the light detector.

From equations 7.35 and 7.36 this light yield will be given by

$$L.Y = \frac{E_L}{E_P} = \frac{(1-\delta)K}{(1-K)} .$$

Eq. 7.38

As described in section 2.8, for calcium tungstate, the proportion of the deposited energy given out as scintillation light is ~8.2 %. Therefore with $K = 0.082$, the light collection efficiency is calculated as $1\text{-}\delta = 0.121$, ie. Only 12% of the scintillation light emitted by the scintillating crystal of the phonon detector is absorbed by the light detector. The ratio of energies for calcium molybdate was calculated as 8.79×10^{-3}. With the proportion of energy given out as scintillation light being ~ 7.8%, this gives a light collection efficiency of $1\text{-}\delta = 0.104$.

Other than the scintillation efficiency there will be other differences between these phonon detectors affecting the light collection efficiency. The calcium tungstate and calcium molybdate crystals have different peak wavelengths for their scintillation – ~420 and ~540 nm respectively. The silicon layer on the light detector used to absorb this scintillation light have a refractive index which varies with wavelength, as in figure 2.19, so that the absorption length for the scintillation light of calcium molybdate will be longer than that for the scintillation light of calcium tungstate. Along with the lower scintillation efficiency, this means that the light collection

efficiency for calcium molybdate would be expected to be slightly lower than for calcium tungstate.

In addition to this, the two crystals were different sizes, with the (15 x 10 x 5) mm^3 calcium molybdate crystal being less than the (20 x 10 x 5) mm^3 calcium tungstate crystal. This would affect the proportion of light that will be reabsorbed by the phonon detector, as would differences in the polish of surfaces for the crystal and the presence of any defects.

Conclusions and future outlook

Cryogenic detectors with NTD Germanium readout were tested for two different absorber crystals – calcium tungstate and calcium molybdate, suitable for dark matter and neutrinoless double beta decay searches.

Detector layout

A set of readout electronics was designed and tested in Oxford for the purpose of biasing and reading out the high impedance NTD germanium thermometers. Alongside this the K400 cryostat in Oxford has now been equipped to test such detectors with shielding for the detector and a method of temperature stabilisation to ensure the detector performance is not limited by the background rate in the detector and variations in the operating temperature.

The relatively high radioactive background in the environment still remains a problem, with many events having to be rejected during analysis because of issues with pile up. Further improvements in Oxford are limited by the dimensions of the cryostat and the mass of any shielding materials. However, the use of this kind of cryogenic detector in a properly shielded underground laboratory would not suffer this problem with background and would allow the detector scaling up to larger masses.

As part of the readout chain, prototype kapton cabling was used. This cabling was designed and made in Oxford to fit the setup in the cryostat, and running the detectors allowed aspects of the cabling, including capacitance and reliability, to be tested for similar cables installed in the EDELWEISS cryostat in Modane.

This set up now allows for the testing of a variety of different scintillating crystals, NTD Ge sensors and detector layouts with these components being easily removed and replaced within the cryostat.

Scaling up

The size of the crystals used in the detector was smaller than the targets that would be used in an actual dark matter or neutrinoless double beta decay experiment. These would have to be increased before the detectors become a viable option for detecting such new physics. In Oxford limitations from radioactive background and the space available in the cryostat kept the crystal size down to ~2 cm^3, a mass of around four grams, but in a larger, more shielded environment scaling up to the large target masses, ~1 kg, used in the current cryogenic experiment is perfectly possible, as has been demonstrated with $CaWO_4$ and other crystals.

Estimations of the detector heat capacity were made in chapter 2.7, and some measurements made through the time constants of the pulses in chapter 7. The measured heat capacity was found to be higher than the estimate, but this was most likely down to uncertainties in the contribution from the NTD Ge which would remain the dominant part. The contribution of the absorber crystals, given by the phonons in the material, was considerably smaller than this and the crystals can therefore increase to a much larger size without having a significant effect on the heat capacity.

With regard to other factors that impact on the detector resolution, such as position dependence, the CRESST collaboration were able to scale up similar detectors from small prototypes to much larger crystals without a negative impact on the resolution of the detector so the same should be possible for these cryogenic detectors with NTD Ge readout, too.

Resolution

A baseline resolution of 1.7 keV was achieved in the calcium molybdate detector and 2.86 keV in the calcium tungstate detector. The difference in these resolutions was likely down to the size of the absorber crystal and the effect of the background rate of events. The $CaWO_4$ crystal was larger and suffered more issues with pile up compared to the $CaMoO_4$. With improvements to the detector environment, to lower the pile up rate, the baseline resolutions of ~2 keV could likely be improved to below 1 keV.

These resolutions had an energy-dependent component as described in equation 7.33. Measurements of this showed that the quadratic in energy term began to dominate at energies above ~400 keV. As with CRESST, scaling up to larger detector masses could reduce these effects and give an improved resolution at higher energies.

Light collection

The ratio of energies measured in the light detector and the phonon detector was 1.08% for the calcium tungstate and 0.88% for the calcium molybdate. Measurements in CRESST typically achieved ratios of ~2% [136,137]. It should therefore be possible to improve the light detector to collect at least double the amount of scintillation currently collected, and thus double the signal size in the light detector. Surface roughness and crystal geometry both have an impact on this, and could be yet be investigated and improved.

Detector design

Several other improvements could be made to the design of the detectors to improve their performance. Firstly, several different NTD Ge sensors were tested in Oxford and for the final version of the detector NTD type 38a was used on the light detector while NTD type 73a was used on the phonon detector. These different germanium

sensors have different characteristics and have different optimum temperature ranges. The best sensitivity for a detector is found for the lower temperature NTD – 38a which minimizes the detector heat capacity reaches 1 MΩ at 9.6 mK, compared 73a and J1 which reach 1 MΩ at 13.0 and 19.9 mK respectively.

Operating the two detectors simultaneously requires different excitations to be sent – the extra exponential boost needed for NTD 38a then increases the temperature of the detector and reduces its sensitivity. With the same type of NTD sensor on both detectors, preferably NTD 73a out of the three tested, the operation of the detectors should be improved.

Further to this, the NTD sensor is the dominant component of the heat capacity for the detector. With a different, smaller sensor with suitable resistance characteristics and lower heat capacity the response of the light detector could be increased, giving a larger signal for the deposited energy.

In the design of the light detector, a layer of chromium was placed under the gold film to help provide adhesion for the film while the other crystals were left without such a layer. No difference was observed in detector response between those detectors with the adhesion layer, despite the potential difference in the thermal model. However the layer does provide an extra contribution to the heat capacity of the detector. As a metal, the heat capacity of the chromium is mostly electronic and varies linearly with temperature therefore it stays significant even when the detector is cooled to lower temperatures. The layer should therefore not be included in future versions of the light detector.

Photomultiplier

As a possible alternative to the NTD Germanium light detector, a low-temperature photomultiplier tube could be used to accurately measure the scintillation output of

the phonon detector. With the low light yield from the cryogenic detectors, the high sensitivity of a photomultiplier tube would allow for a much better resolution that the NTD-based light detector.

One of the major issues with running photomultipliers at the low temperatures required for cryogenic detectors is the noise and heat load produced by the high voltage supply needed to run power the PMT. Work is being carried out in Oxford with a Cockcroft Walton generator designed to run within the cryostat at sub-kelvin temperatures.

Dark matter

Existing dark matter detection experiments such as EDELWEISS or CRESST look for a signal of ~10 keV, with discrimination provided by the simultaneous measurement of energy in two channels (heat and light or heat and ionization). The thresholds required for these experiments are significantly lower than those achieved with the NTD Ge readout in this thesis. Although improvements could still be made with aspects of the detector, improving the shielding or using a smaller NTD sensor to reduce the heat capacity may improve the detector performance and increase the signal size leading to a better resolution and threshold, these detectors are perhaps not the way forward for dark matter detection experiments. Alternative methods of measuring the scintillation light – such as low-temperature photomultipliers however, could be a possibility with the high sensitivity of the photomultiplier giving a much better resolution than the NTD Ge light detector.

Neutrinoless double beta decay

The expected signal for a neutrinoless double beta decay search is a peak in the detector at the Q-value. This value depends on the $0\nu\beta\beta$ decay isotope, but most materials used for experiments will have values around 2 MeV, or higher, away from

the major radioactive backgrounds. At this higher energy, the NTD phonon-scintillation detectors no longer have a problem with threshold (as with dark matter searches) and could more readily be used in experiments for measuring neutinoless double beta decay.

Similar resolutions have been measured for detectors in existing searches, such as CUORE or GERDA. Cryogenic light detectors with NTD germanium sensors could therefore be a particularly useful method for future experiments. NTD germanium sensors of known calibration can be attached to a variety of different scintillating crystals containing candidate isotopes for neutrinoless double beta decay.

Bibliography

[1] G. Bertone, D. Hooper, and J. Silk, *Particle dark matter: evidence, candidates and constraints*, Physics Reports 405 (5-6), 279-390, 2005.
[2] K. Garrett and G. Duda, *Dark Matter: A Primer, Advances in Astronomy*, Advances in Astronomy Volume 2011 (2011), 968283.
[3] M Roos, *Dark Matter: The evidence from astronomy, astrophysics and cosmology*, arXiv:1001.0316
[4] C. Enss (ed.) *Cryogenic Particle Detection*, Topics Appl. Phys 99 1-34 (2005)
[5] M. Sisti, *From Cuoricino to CUORE: investigating neutrino properties with double beta decay*, Journal of Physics: Conference Series 203 (2010) 012069
[6] H V Klapdor-Kleingrothaus, *Seventy Years Of Double Beta Decay: From Nuclear Physics to Beyond Standard Model Particle*, World Scientific Publishing Company (March 25, 2010)
[7] B. Majorovitz et al, *The CRESST Dark Matter search*, arXiv:astro-ph/0411396
[8] F. Zwicky, Republication of*: The redshift of extragalactic nebulae*, General Relativity and Gravitation 41 (1), 207-224, 2009.
[9] A. Liddle, *An introduction to modern cosmology*, Wiley-Blackwell; 2nd Edition edition (27 Mar 2003)
[10] Planck Collaboration, *Planck 2013 results. XVI. Cosmological parameters*, arXiv:1303.5076
[11] E. J. Chun, H. B. Kim, and J. E. Kim, *Dark matter in axino-gravitino cosmology*, Physical Review Letters, vol. 72, no. 13, pp. 1956–1959, 1994.
[12] E. Corbelli and P. Salucci, *The extended rotation curve and the dark matter halo of M33*, Monthly. Notices of the Royal Astronomical Society 311, 441±447 (2000)
[13] D Clowe et al., *A Direct Empirical Proof of the Existence of Dark Matter* Astrophysical Journal Letters 648 L109 2006, arXiv:astro-ph/0608407
[14] M. Bradač et al., Revealing the Properties of Dark Matter in the Merging Cluster MACS J0025.4–1222, The Astrophysical Journal 687 (2), 959, 2008.
[15] G. Hinshaw et al., *Five Year Wilkinson Microwave Anisotropy Probe Observations*, Astrophysical Journal Supplement Series 180, 225-245, 2009
[16] G. Steigman, *Neutrinos and Big Band Nucleosynthesis*, Advances in High Energy Physics, 268321, 2012
[17] F. Iocco et al, *Primordial Nucleosynthesis: from precision cosmology to fundamental physics*, Phys. Rept. 472 1-76, 2009
[18] K. Nakamura et al (Particle Data Group), JP G37, 075021 (2010) and 2011 partial update for the 2012 edition. Available at http://pdg.lbl.gov/index.html
[19] I. Aitchison, *Supersymmetry in Particle Physics, an elementary introduction*, Cambridge University Press (20 Sep 2007)
[20] J. Beringer et al. (Particle Data Group), PR D86, 010001 (2012)
[21] T. Aaltonen et al., *Evidence for the Charmless Annihilation Decay Mode* $B_s^0 \to \pi^+\pi^-$**,** Physical Review Letters 108 211804 (2012)
[22] CMS Collaboration, *CMS Physics Analysis Summary*, CMS-EXO-11-059 (2011)
[23] ATLAS Collaboration, *Further search for supersymmetry at* $\sqrt{s}$ *= 7 TeV in final states with jets, missing transverse momentum and one isolated lepton*, ATLAS-CONF-2012-041 (2012)
[24] G.G. Ra□elt: *Astrophysical Axion Bounds*, Lect. Notes Phys. 741, 51–71 (2008)
[25] M. Arik et al., *Search for sub-eV Mass Solar Axions by the CERN Solar Telescope with He-3 Buffer Gas*, Phys. Rev. Lett. 107 (2011) 261302
[26] Asztalos et al., *SQUID-based Microwave Cavity Search for Dark MatterAxions*, Phys Rev Let 104 041301 (2010)
[27] K. Abazajian, G. M. Fuller and M. Patel, *Sterile neutrino, hot, warm and cold dark matter*, Phys. Rev. D 64 (2001)
[28] A. Mirizzi et al., *The strongest bounds on active-sterile neutrino mixing after Planck data*, arXiv:1303.5368 (2013)
[29] H. Landsman (for the Ice Cube Collaboration) IDM 2006 Conference Proceedings, Rhodes, Greece

[30] B. Feldstein et al, *Neutrinos at IceCube from heavy decaying dark matter,* Phys Rev D 88 015004 (2013)
[31] The Fermi-LAT Collaboration, *Constraints on the Galactic Halo Dark Matter from Fermi-LAT Diffuse Measurements,* Astrophys.J. 761 (2012) 91
[32] G. Bertone et al., *Gamma Ray Lines from a Universal Extra Dimension,* Phys.Rev.D 80, 023512 (2009), arXiv:astroph.HE/0904.1442
[33] W.B Atwood et al., *The Large Area Telescope on the Fermi Gamma Ray Space Telescope Mission,* Astrophys. J. 697:1071-1102 (2009)
[34] W. Menn et al., *The PAMELA Space Experiment,* Advances in Space Research 51 (2013) 209–218
[35] M. Aguilar *et al. First Results from the Alpha Magnetic Spectrometer on the International Space Station : Precision Measurement of the Positron Fraction in Primary Cosmic Rays of 0.5-350 GeV,* Phys. Rev. Lett. 110, 141102 (2013)
[36] M. C. Smith et al., *The RAVE Survey: Constraining The Local Galactic Escape Speed,* Mon. Not. Roy. Astron. Soc. 379 , 755 (2007), astro-ph/0611671
[37] C. McCabe, *The astrophysical uncertainties of dark matter direct detection experiments,* Phys.Rev.D82:023530, (2010)
[38] J.D. Lewin and P.F. Smith, *Review of mathematics, numerical factors, and corrections for dark matter experiments based on elastic nuclear recoil,* Astropart. Phys. 6 87 1996
[39] E. Aprile et al., *Dark Matter Results from 225 Live Days of XENON100 Data,* Phys. Rev. Lett. 109, 181301 (2012)
[40] CDMS collaboration, *Results from a Low Energy Analysis of the CDMS II Germanium Data,* Phys. Rev. Lett. 106:131302, 2011
[41] Z. Ahmed et al., *Results from a Low-Energy Analysis of the CDMS II Germanium Data,* arXiv:0912.3592v1
[42] E. Armengaud et al., *First Results of the EDELWEISS-II WIMP Search using Ge Cryogenic Detectors with interleaved electrodes,* Phys. Lett. B 702 (2011), 329-335
[43] D. Akimov et al, *WIMP-nucleon cross-section results from the second science run of ZEPLIN-III,* Physics Letters B Volume 709, Issues 1–2, 13 March 2012, Pages 14–20
[44] R. Gaitskell, V. Mandic, J. Filippini: http://dmtools.brown.edu/
[45] R. Bernabei et al., *New results from DAMA/LIBRA,* The European Physical Journal C - Particles and Fields 67 (1), 39-49, 2010
[46] E. Daw et al., *The DRIFT Directional Dark Matter Search,* EAS Publications Series, 53 (2012) 11–18
[47] Hiroyuki Sekiya, *XMASS,* arXiv:1006.1473
[48] M.G.Boulay for the DEAP collaboration, *DEAP-3600 Dark Matter Search at SNOLab,* aXiv:1203.0604
[49] E. Aprile, *The XENON1T Dark Matter Search Experiment,* Proceedings of DM2012 at UCLA, arXiv:1206.6288
[50] V. Chepel & H. Araújo, *Liquid Noble Gas Detectors for Low Energy Particle Physics,* JINST 8 R04001 (2013) arXiv:1207.2292v3
[51] Marc Schumann, *Dark Matter Search with Liquid Noble Gases,* arXiv:1206.2169v1
[52] A. Broniatowski et al., *A new high background rejection dark matter Ge cryogenic detector,* Phys Lett B 681 (2009) 305
[53] P. Huff, *The Detector Parameters Determining the Sensitivity of the CRESST-II Experiment,* Doctoral Thesis, Technische Universität München, 2010.
[54] K. Eitel, *The EDELWEISS Dark Matter Search,* IDM 2012, University of Chicago
[55] B. Schmidt, *The EDELWEISS Dark Matter Search: Results and Proposals,* SUSY 2013-08-29, ITCP Trieste, Italy
[56] CDMS Collaboration, *Exclusion limits on the WIMP-nucleon cross section from the first run of the Cryogenic Dark Matter Search in the Soudan Underground Laboratory,* Phys. Rev .D72:052009, (2005)
[57] K. Nakamura et al., *Searches for monopoles, supersymmetry, technicolour etc. (Particle Data Group),* JPG 37, 075021 (2010)
[58] CRESST collaboration, *Results from 730 kg days of the CRESST-II Dark Matter Search,* arXiv:1109.0702
[59] A. Brown et al., *Extending the CRESST-II commissioning run limits to lower masses,* Phys. Rev. D85:021301, (2012)
[60] EDELWEISS collaboration, *A search for low-mass WIMPs with EDELWEISS-II heat-and-ionization detectors,* Phys. Rev. D 86, 051701(R) (2012)
[61] K. Zuber, *Double Beta Decay,* Contemp. Phys. 45 (2004) 491-502

[62] NEMO collaboration, *Measurement of the two neutrino double beta decay half-life of Zr-96 with the NEMO-3 detector*, arxiv.org:0906.2694v5
[63] GERDA collaboration, *Measurement of the two neutrino double beta decay half-life of Zr-96 with the NEMO-3 detector*, arxiv.org:1212.3210v1
[64] H. V. Klapdor-Kleingrothaus et al., *Evidence For Neutrinoless Double Beta Decay*, Modern Physics Letters A, vol. 16, no. 37, pp. 2409–2420, 2001
[65] C. Kraus et al., *Final results from phase II of the Mainz neutrino mass searchin tritium beta decay*, Eur Phys. J C 40, 447 (2005)
[66] N. Aseev et al., *Upper limit on the electron antineutrino mass from the Troitsk experiment*, Physical Review D, vol. 84, no. 11, 2011.
[67] G. Drexlin et al., *Current Direct Neutrino Mass Experiments*, Adv. in High Energy Phys. Vol 2013 (2013)
[68] Bennett, C. L et al. 2012, *Nine-Year Wilkinson Microwave Anisotropy Probe (WMAP) Observations: Final Maps and Results*, arXiv:1212.5225
[69] Das et al., *The Atacama Cosmology Telescope: Temperature and Gravitational Lensing Power Spectrum Measurements from Three Seasons of Data*, arXiv: 1301.1037 (2013).
[70] J. Vergados, H. Ejiri and F.Simkovic, *Theory of Neutrinoless Double Beta Decay*, arXiv: 1205.0649
[71] M. Horoi and C. Stoica, *Nuclear Matrix Element for Two Neutrino Double Beta Decay from ^{136}Xe*, Phys Rev C, 81 024321 (2010)
[72] J. Barea and F. Iachello, *Neutrino-less double-beta decay in the microscopic interacting boson* model, Phys Rev C 79, 044301 (2009)
[73] F. Piquemal, presentation at Neutrino 2012, Kyoto, Japan
[74] GERDA Collaboration, *Results on Neutrinoless Double Beta Decay of 76Ge from GERDA Phase I*, arXiv:1307.4720 (2013)
[75] Alexander Barabash , *SuperNemo Double Beta Decay* Experiment, *J. Phys.: Conf. Ser.* 375 042012 (2012)
[76] A. Gando et al., *Measurement of the double-βdecay half-life of 136Xe with the KamLAND-Zen experiment*, Phys. Rev. C 85 4 (2012)
[77] A. Gando et al., *Limits on Neutrinoless Double Beta Decay of 136Xe with First Phase of KamLAND-Zen experiment and Comparison with Positive Claim in 76Get*, Phys.Rev.Lett.110:062502, 2013
[78] J. Evans presentation, IOP conference 2013, Liverpool, UK
[79] M. Carrettoni, *The CUORE experiment*, Journal of Physics: Conference Series 347 (2012) 012031
[80] Luca Pattavina, *Lucifer: Neutrinoless Double Beta Decay with Scintillating Bolometers*, 2011 J. Phys.: Conf. Ser. 335 012047
[81] Kelvinox 400 Manual, Oxford Instruments
[82] F.Pobell, *Matter and Methods at Low Temperatures*, Springer; 1st. ed. (1992)
[83] P. Colling et al., *Low Energy X-ray Detection in Cryogenic Detectors with Tungsten Thermometers*, Nucl. Instr. And Meth. In Phys Res. A 354 (1996) 408-416
[84] G. Angloher, *Limits on WIMP Dark Matter using Sapphire Cryogenic Detectors***,** Astropart. Phys 18 (2002) 43-35
[85] J. Astr¨om, *Fracture Processes Observed with A Cryogenic Detector*, Phys.Lett. A356 (2006) 262-266
[86] Ed. M.F. L'Amunziato, *Handbook of Radioactivity Analysis*, Academic Press (August 30, 2012)
[87] S.M Seltzer, *Calculation of photon mass energy transfer and mass energy absorption coefficients*, Radiation Research 136, 147-170 (1993)
[88] S. Ingleby, *Cryodetector Readout for Dark Matter Searches*, Doctoral Thesis, University of Oxford, 2012
[89] C. Kittel, *Intro to Solid State Physics*, John Wiley & Sons; 8th Edition (11 Nov 2004)
[90] A. Senyshyn et al., *Thermal structural properties of calcium tungstate*, Phys Rev B 73, 014104 (2006)
[91] E. Olivieri et al., *Excess Heat Capacity in NTD* Ge, Journal of Low Temp Phys May 2006, Vol 143, Issue 3-4, pp 153-162
[92] A.J Dianoux et al., *Inelastic Neutron Scattering in the Amorphous and the Crystalline State: The Phonon-Fracton Density of States*, Phys Rev Let S, Vol 58, 1987
[93] B. I. Shklovskii and A. L. Efros, *Electronic Properties of Doped Semiconductors*, Springer (1984)
[94] E. Pasca et al., *Low temperature properties of NTD Ge: best choice for CUORE experiment*, DOI:10.1142/9789812702708_0016

[95] L.L. *Nagornaya et al.***,** *Tungstate and molybdate scintillators to search for dark matter and double beta decay*, IEEE Transactions on Nuclear Science *56* **(***2009***)**
[96] R Bernabei *et al., Search for double beta decay of zinc and tungsten with low background $ZnWO_4$ crystal scintillators* , 2010 *J. Phys.: Conf. Ser.* 202 012038
[97] V.B. Mikhailik et al., *Luminescence characterisation of $CaWO_4$, $ZnWO_4$ and $CaMoO_4$ scintillating crystals under different excitations*, J. Appl. Phys. 97 (2005) 083523.
[98] V.B. Mikhailik et al., *One and two photon excited luminescence and band gap assignment in calcium tungstate*, Phys. Rev. B 69 (2004) 205110
[99] V. B. Mikhailik, H. Kraus, S. Henry and A. J. B. Tolhurst, *Scintillation studies of CaWO4 in the milli-kelvin temperature range*, Phys. Rev. B, 75 (2007)
[100] V. B. Mikhailik and H. Kraus, *Performance of scintillating materials at cryogenic temperatures*, physica status solidi b (2010) Vol 247, 7, p1583–1599
[101] Y. J. Alloucherie, *Light Energy Conversion of Calcium Tungstate Using A Light Intensifier Tube*, Applied Optics, Vol. 9, Issue 6, pp. 1403-1409 (1970)
[102] Y. G. Zdesenko, et al. *Scintillation properties and radioactive contamination of CaWO4 crystal scintillators*, Nuclear Instruments & Methods in Physics, 538:657-667, 2005.
[103] E.R. Dobrovinskaya et al., *Sapphire: Material, Manufacturing*, Applications, 55 DOI: 10.1007/978-0-387-85695-7_2, (2009)
[104] B.L Zink et al, *Thermal Conductivity and Specific Heat of Thin Film Amorphous* Silicon, 10.1103/PhysRevLett.96.055902
[105] R. Van den Berg et al , *Calorimetric investigation of a-Si and a-Ge in high magnetic fields*, Journal of Non-Crystalline Solids 77 & 78 (1985) 1339-1342
[106] de Dood et al., *Amorphous Silicon Waveguides For Microphonics*, J. Appl. Phys., Vol. 92, No. 2, 15 July 2002
[107] B. Censier et al., *EDELWEISS Read -out electronics and future* prospects, J Low Temp Phys (2012) 167:645–651
[108] ADG1419 Datasheet from Analog
[109] P. Horowitz & W. Hill, *The Art of Electronics*
[110] N. P. Palaio et al., *Neutron Transmutation Doped Germanium Bolometers*, International Journal of Infrared and Millimeter Waves 4 (1983) 933-943
[111] A. Woodcraft et al., *Hopping Conduction in NTD Germanium*, Journal of Low Temperature Physics, Vol. 134, Nos. 3/4, February 2004 (© 2004)
[112] A. L. Efros and B. I. Shklovskii, *Coulomb Gap and Low Temperature Conductivity of Disordered Systems*, J. Phys. C 8, L49 (1975).
[113] D.C Thompson et al., *Characterization of Liquid Crystal Polymer Material and Transmission Lines on LCP Substrates From 30 to 110 GHZ*, IEEE Trans. on Microwave Theory and Techniques, Vol. 52, No. 4, April 2004
[114] S. Chisca et al., *Dielectric and conduction properties of polyimide films*, Semiconductor Conference (CAS), 2011 International (Volume 2) 253 – 256
[115] Galeazzi & McCammon, *Microcalorimeter and Bolometer Model*, J. Appl. Phys. 93, 4856 (2003)
[116] K.D Irwin, *X□ray detection using a superconducting transition□edge sensor microcalorimeter with electrothermal feedback*, Appl Phys Lett 66 1998 (1996)
[117] J.C Mather, *Bolometer Noise: Non-equilibrium Theory*, Appl. Opt 21 1125 (1982)
[118] S.H. Moseley, J.C. Mather & D. McCammon, *Thermal Detectors as X-ray Spectrometers*, J. Appl. Phys. 56, 1257 (1984)
[119] N. Wadefalk et al., *Cryogenic Wide Band Ultra Low Noise IF Amplifiers Operating atUltra- Low DC Power*, IEEE Transactions on Microwave Theory and Techniques, Vol. 51 6 (2003)
[120] Linear Systems LSK 389 Data Sheet
[121] P.L Richards, *Bolometers for Infrared and Millimeter Waves*, J. Appl Phys 76 1 (1994)
[122] J. Zmundias, *Thermal Noise and Correlations in Photon Detection*, Appl Opt 42 4989 (2003)
[123] F. Pröbst, M. Frank, et al., *Model for cryogenic particle detectors with superconducting phase transition thermometers*, J. Low Temp. Phys. 100 (1995) 69
[124] W.S. Boyle and K.F Rodgers, *Performance Characteristics of a New Low Temperature Bolometer*, J Opt Soc Am 49 66 (1959)
[125] P. Gorla et al., *Complete Elimination of 1K Pot Vibrations In Dilution Refrigerators*, Nuclear Instruments and Methods in Physics Research A 520 (2004) 641–643
[126] A. Raccanelli et al., *Eliminating the vibrational noise of continuously filling 1K pots*, Cryogenics 41 (2001) 763–766
[127] C. Kittel and H. Kroemer, *Thermal Physics*, W. H. Freeman; 2nd Edition (January 15, 1980)

[128] J.Lawrence et al.**,** *The thermal conductivity of Kapton HN between 0.5 and 5 K*, Cryogenics Vol 40, Issue 3, March 2000, Pages 203–207
[129] R.B Firestone Table of Isotopes 8th Ed., John Wiley & Sons, 1999
[130] Ed. M.F. L'Amunziato, *Handbook of Radioactivity Analysis*
[131] R.D. Deslattes et al., *X-ray transition energies: new approach to a comprehensive evaluation***,** Rev. Mod. Phys. 75, 35-99 (2003)
[132] EDELWEISS Collaboration, Nucl.Instrum.Meth. A530 (2004) 426-439
[133] A. Brown, *Analysis and Modelling for CRESST-II*, Doctoral Thesis, University of Oxford, 2012
[134] M. Sisti et al. / Nuclear Instruments and Methods in Physics Research A 466 (2001) 499–508
[135] R.S. Graves et al., *The thermal conductivity of AISI 304L stainless steel*, International Journal of Thermophysics, March 1991, Vol 12, Issue 2, pp 409-415
[136] T. Frank, *Development of Scintillating Calorimeters for Discrimination of Nuclear Recoils and Fully Ionizing Events*, PhD thesis, Technische Universität München, 2002
[137] E. Pantic, *Performance of Cryogenic Light detectors in the CRESST-II Dark Matter Search*, PhD Thesis, Technische Universität München, 2008